Structure, chemistry and nanomechanics of grain boundaries in Cu-Ag alloys

Dissertation

zur

Erlangung des Grades

Doktor-Ingenieur

der

Fakultät für Maschinenbau

der Ruhr-Universität Bochum

von

Nicolas Jörg Peter

aus

Köln

Bochum 2020

All paths are the same: they lead nowhere. But one has a heart, the other does not. One makes you strong, the other weakens you.

Carlos Castaneda, The Teachings of Don Juan: A Yaqui Way of Knowledge

Acknowledgment

Henry Ford once said: "The object of education is not to fill a man's mind with facts; it is to teach him how to use his mind in thinking." Every educational system requires teachers to pass on this valuable good - great teachers. During the time I spent completing my dissertation I was lucky enough to have found exactly this in my great mentor Prof. Dr. Gerhard Dehm, who not only expressed his trust by adopting me in his group, but supported me with fruitful discussions, giving valuable advice to proceed my research or to overcome any difficulties. But besides his great mentoring, I also want to express my deepest gratitude of just being a great person; always smiling, lifting people up when needed and mainting a positive atmosphere around him. This really makes life and work feel effortless. Obtainment of my degree formally requires the evaluation of a second supervisor as well. Thus, it is my great honor to have found my second advisor in person of Prof. Dr. Eduard Arzt. His support enabled me to unfold my scientific carrer and finally lead to the destination I chose to perform my dissertation. Besides his continuous support throughout the past years, no question ever remained unanswered reflecting his wisdom and why he belongs in the circle of the great materials scientists. In light of Mr. Ford's words, I am confident to say that my teachers were like candles to me, they partially consumed themselves to light my way into being a scientist.

Besides my supervisors, I have to express my deepest gratefulness to Dr. Christian Liebscher, and now Prof. Dr. Christoph Kirchlechner, the group leaders of the Advanced Transmission Electron Microscopy and the Nano-/ Micromechanics of Materials groups, respectively. Both always had an open door for discussions about any challenges, tought me plenty of techniques

At the end, I have to thank some people who were not only scientifically involved in the accomplishment of this thesis work, but as very well known by world leading sports athletes: behind every great achievement there are also people who help with apparently tiny aspects of the big goal. But big goals, like completing a doctorate, are accomplished by a series of small things brought together. So thank you Dr. Marco Zeiger for being and staying my best friend ever since we entered university and thank you Dr. Andreas Schneider for having been a great group leader back at Leibniz INM encouraging me to step out of my comfort zone and venturing to many new adventures. At the end, I want to point out that small things are becoming great things when done with love. And love is essential in this world to find true happiness. I can only thank my family, not only for their support, but also their trust, for being with me in the good times but also and especially in the bad times. I would not be where I am without you. This includes a special person that I was luckily enough to meet along the way and got to call my love ever since. Thank you Ina for making every step a miracle and supporting me when support was needed. Although spatially seperated in recent years, my mother always found the right words: "The wind is the same to fire as is the absence to love. Sometimes a small blow can turn a small spark into the wildest fire". Thank you for everything.

Abstract

The behavior of a material such as metals, typically strongly depends on the perfectness and purity of its microstructure and crystal lattice. Lattice defects such as dislocations and grain boundaries are known to strongly influence the mechanical performance of metals, often increasing their strength and decreasing their ductility with increasing defect densities. Therefore, whole research fields are solely focusing on e.g. discovering and understanding new plasticity mechanisms or how to tailor a materials grain boundaries to improve the metals properties under special conditions. Solute or impurity atoms inside a crystal lattice typically require the creation of a strain field to be accomodated, therefore these atoms prefer segregation to crystal defects to reduce their energetic contribution to the system. So these atoms not only may alter a materials performance by forming new phases, but also may have a strong influence on defects, which in turn can lead to catastrophic material failure, as e.g. known for the Cu(Bi) system. The aim of this thesis work is to understand how a grain boundary's structure is affected by solute atom segregation on an atomic scale and if the interaction of these is capable of resulting in a noticable change of macroscopic material properties; in this case the mechanical properties or plastic deformation behavior.

A nanofaceting transition at an asymmetric tilt grain boundary in Cu is investigated, which is induced by Ag segregation. Aberration-corrected scanning transmission electron microscopy, atom probe tomography and atomistic simulations were used to explore this grain boundary phase transition The initial reference boundary decomposes into a new, Ag-lean, asymmetric facet segment and a Ag-rich, symmetric $\sum 5$ (210) segment and thus exhibits a preferential segregation behavior. Although, a regular distribution of 1 - 2 nm long segments was iden-

tified first, investigation of the concentration dependence revealed a constant length for the asymmetric segments while the symmetric segments that increase linearly in length with the Ag solute excess and the corresponding bulk concentration. In addition, the initial reference boundary (Ag-free asymmetric grain boundary) was found to adsorb Ag solute excess until a critical threshold before the grain boundary phase transition occurs and was thus identified as first order grain boundary transformation. At high Ag concentrations, the Ag-rich symmetric segments grow in lentgh until all asymmetric segments are consumed and the boundary becomes a continuous Ag-rich, symmetric $\sum 5$ (210) boundary. The experimental results enabled the formation of the first nanofaceting diagram.

Besides the high spatial resolution achieved in aberration corrected scanning transmission microscopy, beam induced dynamic effects have to be considered for quantitative chemical characterization on the level of single atomic columns. Making use of the atomic spatial resolution, the present thesis work is additionally focused on the dynamics of atomically resolved quantitative chemical information, thereby using the capabilities of scanning transmission electron microscopy to explore time related phenomena at a Ag segregated, nanofaceted Cu grain boundary. One of the main findings is that shortest acquisition times just above a reasonable signal-to-noise ratio of many images in combination with a cumulative averaging result in chemical characterization of individual atomic columns, as shown by simulations, even capturing their respective fluctuations over time.

The investigated Ag segregation induced grain boundary nanofaceting transition at an asymmetric tilt grain boundary in Cu was examined in terms of how it influences mechanical performance and especially the plastic deformation mechanisms. The obtained results from *in situ* TEM and atomistic simulations confirmed that a GB phase transition can influence the plastic deformation behavior as the segregation induced nanofaceting transition had structural and chemical implications. Changes in GB structure and introduction of facet junctions prevented deformation twin growth in Cu(Ag), which prevails in pure Cu, and results in frequent nucleation of extended stacking faults along the boundary. Ag absorption at the symmetric $\sum 5$ (210) boundary portions inverted the sign of the resolved shear stress,

which consequently opposed dislocation emission from the boundary. Regarding the correlation with macroscopic properties, the presented results indicate for the first time that a grain boundary phase transition may impact a material's properties other than diffusion or migration, by changing the governing plasticity mechanisms.

Preface

The following publications/manuscripts are imbedded in this thesis:

Manuscript I:

Segregation induced nano-faceting transition at an asymmetric tilt grain boundary in copper

Nicolas J. Peter, Timofey Frolov, Maria J. Duarte, Raheleh Hadian, Colin Ophus, Christoph Kirchlechner, Christian H. Liebscher, Gerhard Dehm

Physical Review Letters, **vol. 121,** pp. 255502, 2018

Manuscript II:

Beam-induced atomic migration at Ag-containing nanofacets at an asymmetric Cu grain boundary

Nicolas J. Peter, Christian H. Liebscher, Christoph Kirchlechner, Gerhard Dehm

Journal of Materials Research, **vol. 32,** no. 5, pp. 968-982, 2017

Manuscript III:

Faceting diagram for Ag segregation induced nanofaceting at an asymmetric Cu tilt grain boundary

Nicolas J. Peter, Maria J. Duarte, Christoph Kirchlechner, Christian H. Liebscher, Gerhard Dehm

Acta Materialia, **vol. 214,** pp. 116960, 2021

Manuscript IV:

Grain boundary nanofaceting transition in copper influencing plastic deformation

Nicolas J. Peter, Tobias Brink, Subin Lee, Blazej Grabowski, Christoph Kirchlechner, Christian H. Liebscher, Gerhard Dehm

Manuscript to be submitted

Author contributions following the CRediT system [1]:

Manuscript I:

Nicolas Peter: Conceptualization, Methodology, Investigation (STEM), Formal analysis, Writing - Original Draft, Visualization **Timofey Frolov:** Methodology, Software, Investigation (Simulations), Writing - Review and Editing **Maria J. Duarte:** Investigation (APT), Formal analysis **Raheleh Hadian:** Investigation (Simulations) **Colin Ophus:** Software, Investigation (STEM image simulation) **Christoph Kirchlechner:** Writing - Review and Editing **Christian Liebscher:** Conceptualization, Writing - Review and Editing **Gerhard Dehm:** Conceptualization, Writing - Review and Editing, Supervision, Funding acquisition

Manuscript II:

Nicolas Peter: Conceptualization, Methodology, Investigation (STEM), Formal analysis, Writing - Original Draft, Visualization **Christian Liebscher:** Conceptualization, Software, Formal analysis, Investigation (Cross-correlation, STEM image simulation), Writing - Review and Editing **Christoph Kirchlechner:** Writing - Review and Editing **Gerhard Dehm:** Conceptualization, Writing - Review and Editing, Supervision, Funding acquisition

Manuscript III:

Nicolas Peter: Conceptualization, Methodology, Investigation (STEM), Formal analysis, Writing - Original Draft, Visualization **Maria J. Duarte:** Investigation (APT), Formal analysis **Christoph Kirchlechner:** Writing - Review and Editing **Christian H. Liebscher:** Conceptualization, Writing - Review and Editing **Gerhard Dehm:** Conceptualization, Writing - Review and Editing, Supervision, Funding acquisition

Manuscript IV:

Nicolas Peter: Conceptualization, Methodology, Investigation (STEM), Formal analysis, Writing - Original Draft, Visualization **Tobias Brink:** Methodology, Software, Investigation (Simulations), Writing - Review and Editing **Subin Lee:** Investigation (STEM) **Blazej Grabowski:** Funding acquisition **Christoph Kirchlechner:** Writing - Review and Editing **Christian H. Liebscher:** Conceptualization, Writing - Review and Editing **Gerhard Dehm:** Conceptualization, Writing - Review and Editing, Supervision, Funding acquisition

Contents

Nomenclature

A	Area
a	Atom size
a	Lattice parameter
A_{probe}	Probe area
a_0	Bohr radius
ABF	Annular bright field
ADF	Annular dark field
α	Semi-convergence angle
APT	Atom probe tomography
ASL	Asymmetric segment length
$\vec{b}$	Burgers vector
$\vec{b_i}$	DSC unit cell vectors
β	Enrichment factor
β	Semi-collection angle
c	Speed of light
C_i	Fitting constants
$C_{(i)}$	Concentration of element i in a reference
C_c	Chromatic aberration
CCD	Charge coupled device
C_i	Concentration of element i in a sample
CMOS	Complementary metal-oxide-semiconductor
C_s	Spherical aberration
CSL	Coincide site lattice

CTEM	Conventional transmission electron microscopy
D	Dislocation spacing
D	Grain size
d_0	Circular probe diameter
D_{acc}	Accumulated electron dose
D_{glo}	Global electron dose
D_{loc}	Local electron dose
d_c	Probe size for chromatic aberration contribution
ΔE	Electron beam's energy spread
$\Delta \gamma$	Change in energy of faceted GB
Δx	Twin width increase
ΔG_S^0	Change in Gibbs energy
$\Delta \mu$	Chemical potential difference
ΔR	Separation of two objects
ΔV	Excess GB volume
Δz	Depth of field
DFT	Density functional theory
d_d	Probe size for diffraction limit contribution
d_s	Probe size for spherical aberration contribution
DSC	Displacement shift complete lattice
d_t	Twin spacing
DXA	Dislocation extraction algorithm
E	Energy per unit area
$E_{Cu(Ag)}^{Junction}$	Energy for partial dislocation emission from facet junction in Cu(Ag)
$E_{Cu}^{Emission}$	Energy for partial dislocation emission in Cu
ΔE_{seg}	Segregation energy
E_{strain}	Strain energy
E_{strain}^{Bulk}	Solute's strain energy in bulk
E_{strain}^{GB}	Solute's strain energy at GB

$E_{Strain}^{Junction}$	Strain energy of facet junction
$E_{Cu}^{Twingrowth}$	Energy for twin growth in Cu
E_0	Electron beam energy
EAM	Embedded atom method
E_c	Dislocation core energy
EDS	Energy dispersive X-ray spectroscopy
E	Young's modulus
EELS	Electron energy loss spectroscopy
ϵ	Energy well depth of Lennard-Jones potential
ETD	Everhart-Thornley-Detector
E_X	Energy of a Bremsstrahlung X-ray
$\vec{f}$	Force experienced by atom
F	Embedding energy
fcc	Face centered cubic
FIB	Focused ion beam
FK	Filled kite structure
FSR	Facet segment ratio
G	Shear modulus
γ_{GB}	Energy of faceted GB
γ_i	Facet segment energy
γ_{ISFE}	Intrinsic stacking fault energy
γ_j	Facet junction energy
Γ_s	Adsorbed solute at the GB
γ_{TFE}	Twin fault energy
γ_{USFE}	Unstable stacking fault energy
γ_{UTFE}	Unstable twinning fault energy
γ_{GB}	GB potential energy
GB	Grain boundary
G	Facet coarsening factor

GPFE	Generalized planar fault energy
$H^{\text{sub}*}$	Sublimation enthalpy
HAADF	High angle annular dark field
HAGB	High angle grain boundary
$[hkl]$	Miller indices of a direction
(hkl)	Miller indices of a plane
I	Probe current
$I_{(i)}$	Measured X-ray intensity of element i of a reference
$I(\vec{r})$	Image intensity
ICP-OES	Inductively coupled plasma - optical emission spectroscopy
I_i	Measured X-ray intensity of element i of a sample
$\vec{K}$	Reciprocal space wavevector
K	K-factor
K	Kramer's constant
k_{ab}	Cliff-Lorimer factor for element combination a and b
LAADF	Low angle annular dark field
LAGB	Low angle grain boundary
λ	Wavelength
Λ	Facet period
λ_{MFP}	Mean free path for elastic scattering
M	Atomic weight
M	Taylor factor
m	Atom mass
m	Size scaling exponent
m_0	Electron mass
μ	Chemical potential
MC	Monte Carlo simulations
MCMD	Monte carlo molecular dynamics hybrid simulations
MD	Molecular dynamics simulations

m	Schmid factor
$\vec{n}$	Grain boundary plane normal vector
N	Number of components
$N(E)$	Amount of produced Bremsstrahlung X-rays of energy E
ν	Poisson ratio
$[N_{Ag}]_N$	Number of Ag atoms
NK	Normal kite structure
N	Avogadro's number
NVT	Canonical ensemble
$O(\vec{r})$	Object function
P	Pressure
$P(\vec{r})$	Point spread function
$p(\vec{r})$	Propagation function
$\phi(\vec{r})$	Specimen potential
PIPS	Precision ion polishing system
$\Psi(\vec{r})$	Electron wave function
$\Psi_{exit}(\vec{r})$	Electron wave function at exit surface
$\Psi_{inc}(\vec{r})$	Incident electron wave function
$\vec{R}$	Rotation axis
$\vec{r}$	Coordinate space vector
R	Gas constant
R	Radius of curvature of dislocation line
r	Distance from nucleus
r_0	Atom separation of Lennard-Jones potential
ρ	Element density
ρ	Electron density
RSS	Resolved shear stress
$\vec{s}$	Dislocation line vector
S	Entropy

SEM	Scanning electron microscopy
σ	Grain boundary energy per unit area
σ_i	Atom's high angle scattering cross-section
ς	Aberration function
SK	Split kite structure
S	Scattering matrix
SSD	Silicon drift detector
SSL	Symmetric segment length
STEM	Scanning transmission electron microscopy
$\vec{T}$	Translation vector
T	Temperature
$t\left(\vec{r}\right)$	Transmission function
t_F	Frame time
t_P	Pixel dwell time
t_S	Seriel time
τ	Stress acting on a dislocation to bow out
τ_{ii}	GB stress tensor components
τ_{RSS-i}	Resolved shear stress acting on the slip planes of grain i
TEM	Transmission electron microscopy
θ	Misorientation angle
θ_0	Characteristic screening angle for scattering
U	Internal energy of a system
$\mathcal{U}\left(\vec{r}^{N}\right)$	Potential energy function with respect to all atomic positions
V	Volume
ω	Characteristic X-ray yield
X_S	Solute concentration in the bulk
X_S^{GB}	Actual solute concentration at the GB
$X_S^{GB,sat}$	Saturation concentration of the GB
ZA	Zone axis

ζ   Friction coefficient for atomistic simulations

Z   Atomic number

Chapter 1

Introduction

1.1 Introduction

Polycrystalline metals remain major contributors for structural and electronic applications. For structural applications, typically macroscopic property requirements need to be met, while for miniaturized systems that are necessary in modern electronic applications, the microscopic properties have to be considered. In either case, the underlying atomic structure and behavior have to be understood to successfully tune a metal's performance to its specific purpose. Properties of pure crystalline metals highly depend on imperfections. For many properties, one-dimensional line defects (dislocations), two-dimensional interfacial defects (grain boundaries), and their interaction are crucial to understanding a metals response at different length scales. Grain boundaries (GB) are interfaces that seperate perfect crystallites (grains) in a polycrystal and are consequently arranged differently compared to their adjacent grains, thus exhibiting their own structure and energy. As a consequence, dislocations generally cannot simply be transmitted from one grain to a second across the boundary, as the change in direction requires additional energy compared to unhindered motion within a perfect grain. The Hall-Petch relation relates such a grain boundary-dislocation interaction with the resulting flow stress of a metal [2, 3]. The smaller the grain size the stronger the material, as less dislocations can pile up in front of the boundary to effectively lower the transmission stress.

While pure metals and their defects are relatively well understood, metal mixtures (alloys) provide a huge playground for obtaining exciting new metal properties and applications. In metallic alloys, line and interfacial defects might be more complex to understand due to segregation of solute atoms to these defective structures as compared to a pure metal. In addition to changing their properties, new phases might even precipitate from these defects and form phase boundaries, creating a new type of interfacial defect from these preexisting ones. The aforementioned Hall-Petch relation indicates that it is beneficial to reduce grain size far below 100 nm for increasing the hardness the most. However, energetically, this is very costly, due to the creation of many new interfaces. Thus, nanocrystalline metals tend to undergo coarsening of their grain structure intrinsically at room temperature [4, 5], thereby reducing the desired hardening effect. Recent research efforts were able to identify segregation of an additional solute element in binary alloys as a means to suppress the coarsening and consequently to act as a stabilizer of nanocrystalline metals by either a kinetic (grain boundary pinning) [6, 7] or thermodynamic (grain boundary energy reduction) [8] approach. However, in addition to the beneficial effect that was found, grain boundary segregation was also found to cause detrimental effects such as embrittlement [9].

To add to the topics complexity, J. W. Gibbs found already in the 19th century that interfacial transitions are possible within the thermodynamic framework [10]. Hart dicussed these transitions later in the 1960s for grain boundaries and referred to them as "two-dimensional

phase transitions" [11]. These structural transitions were then categorized and described as congruent and faceting transitions by Cahn [12] and Rottman [13] in the 1980s and are nowadays termed "grain boundary phase transitions" [14] or "grain boundary complexion transitions" [15]. Although such transitions bare the potential of modifying material properties by targeted grain boundary transitions, such transitions have so far been mainly studied by computational work or by indirect experimental proof like diffusion anomalies. But more challenging, and thus not yet found experimentally, remain the correlation between such structural transitions and their impact on material properties.

Making use of such effects requires not only clarification of the grain boundary structures as well as how and where solute species are absorbed, but also how the energetics are influenced in the process. To resolve grain boundary structures and characterize segregation at the atomic scale, methods of highest spatial and chemical resolution are required, such as aberration-corrected scanning transmission electron microscopy (STEM). In combination with analytical methods such as energy-dispersive X-ray spectroscopy (EDS), electron energy loss spectroscopy (EELS), and atom probe tomography (APT), STEM can be used to obtain chemical information from complex material systems and their interfaces with (close to) atomic resolution. Besides atomically resolved grain boundary structure extraction being difficult by itself and crystallographically a wealth of different structures for different boundaries being possible, structural transitions have hardly been captured experimentally and remain predominantly captured by atomistic simulations. The investigation of different grain boundaries and their influence on plastic deformation remain a tedious task but have been explored by different techniques and carefully performed *in situ* experiments over the last decades [16, 17]. Yet, the correlation of grain boundary structure after interaction with a dislocation has hardly been achieved and experimental proof of structural grain boundary transitions influencing plastic deformation mechanisms is missing completely. The correlation between grain boundary energy, structural changes and mechanical properties is crucial for advancing applications of polycrystalline materials in the frame of research fields like grain boundary engineering.

1.2 Aim and outline of the present thesis work

The aim of the work described in the following pages is the investigation of changes in grain boundary structure and their influence on mechanical properties upon solute segregation. The Cu-Ag binary system was chosen as model system for the study. A Cu bicrystal containing a defined tilt grain boundary was grown utilising the Bridgman technique. Ag was chosen to chemically induce changes in grain boundary structure due to the large miscibility gap of Ag in Cu and the lack of intermetallic compounds in this binary system.

Many topics regarding grain boundaries remain unsolved in literature so far. Especially experimental evidence of grain boundary structures at atomic resolution, and, even more challenging, the transition between two grain boundary states and their correlation to macroscopic physical properties are hardly described. Consequently, the ultimate goal of the present study is to investigate a predefined grain boundary at atomic resolution and identify structural transitions of that grain boundary upon segregation at the same length scale. Besides this static approach, *in situ* experiments should clarify if the observed atomic structures are stable under high-energy electron irradiation conditions and how quantitative information can be extracted for such a complex experimental requirements. Finally, the identified structural transition is correlated to changes in plastic deformation mechanisms and mechanical performance by dedicated *in situ* experiments and atomistic simulations to describe the influence of the transition on plasticity.

The boundary of interest is of asymmetric nature to represent a more realistic scenario, as in common materials special symmetric grain boundaries are less frequent compared to asymmetric and especially random boundaries. Experimentally, methods such as vacuum annealing, diffusion couple approaches, aberration-corrected STEM along with EDS and APT were applied in this work in combination with atomistic simulations aiming to reproduce and understand the observed grain boundary transitions. Targeted miniaturized tests were performed *in situ* inside the scanning electron microscope (SEM) and transmission electron microscope (TEM) in order to observe deformation and scaling behavior and thereby to obtain the first experimental proof of grain boundary transition induced changes in the mechanical performance of the investigated bicrystals.

In particular, the main chapters of this thesis are investigating the following aspects of the chosen asymmetric 34° [001] (920)/(110) tilt grain boundary:

1. The occurance of a chemically triggered grain boundary dissociation from an asymmetric tilt grain boundary into a nanofaceted grain boundary upon Ag segregation, including preferential segregation to special facet segments of this grain boundary. The obtained experimental atomic resolution STEM results are complemented by atomistic Monte Carlo / Molecular Dynamics simulations performed by T. Frolov.

2. In an attempt to advance imaging methodolgy for bicrystals with special STEM imaging condition requirements, the grain boundary was studied under electron beam induced atomic migration conditions. Optimum imaging conditions were identified and STEM image simulations performed to confirm experimental results. Through the dynamic *in situ* study, the facet segment stability could be shown in terms of Ag distribution along the preferentially segregated nanofaceted boundary.

3. The Ag concentration dependence of the observed nanofaceting was investigated by

a diffusion couple approach. Thereby, we could show a concentration dependence of the faceting in terms of facet length. While asymmetric segments remain constant in length, symmetric segments become longer with increasing Ag solute excess concentration. Three distinct grain boundary states were identified, the Ag segregated asymmetric boundary (bulk), the symmetric $\sum 5$ (210) boundary (surface), and the nanofaceted window inbetween these two extremes.

4. The connection between structural changes investigated above and changes in deformation behavior induced by Ag segregation via *in situ* small scale mechanical testing inside the SEM/TEM and atomistic simulations (performed by T. Brink) was established. It was shown that the actual deformation behavior changed from deformation twin growth along pure Cu grain boundaries, to partial dislocation and extended stacking fault emission from the Ag-segregated nanofaceted boundary, due to stress concentration sites at the junctions of the nanofacets. The Ag-segregated, symmetric $\sum 5$ (210) boundary did not show dislocation emission, as Ag introduction reduced the acting resolved shear stress to counteract dislocation emission from the grain boundary.

Chapter 2

Background

2.1   Cu and the Cu-Ag systems

Cu is one of the most used metals on earth. It crystallizes in a face-centered cubic (fcc) crystal structure. Due to its favorable properties, such as good thermal and electrical conductivity, its unique color and being antimicrobial, it is used in a variety of applications like in building construction, electric power generation and transmission as well as in the car industry. Around 34 % of the entire market share of semi-finished Cu products is occupied by the electrical power and power utility sectors, with principal products being building wire and power cables [18]. The importance of Cu is even increasing in future, as e.g. according to research commisioned by the International Copper Association the global Cu demand for solar and wind energy technologies will increase by 56 % by 2027, as compared to 2018 levels [19, 20]. Cu is one of the most intensely studied metals, and often acts as a model system to study a variety of physical properties, e.g. solid state diffusion [21–23] and mechanical properties and deformation mechanisms [24–28].

Another advantage of Cu is its great alloying capabilities with many other elements. Cu(Zn), referred to as brass, enhances corossion properties, thermal conductivity and makes the alloy more workable and durable. Cu(Ni) is used in coins to achieve excellent corrosion resistance, increase strength and toughness at the cost of reduced thermal and electrical conductivity. Lastly, Cu(Sn), referred to as bronze, exhibits increased hardness and corossion resistance along with low metal on metal friction, while compromising ductility. These alloys are prominent examples, which broaden the application range of Cu significantly. However, there are also detrimental alloying elements, for example, Bi, which is one of the strongest embrittlement inducing elements [9]. To understand the causes of this detrimental influence, Cu-Bi alloys have been subject to numerous experimental and simulation studies.

Another special Cu alloy is the Cu(Ag) system. Regarding its phase diagram studied by Subramanian and Perepezko (Figure 2.1) [29], there are three main phases: (i) a Cu-rich phase with Ag being in solid solution for a maximum of 8 wt. % (4.9 at. %), (ii) a Ag-rich phase with Cu being in solid solution up to 8.8 wt. % (14.1 at. %) and (iii) a liquid phase. There is a miscibility gap present between the two solid phases and an eutectic at 779°C, at a Cu concentration of 28.1 wt. % (39.9 at. %), which is the temperature with highest solid solubility of the two solid phases. The Cu(Ag) system is special, as its limited solid solubilities do not agree with the corresponding Hume-Rothery rules [29]. The two solid phases are both face centered cubic phases (space group $Fm\bar{3}m$, Strukturbericht designation A1).

Low Ag alloyed Cu provides some benefits over pure Cu, which make these alloys attractive to applications that require good electrical conductivity in combination with oxidation resistance such as printable and flexible electrodes [30]. Alloying up to 0.1 at. % results in increased strength, wear resistance, and heat resistance due to solid solution formation, while the

thermal and electrical conductivity remain almost unaffected [31]. These alloying benefits unfortunately cannot be further improved by additional alloying, as, according to the Cu-Ag equilibrium phase diagram [29] (Figure 2.1), the room temperature solid solubility is around 0.1 at. %. In fact, for higher concentrations, the phase diagram exhibits a huge miscibility gap from about 0.1 at. % Ag in Cu to about 99.9 at. % of Ag in Cu at room temperature. Furthermore, no additional stable phases, such as intermetallic compounds, are present in this system. Although this might seem unfavorable for industrial applications, there are a few studies showing promising properties of Cu-Ag alloys with Ag contents above the solid solubility limit. For instance, Li et al. reported ultrahigh oxidation resistance and high electrical conductivity in Cu-Ag powder (3 at. % Ag) with a continuous Ag network precipitated along the powder particles' grain boundaries [32]. Y. Sakai and H.-J. Schneider-Muntau reported ultra-high strength and high conductivity in Cu-Ag wires with Ag contents up to 24 wt. % (about 16 at. %) as candidate conductors for high-field pulse magnets [33].
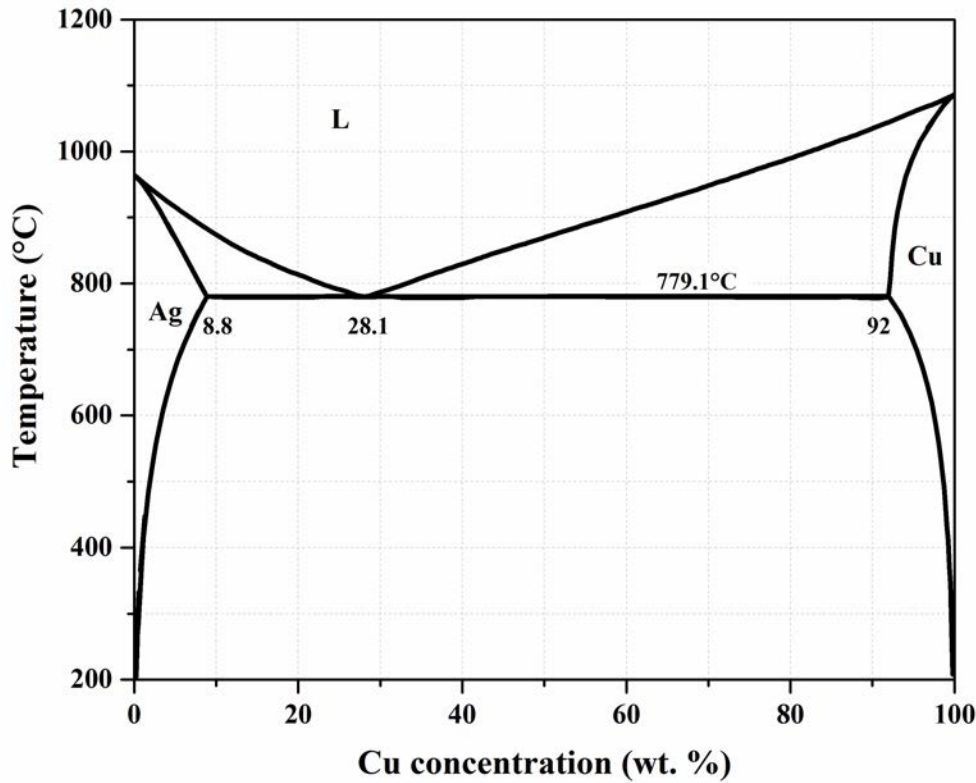
Figure 2.1: Redrawn, experimentally determined Ag-Cu phase diagram as assessed by P.R. Subramanian and J.H. Perepezko in [29].

Besides the technically relevant properties of Cu-Ag, the low solubility and large difference in atomic number ($Z_{Cu} = 29$, $Z_{Ag} = 47$) make this system an ideal model system to study segregation phenomena inside the transmission electron microscope. The miscibility gap in the Cu-Ag alloy acts as driving force for Ag segregation to internal crystal defects, especially

grain boundaries. By adsorption of solute atoms, the excess free energy of these defects generally decreases [8]. Exceeding the solubility limit would lead to the formation of Ag precipitates, which is not studied here, but can act as indicator if the solubility limit has been exceeded.

Generally speaking, it is known that grain boundaries, and solute segregation to these internal interfaces, play a crucial rule for a material's overall mechanical behavior. In an attempt to rate the influence of many different solute species on mechanical properties - in terms of grain boundary cohesion, which is related to embrittlement - Seah formulated a theoretical pair bonding or "quasichemical" approach in the 1980s [34]. He formally found that the loss in fracture energy of the grain boundary atoms is proportional to the difference in sublimation enthalpy H^{sub*} of the matrix and segregant atoms. The predictions obtained are redrawn in a sublimation enthalpy vs. atom size diagram in Figure 2.2 and were confirmed experimentally for several cohesion enhancing solutes, e.g. B [35], Ni [23] and Co [23], as well as for several GB embrittling solutes, e.g. O [36], Na [37], Se [23], Ge [23] and S [38].

Following the predictions of Seah, it becomes apparent that Ag segregation to grain boundaries in Cu might have a detrimental effect on grain boundary cohesion. However, despite many systems confirming Seah's predictions, whether Ag is an embrittling species is still uncertain. It was shown by calculations to "destrengthen" a Cu grain boundary [23], but was also reported to compete with S in terms of vacancy attraction, and may therefore reduce embrittlement induced by S [39]. Even if this does not reflect the inherent tendency of Ag to increase grain boundary cohesion, it becomes clear that the effect of solute segregation to grain boundaries may be much more complex than it appears in the model established by Seah. In addition, Seah did not consider structural transitions induced by solute segregation to such interfaces that may change macroscopic material properties.

In conclusion, the Cu and Cu-Ag systems are not only relevant for industrial applications, but also provide a suitable model system to comprehensively perform a multitude of experiments and atomistic simulations, especially regarding segregation phenomena and mechanical properties.

2.2 Grain Boundaries

All crystalline solids and especially metals arrange their atoms on distinct crystal lattices, which always contain crystal defects of some sort as a consequence of equilibrium thermodynamics. In fact, the macroscopic properties of crystalline metals are governed by the amount and type of defects within the material, which are briefly introduced here based on [40]. Crystal defects are conventionally categorized according to their dimensionality into 0-D, 1-D, 2-D and 3-D defects.
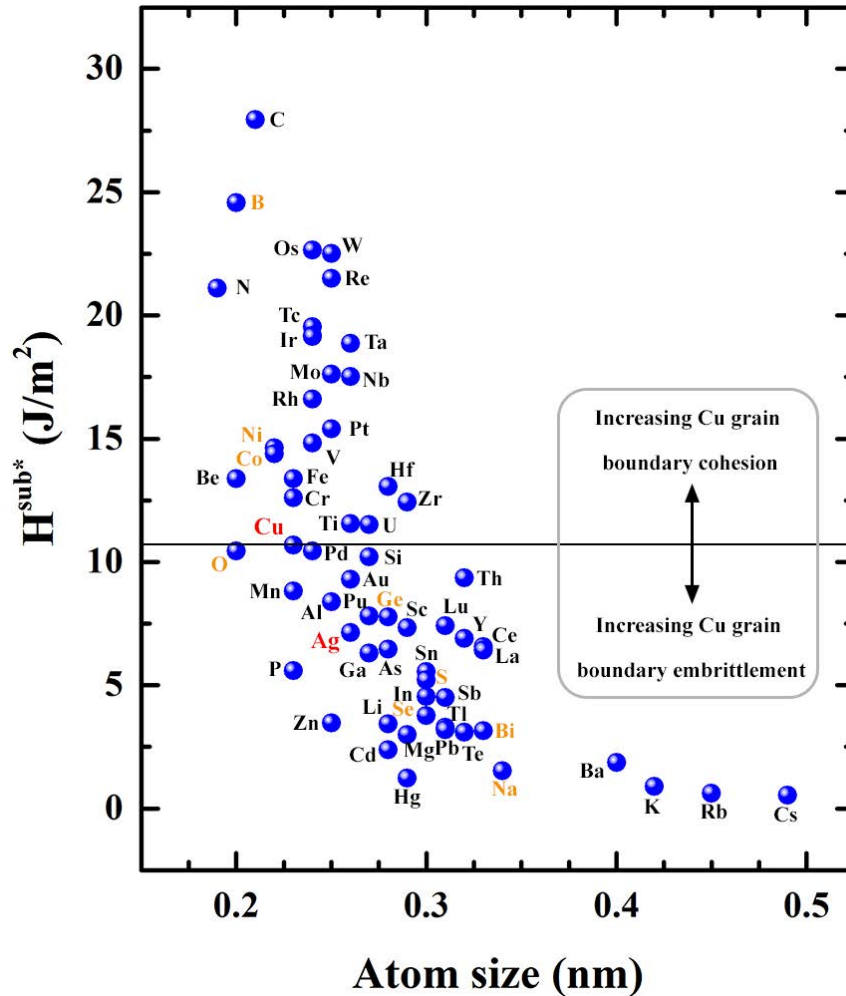
Figure 2.2: Cohesion/embrittlement plot for matrix and segregant elements based on the compilation of H^{sub*} (sublimation enthalpy per unit area) values as a function of the atom size a (calculated from the atomic weight M and the element's density ρ according to $M = \rho N a^3$ with N being Avogadro's number). The horizontal line represents the locus dividing those elements which reduce the fracture energy of Cu (embrittling) from those which increase it (cohesion enhancing). The present Cu-Ag system is highlighted in red letters, while elements in orange were confirmed to follow the predictions by experiments or simulations [23, 35–38]. The plot is redrawn from [34].

Zero-dimensional defects (0-D), also called point defects, are mainly vacancies (missing atoms), interstitial or substitutional atoms in the lattice, and a combination of a vacancy and a displaced interstitial atom, commenly referred to as Frenkel pair. Vacancies, for example, are of major importance for diffusion processes in metals, including diffusion based phase transformations.

One-dimensional defects (1-D) are crystalline line defects, also referred to as dislocations. The main types of full dislocations are edge-type, screw-type and mixed dislocations, which are composed of a mixture of the first two types. All dislocations are characterized by their line vector $\vec{s}$ and Burgers vector $\vec{b}$. The Burgers vector is determined, amongst other

means, by a Burgers circuit around the dislocation core, and remains constant along the dislocation line. The line vector can change along the dislocation line, as is the case for mixed dislocations. Dislocations typically glide or slip only on planes of highest packing density, e.g. the {111} type planes for fcc material, as their resistance to glide on less densely packed planes, expressed by the Peierl's-Nabarro equation [41, 42], does increase significantly. The same holds true for a fcc metal's slip direction, which is of <110> type. Thus fcc materials like Cu and Ag generally deform on a {111}<110> type primary slip system; 12 distinct systems of such type exist, with a Burgers vector $\vec{b} = \frac{a}{2} < 1\bar{1}0 >$ (a being the lattice parameter). Instead of atomic glide along the <110> direction, it is energetically easier to glide via two partial steps along the <112> direction, which results in the same end point. Thus, full dislocations in fcc materials split into two partial dislocations according to the dislocation reaction $\frac{a}{2}[\bar{1}01] = \frac{a}{6}[\bar{2}11] + \frac{a}{6}[\bar{1}\bar{1}2]$. Thus, partial dislocations have a Burgers vector of type $\vec{b} = \frac{a}{6} < 112 >$. This splitting reaction reduces strain energy of a full dislocation U_{FD} from $U_{FD} = G\vec{b}^2 = Ga^2/2$ to the sum of $G\vec{b}^2$ for the two partials $U_{PD} = Ga^2/3$. Upon splitting, the two partial dislocations repel each other. As a consequence, a so-called stacking fault is formed between the leading and trailing partial dislocations. As this stacking fault creation requires energy, it stabilizes the separation of partials to a distinct width, from which the stacking fault energy can be determined. If more stacking faults are formed by partial dislocation creation and if these stacking faults overlap, a twin is formed with twin boundaries enclosing the twinned area.

Two-dimensional (2-D) or planar defects are internal material interfaces. Two main types of such interfaces can be discriminated. On the one hand, interfaces separating two crystalline regions of the same chemical composition and crystal structure, but different crystal orientation, i.e. two misoriented grains, are referred to as grain boundaries (homophase boundaries). Stacking faults and twin boundaries, described in the context of partial dislocations above, are also considered homophase boundaries and thus are two-dimensional defects. On the other hand, interfaces separating regions of different chemical composition and, but not necessarily, different crystal structures or crystal orientations are formed between two different phases and are thus referred to as (hetero)phase boundaries.

Finally, volume defects (3-D) are second phase inclusions like oxides, nitrides, carbides or intermetallic precipitates. However, these volume defects can also form by aggregation of point defects, e.g. in the form of voids when vacancies aggregate. The defect size can be as small as few nanometers, but can also be on the order of several micrometers.

2.2.1 Grain boundary descriptions

The description of grain boundaries in this section is mainly based on [40, 43–45]. Following Lejček, "a grain boundary in a solid crystalline material is a region separating two crystals

(grains) of the same phase. These two grains differ in mutual orientations and the grain boundary thus represents a transition region, where the atoms are shifted from their regular positions as compared to the crystal interior." [43]. To unambiguously describe a grain boundary, at least eight parameters were identified that have to be considered, which are schematically illustrated in Figure 2.3. Three parameters are assigned to the misorientation of two grains, which is commenly defined using a rotation axis $\vec{R} = [h_0 k_0 l_0]$ and a rotation (misorientation) angle θ. Two parameters are required to define the grain boundary inclination, which is achieved by defining two grain boundary plane normal vectors $\vec{n} = [h_n k_n l_n]$ with reference to their respective, adjacent grains. These five parameters can be influenced externally and are generally referred to as the five macroscopic grain boundary degrees of freedom (Figures 2.3a and 2.3b). With these parameters grain boundaries are in general denoted formally as $\theta° \left[h_0 k_0 l_0 \right], \left(h_{n_A} k_{n_A} l_{n_A} \right) / \left(h_{n_B} k_{n_B} l_{n_B} \right)$. However, there are at least three more (microscopic) parameters for a so-called translation vector $\vec{T}$ (rigid body translations) (Figures 2.3c and 2.3d). This vector originates from the grain boundary being constrained by
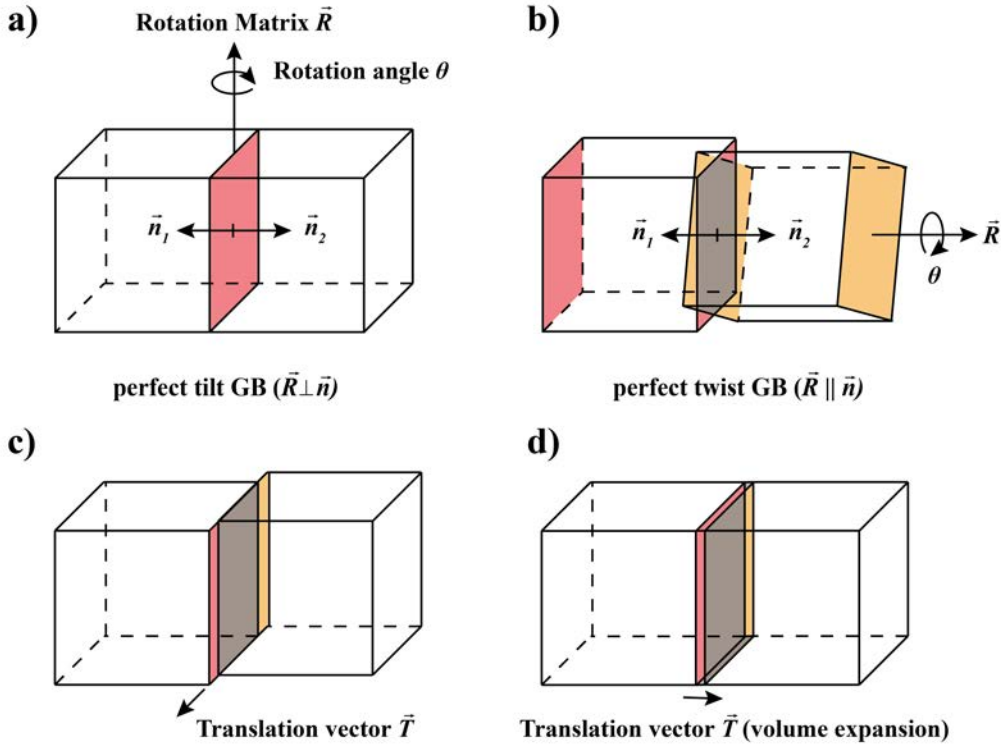
Figure 2.3: Illustration of at least eight parameters for a GB to be defined. (a) and (b) represent the five macroscopic parameters $\vec{R}$ and θ from the misorientation and GB normal $\vec{n}_i$, while (c) and (d) show two modes of rigid body translations $\vec{T}$, one being associated with a volume expansion of the boundary (d).

adjacent grains. In an attempt to reduce the boundary's energy, it dictates the equilibrium structure of the boundary under actual external thermodynamic variables such as temper-

ature, pressure and chemical potential. This fact already indicates that a grain boundary's structure can be influenced by changing one or more of these variables. Finally, all parameters together dictate the grain boundary properties, especially the grain boundary energy. In an attempt to classify different grain boundaries it has become standard to put the rotation axis in relation to the grain boundary normal. As a result, grain boundaries are distinguished as either perfect tilt ($\vec{R} \perp \vec{n}$, compare Figure 2.3a), perfect twist ($\vec{R} \parallel \vec{n}$, compare Figure 2.3b), or mixed grain boundaries. In addition, grain boundaries are classified as symmetric or asymmetric. For a symmetric boundary, the boundary plane is actually a plane of mirror symmetry between the two grains (compare Figure 2.5d). In this case the general boundary notation collapses to $\theta° [h_0 k_0 l_0] (h_n k_n l_n)$, as the plane normals have to be of the same family to fulfill symmetry. All grain boundaries that do not fulfill this prerequisite, are classified as asymmetric.

The variability of the translation vector indicates already that the atomic arrangement of a grain boundary can be very complex and theoretically results in an infinite amount of distinct grain boundaries with defined structures. However, experimentally there is a much smaller number of discrete structures due to energetic reasons. Although initially grain boundaries were anticipated to be amorphous [46, 47], bubble raft experiments indicated ordered arrangements of atoms (Figure 2.4a) [48, 49]. Many models emerged to describe these arrangements, which were summarized and critically discussed by Gleiter [44]. Although some work on the initial idea of amorphous grain boundaries can still be found occasionally [50], it is generelly accepted that these interfaces contain ordered structures in most cases.

From a structural point of view two distinctly different types of atomic arrangements can be found. For small misorientation angles θ termed low angle grain boundaries (LAGB), the lattice mismatch can be accommodated by creating a dislocation wall (edge dislocations for tilt boundaries and screw dislcoations for twist boundaries) (Figure 2.4a). It was found experimentally, within the dislocation model, that increasing the misorientation leads to a reduced dislocation spacing in the wall, which creates the grain boundary (Figure 2.4b). Read and Shockley developed a theoretical, still valid model that formally described the dependence of misorientation θ on the magnitude of the Burgers vector $\left|\vec{b}\right|$ and the dislocation spacing D according to $\frac{|\vec{b}|}{D} = 2\sin\frac{\theta}{2} \approx \theta$ [51]. Based on elastic continuum theory, the elastic contributions of every dislocation in the wall can be summed up and the LAGB energy E per unit area was calculated to follow

$$E = \frac{\theta}{\left|\vec{b}\right|} \left[\frac{G\vec{b}^2}{4\pi (1 - \nu)} \ln \frac{1}{\theta} + E_c \right] = \theta(A - B\ln\theta) \tag{2.1}$$

[43, 51] with G being the shear modulus, ν the Poisson ratio and E_c the energy of the
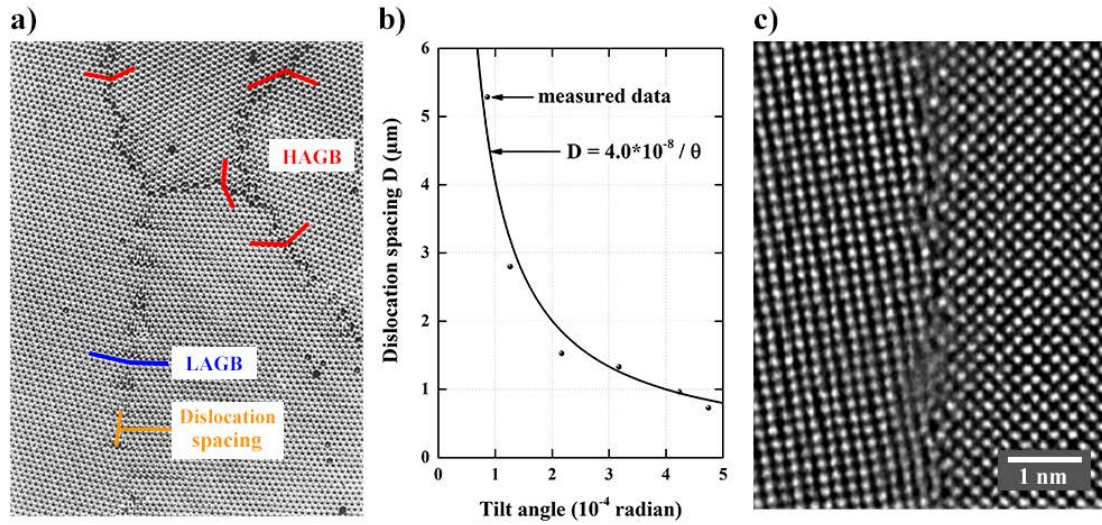
Figure 2.4: Discrimination between low angle grain boundaries (LAGB) and high angle grain boundaries (HAGB) is based on exceeding a 15° misorientation angle, as exemplified in a bubble raft model system in (a) [43, 48]. LAGBs are made of dislocation walls, which follow the Read-Shockley model of decreasing dislocation spacing to accommodate higher misorientations (b) [40]. At 15° the model breaks down and grain boundary structure becomes a complex reorganisation of atoms, as shown in the aberration-corrected electron micrograph of an asymmetric tilt grain boundary in [001] zone axis orientation in Cu (c).

dislocation core. This model holds well for LAGB with $\theta \lesssim 13 - 15°$ corresponding to $D \approx 4 \left| \vec{b} \right|$ [43] and was developed on basis of edge-type dislocations in low angle tilt grain boundaries.

Generally, 15° misorientation has been accepted to mark the transition between the LAGB and high angle grain boundary (HAGB) domains, as experiments have also shown that around these angles, grain boundary properties change abruptly [52–54]. Above this limit, the dislocation density would just be too high to be accomodated, i.e. dislocations would overlap, and the atoms of the grain boundary start rearranging (Figure 2.4c). The structure, but also the energy, of a HAGB become hard to predict and generally have to be observed experimentally or be determined by simulation work. These boundaries are categorized as either being general or special grain boundaries. The latter ones "exhibit sharp extremes at any property" according to [43], such as for example, distinctly reduced grain boundary energy, as shown in Figures 2.5a and 2.5b for many Cu tilt HAGBs. Deep energy cusps are visible for some boundaries in the energy-misorientation plots.

For energetic reasons, atoms in a perfect crystal occupy positions to keep the crystal at its lowest free energy state. Any displacement of atoms increases the energy and is thus not favored. At grain boundaries, the perfect arrangement of atoms is disrupted. Consequently, atoms should arrange in a way as to get as close to the perfect crystal lattice as possible or even contain atoms that are shared by both abutting grains. Such atomic positions are
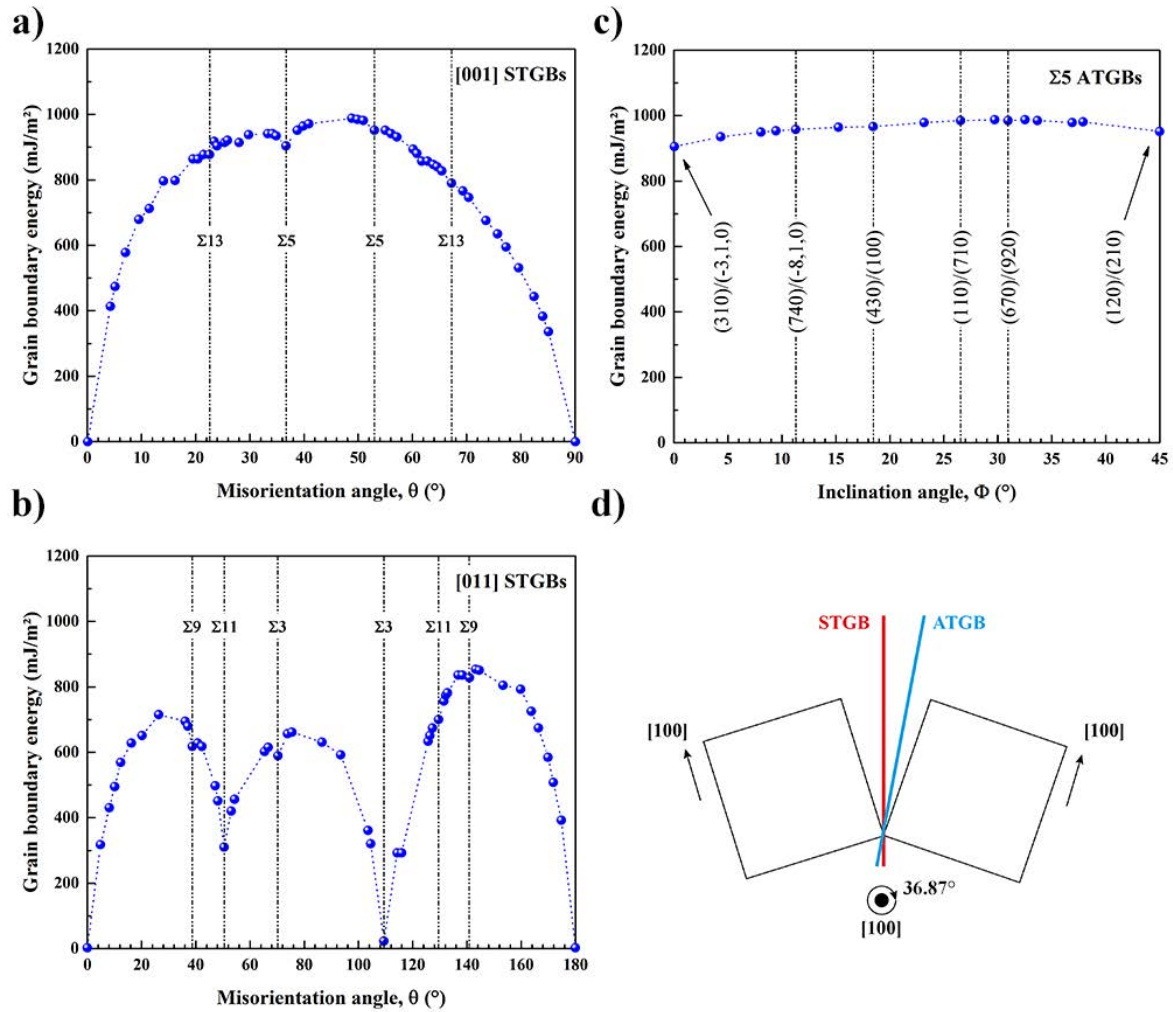
Figure 2.5: Grain boundary energy dependence on misorientation angle θ for symmetric Cu tilt grain boundaries (STGBs) for (a) the [001] rotation and (b) the [011] rotation axis systems. For asymmetric tilt grain boundaries (ATGBs) the grain boundary energy dependence on the inclination angle Φ is depicted in (c). All graphs originate from atomistic simulations and are redrawn from [55]. The difference between symmetric and asymmetric tilt grain boundaries is schematically shown in (d) for the $\Sigma5$ system, corresponding to a 36.87° rotation around the [001] rotation axis between both abutting grains.
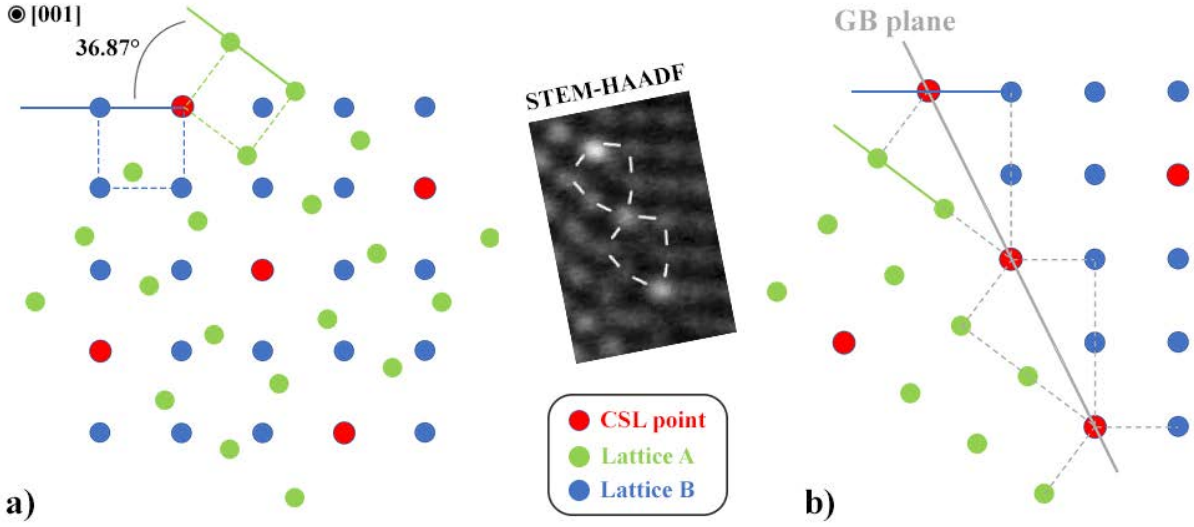
Figure 2.6: (a) Coincide site lattice (CSL) construction exemplified at a Σ5 grain boundary (36.87° misorientation). If two identical lattices (green & blue) are overlaid and misoriented by distinct angles, some atoms sites coincide (red). Because of symmetry, these points form a new, bigger lattice - the CSL (in the example every fifth atom of one lattice's plane is a CSL position). (b) Forming a symmetric Σ5 (210) grain boundary, the mirror plane runs exactly through the CSL positions. Atoms from lattices A or B not belonging to the respective grains have been removed. Comparison of this model reveals very good agreement with experiments for the shown case of an experimental Cu grain boundary (STEM image taken from [57]).

termed coincide sites, which form the foundation of the coincidence site lattice (CSL) model. This concept was first described by Kronberg and Wilson in their study on recrystallization behavior of Cu [56]. The CSL can easily be obtained for tilt rotations of two crystals as exemplified in Figure 2.6. Two cubic lattices (green & blue) are superimposed in a way that all atom positions coincide (full self-coincidence). One of the two lattices is rotated around the common tilt axis normal to the paper plane by distinct angles (Figure 2.6a). Initially, no atoms will coincide anymore but eventually distinct patterns emerge at which high densities of atoms (red atoms in Figure 2.6) of both crystals coincide again (partial self-coincidence). These atoms form a new bigger lattice than the lattices of the two constituent grains, i.e. the CSL. A 36.87° rotation around a common [001] axis is one of these distinct rotations with a high density of coincide sites as exemplified in Figure 2.6a. In fact, every fifth atom of each respective lattice coincides with an atom of the second lattice. Based on this CSL model, HAGB are often characterized by their Σ value. It is defined as:

$$\Sigma = \frac{volume \; elementary \; cell \; of \; CSL}{volume \; elementary \; cell \; of \; crystal \; lattice} \tag{2.2}$$

For the 36.87° [001] rotation, $\Sigma = a\left(a\sqrt{5}\right)^2/a^3 = 5$, i.e. every fifth atom occupies a coincide site (a being the lattice parameter). Ranganathan recognized an alternative to obtain the Σ value of symmetric boundaries in cubic materials according to $\Sigma = \delta(h^2+k^2+l^2)$, with δ being
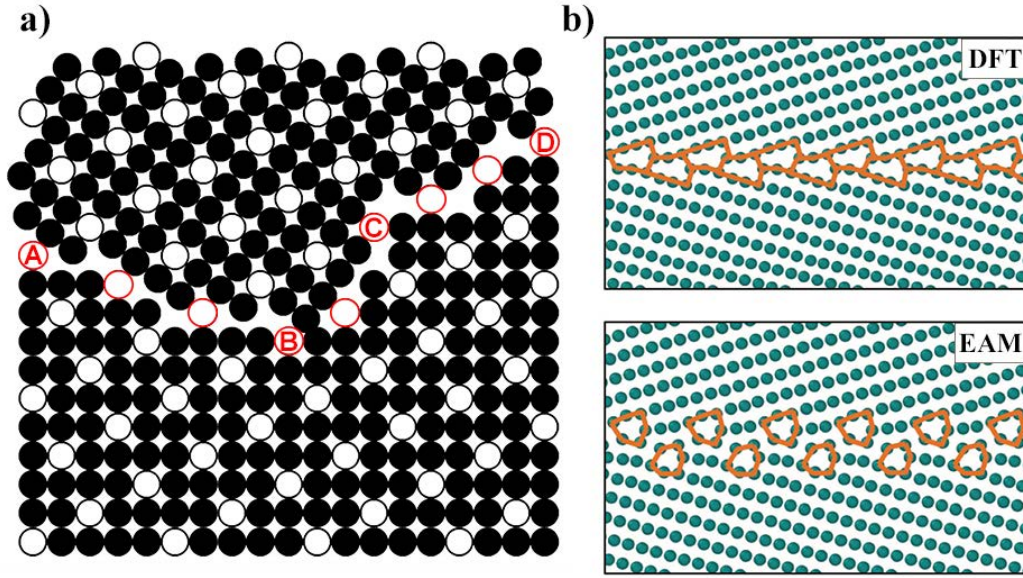
Figure 2.7: (a) Geometric model of the 36.9° [100] tilt bicrystal with simple cubic lattice. The circles represent the positions of individual atoms in misoriented crystals, the empty circles denote the coincidence sites (red circles for the sites inside the grain boundary). The orientation of the grain bonudary varies from {013} symmetrical (A-B), through (001)/(034) asymmetrical (B-C) to {012} symmetrical (C-D). The figure is redrawn from [43]. (b) Comparison of γ-surface constructed Σ27(552)[1$\bar{1}$0] grain boundaries in W using DFT and two EAM potentials highlighting the need for experimental confirmation (images taken from [59]).

either 1 or ½ for $(h^2 + k^2 + l^2)$ being odd or even, respectively [58]. A list of the few rotations resulting in high density CSL positions and thus low Σ boundaries are tabulated in [58]. As mentioned above, it was observed that some special boundaries reveal special properties in terms of recrystalization. There are also special boundaries exhibiting comparably low grain boundary energy. These could be linked to high density coincide site boundaries, i.e. low Σ boundaries (compare e.g. Figure 2.5b). Regarding energy this makes sense, as these boundaries contain a high density of "perfectly fitting" atoms, which do not increase the free energy significantly. The drawback of this popular model is that the CSL model is based purely on geometry. Thus, it does not consider atom position relaxations and their associated differences in bonding, for instance. In addition, CSL boundaries may be of symmetric or asymmetric character, while retaining their misorientation, as illustrated in Figure 2.7a. Thus, the model is only of limited use to determine or even predict grain boundary structures. Specific methods have been established to determine the distinct structures and energies of such planar defects. For instance, high-resolution (S)TEM has been used to determine grain boundary structures [60] and is becoming more and more a standard technique for extraction of quantitative information with aberration-corrected microscopes [61]. In terms of grain boundary energy determination, grain boundary grooving experiments have become standard experimental techniques [62, 63]. Atomistic simulations like molecular dynamics
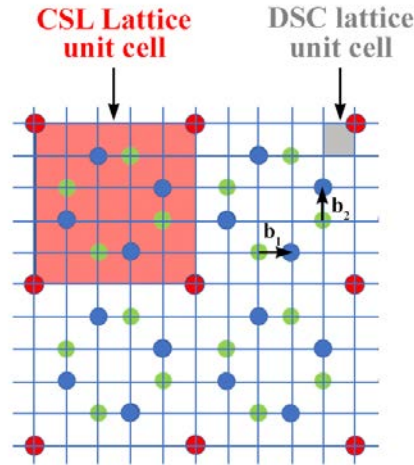
Figure 2.8: Illustration of a dichromatic pattern of two simple cubic crystals, green and blue dots) rotated by 36.87°, as the case for a $\Sigma5$ {210} grain bonudary). In the pattern there are points that overlap, which are colored red and form the CSL lattice. A CSL unit cell is highlighted by a red square. The blue grid is composed of two vectors b_1 and b_2, which form the DSC lattice. A DSC unit cell is highlighted by a grey square. Both lattices describe a translational symmetry of the entire bicrystal (CSL lattice) and the relative displacement between two grains (DSC lattice). [68]

(MD), embedded atom method (EAM) and density functional theory (DFT) calculations are also prominent methods for structure and energy determination of grain boundaries [64–67]. Very recent computational work using evolutionary algorithms has been able to perform automated searches of a multitude of grain boundaries in a given system and thereby predict new grain boundary structures based on lowest energy considerations [59]. It has to be stressed, however, that structure and, in the best case, energy predictions from computational work should always be validated by experiments, if possible, to avoid ambiguities (Figure 2.7b). Grain boundaries may not always be perfect, in fact, they may contain defects like steps, dislocations or disconnections (a combination of both). To analyze such defects another important lattice has been introduced, the "displacement shift complete" (DSC) lattice [69], which has been referred to also as "displacements which are symmetry conserving" [70]. A thorough introduction and applications of this lattice is provided for example in [68]. The construction of this lattice starts analogous to the CSL lattice (compare Fig. 2.6a) with the dichromatic pattern of two simple cubic crystals, green and blue dots in Figure 2.8, being rotated by 36.87° around a common axis, the dichromatic pattern. Overlapping points forming the CSL lattice are highlighted in red and a CSL lattice unit cell is also highlighted in red. Two vectors can be found that connect a position of the green lattice with its closest neighbor from the blue lattice, i.e. b_1 and b_2. Replication of these vectors forms the blue grid, which is the DSC lattice. A unit cell of the DSC lattice is highlighted in grey. This lattice is useful to disconnections for instance. For a symmetric $\Sigma5$ (210) grain boundary, for

instance, which results from the described dichromatic pattern, a disconnection is composed of a dislocation with a Burgers vector equivalent to b_1 or b_2 of the DSC lattice shown in Figure 2.8 and an additional step. Any movement of the pattern along one of these nearest neighbor vectors will conserve the lattice and just shifts it. Thus, while the CSL lattice implies the translational symmetry of the entire bicrystal, the DSC lattice implies this symmetry of the relative displacement between two grains [68].

2.2.2 Grain boundary thermodynamics and transitions

Grain boundaries have been introduced as interfacial defects. Consequently, they should follow the general description of interface - and the even better described - surface thermodynamics [71]. If a three-dimensional network of grain boundaries in a polycrystal is considered, the stable arrangement of the network terminating at the surfaces indicates that the network remains in a local minimum of a potential. Therefore, each component (grain boundary) can be treated thermodynamically and the thermodynamic state functions are needed, although grain boundaries themselves are non-equilibrium defects compared to, for example, vacancies. The first thermodynamic description of interfaces was provided by Gibbs over one century ago [10] and was based on dividing surfaces. Cahn later established a still valid equivalent concept [72]. Consider a bicrystal with two grains differing only by their orientation and being separated by a planar grain boundary. When a bicrystal grows, Gibbs noted already that the internal energy U of the system increases according to

$$dU = TdS - PdV + \sum_{i=1}^{N} \mu_i dn_i + \sigma dA \tag{2.3}$$

with T being the temperature, S the entropy, P the pressure, V the volume, N the number of components in the system, μ the chemical potential, σ the grain boundary energy per unit area and finally A the grain boundary area. Cahn defined σ as

$$\sigma = \left(\frac{\partial U}{\partial A}\right)_{S,V,n_i}, \tag{2.4}$$

which represents the change in the internal energy of a closed system with a change in grain boundary area for constant system entropy and volume [72]. This relation can be rewritten using the fundamental thermodynamic relation $G = U + PV - TS$ to

$$\sigma = \left(\frac{\partial G}{\partial A}\right)_{T,P,n_i}. \tag{2.5}$$

Lejček highlighted this equation as "probably the most important representation of the grain boundary energy per unit area" [43]. It suggests an increase in Gibbs energy of a crystal in

the presence of grain boundaries. However, the exact increase of the Gibbs energy depends on the grain boundary energy, which strongly depends on crystal orientations and thus also on the atomic structure of a grain boundary (compare energy vs. misorientation plots in Figure 2.5). In addition, the GB energy depends on the state variables: temperature, pressure and composition, as seen in Equation 2.5.

As GB energy and structure are related to thermodynamic state variables, phase spaces were considered for grain boundaries similarly to phase spaces of bulk alloys that are commonly known as phase diagrams. Theoretical investigation of transitions at interfaces dates back to some work carried out by Gibbs, where he considered the possibility of different interfacial states and derived the criteria for their equilibrium and stability [73]. Transitions at planar GBs were later discussed by Hart [11, 74], who referred to them as "two-dimensional phase transformations". He discussed that if a grain boundary has two distinct states (phases), these both have their own state function and dependence of energy on, for instance, temperature (Figure 2.9a). If there is a point at which the two energy curves intersect each other, there is a transition of the lowest energy state from one phase to the other, which should involve a transition of the grain boundary phase. Theoretically, the intersection point is a point of coexistance of both phases. Experimental evidence of such transitions was found mainly by indirect observations. Similar to the diagram already anticipated by Hart, recent experimental studies by Divinski et al. explained abrupt changes of materials properties by structural transitions at grain boundaries [22, 75]. It was found in their experimental work that diffusivity of Ag at a $\Sigma 5$ [001] (310) grain boundary in Cu does not follow a simple Arrhenius behavior for different temperatures, but rather exhibits a transition point as indicated by Hart's early discussion (Figure 2.9b - black triangles). Frolov et al. were able to verify this transition behavior of diffusivity through atomistic simulations and established the two curves for both grain boundary states in the case of Ag diffusion at the Cu grain boundary, but also and additionally for Cu self-diffusion at the same Cu grain boundary (Figure 2.9b - colored symbols, in analogy to Figure 2.9a) [75]. Moreover, the authors were able to extract the grain boundary structure from their simulations for both cases and found the two grain boundary states to correspond to two unique grain boundary structures, termed kite - and split-kite structures. In the case of Ag diffusion, these were decorated with Ag at distinct locations along the boundary, while the same transition also occured for pure Cu, but at slightly different temperature (Figures 2.9c and 2.9d). As the diffusivity changed abruptly at a single transition point and was accompied by a change in grain boundary structure, this example describes a first order structural transition. While some studies associate discontinuous changes in grain boundary structure with important materials phenomena such as abnormal grain growth in ceramics [15], liquid metal embrittlement [76], and activated sintering [77], the atomic structure of most grain boundary phases remains elusive. More
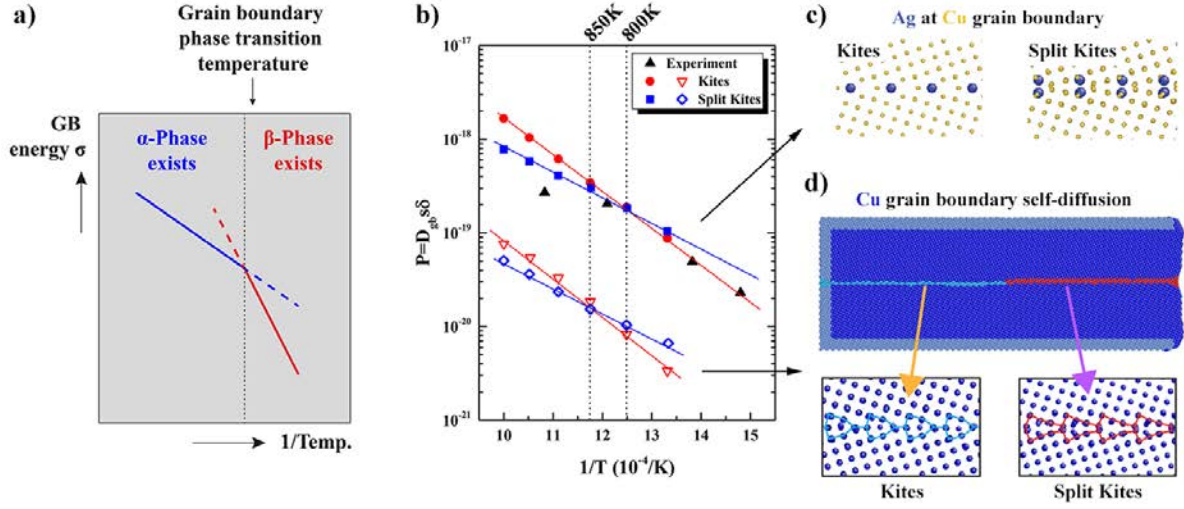
Figure 2.9: (a) Schematic representation showing a discontinuity in slope for the grain boundary energy as function of 1/T at a grain boundary transformation, as proposed by Hart [74]. The vertical dashed line represents the transformation temperature, the blue line the grain boundary energy of the high temperature stable phase, the red line the grain boundary energy of the low temperature stable phase. (b) Summary of experimental (black) and atomistic simulation data of Ag (closed colored symbols) and Cu (open colored symbols) (self-)diffusion along Cu grain boundaries. The graph representing Ag diffusion could be linked to a first order transition from a monolayer decoration of the grain boundary to a bilayer decoration at about 800 K (c), while the Cu self-diffusion data was linked to a purely structural transition occuring at about 850 K (d). Data in (b) and images in (c) and (d) were taken from [75].

recently, transitions at planar grain boundaries have been studied extensively with phase field models [78], atomistic simulations [64], and lattice-gas models [79].

In addition to the conventional thermodynamic variables that can trigger changes in grain boundary structure, Cahn, Rottman and Cantwell et al. introduced orientational degrees of freedom. They also categorized transitions at grain boundaries into congruent and non-congruent types, with the latter type being sub-divided into dissociation and faceting transitions (Figure 2.10a) [12,13,80]. For congruent transitions, the misorientation, grain boundary plane normal $\vec{n}$, and chemistry remain the same, while only the core structure itself changes. For non-congruent transitions, one or more of these parameters changes. Faceting keeps overall chemistry and misorientation constant, while the boundary plane $\vec{n}$ decomposes into two new planes $\vec{n_1}$ and $\vec{n_2}$, which can differ in chemical composition. When a grain boundary dissociates, two new grain boundaries form with a bulk phase in between them. Here, plane normals and chemistry might differ from the initial boundary existing before the transition. While the overall misorientation remains the same, the misorientation of the newly formed boundaries between an abutting grain and the new bulk phase can be different. The described transitions can occur for pure but also for multicomponent systems.

Cahn discussed that most GBs undergo faceting transitions in 1982 [12] and in fact, many faceting transitions have been observed to date in experiments for a variety of materials [81–

83]. Most of the investigated faceting transitions were stimulated by temperature (annealing treatments) and found in pure metal GBs [61,82,84,85], while facet formation and coarsening mechanisms have been explored predominantly by atomistic simulations in single component systems [55,65,85–87]. Some work also focused on how structural defects of a grain boundary (GB dislocations) may influence faceting by pinning or dragging facets during defect motion [88]. Straumal et al. summarized a variety of faceting-roughening aspects recently for a variety of GBs and material systems. For faceting to be induced, an initial GB has to transition into facets of period Λ and two segments with different GB plane normal, and consequently with different (GB) facet segment energies γ_1 and γ_2. The junctions between both segments are in general regarded to contain a line defect with a distinct Burger's vector and energy γ_j. Although faceting intuitively increases the grain boundary area and thereby the energy of the system, the changing contributions of the facet segments, in fact reduce the overall energy and thus allows for faceting to occur. Initially, the facet segments are likely small, and therefore junctions close to each other possibly interact with each other. This allows for a general GB energy formulation according to $\gamma_{GB} = \gamma_1 + \gamma_2 + \frac{2\gamma_j}{\Lambda} + \frac{\gamma_{j-j}}{\Lambda}$, with γ_{j-j} being the interaction between junctions. Hamilton et al. looked at the energetics involved in this and found that the further separated the junctions, the higher the energy reduction [86]. They found that the amount of energy reduction follows a $\frac{1}{\Lambda}$ type relation, i.e. $\Delta\gamma = \left(\frac{C_1}{\Lambda}\right)\ln(\Lambda) + \frac{C_2}{\Lambda}$ (C_1 and C_2 being fitting constants), which favors the furthest separation of facet junctions. They pointed out, that for $C_1 > 0$ infinite facet lengths are observed. Although this theory was confirmed by Medlin et al. [89] and Wu et al. [65], this analysis does not consider kinetic effects. The latter study by Wu and co-workers investigated different boundaries by simulation work and found that indeed migration kinetics during coarsening can lead to finite length facets. Instead of a continuous decrease in energy for increasing facet periods, migration of facet segments can impose a multitude of energy barriers depending on the structure of the facet segment resulting in the inhibition of further migration and therefore stabilization of finite length facets. They also introduced a factor $G = \sqrt{\frac{h^2+k^2+l^2}{o^2+p^2+q^2}}$, which involves the Miller indices of a facet segment, and thus the grain boundary structure. For integer values of G, the facet can coarsen, although high numbers reduce the coarsening tendency, while for irrational numbers, the kinetics prevent coarsening.

On the other hand, while segregation is studied comprehensively in planar GBs and for temperature stimuli, the effect of solute segregation on faceting is much less understood. Changing the chemistry at GBs by adsorption of solute excess significantly changes the energy of such boundaries and consequently structural transitions are likely to occur. The evolution of microscopically faceted boundaries was often observed in Bi doped Cu bicrystals with increasing temperature and Bi concentration [9], while the direct observation of a reversible faceting transition in a well defined boundary was demonstrated experimentally only in a
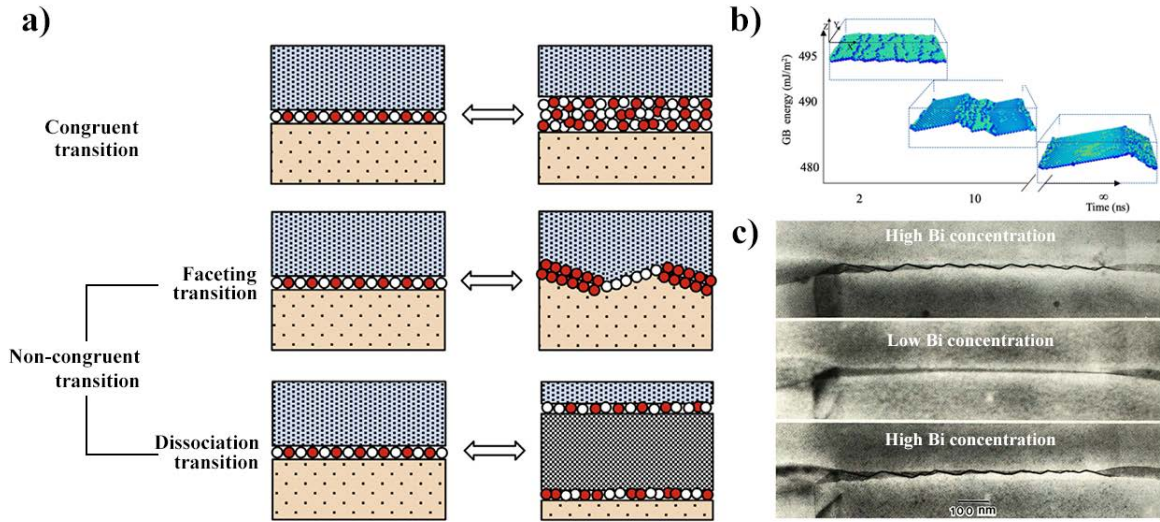
Figure 2.10: (a) Categorization of grain boundary transitions into congruent and non-congruent types according to Cahn and Rottman [12,13] (visualized and taken from Cantwell et al. [80]). (b) MD simulation results showing facet coarsening over time at high temperatures [87]. (c) Direct observation (in situ TEM) of a reversable and chemically triggered non-congruent faceting transition at a Bi doped Cu grain boundary, as reported by Ference and Balluffi [90].

single *in situ* TEM study by Ference and Balluffi for the Cu-Bi system (Figure 2.10c) [90]. However, neither study was able to resolve the atomic structure of the segregated boundary, instead detecting only relatively large facets with the size of several tens to hundreds of nanometers. Four decades ago Loier and Boos demonstrated already how small additions of Bi induce striations and faceting of Ni grain boundaries [91]. More recently, Kundu et al. observed bilayer Bi segregation on approximately 100 nm long facets in a Cu grain boundary, but Bi decoration of the other facet type could not be determined [92]. Yu et al. recently found distinct segregation patterns of Bi solutes at a microfaceted general GB in Ni [93] after having shown that such patterns may be the underlying reason for detrimental effects of Bi segregation on mechanical properties in Ni [76]. Our recent work combining atomic resolution imaging and atomistic modelling demonstrated that Ag segregation can act as chemical trigger promoting a nanofaceting transition of an asymmetric tilt grain boundary in Cu [94]. However, temperature [64], pressure [95] or solute excess concentration [90,96] strongly influence GB transitions [97] and their concentration dependence is usually established by atomistic modeling. Stable nanofaceted grain boundaries were observed using high resolution STEM in elemental systems and could potentially exist in doped systems [98,99]. Such small facets can be observed only with atomic scale resolution and could thus have been overlooked by previous studies.

2.2.3   Grain boundary segregation

As described in the previous section, a grain boundary containing crystal has an increased Gibbs energy compared to a single crystal, i.e. it contains the grain boundary energy σ. However, every system tries to minimize its energy as far as possible and this applies as well to such bi- or polycrystals. In fact, there are many ways to achieve this, one being the interaction of grain boundaries with other crystal defects such as point defects. In the case that solute atoms (alloying or impurity atoms) reduce the system energy by occupying defective crystal sites, they will accumulate at all defects including grain boundaries as thermodynamically driven process. As a result, grain boundary segregation is defined as, "all changes of concentration of any element at a grain boundary in the form of a solid solution" [43, 100]. If the solid solubility at the grain boundary is exceeded, secondary phase particles will form, similar to bulk materials. This phenomenon is refered to as grain boundary precipitation. However, existence of just a few atomic layers of solute atoms covering a grain boundary is still considered grain boundary segregation, e.g. in [76, 101, 102].

Grain boundary segregation is generally divided into equilibrium and non-equilibrium segregation. The latter deals with segregation processes in which the solute concentration at the boundary is changing over time and thus kinetics of solute diffusion have to be considered. These kinetic effects usually depend on the material's processing history and involve the introduction of additional point defects, which interact with the solute atoms. Examples include thermal-, radiation- and stress-induced segregation, which are discussed in greater detail in [43], and some of which are reviewed by Faulkner in [103]. The present thesis work, however, uses materials that are assumed to be at least close to thermal equilibrium, due to their thermal treatments, and thus equilibrium segregation is of much greater importance. This type of segregation describes the accumulation of solute atoms as a consequence of purely thermodynamic driving forces, i.e. the reduction of the Gibbs energy (grain boundary energy). Consequently, the amount of solute segregation is characterized solely by the thermodynamic boundary conditions.

As discussed above, grain boundary energy is influenced by thermodynamic variables like temperature, pressure, etc., but it also depends on the grain boundary's crystallography and as a result also (and especially) on its structure. The reduction of the Gibbs energy can be mainly explained by two common types of effects, namely electronic and elastic effects for a solute atom sitting at a grain boundary. These effects originate from the fact that a solute atom may be energetically not favored to sit in a grain's perfect crystal lattice, but rather in the less ordered grain boundary. The details of these effects are connected to the famous Hume-Rothery rules [104]. For the case of electronic effects, bonding is influenced by differences in electronegativity and valence state (2nd and 3rd rule), while the elastic effects mainly stem from strain energy resulting from atomic size differences between solute and

solvent elements (1st rule) and the associated strain fields. From these considerations, the segregation energy ΔE_{seg} can be formally defined as the difference between a solute's strain energy at the grain boundary E_{strain}^{GB} and in the bulk E_{strain}^{Bulk} according to [45],

$$\Delta E_{seg} = E_{strain}^{GB} - E_{strain}^{Bulk}. \tag{2.6}$$

Besides the strain portion, there are additional elastic effects that should be considered, namely, the differences in elastic modulus between solute and solvent atoms, as well as possible anisotropy between the two crystals adjacent to the boundary. Priester describes the segregation as follows: "having its driving force from long-range elastic interactions, once in the grain boundary, the solute atom may find a more or less favorable site to its localization. The choice of this site (favorable bonding configuration) is dictated by the short-range electronic interaction" [45].

As mentioned above, the grain boundary energy, and thus also the equilibrium segregation behavior, can be influenced by thermodynamic variables such as temperature and pressure. Different models have been derived in an attempt to predict this segregation behavior. The more classical models will be briefly introduced in the following. These models were developed to predict the average segregation at random grain boundaries in a polycrystal, i.e. the Gibbs adsorption isotherm and the Langmuir-McLean isotherm, depending either on temperature or bulk solute concentration for dilute binary systems. It should be noted that there are more recent (but also more complex) models that attempt to correlate segregation to specific grain boundaries characterized in detail in terms of the macroscopic degrees of freedom, and also in terms of structure. The more simple Gibbs adsorption isotherm can be formally derived from equation 2.3 as [43, 45, 73],

$$\Gamma_S = -\frac{1}{RT} \cdot \left(\frac{\partial \sigma}{\partial \ln (X_s)} \right)_{P,T} \tag{2.7}$$

with Γ_s being the adsorption of solute at the grain boundary, X_S the molar fraction of the solute in the bulk, and R and T being the gas constant and temperature, respectively. Summarized, this equation relates a change in grain boundary energy due to a changing bulk solute concentration to how much solute will be adsorbed at the grain boundary for fixed pressure and temperature on a purely thermodynamic basis. The higher the energy reduction, the more solute will be adsorbed. This model has been successfully applied to quantify solute excess in the first segregation studies [43]. A further example can be found in [105] and several more are reviewed by Hondros and Seah in [106]. Although it has been successfully applied, the Gibbs adsorption isotherm is not very practical because of the difficulty in measuring precise bulk solute concentration at different temperatures. McLean therefore proposed a different approach in which he kept the thermodynamic treatment and

combined it with a statistical mechanics formalism [107]. The assumption in his description is that there is a finite number of atomic sites in the grain boundary that can be occupied by either a solvent or a solute atom and, consequently, the grain boundary can reach saturation when all sites are filled with solute. This scenario represents a monolayer coverage of the grain boundary. In addition, an energy reduction by the amount of the segregation energy is assumed, as caused by the occupation of atomic sites by solute atoms. Formally, the classical Langmuir-McLean isotherm can be derived as,

$$\frac{X_S^{GB}}{X_S^{GB,sat} - X_S^{GB}} = \frac{X_S}{1 - X_S} \exp\left(\frac{-\Delta G_S^0}{RT}\right).$$ (2.8)

In this equation, the saturation concentration of the grain boundary $X_S^{GB,sat}$ and the actual solute concentration at the grain boundary X_S^{GB} are related to the solute concentration in the bulk X_S and the change in Gibbs energy due to segregation ΔG_S^0. This equation is formally equivalent to the Langmuir isotherm for the adsorption of an element on a free surface [45]. Compared to the Gibbs adsorption isotherm, X_S^{GB} and X_S are experimentally fairly easy to determine, which explains why this formalism is favored. If saturation is reached ($X_S^{GB,sat} = 1$), the equation can be rewritten and approximated to obtain the so-called enrichment factor β [108],

$$\beta = \frac{X_S^{GB}}{X_S} = \exp\left(\frac{-\Delta G_S^0}{RT}\right).$$ (2.9)

2.3 Methods

2.3.1 Metallographic preparation of electron microscopy samples

For any characterization method a sample is required that fulfills distinct quality criteria. Metallographic procedures have been developed in the past to prepare suitable samples with respect to size and condition from macroscopic bulk materials, which are well summarized by Petzow in [109]. The goals of these procedures are usually the same, i.e. a plane sample surface that is free of deformation artifacts, while all microstructural elements have to be retained. They are usually obtained by mechanical removal of material at successively finer steps until the desired surface quality is reached. The action sequence typically includes planarization and fine grinding with different abrasive papers that are coated with diamond or SiC grains of uniform diameters, down to a few micrometers. Subsequently, the sample surface is polished with colloidal diamond or silica solutions, which are applied on more resilient cloths as compared to the hard abrasive paper used during grinding. The particles in the solution can range down to few tens of nanometers if necessary. Successive steps of finer abrasive particles are required as any mechanical material removal results in a deformation

zone approximately three times the size of the particles. Consequently, even finest polishing steps may still result in surface deformation layers. Especially for S/TEM investigations this is not desired, as samples are typically on the order of 100 nm thick but still should represent the initial sample condition.

Electropolishing is a means to create a deformation free, high quality sample. To achieve a well electropolished metal surface, it has to be the anodic side of an electrolytic cell, immersed into a suitable, material-specific, electrolyte. Application of a specific voltage to ensure gentle polishing, in contrast to aggressive etching, carefully dissolutes the surface without plastic deformation artifacts. Conventional preparation of S/TEM samples thus consists of initial grinding and polishing of 3 mm diameter discs from both sides down to a thickness of about 100 µm. Directing electrolyte streams from both sides onto both sample surfaces under an applied voltage (known as twin-jet electropolishing) removes material from both sides of the disc until a hole is formed in the disc's center. The edges around the hole are typically thin enough and deformation-free for reliable TEM characterization. Twin-jet electropolishing of Cu TEM samples is achieved, for instance, using a 70 % methanol + 30 % nitric acid solution, which is cooled down to - 30 °C with 6 V being applied for about 5 minutes. More recipes for different materials are well documented in [109].

2.3.2   Scanning electron microscopy (SEM)

The scanning electron microscope working principle is based on an electron source, which is typically either a W filament, a LaB_6 crystal or a (cold) field emission gun. The extracted electrons are accelerated by a tunable field, typically between 1-30 kV. With the help of a Wehnelt cylinder, the electrons are collected to form a coherent primary beam, which is focused on, and rastered across the sample by an electromagnetic lens system. The electron beam can interact with the sample by many different physical processes that are depicted in Figure 2.11. The depth of the interaction volume is material dependent and is positively correlated with the acceleration voltage (Figure 2.11a). The scattering mechanisms are schematically shown in Figure 2.11b.

Inelastic scattering involves two distinct cases, i.e. the Coulomb interaction between an electron from the incoming primary electron beam and a sample atom's nucleus, as well as the direct interaction between a primary beam electron and an inner core (shell) electron of a sample atom. In the former case, namely the electron-nucleus interaction, the incoming electron is deflected from its original path, due to the attractive force from the positively charged nucleus and thereby the electron is decelerated. The change in the electron's kinetic energy is related to its velocity change and results in the emission of a so-called Bremsstrahlung X-ray photon, with an energy being equal to the change in kinetic energy upon deceleration. As the Coulomb force decays monotonously as a function of $1/r^2$ (r being the distance from

the nucleus), the change in kinetic energy and therefore also the Bremsstrahlung spectrum is a continuous energy distribution, which can be approximated roughly using Kramers cross-section $N(E) = \frac{KZ(E_0 - E_X)}{E_X}$ for Bremsstrahlung X-ray energies $> 2\text{keV}$, and more precisely with more recent approaches like in [110]. K refers to the Kramer's constant, Z to the atomic number, E_0 to the incoming electron's energy (electron beam energy), E_X to the X-ray energy and $N(E)$ to the amount of produced Bremsstrahlung X-rays of energy E. In case that an incoming primary beam electron interacts directly with an inner core electron, the latter is ejected from the atom becoming a secondary electron and leaving the atom in an excited (also referred to as ionized) state. After an electron from a higher shell is occupying the empty lower energy state, two different processes can follow. Either a characteristic amount of energy is released by emission of a characteristic X-ray photon or an Auger electron. In both cases, the energy of the respective emission is characteristic of the atom's Z-number and the difference in energy between the shells that are involved in the de-excitation (also referred to as relaxation) process. If this process only consists of an energetically higher electron filling the empty, lower energetic state, a characteristic X-ray photon is emitted. As higher order shells are divided into several subshells, a multitude of transitions are possible to emit these X-rays. However, not all possible transitions occur, due to quantummechanical reasons. Transitions have a distinct nomenclature. In general, the shell that is being filled is stated first, followed by a Greek subscript indicating from how many shells above the empty state it is filled. For example, a K_α-transition occurs, when an electron from the L-shell fills up an empty K-shell state. In contrast, a K_β-transition occurs, if a M-shell electron is filling up the empty state. Considering the de-excitation process as single event is a rather simplified view. In fact, core shell electron emission (excitation) involves a sufficient amount of energy for a whole de-excitation cascade to happen. Therefore, one inelastic scattering event can lead to multiple, different characteristic X-rays.

The emission of an Auger electron functions similar to the emission of a X-ray photon, but is in fact a process involving three electrons. After excitation, the empty state is also filled by an electron from an energetically higher electron shell. However, instead of emitting a characteristic X-ray to release the resulting energy, as described above, the energy is transferred to another outer shell electron of the same atom. This electron is consequently released as an Auger electron with a kinetic energy given by the difference between the binding energy of that emitted Auger electron and the energy it obtained from the prior, characteristic shell transition.

Auger electrons are collected from within about 1 nm below the surface, while secondary electrons are generated from within few tens of nanometers and characteristic X-rays from within few micrometers.

In contrast, incoherent elastic scattering events result in generation and emission of backscat-
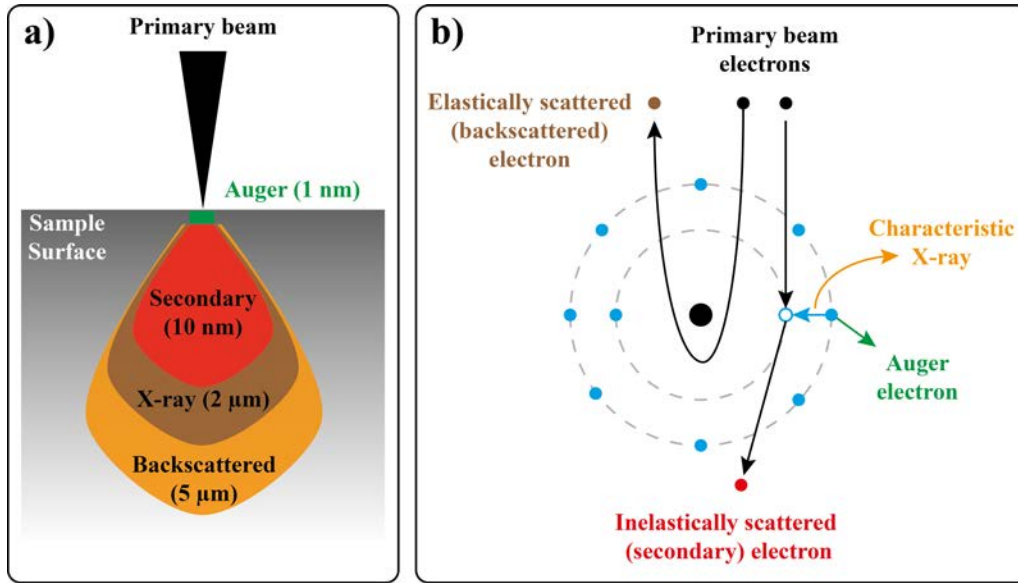
Figure 2.11: Visualization of the electron-sample interactions. In (a), the projected interaction volume is depicted (not to scale) and from which depth the different signals are mainly generated. Note that the depths are only approximations, as they do depend on acceleration voltage of the primary beam and the material. The two principle interaction (scattering) mechanisms are schematically shown in (b), namely inelastic and elastic scattering, along with the resulting particles that can be collected with different detectors.

tered electrons from within few hundreds of nanometers below the surface. This scattering type is based on the interaction of an incoming primary beam electron with the nucleus of a sample atom. Because of the charge difference, an incoming electron's path is changed by the attraction of the negatively charged electron to the positively charged nucleus. The change of the incoming electron's path (elastic scattering strength) is therefore material (Z-number) dependent and can result in the complete inversion of the electron's path. Thus, the name of these electrons is owed to this drastic change in direction, i.e. backscattered electrons.

Each of these particles, resulting from the different interaction types, can be used to visualize different sample properties if collected by a suitable detector, e.g. secondary electrons for topography, backscattered electrons for phase identification and element specific X-rays to characterize the sample's elemental composition. These electron-sample interactions are also applicable for STEM, which is described in section 2.3.4. The primary beam is raster scanned over the sample and the required signal collected at each position. Typical image types are secondary and backscatter images. To form a secondary electron image, the emitted low energy secondary electrons are collected commonly with Everhart-Thornley-Detectors (ETDs). A small positive voltage is applied to this Faraday cage-like detector to attract the electrons of interest. However, usually some backscattered electrons also reach the detector to form a mixed image. In order to suppress this mixture, so-called in-lens detectors have been developed that are sitting inside the electron beam column behind an edge. These detectors

suppress the collection of back scattered electrons as they have too high velocities (higher energies) compared to the secondary electrons. Consequently, these detectors are capable of forming "pure" secondary electron images. Backscattered electron detectors, in contrast, are typically annular detectors sitting between sample and column, as these electrons are usually emitted back towards the electron beam column. Slightly negative bias voltages on a backscatter detector suppress the collection of low energy secondary electrons. A comprehensive summary of many aspects concerning scanning electron microscopy is provided by Reimer in [111].

2.3.3 Focused ion beam microscopy (FIB)

The focused ion beam (FIB) microscope is very similar to the SEM in terms of image acquisition. It is also rastering the sample surface and collecting mainly the same type of signals from the sample, i.e. secondary electrons, etc. However, the main difference is the use of Ga^+ ions to form the primary beam (some modern machines also use He^+ or Xe^+ ions), in contrast to electrons. Of course, the use of these heavier ion species also enables more or less agressive, but targeted, sputtering of atoms off the sample's surface and thus cutting at nanometer precision is possible with these machines. The common Ga^+-based FIBs require a liquid Ga ion source that operates at low temperature, has a low vapor pressure and a good wettability on a required W needle to form a Taylor cone at the tip, where high voltages are applied (typically also 1-30 kV). Ga has effectively proven to fulfill these requirements best and has thus become a standard material for FIB microscopes. However, besides the common Ga^+ sources, gaseous ion sources as mentioned in case of He^+ or Xe^+ ions, or other metal (alloy) ion sources exist, such as e.g. Au, SnPb or MnGe sources. After ion extraction, a similar optical system, based on electrostatic lenses instead of electromagnetic lenses is used to form the beam and raster it across the sample, as compared to the SEM. However, the amount of ions hitting the surface is much more critical as every collision event from incoming ions with the sample create collision cascades and consequently induce damage to the material in form of point defects, or even sputter atoms away. To control these adverse effects, the beam current can be adjusted by apertures depending on the desired application and modern systems are coupled to an electron beam column to use the SEM mode for imaging; the FIB mode mainly for targeted material removal. In addition to the ion beam column, most modern FIB systems also incorporate a gas injection system to deposit protective layers by beam induced precursor gas decomposition - in general Pt, W or C layers can be created - and a micromanipulator is used to transfer material from the sample to a TEM grid for example. In addition, different imaging modes are available based on secondary electrons, secondary ions and backscattered electrons. Supression of introduced defects is of special importance for the preparation of TEM samples, as these are typically very thin,

i.e. below 100 nm in thickness. Additionally, the features of interest in this thesis work, i.e. grain boundaries, are defects themselves. Introduction of additional defects from sample preparation should therefore be avoided and the benefits of high spatial resolution and site specific sample preparation might be overruled. In this case, conventional electropolishing might outperform FIB prepared samples. Comprehensive overviews of this technique can be found in [112, 113].

2.3.4 Scanning transmission electron microscopy (STEM)

The central portion of the present thesis work is focused around transmission electron microscopy. This method counts as one of the most versatile methods to characterize structure of materials from the micrometer scale down to the atomic scale. Required for using this method is the generation of a high energy electron beam (typically few hundred keV) and a suitable sample thickness for the chosen acceleration voltage (generally below 100 nm). As stated in the name, the produced electron beam is transmitted through the sample, thereby interacting with the contained atoms and leading to different effects that can be used for image formation or chemical analysis. For comprehensive overviews on transmission electron microscopy it is referred to [114–118]. In the following, the relevant methodolgy for the performed experiments in the present work is summarized following their description.

The formation of the electron probe is achieved similar as in the SEM (section 2.3.2), the only difference being that the electrons are accelarated to higher energies. The primary beam is then focused onto the sample by an electromagnetic condenser lens system. The microscope has two distinct working configurations; one referred to as TEM mode and one referred to as STEM mode. In the former one, the sample is illuminated with a parallel beam, while in the latter one, the sample is raster scanned with a small converged beam (probe). In STEM, the condenser system is effectively used as a probe-forming objective lens and sits above the sample. Passing through the sample, the electron beam can interact with atoms in different ways, namely by inelastic and elastic scattering, as described in section 2.3.2, or without any interaction at all due to the thin sample but high beam energy. Elastic (Rutherford) scattering is the most important and main mechanism for image formation in high angle annular dark field (HAADF) imaging. In contrast to STEM, the transmitted electrons in TEM mode are entering an objective lens after passing the sample. Before the electrons hit an electron detector, typically a charge coupled device (CCD) or complementary metal-oxide-semiconductor (CMOS) camera, they typically pass some more lenses such as an intermediate lens, which either projects the image or a diffraction pattern on the detector. The basic electromagnetic lens arrangement in conventional TEM (CTEM) and STEM are depicted in Figure 2.12. Only the objective lens and aberration-corrector locations are depicted to show the equality of both modes if the beam direction is inverted for both modes (reciprocity
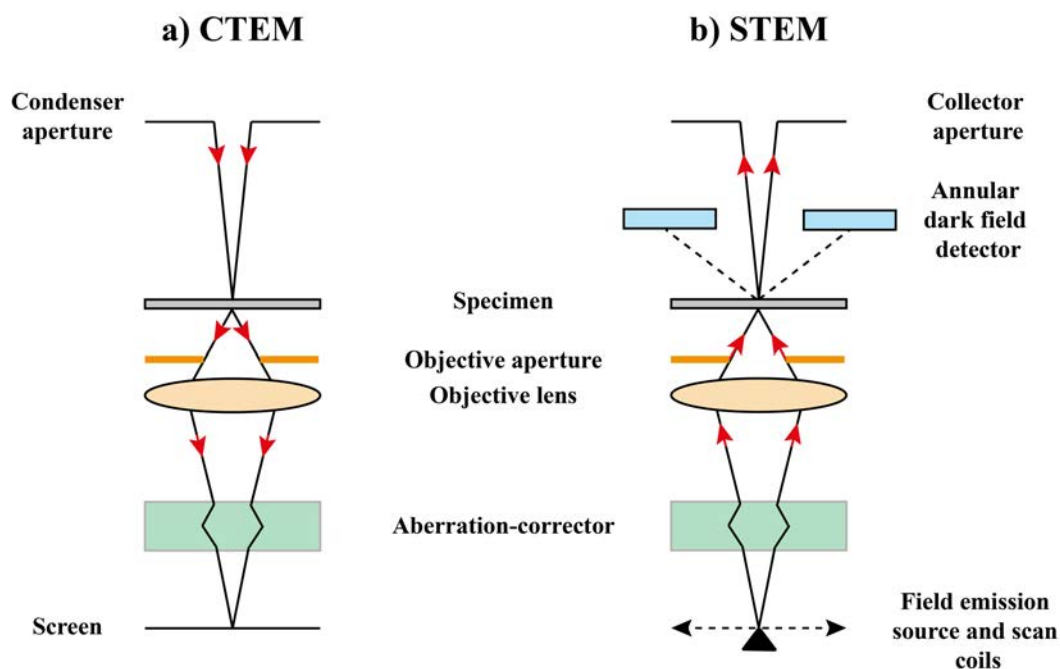
Figure 2.12: Basic electromagnetic lens arrangement of (a) CTEM and (b) STEM. Note the inversion of the electron beam direction, but otherwise equivalence in imaging conditions. Real microscope consist of course of more lenses such as condenser lenses. Special for STEM mode is the capability of simultaneously acquiring bright field and annular dark field images using annular detectors. Redrawn from [119].

principle). This holds only true for STEM bright field imaging, but simultaneous acquisition of the incoherent elastic HAADF signal provides an important extension. A schematic of the detector setup in a STEM is provided in Figure 2.13 along with the definitions for the STEM semi-convergence (α) and semi-collection angle (β). The distance of the detector from the sample can be adjusted by changing the microscope's camera length, which in turn controls the semi-collection angle β, as does the semi-convergence angle. The semi-collection angle for the different imaging conditions consists of an inner and an outer angle. However, the inner angle is more important to distuingish the different imaging conditions. Therefore, the semi-collection angle usually only refers to the inner semi-collection angle. Depending on β, different imaging conditions are referred to, i.e. below 10 mrad annular bright field (ABF), 10 - 50 mrad low angle annular dark field (LAADF) and above 50 mrad HAADF in case of a semi-convergence angle α of about 24 mrad. Transitions between these conditions are rather gradual than abrupt. Each imaging condition has special characteristics, rendering them favorable for different scientific questions.

The big advantage of using electron beams as compared to light for imaging is the drastically reduced wavelength λ of the former compared to the latter. In fact, the resolution of a transmission electron microscope is typically not limited by the picometer wavelength of the electrons, but by the aberrations of the electron beam originating from the electromag-

netic lenses. There is a multitude of aberrations including more common ones like first-order astigmatism and coma, but also many more higher order aberration of this type, especially spherical and chromatic aberrations. Correction of these resolution limiting factors is not trivial and requires very complex assemblies of electromagnetic lenses to compensate them. Such aberration-correctors have been developed just recently, but improved the resolution of S/TEMs significantly. For instance, spatial resolution of 40.5 pm was reported by Morishita et al. using a 300 kV STEM equipped with a fifth order aberration-corrector [120]. The particular resolution of a STEM is only limited by the size and the shape of the electron beam, not to be confused with its magnification, which is depending on the scanned sample area and is therefore associated to the lens system above the sample. Preferably, the probe is as small as possible, and has a Gaussian intensity distribution. The probe intensity (point spread) function $P(\vec{r})$ can be expressed as integration over the probe $P(\vec{r}) = \int_{probe} e^{i[\vec{K}\cdot(\vec{r}-\vec{r}_0)+\varsigma(\vec{K})]}d\vec{K}$, $\vec{K}$ being the reciprocal space wavevector ($\vec{K} = \frac{\alpha}{\lambda}$) and corresponding to a partial wave converging at a (semi-convergence) angle α at the sample, ς contains the aberrations from the objective lens [121]. So, aberrations from the probe-forming (objective) lens are one factor to prevent an ideal probe shape but can meanwhile be well compensated by aberration-correctors. Further impact on a STEM's resolution has the radius and diffraction limit of the probe forming aperture, which is strongly correlated with the semi-convergence angle α of the beam. The bigger the aperture, the higher the angle and the better the resolution with the trade-off being that increasing the aperture angle too much, other aberrations adversely affect the beam shape increasingly e.g. chromatic aberrations. Thus, a balance has to be found for optimal STEM resolution. Due to the invention of the aberration-corrector, the compensation of higher-order aberrations, especially the spherical aberration, allowed for increasing the semi-convergence angle from about 10 mrad in an uncorrected STEM to ≥ 23.8 mrad (used in the present work) and thus to form probes with a diameter well below the lattice parameter of several hundred picometers for most elements. In fact the probe size is governed by three main contributions, i.e. the effect of a finite source size, lens aberrations (especially spherical aberration) and the diffraction limit [122]. Using a field emission gun, as used in the present work, the electron source contribution becomes negligible. For the other two effects a probe diameter can be calculated according to $d_s = 0.5 \cdot C_s \alpha^3$ (spherical aberration C_s term) and $d_d = 0.61 \cdot \frac{\lambda}{\alpha}$ (diffraction term) to be around 3 and 51 pm, respectively, for typical microscope settings used in this work ($C_s = 500$ nm, $\alpha = 23.8$ mrad, $\lambda = 2$ pm for 300 keV beam energy). However, without chromatic aberration (C_c) correction, this additional contribution becomes relevant for increasing semi-convergence angles. The beam diameter for this contribution d_c can be calculated according to $d_c = C_c \alpha \left(\frac{\Delta E}{E_0}\right)$ to be around 80 pm for a C_c of 1 mm, $\alpha = 23.8$ mrad, an electron beam energy spread ΔE of 1 eV and a beam energy of 300 keV. This clearly indicates that spherical aberration no longer
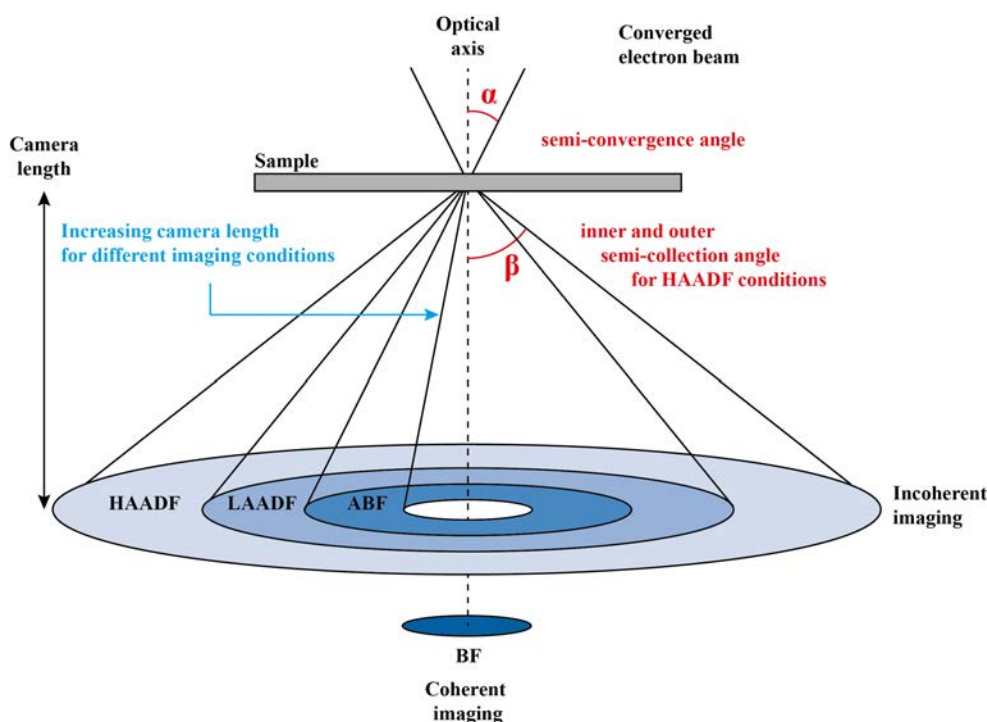
Figure 2.13: STEM image formation system. Contrast formation in STEM mainly originates from incoherent, large-angle scattering. The semi-convergence angle α describes how much the electron beam is focused. Changing α or the camera length changes the semi-collection angle β, which leads to different imaging conditions by using an annular detector. The different angular regimes for the different STEM imaging modes are highlighted. The semi-collection angle for the different imaging conditions consists of an inner and an outer angle. However, the inner angle is more important to distinguish the different imaging conditions. Therefore, the semi-collection angle usually only refers to the inner semi-collection angle.

is the limiting factor for the beam diameter and that the beam diameter is well below the lattice parameter. As a consequence, in well oriented crystalline specimen (tilted to zone axis orientation), direct visualization of atomic columns is easily achieved in aberration-corrected STEM. The small probe diameter also increases the probe current significantly, thus increasing signal. Especially analytical methods such as EDS and EELS benefit from the increased beam current and complement the aberration-corrected STEM perfectly by making use of the high spatial resolution [123–125]. It was shown that these methods are able to distinguish elemental composition on an atomic column by column basis.

HAADF STEM imaging is a high contrast, chemically sensitive imaging mode, which is based on elastic Rutherford scattering. It was explained above already that the resolution is dependent on the probe size and that aberration-correctors are capable to shape probes smaller than the lattice parameter in modern instruments. Therefore, while the probe is scanned across the sample, every atom can be regarded as a scattering center. The scattering strength is proportional to the elastic Rutherford scattering cross-section considering

screening of the nucleus by the electron cloud

$$\sigma\left(\beta\right) = \frac{\left[Z\lambda_{MFP}\left(\frac{a_0}{Z^{0.33}}\right)\left(1 + \frac{E_0}{m_0 c^2}\right)\right]^2}{\pi\left(a_0\right)^2\left(1 + \left(\frac{\beta}{\theta_0}\right)^2\right)} \tag{2.10}$$

where Z is the atomic number, λ_{MFP} is the mean free path for elastic scattering, a_0 the Bohr radius, θ_0 the characteristic screening angle, E_0 the beam energy, m_0 the electron mass and c the speed of light [114]. Thus, the specimen can be described as an object being composed of many scattering centers, which can be approximated as delta functions. Formally, this leads to an object function $O\left(\vec{r}\right) = \sum_i \sigma_i \delta\left(\vec{r} - \vec{r}_0\right)$, with σ_i being each atom's high angle scattering cross-section [126]. Annular detectors with a central hole (see Figure 2.13) can collect electrons scattered to these high angles, typically above 50 mrad to achieve HAADF conditions. For these angles, the cross-section is almost propertional to Z^2. In fact, it was shown for HAADF conditions that the Z-dependence is experimentally rather $Z^{1.6}$ - $Z^{1.9}$ due to the shielding effect of the electron cloud on the nucleus [127]. Because of this Z-number dependence of the image intensity, chemically distinct areas can be identified readily in HAADF micrographs or atomic columns being constituted by different elements. Consequently, HAADF STEM imaging is ideal to study segregation phenomena down to the atomic level.

The key difference between phase contrast imaging in TEM mode and HAADF imaging in STEM, is the coherency of the electrons. Coherent imaging means that electrons passing the sample have a permanent phase relation, which occurs for the illumination of the entire sample by a plane electron wave. This happens while imaging in TEM mode and as a consequence TEM imaging can be considered coherent imaging (and due to the reciprocity theorem also STEM bright field imaging). In contrast, for HAADF STEM imaging every atom is an independent scattering center. Therefore, there is no phase relation between neighboring atoms, rendering this imaging mode incoherent. This leads to the fundamental equation of image intensity $I\left(\vec{r}\right)$ from incoherent imaging: $I\left(\vec{r}\right) = O\left(\vec{r}\right) \otimes \left|P\left(\vec{r}\right)\right|^2$ meaning that the image intensity results from a convolution of the object function with the squared point spread function (Figure 2.15). It can be shown that, physically, incoherent imaging has an improved resolution as compared to coherent imaging. Under optimal imaging conditions the resolution limits can be derived to be $0.43 \cdot C_s^{\frac{1}{4}}\lambda^{\frac{3}{4}}$ in the incoherent case, and $0.66 \cdot C_s^{\frac{1}{4}}\lambda^{\frac{3}{4}}$ for the coherent case (C_s being spherical aberration). This can be made visible by plotting the coherent (TEM and STEM bright field) and incoherent (STEM HAADF) transfer functions (Figure 2.14). The transfer function in reciprocal space describes how much phase signal is transmitted to the real space wave function, which is forming the image. For coherent TEM imaging (phase relation between electrons exists) the image is based on interference of
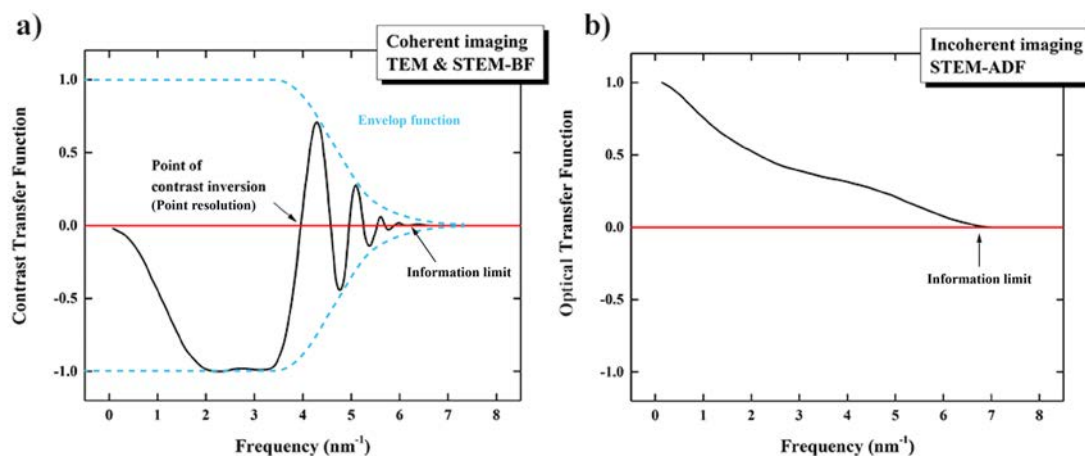
Figure 2.14: (a) Contrast transfer function for a microscope without aberration-correction containing several points of contrast inversion for coherent imaging in TEM mode (also for BF imaging in STEM mode) and (b) the optical transfer function for incoherent imaging in STEM HAADF mode. Redrawn from [128]

scattered and unscattered plane waves and thus oscillations of the phase information occurs, which can be seen in the phase contrast transfer function (Figure 2.14a). The consequence of these oscillations is, that for frequencies of 0 contrast transfer, the image will not contain any information. In addition, when the function transitions from negative to positive or vice versa, the image's contrast is reversed. For this scenario, image simulations are required to determine actual feature locations. The maximum point resolution is obtained at the first contrast inversion, while the information limit is at much higher frequencies. Due to aberrations from e.g. lenses and the objective aperture, the function's amplitude is damped by an envelope function, effectively cutting of the information limit. In contrast, for incoherent STEM imaging, the Fourier transform of the point spread function gives the equivalent power spectrum referred to as optical transfer function (Figure 2.14b) [118]. It is obvious that for incoherent imaging no contrast reversal is observed, as well as the point resolution almost reaching to the information limit. Thus, without aberration-correction, STEM provides some important advantages over TEM imaging.

As an annular detector is responsible for cutting of electrons that have been scattered to low angles only, it can be considered as a coherency filter, as remaining coherency can be reduced as much as desired by increasing the inner hole of the detector. This is, where different detectors are used to pick up the ABF and LAADF signals, which are more coherent in nature (Figure 2.13). As guideline for imaging to be incoherent, Pennycook reported that the collection angle needs to be much wider than a typical Bragg angle for the transverse coherence length to become less than the atomic separation and thereby the image incoherent [118]. As typical collection angles for HAADF STEM are bigger than 20 mrad and typical Bragg angles on the order of 2-3 mrad, this requirement is fulfilled. In fact, Pennycook provides
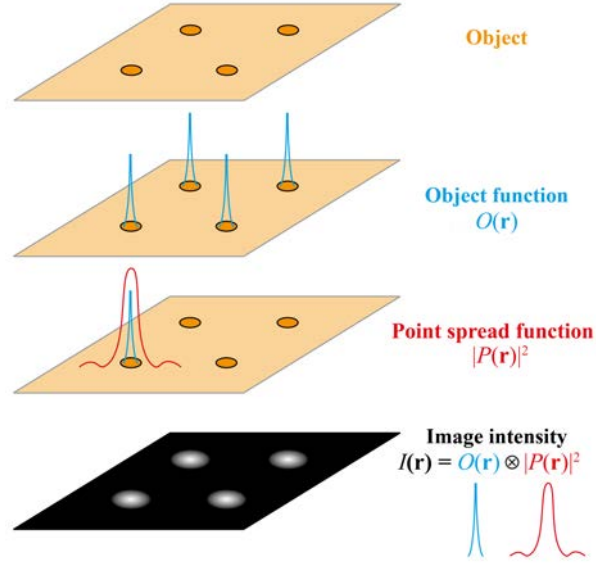
Figure 2.15: Schematic visualization of incoherent (HAADF) imaging of a crystalline sample in STEM. (a) Monolayer of cubic crystal. (b) the object function of the sample represents the Z-number dependent scattering strength, which is localized at each atom. (c) Illumination of one atom with a Gauss shaped probe. Scanning of the probe across the sample maps its the object function and results in (d) an incoherent image, in which the intensity is a convolution of the object function and the point spread function. Redrawn from [131].

an additional criterion for a detector's minimum collection angle β to achieve incoherent imaging of two objects separated by ΔR and where the image intensity varies less than 5% from incoherent imaging: $\beta_{min} = 1.22\frac{\lambda}{\Delta R}$ [118]. From this, the HAADF inner collection angle of at least around 50 mrad originates, as shown in the original work. The only physical effect preventing arbitrary large inner collection angles is the reduced intensity reaching the detector, which decreases the signal-to-noise ratio with increasing angles.

In addition, the increased convergence angle of an aberration-corrected STEM reduces the depth of field Δz significantly to only a few nanometers according to

$$\Delta z \propto \frac{\lambda}{\alpha^2} \tag{2.11}$$

were λ is the electron wavelength and α the semi-convergence angle [129, 130]. Although a reduced depth of field might seem disadvantageous at first, it might be beneficial e.g. in the case of grain boundary structure determination. This is because grain boundaries are hardly ever oriented perfectly edge-on with both abutting grains in perfect zone axis (ZA) orientation, and might even reconstruct along the beam direction (in depth). Large depths of field would capture such effects and thereby potentially blur the boundary structure. Thus, although S/TEM images being projection images, the reduced depth of field might allow to retrieve some three dimensional information of the sample. The longitudinal direction is

also interesting in terms of coherency, as this direction (along an atomic column) provides much less phase difference as compared to the transverse direction and is therefore much more coherent. However, thermal vibrations in the transverse direction (thermal diffuse scattering or phonon scattering) effectively break the coherency in the longitudinal direction by inducing additional phase changes. In conclusion, a detector with a large inner collection angle is needed to break the transverse coherency between neighboring columns, and at the same time thermal vibrations break the coherency along individual columns as well.

2.3.5 Energy dispersive X-ray spectroscopy (EDS)

For chemical identification of segregated solute atoms to a grain boundary, as necessary in the present work, an analytical method is needed with a spatial resolution down to the atomic level and sufficiently low detection limit. S/TEM images provide already a wealth of information, but differentiating chemical concentrations of the investigated sample's elements adds a very important information needed for further interpretation of that sample's condition. With spatial resolution at the atomic level in aberration-corrected STEMs and a detection limit that then depends mainly on sample thickness, beam energy and analysis time, EDS has proven to be an effective tool for chemical characterization [125]. Using this method enables, in best cases, detection of only few dissolved atoms in an homogeneously low-alloyed material [132].

EDS relies on X-ray radiation originating from inelastic scattering events between incoming beam electrons and electrons belonging to atoms of the sample (see section 2.3.2), in contrast to elastic scattering responsible for HAADF STEM contrast as discussed in section 2.3.4. However, HAADF STEM images and EDS spectra can be acquired complementary at the same time. The specific mechanism of the relevant inelastic scattering event is depicted again in Figure 2.16a using the Bohr atomic model. An incoming beam electron interacts with an inner shell electron and transfers enough energy to excite the shell electron, which is consequently emitted as secondary electron, while the incoming beam electron is scattered mostly to just small angles (strong forward scattering). The atom is handling this ionized state by transitioning an electron from a higher shell to the electron vacancy by emitting a X-ray photon carrying the exact energy of the shell transition. The energy of the photon is therefore characteristic for a unique shell transition in a specific element. For example, if an electron in the K-shell is emitted and the vacancy filled by a L-shell or M-shell electron, the generated X-ray photon is a K_α or K_β-type photon, respectively. The type and number of possible transitions depend on the available electrons inside an element's atom, which have to obey the quantummechanically imposed transition rules, and are therefore also element specific. While strong forward scattering prevails for electrons, characteristic X-rays are emitted isotropically in all directions and could theoretically all be detected. However, only
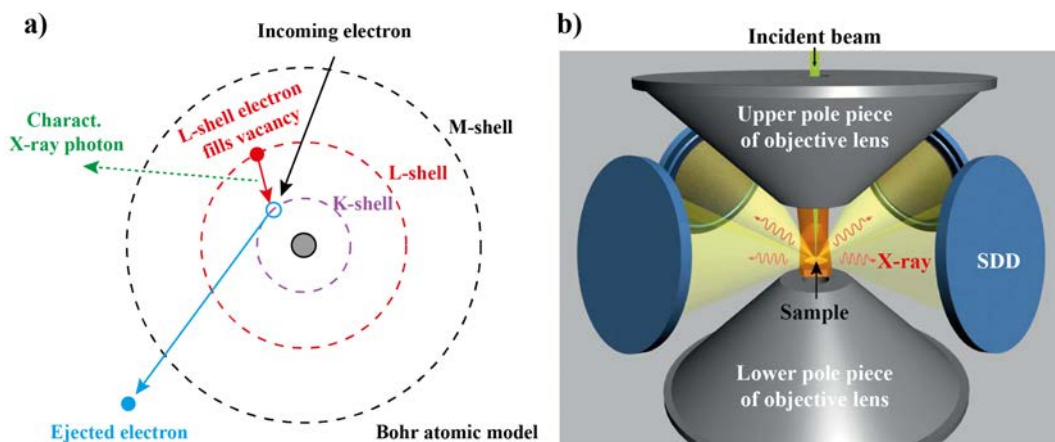
Figure 2.16: Energy dispersive X-ray spectroscopy (EDS) principles and experimental arrangement. The atomic origin of characteristic X-ray photons is presented in (a). An incoming electron hits a core shell electron leading to ejection of this electron (excitation). The created empty state is filled by a higher shell electron. The shell transition releases energy in form of a characteristic energy containing X-ray photon. (b) The electron beam causes isotropic, characteristic X-ray radiation being generated at the location of where the beam passes the sample. However, only the angular fraction hitting the X-ray detectors (silicon drift detector - SDD), which sit between the upper and lower pole piece of the objective lens, can be used for chemical analysis. The image is based on the official FEI application note [133].

a radial fraction is detected by one or more X-ray detectors as the radiation is typically shielded by the specimen holder. In addition, geometric considerations do not allow to include a spherical detector covering the entire angular range of radiation, as the sample is sitting between the pole pieces of the objective lens. Therefore, there is only very limited space to include as much detector area as possible to increase the signal-to-noise ratio. In modern microscopes, aberration-correction is beneficial for improved detector arrangements, as it allows for increased distances between the upper and lower pole piece and thus larger detector areas. In addition, multiple detectors can be used at the same time, instead of just one, to collect X-rays from many angles and increase the total detector area. A possible four-detector arrangement, as equipped on the used microscope here, is shown in Figure 2.16b. Typical X-ray detectors are windowless silicon drift detectors (SDD), which use pure silicon as sensor. Incoming X-rays create electron hole pairs, which are separated by circular electrodes and therefore create a signal. The higher energy a X-ray carries, the higher the charge created. Each X-ray is counted and, depending on the produced charge, is added to a distinct channel. The number of counts is finally plotted as intensity against the X-ray energy (higher signal-to-noise ratios) to create a characteristic spectrum, the sample's chemical fingerprint, which is generally of better quality for longer times (more counts). A typical spectrum containing the characteristic spectrum on top of the Bremsstrahlung (see section 2.3.2) background is shown in Figure 2.17a and in logarithmitic scale in Figure 2.17b. While all major peaks can be seen in the characteristic spectrum, the logarithmic scale emphasizes the Bremsstrahlung background
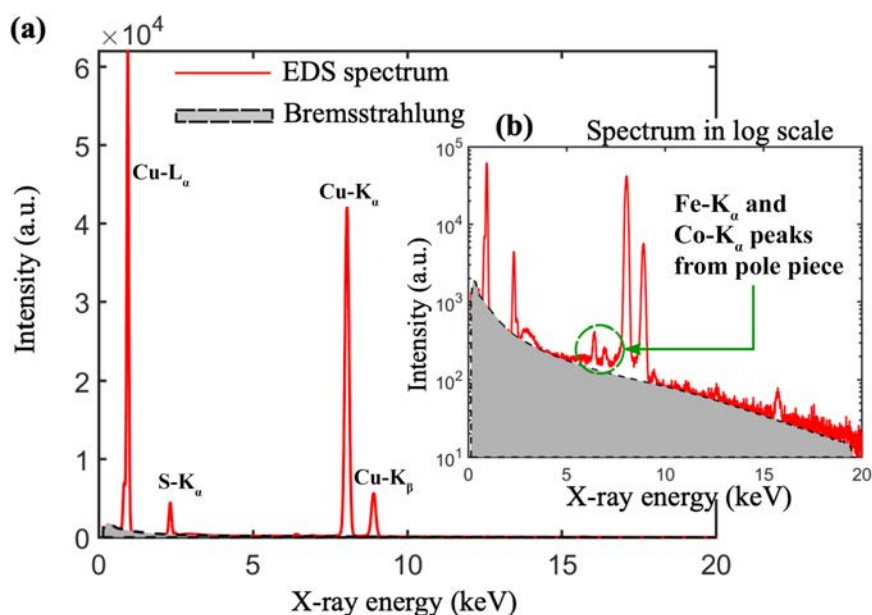
Figure 2.17: Typical EDS spectra: (a) Typical EDS spectrum (red) showing some characteristic Cu and S peaks. The Bremsstrahlung spectrum is visible as gray background. (b) shows the same spectrum in a logarithmic scale, in order to better visualizes the Bremsstrahlung. Additional small Fe and Co peaks become visible (highlighted by green dashed circle) resulting from the microscope's interior. The image is taken from [134].

and additionally smaller peaks originating from the holder or parts of the microscope, such as Fe and Co peaks. For parallel illumination of a large sample area in TEM, only one spectrum is obtained representing the entire illuminated area. In this case, the advantage of STEM becomes obvious, i.e. in STEM mode a spectrum as examplified in Figure 2.17 is acquired at every pixel that is scanned by the beam. Analysis of these spectra allows plotting them as qualitative intensity maps and after quantification as elemental concentration maps (often referred to as EDS maps) or line profiles. Especially for aberration-corrected microscopes, atomic resolution elemental mapping has been shown [123–125]. In this case, the spatial resolution of EDS is limited by beam broadening and becomes worse for increasing sample thickness.

Quantification of EDS spectra is accomplished in a simplified fashion, therefore, a quantitative analysis has limited capabilities. The first obstacle is that it is virtually impossible to measure a sample's entire generated X-ray intensity for geometric reasons discussed above. Therefore, Castaing first proposed a ratio method of measured intensities for X-ray analysis of bulk specimen comparing a sample's measured intensity I_i of element i with the measured intensity of element i in a well characterized standard reference sample $I_{(i)}$ [135]. The ratio of these intensities can then be related to the concentrations C of element i in weight percent according

to

$$\frac{C_i}{C_{(i)}} = K \frac{I_i}{I_{(i)}} \tag{2.12}$$

Three effects are generally contributing to the K-factor proposed by Castaing: (i) the Z-number dependent ionization cross-section of an element, (ii) the absorption of X-rays in the sample and (iii) the fluorescent yield of X-rays within the sample. It is important to realize that the K-factor is not a constant. Going forward, it has been recognized that point (ii) the absorption and (iii) the fluorescence, do not need to be considered for thin S/TEM samples (thin foil criterion). In addition, Cliff and Lorimer proposed in 1975 that the use of standards can be avoided, if the intensity ratio between two elements a and b is regarded, which were recorded simultaneously [136]. The neccessity to exclude standards originates from the fact, that in TEM, analysis of the specimen and a standard involves stopping the electron beam to change samples. Therefore, beam currents may vary for the two samples, which results in differences in X-ray yield and introduces errors. In addition, variations due to thickness can be excluded for individual spectra, as they are recorded at an identical location (still to be regarded in elemental maps). The formalism proposed by Cliff and Lorimer only slightly changed Castaing's equation (Equation 12) to

$$\frac{C_a}{C_b} = k_{ab} \frac{I_a}{I_b} \tag{2.13}$$

Castaing's K-factor is replaced in this case by the Cliff-Lorimer factor k_{ab}, which is specific for each element combination that is investigated and is also not a constant. This equation can easily be extended to alloys containing more than two elements. To date, this is the most commonly used procedure to (semi-)quantify individual EDS spectra in terms of elemental composition. Note that the Cliff-Lorimer quantification does not hold true anymore in aberration-corrected STEMs under strong channeling conditions, e.g. in ZA-orientation and intensive simulation work would have to be performed to account for such effects [137]. A newer approach is referred to as ξ-method. Further details for this method can for example be found in [114]. A critical point to consider when acquiring long EDS spectra or maps is beam damage. Positioning the electron beam may result in different detrimental effects from energy input by the different scattering mechanisms, such as sample heating, atomic displacements, removal of atoms or even hydrocarbon contamination. A comprehensive overview of possible damage types can be found in [138]. EDS is particularly useful to detect heavy elements. For lighter elements with Z-numbers below 4-10, detection is hardly possible. This is related to the yields of the inelastic scattering products, i.e. the characteristic X-ray and Auger electron yields. The sum of the X-ray and Auger yields equals unity. Consequently, if one emission process dominates, the other is hardly occuring. Considering that the X-ray yield ω is strongly Z-number dependent with a common expression for the relation being

$\omega = \frac{Z^4}{a+Z^4}$ (a is typically 10^6 for the K-shell) [114]. Consequently, for Z-numbers below 4-10, the X-ray yield becomes too low and Auger electron emission prevails. For instance, C (Z = 6) emits 999 Auger electrons and only one X-ray photon for 1000 excitations. An alternative for such lighter elements is EELS [114, 123], which is not used and discussed in the present work. While EDS is detecting X-ray photons directly for elemental characterization, EELS measures how much energy an electron has lost during a scattering event.

2.3.6 Quantitative STEM image analysis

Aberration-corrected STEM provides sub-Ångstrom spatial resolution at pm precision, thereby being capable to characterize the structure of crystalline materials on the atomic level [139]. In combination with analytical methods such as EDS and EELS, chemical information can even be obtained from complex material systems and their interfaces with atomic resolution [140]. However, these techniques usually require acquisition times on the order of minutes translating into high electron doses [141] that may influence the sample material by beam-induced effects like knock-on and ionization damage, radiolysis, sputtering, etc. [138]. The high electron doses required in analytical measurements can activate atomic migration leading to blurring of the X-ray or EELS signal. Since the contrast of atomically resolved HAADF STEM images is proportional to the mean atomic number of the atom columns (Z-contrast imaging), this imaging technique provides an alternative to extract qualitative and quantitative chemical information with a much lower required electron dose [142]. Recent studies even achieved to extract the number of atoms in individual mono-elemental atomic columns out of HAADF images of lead nanoparticles embedded in a silicon matrix [143], germanium clusters [143], a gold nanorod [143] or platinum/iridium nanoparticles on a 3D carbon black support [144]. It is currently investigated if this so-called "atom-counting" approach can predict numbers and positions of a second elemental species inside an individual column [145]. Instead of taking the peak intensities of atomic columns, this analysis uses integrated peak intensities that are related to the scattering cross-section. It was found that the peak intensity of a homogenously filled atomic column increases monotonically but strongly nonlinear with sample thickness and eventually reaches saturation at about 10 nm sample thickness, while the scattering cross-section of that same column was found to also increase monotonically but much closer to a linear behavior [146]. Applying this approach to atom-counting, it was shown that reliable results can be obtained from single atoms and atom clusters up to 40 atoms inside individual columns [143], however, there are still restrictions associated to that method. Besides beam sensitive materials that decompose or change structure under an incident electron beam, factors like background intensity and dose dependence have to be considered as shown by De Baker et al [144]. This study also showed that deviations of only a few mrad from an exact zone axis orientation might already strongly influence

the measurement due to a reduction of electron channeling in the atomic columns. The situation becomes even more difficult for thicker samples when cross-talk between columns occurs influencing the integrated scattering cross-section by up to 11% and 16% in the case of pure platinum and palladium columns, respectively, for 10 nm thick samples [146]. In contrast to these atomically precise characterization methods in more or less ideal nanostructures, interfaces of thicker sample systems raise the level of complexity. Moreover, interfaces like grain boundaries involve a high number of vacancies, consequently atomic reconstructions within the interface along the electron beam direction and slight deviations from the perfect zone axis orientation represent challenges that have to be addressed in future experiments on more complex material systems. Recently, different groups explored the possibilities of fast sequential STEM image acquisition under HAADF imaging conditions to distinguish single atoms and track their movement over time. However, most of these studies either investigated beam-induced migration of single atoms in or on homogeneous and stable ceramic substrates like cerium and manganese doped wurtzite-type AlN [147] or of single iridium atoms and clusters on MgO [148]. Bowers et al. recently showed dynamical beam-induced step coalescence at a grain boundary in Au in an aberration-corrected STEM [61]. They stress the importance of careful knowledge about acquisition time related phenomena induced by electron beam radiation during image or spectrum acquisition. Regarding the random walk model of lattice diffusion, for instance, it is clear that atomic motion is at least linearly related to time if not even on a higher order considering the less densely packed structure of grain boundaries compared to the bulk. This is especially important for probe corrected microscopes that have sub-Ångstrom beam diameters, since the electron dose is inversely proportional to the square of that diameter. Critical steps to extract meaningful information from such image series are the alignment of the individual frames and how to deal with artifacts originating for instance from the scanning system, especially in STEM. Nonrigid registration is a currently often used method to achieve this and was shown to be able to increase precision for locating atomic column positions to the sub-pm regime [149]. Other parameters such as scan and environmental noise and dose effects are currently investigated, along with suggestions of how to analyze and interpret these effects [150].

2.3.7 S/TEM image simulation

Transmission electron microscopy is a very versatile tool to determine a metal's microstructure, crystal structure, chemical composition and oxidation state, just to name a few. Especially high-resolution micrographs serve as powerful tool to discriminate atomic columns (intensities) and their elemental occupation, thus the sample's crystal structure is in principle possible to be extracted from such images. However, contrast of S/TEM micrographs is very sensitive for example to sample thickness, deviations from zone axis orientation, defocus
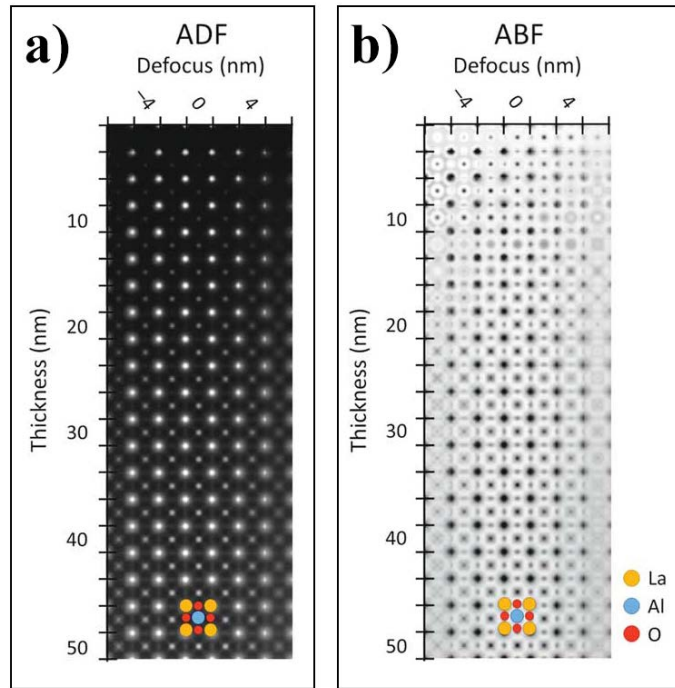
Figure 2.18: Simulated (a) ADF and (b) ABF images for different thicknesses and defocus of a SrTiO$_3$ single crystal (adopted from [151]).

and other aberrations. These micrographs are intensity maps of the arriving electron wave $\Psi(\overrightarrow{r})$, which thus lost its phase information. In particular, the intensity of a coherent TEM image is proportional to a convolution of the incoming wave and the specimen potential $\phi(\overrightarrow{r})$ according to $I(\overrightarrow{r}) =\mid \Psi(\overrightarrow{r}) \otimes \phi(\overrightarrow{r}) \mid^2$, while for incoherent imaging a convolution occurs according to $I(\overrightarrow{r}) =\mid \Psi(\overrightarrow{r}) \mid^2 \otimes \mid \phi(\overrightarrow{r}) \mid$ (note that BF imaging in STEM is coherent and follows the previous relation). Therefore, extraction and interpretation of quantitative intensity values, not to mention contrast interpretation due to contrast inversion, among others, are difficult, as the phase information of the wave function arriving at the detector is lost. A well established way to overcome these challenges is to complement the experimentally acquired intensity maps (images) with image simulations that may, for instance, sample some parameters such as defocus and sample thickness to match the experiment. An example of such an approach is given for simulated annular dark field (ADF) and ABF STEM images in Figure 2.18 with respect to defocus and sample thickness [151].

There are two common image simulation techniques, i.e. Bloch waves and multi-slice techniques. While the latter approach was used in chapter 4.2 for a small simulation cell, a recently developed combination of both methods referred to as PRISM was used in chapter 4.1. Therefore, a brief description of these methods is provided here following [152] and [153]. For the Bloch wave theory, the sample can be considered a converter that converts the in-

cident electron wave $\Psi_{inc}\left(\vec{r}\right)$ into a superposition of Bloch waves inside the sample. The Bloch waves initiated in the sample are determined by the required boundary condition of a continuous wave function at the entrance surface of the sample. After entering the specimen, the electrons travel through the sample as Bloch waves. Finally, the Bloch waves forming the electron wave at the exit surface $\Psi_{exit}\left(\vec{r}\right)$ represent the actual periodic crystal structure in the specimen. The formalism defines the electron wave function $\Psi\left(\vec{r}\right)$ as the sum of linear combinations between a basis set and many scattering factors. The basis set and the sample's potential are inserted into the Schrödinger equation and the eigenvalues and eigenvectors of the resulting equation have to be calculated. Finally, all scattering factors have to be determined by adjusting the wave equation to match the wave function inside the sample with the incident electron wave $\Psi_{inc}\left(\vec{r}\right)$. The result is stored in a huge scattering $\mathbf{S}$-matrix according to $\Psi_{exit}\left(\vec{r}\right) = \mathbf{S}\Psi_{inc}\left(\vec{r}\right)$. Practically, this matrix becomes very large with increasing simulation cell size and eventually not practical to use regarding the computational time for the eigendecomposition. In addition, the Bloch wave method works best for perfectly periodic crystals without defects.

In the present work, however, simulations are used to complement experiments performed on grain boundary containing samples, i.e. simulation cells without a perfectly periodic unit cell. Thus, the multi slice approach is the method of choice in this work as it is more flexible for simulation cells containing crystalline defects or even amorphous samples and requires less computation time [152]. This approach assumes an incoming wave function for the incoming electrons and slices the artificial crystal into many thin slices containing the projected potentials of the contained atoms (Figures 2.19a and 2.19b). The slices themselves can be considered weak phase objects, meaning they do not change the amplitude of the incoming wave but only slightly change its phase due to interaction with the potentials. The exit wave function Ψ_{exit} consequently consists of the wave function $\Psi\left(\vec{r}\right)$ multiplied by a transmission function $t\left(\vec{r}\right) \cdot \Psi\left(\vec{r}\right)$. According to the Huygens principle, the exit wave initiates new wavelets from every point along the wave front and the new wave front is obtained by Fresnel interference of these wavelets. This part is considered the propagation part of the simulation, which results in a convolution of the transmitted wave with the propagation function $\Psi_{exit}\left(\vec{r}\right) = p\left(\vec{r}\right) \otimes t\left(\vec{r}\right) \cdot \Psi\left(\vec{r}\right)$ [152]. These operations can be performed efficiently by switching back and forth between Fourier space and real space, as convolutions are simple multiplications in Fourier space. Consequently, the transmission operator is multiplied in real space, while the propagation operator is multiplied to the Fourier transform according to $\Psi_{exit}\left(\vec{r}\right) = \mathcal{F}^{-1}\left\{\mathcal{F}\left\{t\left(\vec{r}\right) \cdot \Psi\left(\vec{r}\right)\right\} \cdot p\left(\vec{r}\right)\right\}$ [153]. This procedure is then repeatedly applied for all slices (Figure 2.19c). In case of STEM image simulations, the probe function has to be simulated for every pixel in one slice for all slices, which highlights why such simulations are computationally costly. So far the simulations have been considered as ideal, however, exper-
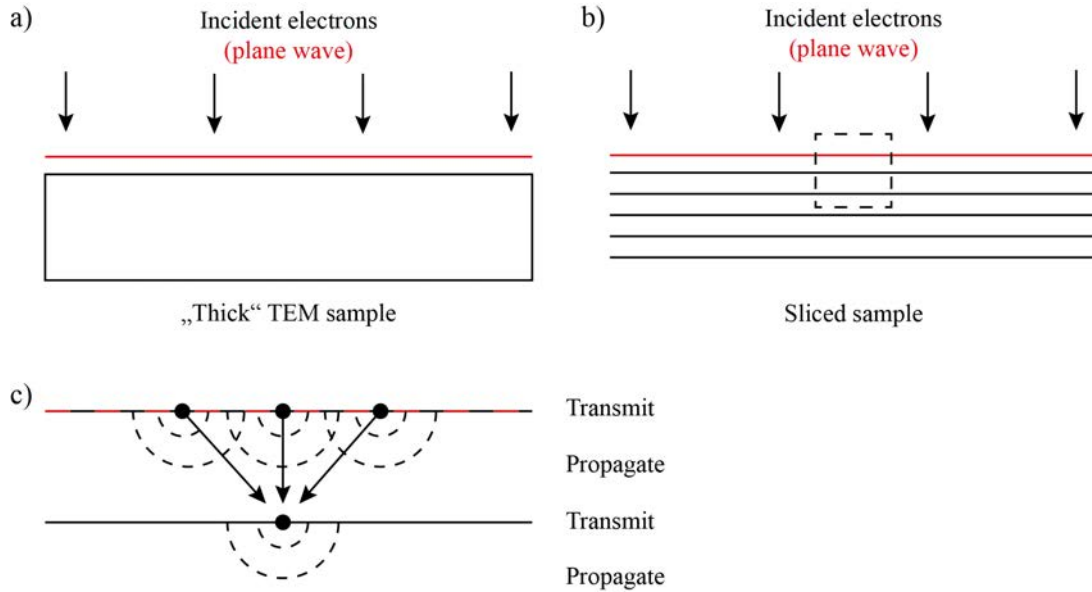
Figure 2.19: Multi slice image simulation principle based on Figures in [152]. (a) shows the experimental situation of an incoming wave at the surface, while (b) shows the sliced sample used for the image simulation. (c) illustrates the consecutive transmission and propagation steps by interaction with the projected potentials and via the Huygens-Fresnel principle, respectively.

imental micrographs are recorded at room temperature (300 K). Thus atoms slightly vibrate around their equilibrium position, which results in a thermal diffuse scattering background in experimental images. To mimic this behavior for the simulation, a random displacement is imposed on the ideal positions of all atoms in each slice, i.e. a frozen phonon configuration is simulated. Several simulations have to be performed to account for thermal vibrations. Thus all slices are simulated consecutively for one frozen phonon configuration, which is then repeated by the desired number of frozen phonon configurations. Ultimately, the final image is the intensity $|\Psi(\vec{r})|^2$ averaged over several frozen phonon configurations. The reason why all slices have to be simulated completely for one frozen phonon configuration before calculating the next one is that only intensities can be averaged, not wave functions. For simulations containing large amounts of atoms (large cell sizes) or defects, both described methods run into problems, due to increasing computation times. As a consequence a new simulation methodology referred to as PRISM was recently developed by Ophus et al. [153, 154], which combines the benefits of the Bloch wave and multi-slice methods achieving a great reduction of computation time. After slicing the simulation cell and calculation of the projected potentials, an interpolation factor f has to be chosen, which can be translated into only every f^{th} beam has to be simulated. This describes the key point of the new simulation scheme, which assumes that "highly converged STEM probes converge to zero quickly with distance from the probe center position, they can be cropped out of the full **S**-matrix in a highly accurate Fourier interpolation scheme" [153]. For the reduced amount of beams, the scattering factors

are calculated directly into the reduced **S**-matrix and all the probe coefficients are calculated for the interpolated coordinate system. The sum of all **S**-matrix values (all zeros are skipped) multiplied by the coefficients finally results in the output probe.

2.3.8 Atom probe tomography (APT)

For chemically quantitative analysis at currently highest precision regarding experimental techniques, local electrode APT established itself as a key analysis tool besides TEM-based techniques. While the spacial resolution has been advanced to lattice plane resolution in special cases, the big advantage of this destructive method is a chemical detection limit of few ppm depending on the element. Samples are required to possess a needle-like shape with a tip radius of below 100 nm. Therefore, Thompson et al. [155] and Miller et al. [156] proposed strategies to fabricate adequate samples via FIB milling. These strategies were followed in the present work.

The method's working principle is schematically shown in Figure 2.20a. For the method to work, the needles need to be cooled down to about 60 K and the chamber must be evacuated to accomplish ultra high vacuum. A local electrode is positioned in close proximity to the fabricated needles and a base voltage is applied. For controlled field evaporation from a needle's tip, either voltage pulses or laser pulses are used. Each pulse starts the timer of a time-of-flight mass spectrometer, which is stopped by an ion arriving at the detector. This spectrometry method determines the ion specific mass-to-charge ratio as fingerprint of the materials constituents. The location of arriving ions at the position sensitive detector is stored together with the mass spectrometry result for every detection event. From the number of detected ions and their respective volumes in combination with the projected, quadratic sample surface, a depth calibration can be performed, which is capable of reconstructing the sample's composition almost at an atomic scale and in three dimensions with very high precision. A further improvement of the spatial resolution is achieved by introducing a further correction term accounting for the tip curvature. Ultimately, lattice plane resolution is achievable in direction of evaporation (the needle's long axis). In Figure 2.20b a representative tip reconstruction shows ZnSe-precipitates in a $Cu_2ZnSnSe_4$ matrix [157]. From such reconstructions, further analyses can be performed including chemical profiling, excess solute determination [158, 159], cluster analyses, etc. Illustration of how the solute excess concentration at a GB is determined from an APT sample's reconstructed volume is provided in Figure 2.21. A cylinder of known diameter is introduced into the reconstructed volume perpendicular to the solute enriched grain boundary resulting in three regions along that cylinder, i.e. the left grain A, the grain boundary B and the right grain C (Figure 2.21a). Along the cylinder, across the GB, both the number of solute (Ag) atoms and the total number of atoms contained in the cylinder are counted and plotted against each other
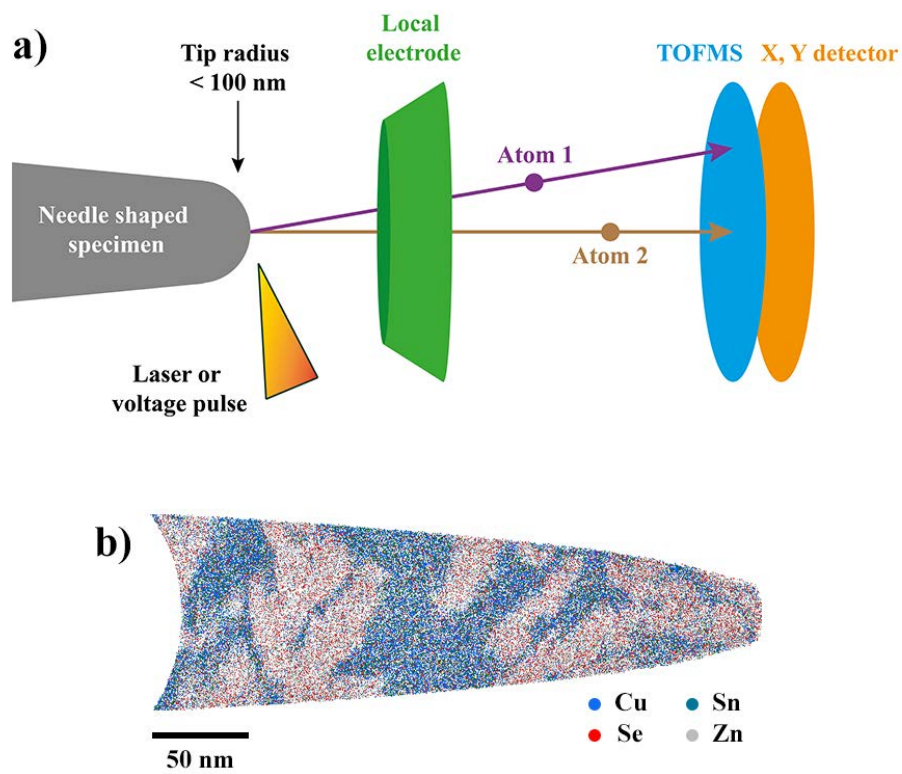
Figure 2.20: Schematic of the local electrode atom probe tomography (APT) working principle. (a) From a nanometer sized, needle shaped specimen, atoms are evaporated by consecutive energy pulses by a local electrode. Evaporated atoms are analyzed chemically by a time-of-flight mass spectrometer (TOFMS) and spatially correlated by a X and Y sensitive detector. (b) Representative 3D specimen reconstruction of ZnSe-precipitates in a $Cu_2ZnSnSe_4$ matrix (adopted from [157])
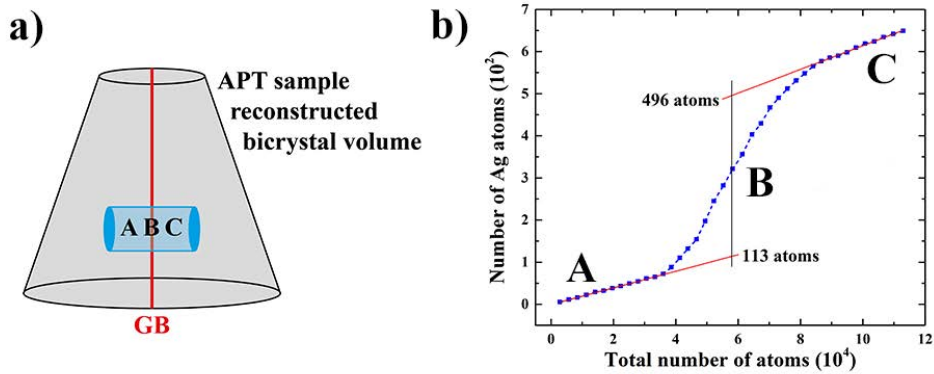
Figure 2.21: Illustration of how the solute excess concentration at a GB is determined from an APT sample's reconstructed volume. (a) Schematic visualization of the reconstructed sample volume of a bicrystal containing a Ag segregated GB. To determine the solute excess concentration, a cylinder of known diameter is introduced into the volume perpendicular to the grain boundary resulting in three regions along that cylinder, i.e. the left grain A, the grain boundary B and the right grain C. Along the cylinder, across the GB, both the number of solute (Ag) atoms and the total number of atoms contained in the cylinder are counted and plotted against each other as shown in (b). The solute species increases linearly inside the grains (regions A and C), however, in the GB region B the slope is higher due to the accumulation of Ag solute excess. The difference between the amount of atoms in the center of region B devided by the cylinder's surface provides the solute excess concentration in atoms/ nm^2.

as shown in Figure 2.21b. The solute species increases linearly inside the grains (regions A and C) with the same slope due to equal solid solubility inside the grains, however, in the GB region B the slope is higher due to the accumulation of solute excess. The lines of regions A and B are extrapolated and their amounts of solute atoms in the central part of the GB region B are determined, in this example to 496 and 113 atoms. In a final step, the difference of these amounts has to be devided through the cylinders cross sectional area to obtain the solute excess concentration in atoms/nm^2. Detector efficiencies of 37 % up to currently 80 %, but significantly below 100 %, limit the reconstruction's resolution and concentration limit. In addition, the lateral resolution is significantly worse than the resolution along the needle's long axis due to the inaccuracy of the surface back-projection, as the exact location of atoms (ions) field evaporated from the APT tip is not known. Finally, local chemical inhomogeneities from precipitates, grain boundary solute atoms and related microstructural features change the needle's field evaporation behavior, leading to uncertainties of the tip's curvature and thus to the so called "local magnification effect". In such cases, exact dimensions are very hard to determine. More details about the technique can be found in [160].

2.3.9   Atomistic simulations

Scientific questions in the field of materials science tend to become more focused on fundamental mechanisms of phenomena, such as phase transitions, phase separations, structural grain boundary transitions and their interplay with solute atoms. Often, the atomic mechanisms involved in these phenomena are not easily accessible or separable, if at all, with our current experimental methods on hand. In this situation, computational work has been continuously developed to complement experiments on various time and length scales, depending on the question to be solved. While macroscopic bulk or rather application related properties can usually be treated by continuum methods like finite element analysis, many different methods have been developed to perform atomistic simulations, which are build on different bases. The most precise atomistic simulations are based on quantum mechanical methods solving the respective equations ab-initio, as for instance density functional theory. However, these calculations typically only allow for very small simulation cells containing only few atoms but being computationally very costly. For studying grain boundaries and especially of asymmetric type (large or no CSL lattice) and in relation with segregation phenomena, such simulations are not very suitable due to these limitations.

The branch of atomistic simulations pursued in the present work is based on methods, which do not require the full calculation of quantum mechanical effects, but rather perform classical calculations that contain the quantum mechanical properties in some way, for instance within used pair potential functions. Thus, atomistic effects can be performed much faster compared to ab-initio quantum mechanical simulations, however, the precision always needs to be regarded; a wrong pair potential function may lead to wrong simulation results compared to the real world. On the one hand, molecular dynamics (MD) simulations are employed in the present work, which allow relatively large simulation cells (commonly containing about half a million atoms) by solving numerically, step-by-step (time steps of about 1 femtosecond), Newton's classical equations of motion

$$m_i \ddot{\vec{r}}_i = \vec{f}_i \tag{2.14}$$

$$\vec{f}_i = -\frac{\partial}{\partial \vec{r}_i} \mathcal{U} \left(\vec{r}^N \right) \tag{2.15}$$

for every single atom i and its interaction with all other atoms; m being atom mass, $\vec{r}_i$ atomic coordinates of individual atoms in the coordinate space, $\vec{f}_i$ force experienced by an atom derived from the potential energy function $\mathcal{U} \left(\vec{r}^N \right)$ with respect to all atomic positions [161]. The following introduction of the MD method is based on [161] and [162]. Requirement to solve these equations is the potential energy function that describes the interaction between neighboring atoms. A very popular pair potential is known to be the 12-6 Lennard-Jones

potential [163]

$$\mathcal{U}(r) = 4\varepsilon \left[\left(\frac{r_0}{r} \right)^{12} - \left(\frac{r_0}{r} \right)^{6} \right] \tag{2.16}$$

with r_0 and ε being the atom separation at zero potential energy and the energy well depth, respectively. Here, r represents the separation distance between two atoms. The fist term represents the repulsive short range potential, while the second term stands for the longer range attractive potential. For condensed matter physics, in particular metals, the embedded atom method (EAM) has become a prominent approach to describe the interactions between atoms in a simulation cell. The assumption made for this method to work is that an atom is placed at position $\vec{x}_i$ inside a host lattice of all other atoms and experiences a uniform environment at this position. It has been shown that the energy of the inserted atom is a functional of the electron density ρ at $\vec{x}_i$ [164], which depends on the atomic number or in other words on the species of that atom. The embedding energy F of atom i thereby describes the energy difference between an isolated atom and an atom that is experiencing an uniform electron gas. The important interaction between atom cores i and j, separated by a distance r, is finally added as simple pair potential function $\phi\left(r_{ij}\right)$ to result in the basic EAM equation (the cohesive energy in the ground state) as originally proposed by Daw and Baskes [165]

$$E_{tot} = \sum_i F_i \left[\rho\left(\vec{x}_i\right) \right] + \frac{1}{2} \sum_{\substack{i,j \\ j(\neq i)}} \phi\left(r_{ij}\right) \tag{2.17}$$

The step-by-step calculation is analytically impossible, but numerically realized by a form of the Verlet algorithm, which first calculates the forces for a small time step, from this calculates all atomic coordinates and finally updates again the forces. The advantages making the Verlet algorithm advantageous for MD simulations are five-fold [161]: (i) it is exactly time reversible, (ii) simplectic, (iii) low order of error in time, (iv) it only needs to calculate the forces once per time step and is (v) easy to program. Although half a million atoms in a typical simulation cell may appear bulk-like, this would still leave about 8 % of all atoms at the surface of a cubic simulation cell. Thus, periodic boundary conditions can be introduced to the simulation cell in chosen directions to eliminate the surface effects and treat the limited amount of atoms like an infinite bulk in that direction. In practice, this is achieved by treating atoms leaving the cell in one direction with periodic boundary conditions as if they were re-introduced at the same place on the opposite side of the cell creating a virtual copy of the simulation block. Besides creating a virtually infinite simulation cell, this approach effectively eliminates the surface without needing any additional calculations for any additional atoms. Finally, MD simulations are often, but not exclusively, run with a canonical (NVT) ensemble, meaning that number of atoms N, volume V and temperature T are kept constant. However, the equations of motion by Newton are conserving energy. Therefore, a thermostat (heat bath)

is typically required, which is implemented as a 'friction coefficient' ζ. If the system is too hot, ζ will increase and thus the atoms cool off (energy is leaving the system). The opposite happens if the system becomes too cool (energy is added to the system, $\zeta < 0$). A popular thermostat is the Nosé-Hoover thermostat [166,167]. In conclusion, this simulation procedure allows for relatively accurate position determination of every atom over time and is suitable for revelation of structures and structural changes, for example of grain boundaries or other defects in a crystal lattice.

The second classical method used in the present work is based on a stochastic approach intended to simulate the evolution of processes with comparably large time scales, on the atomic scale. This is achieved in Monte Carlo (MC) simulations, which are commonly performed within the canonical (like MD) or semi-grand-canonical ensemble. Both ensembles have their advantages and disadvantages regarding atomistic simulations but especially simulations involving defect-type structures such as grain boundaries usually contain a large amount of atoms (hundreds of thousands) and need to be efficiently parallelizable. This is hard to achieve for the canonical ensemble but easy in the semi-grand-canonical one, while concentrations inside a miscibility gap cannot be simulated in the semi-grand-canonical ensemble. Thus, Sadigh et al. established a MC algorithm that takes advantage of both ensembles and is efficient to compute, in order to study precipitation in alloys [168]. Besides other MC simulation algorithms, like the Metropolis-Hastings algorithm [169] or lattice-model MC [170], this mehtod has been used in the present study and therefore the following description is based on Sadigh et al.'s work [168]. If a box of volume V is assumed with N atoms and each atom being of a different element, e.g. either Cu or Ag, then the system can be described with all atoms' positions inside the box $\vec{x}^{3N}$ and the element they belong to, given as N-dimensional vector σ^N. The energy of the system is consequently a function of both these parameters. In the canonical (NVT) ensemble, the system is chemically isolated and therefore the number of members of each element is fixed. Sampling this ensemble by a MC algorithm involves two kinds of trial moves: (i) partial displacements of the atoms $\vec{x}^{3N} \rightarrow \vec{x}_t^{3N}$ and (ii) compositional changes via random selection of two atoms and exchange of their element identity $\sigma^N \rightarrow \sigma_i^N$. In contrast, within the semi-grand-canonical ensemble, temperature and chemical potential for each species are kept constant and the system is in contact with an infinite reservoir resulting in a set of configurations with varying compositions. The trial move (i) remains the same, while (ii) focusing on $\sigma^N \rightarrow \sigma_i^N$ differs. At first, a particle is randomly selected, subsequently its elemental identity is flipped and finally the change in energy and concentration of the system are computed. Instead of requiring two atoms, which may be located on different processors during calculation, this ensemble only requires one atom and is therefore much more easy to parallelize. Sadigh et al.'s developed "variance-constrained" semi-grand-canonical, ensemble can be considered as a generalization of both ensembles and

is controlled by two independent parameters that can push the ensembles more towards the two pure ensembles discussed above [168]. The trial moves here are the same as for the semi-grand-canonical ensemble, except an additional calculation of the concentration variance, which can be constrained.

In semi-grand-canonical MC simulations two trial moves are required: one sampling structural degrees of freedom (displacement MC trial moves) and one sampling chemical ones (transmutational MC trial moves) [168]. These two distinct trial moves are efficiently sampled by different techniques, i.e. displacement trial moves are performed by MD simulations, while transmutational moves remain in the MC simulation. In practice, a MD simulation is run, which is repeatedly interrupted after a fixed amount of steps to perform a number of MC steps. This hybrid MCMD procedure was succesfully applied to study Cu decoration/precipitation at Fe grain boundaries in the original paper [168], but also e.g. to investigate segregation-induced phase transformations in grain boundaries [96], which provided similar questions to be answered as in the present work. Therefore, the chosen hybrid MCMD method has been chosen to study segregation-induced nanofaceting in chapter 4.1.

Chapter 3

Materials and Methods

3.1 Bicrystal Growth

Investigated Cu and Cu-Ag samples were based on commercially available, high-purity, granular Cu. Chemical analysis of this base material detected few major impurities of O, C, N, S, Al and Ca. The measured concentrations are summarized in Table 3.1. It was checked for more elements (As, B, Bi, Cd, Co, Cr, Fe, Mg, Mn, Ni, P, Pb, Se, Si, Sn, Te, Ti, V and Zn), however, all measured concentrations for these elements were below their respective detection limit of typically a few ppm (depending on the element). Thus, the Cu purity was determined to be 99.90 at. %, based on inductively coupled plasma - optical emission spectroscopy (ICP-OES) for metal impurities, infrared absorption measurements after combustion under oxygen atmosphere for C and S impurities, infrared absorption measurements after melting in a graphite crucible under helium atmosphere for O and thermal conductivity measurements after melting in a graphite crucible under helium atmosphere for N impurities. From the granular raw material, a polycrystalline Cu rod was produced, which was subsequently transformed into a bicrystal by making use of the Bridgman technique. The two required single crystalline Cu seed crystals were attached to the polycrystal with their respective [001] crystallographic directions being parallel to each other and parallel to the growth direction. The seed crystals were rotated relative to each other by a 54° misorientation around the [001] axis. This set-up was used to create an asymmetric, non-coincide lattice, tilt grain boundary in the $\sum 5$ system, with a 31° asymmetric inclination angle. The targeted bicrystal fabrication procedure ensures optimal imaging conditions in the TEM for most of the performed experiments, as both grains, can be oriented in the same [001] zone axis (ZA) orientation. During growth, the seed crystals are partially melted in a melting zone. Slow movement of this zone towards and along the polycrystal allows the trailing material to solidify and at the transition from the singlecrystals to the polycrystal to adapt the predefined misorientation. A grain boundary (bicrystal) is formed that extends throughout the entire Cu rod. The process was performed under 99.999 at. % He atmosphere and a pressure of 700 mbar with the seed- and polycrystal combination being embedded in dense graphite powder. A schematic of a grown bicrystal is shown in Figure 3.1a.

Table 3.1: Chemical analysis results of the detected impurities in the commercially obtained granular base Cu.

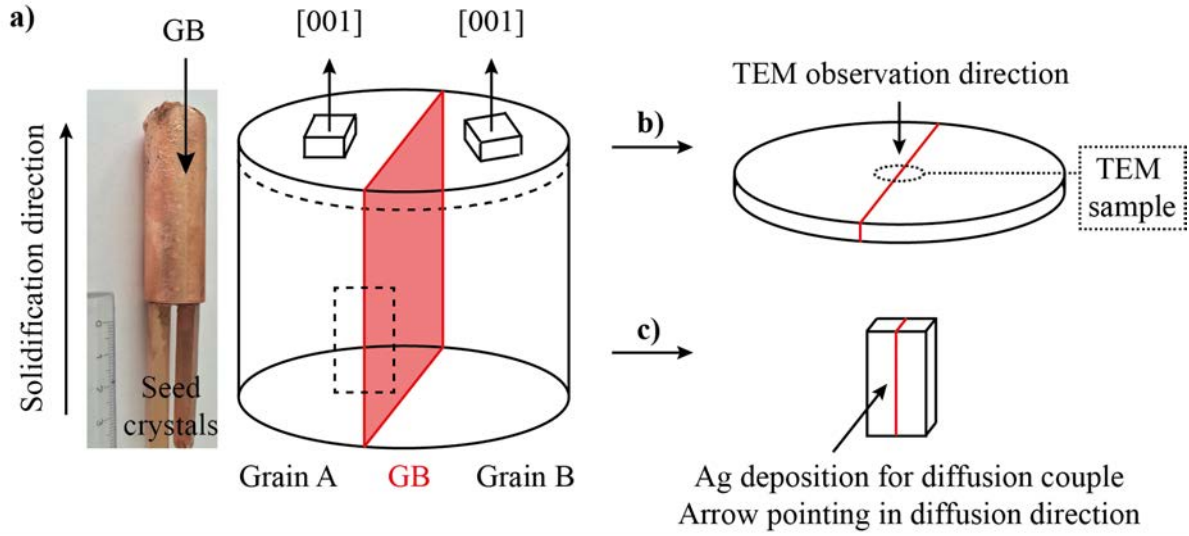| Element	O	C	N	S	Al	Ca
Concentration (ppm)	830	140	20	20	10	10

Figure 3.1: (a) Optical micrograph of the grown bicrystal (scale in cm) obtained from the Bridgman method, along with a schematic overview of the bicrystal, including solidification direction, and [001] direction of the constituent grains. It has to be noted that Grain B is rotated around the [001] axis by 54° relative to Grain A's [001] axis. (b) shows the overview of sample fabrication and observation direction of samples for structural boundary investigations. (c) The same observation direction remains for samples used to create the diffusion couple; the arrow indicates the direction of Ag diffusion along the boundary, while the TEM observation direction remains the same as in (b).

3.2 Sample Preparation

3.2.1 Samples for structural investigations of grain boundaries

Structural changes of the asymmetric tilt grain boundary induced by Ag segregation were studied as part of this work (chapter 4.1 and 4.2) [57, 94]. Alloying Ag into Cu is used to force segregation of Ag atoms to the grain boundary of interest, in order to examine segregation influences at the atomic scale. The difference in Z number is especially beneficial for determining which atomic positions Ag segregates to, by making use of high resolution STEM, particularly using HAADF Z-contrast imaging conditions obtained with a converged beam and annular detector.

Grain boundary containing discs of 500 μm height and about 2 cm in diameter were spark eroded from the bicrystal perpendicular to the [001] growth direction as illustrated in Figure 3.1b. Three types of samples were analyzed based on this geometry: (1) as-grown samples prepared from such discs, (2) thermally annealed pure Cu samples and (3) Ag segregated samples. Thermal annealing was performed in a custom-made vacuum chamber at 800°C for 120 h, and about 10^{-6} mbar pressure. Samples were not quenched but slow cooling under
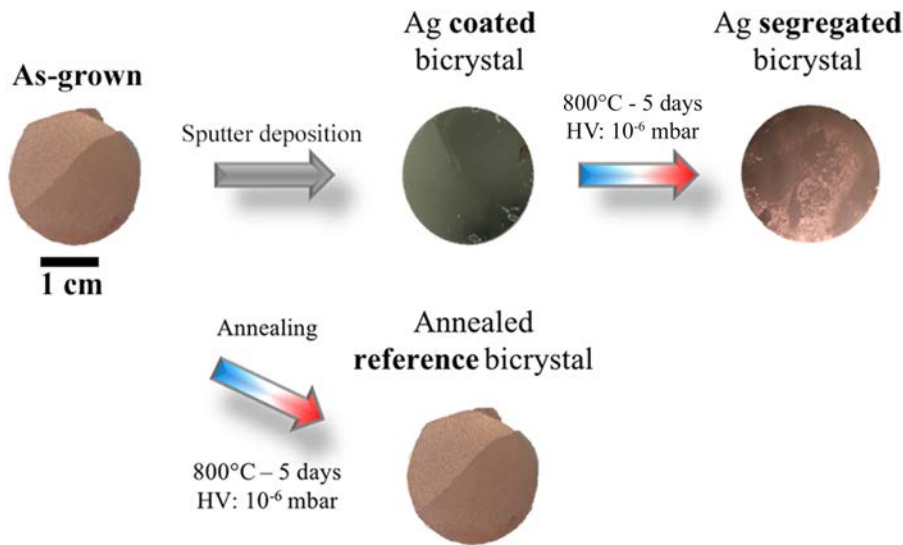
Figure 3.2: Experimental sequence of prepared boundary containing Cu discs for Ag segregation experiments and thermal treatment of pure reference samples. From the grain boundary containing center, TEM samples were prepared.

vacuum was realized by simply turning off the heater to reach at least close to equilibrium conditions. Upon cooling, the vaccum decreased to about 10^{-7} mbar. Pure Cu discs without deposited Ag were annealed at these exact same conditions as reference samples in order to decouple temperature and chemistry effects. Finally, Ag was sputter-deposited on both sides of such discs to a thickness of 500 nm, respectively, and annealed under the exact same conditions as the pure Cu samples before. An overview of the experimental sequence is visualized in Figure 3.2 with optical micrographs of real discs and the equilibrium phase diagram at ambient conditions of the Cu-Ag system is presented for reference in Chapter 2.1 (Figure 2.1) as investigated by Subramanian and Perepezko [29]. From the differently treated discs, TEM samples (3 mm diameter) were spark eroded out, always in the central part of the disc to ensure the boundary being as identical as possible in all investigated samples and as centered in the sample as possible. The location is highlighted by a dashed circle in Figure 3.1b. The eroded samples were metallographically grinded to a thickness of about 100 µm prior to twin-jet electropolishing. Samples were polished until hole formation, which never happened to occur at the grain boundary. Consequently, the hole was slightly enlarged by low kV Ar^+ ion polishing in a precision ion polishing system (PIPS). This method was occasionally also applied briefly for oxide removal just before sample insertion into the TEM.

3.2.2   Samples for diffusion couple analysis

From the grown bicrystal, rectangular pieces of 10 mm x 5 mm and a thickness of about 1 mm were spark eroded out parallel to the solidification direction as illustrated in Figure 3.1c. These were metallographically ground and electropolished only on one side. Ag was sputtered on the polished side of these samples after an Ar sputtering step to remove remaining oxides and other residues to ensure direct contact of the sputtered Ag and the Cu substrate. This Cu-Ag stack was subsequently annealed exactly as described in the previous section, and again shortly electropolished to obtain best surface quality. In this way, a diffusion couple was created with a concentration gradient along the boundary, which was used to investigate the influence of Ag segregation on the boundary's faceting behavior. All different samples fabricated from this diffusion couple were produced by site-specific FIB machining with the Ga^+ ion beam acceleration voltage set to 30 kV for coarse milling and 5 kV for final polishing - if not stated differently. Big TEM lamellae were extracted with a depth of about 20 µm to observe the entire diffusion gradient along a GB and the influence it has on the atomic structure of the boundary.

3.3   Methods

3.3.1   Conventional TEM sample preparation

Grinding and polishing was followed by the well established metallographic route as described in Chapter 2.3.1. In particular, samples were grinded with a sequence of papers starting at European grade P800 (grain diameter of about 26 µm), continuing with grade P1200 (ca. 15 µm) and P2400 (ca. 6-7 µm), finally finishing with a grade of P4000 (ca. 2-3 µm). To reveal the grain boundary on such samples, immersion in orthophosphoric acid was used.
Electropolishing was achieved in either a LectroPol (big samples) or a TenuPol twin-jet electropolishing (TEM samples) device by the company Struers always using an electrolyte composed of 70 % methanol and 30 % nitric acid. In the former case, polishing was achieved at room temperature and at an applied voltage of 20 V, while in the latter case, 6 V were applied and the electrolyte cooled to -30°C. In both cases, polishing usually lasted about 2-4 minutes until hole formation.
Holes in TEM samples, obtained by electropolishing, typically had to be enlarged. This was achieved using a precision ion polishing system (PIPS II) by the company Gatan Systems Inc. Each sample had different parameters depending on the location of the formed hole relative to the grain boundary, but typical polishing sequences were: (i) 30 min. polishing at

around 3-5 kV, (ii) 5 min. at 0.9 kV, (iii) 5 min. at 0.6 kV, (iv) 5 min. at 0.3 kV and finally (v) 5 min. at 0.1 kV, in order to keep knock-on damage as little as possible.

Ag was sputter deposited from targets of 99.99 at. % purity after sputter cleaning with Ar ions for 600 s to remove contaminants and the native oxide layer. Deposition was performed in an ATC-2200V machine (AJA International) by Tobias Oellers (Ruhr-Universität Bochum).

3.3.2   SEM operation

The SEM was commonly used to check the sample quality of different samples, check locations for TEM sample preparation and initial checks for GB plane orientations via electron backscatter diffraction. Typical acceleration voltages were only few kV to observe the topography of the sample, and to identify locations, while 10-20 kV were used for orientation determination. For these purposes, mostly secondary images were acquired in a Thermo Fischer Scientific Quanta or a Helios 600(i) dual-beam machine, except for cases that required highest resolution. For these, the in-lens detector equipped at a Zeiss Auriga instrument was used.

3.3.3   FIB sample preparation of TEM samples

The main purpose of using the FIB, was to site-specifically extract TEM samples. Therefore, grain boundary locations were chosen in SEM mode of Thermo Fischer Scientific Quanta or Helios 600(i) dual-beam machines, and a thin, protective Pt-layer was deposited with the electron beam to a thickness of around 100 nm for further processing. This protective layer was than thickened to around 1 µm using the faster ion beam Pt deposition. Areas for sample extraction were typically 10 µm x 5 µm in size and 10 µm deep. There, trenches were cut next to the areas of interest at high currents of around 15 nA and undercuts performed at approximately 7 nA. After lamella extraction with a micromanipulator and transfer to a Cu support grid, the sample was attached to the support grid with Pt and finally thinned to electron transparancy with progressively smaller beam currents. All prior steps were performed with an ion beam acceleration voltage of 30 kV. For the final cleaning step, the voltage was reduced to 5 kV and a short ion shower applied to remove knock-on damage layers from the sample.

3.3.4   STEM operation

High resolution, aberration-corrected STEM micrographs were acquired in the present work in a Thermo Fischer Scientific Titan Themis 60-300 kV microscope at an acceleration voltage of 300 kV. Semi-convergence and semi-collection angles were set to 23.8 mrad and 73-200 mrad, respectively, thereby resulting in HAADF Z-contrast imaging conditions. Typical beam currents were set around 80 - 100 pA. Because of that Z-number dependence of the image intensity, chemically distinctly different areas can be identified readily in HAADF mi-

Table 3.2: Pixel dwell times (t$_P$), frame (t$_F$) and series times (t$_S$) translate into local (D$_{loc}$), global (D$_{glo}$) and accumulative (D$_{acc}$) electron doses of the applied imaging conditions.

	t$_P$ (s)	D$_{loc}$(e$^-$/Å^2)	t$_F$ (s)	D$_{glo}$ (e$^-$/Å^2)	t$_S$ (s)	D$_{acc}$ (e$^-$/Å^2)
Single frame	15 x 10^{-6}	1.5 x 10^4	18.87	1.9 x 10^{10}	—	1.9 x 10^{10}
Slow Scan	5 x 10^{-6}	5 x 10^3	6.29	6.3 x 10^9	107	1.1 x 10^{11}
Fast Scan	1 x 10^{-6}	1 x 10^3	0.31	3.1 x 10^8	63	6.3 x 10^{10}

crographs or atomic columns being constituted by different elements. Consequently, HAADF imaging is ideal to study segregation phenomena down to the atomic level. At highest magnifications, image sequences were acquired, cumulatively averaged and filtered to reduce scan noise and thus enhance structural visibility.

In the methodological part of this work (Chapter 4.2, [57]), image acquisition and processing was of special importance and is therefore described in depth here for the different data sets. Image acquisition followed three distinct procedures: (1) standard single frame acquisition (Single Image), (2) serial image acquisition of 17 frames at slow acquisition times (Slow Scan), and (3) serial image acquisition of 200 frames at fast acquisition times (Fast Scan) to capture more of the dynamics of Ag solutes at the boundary. For the Fast Scan, a pixel dwell time of 1 µs was chosen as lower bound to reach a sufficiently high signal-to-noise ratio to extract meaningful information. Estimation of the electron dose D was calculated according to

$$D = \frac{It}{A_{probe}} = \frac{4It}{\pi d_0^2} \tag{3.1}$$

where I is the probe current, t the time, and A_{probe} the probe area. A circular probe diameter d_0 of 80 pm was assumed for 300 kV and full compensation of up to third order aberrations. An electron dose rate of 1 x 10^9 e$^-$/Å^{2}s was calculated for the used microscope set up. The individual pixel dwell times (t$_P$), frame times (t$_F$), serial times (t$_S$) as well as their respective local (D$_{loc}$), global (D$_{glo}$), and accumulated (D$_{acc}$) electron doses, which were calculated according to Equation 3.1 and by using the respective times mentioned above, are given in Table 3.2. The single frame image was acquired at lower magnification to capture more Ag columns, show the regular arrangement of Ag, and to minimize a possible contamination of the imaged area for the subsequent serial image series as any carbonaceous contamination layer would increase the background intensity and therefore change the intensity ratio and thus the precision for a quantitative data interpretation. Slow Scan (1024 x 1024 pixels) and Fast Scan (512 x 512 pixels) were both acquired on the exact same location of a zoomed-in region of the static image (1024 x 1024 pixels) and analyzed following the exact same procedures to ensure comparability.
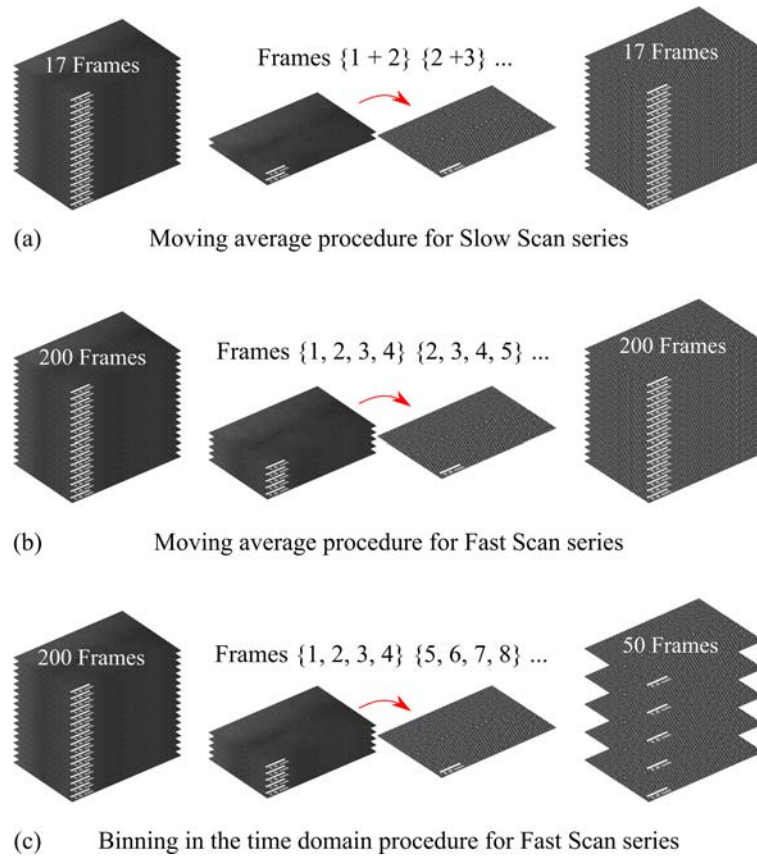
Figure 3.3: Schematic representation of the applied procedures for the acquired image series. For the Slow Scan Series and Fast Scan series, a moving average evolution was applied with two (a) and four (b) images being averaged, respectively. For the Fast Scan series, an additional binning procedure in the time domain was applied that also averages 4 images (c).

The presented electron micrographs are modified using image processing tools, i.e., different filters and averaging techniques, to extract quantitative information. Nevertheless, a raw image and for the image series also an intermediate image are presented, along with the filtered images, to visualize the influence of the applied processing tools. Three main types of image filtering were implemented in Matlab, namely Median, Gaussian, and Butterworth filtering. Filtering is performed to have a first noise reduction of the raw images in the scan series, to smooth the micrographs for peak fitting and precise peak position determination as well as to reduce low frequency noise being manifested as background intensity variations in the real image to accurately compare peak intensities after correlating the sequential images. Special attention was paid to proper alignment of sequentially acquired images. Generally, the procedure to extract quantitative information involved the following steps. First, images from a series were aligned by cross-correlation, where image shifts between consecutive images were refined by determining the atomic column position of the brightest atomic column containing Ag to account for sample drift. Cross-correlation was previously shown to yield

a column position precision of at least several picometers [150]. For comparison, a nonrigid registration approach developed by Jones et al. [171] was additionally applied with almost the same outcome to further account for scan distortions (comparison of both approaches can be seen in the supplementary material section of chapter 4.2). In terms of noise levels, aberration-corrected TEM would be beneficial to avoid scan distortions and use lower dose rates compared to STEM, but direct elemental information would be lost and techniques such as exit-wave reconstruction [172] along with intensive image simulations would be required. Additionally, the alignment of images to the position of the brightest Ag-containing column strongly reduces smearing out of the columns' intensity profile, which is especially important for the few Ag-containing columns, as the Cu background intensity is averaged over many columns, and for cumulatively averaged images of longer acquisition times. In the second step, the atomic column positions and the corresponding peak maxima were obtained by a peak fitting algorithm for all images. Peak intensity ratios were chosen over scattering cross-sections in this study, to actually make use of the saturation effect to get a stable separation between Ag and Cu columns. The peak intensity ratio can be compared to STEM image simulations and is used as first estimate of Ag occupancy and how it depends on the imaging conditions. The Ag-containing atomic columns were deduced by thresholding the peak intensities; the mean peak intensity within the Cu grains was taken as an internal reference for the computation of peak intensity ratios. These reference columns within the grain may contain randomly diffusing Ag atoms that are in solid solution within the Cu. Polynomial background subtraction was performed to account for enhanced Bragg scattering due to a slight twist component of the grain boundary to obtain uniform Cu column intensity within both grains, which is important for precise ratio determination of a rather pure Cu column to a partially Ag-filled column. The peak intensity ratio was determined by dividing the Ag-containing column intensity by the mean atomic column intensity within both grains.

The chosen datasets were treated similarly but with necessary minor adjustments explained in the following, especially for the scan series. The single frame images were analyzed following the general procedure above on as-captured images and the corresponding filtered images (Gaussian and Butterworth) to assess the influence of filtering on quantitative chemical characterization. The Fast Scan series was treated in two distinct ways, one exactly as the Slow Scan series, the second in a way to effectively approach the Slow Scan series dose wise by cumulatively averaging several images of the series and then doing the same analysis. The individual raw frames were summed up in both cases and the resulting images filtered (Gaussian and Butterworth). Chemical information was then extracted as in case of the Single Image following the general procedure. To capture dynamic changes of individual Ag columns in the Slow Scan series, two successive raw frames were first Median filtered

and subsequently cumulatively averaged to increase the signal-to-noise ratio. The resulting image was filtered by a Gaussian and Butterworth filter and an area only containing three Ag columns was cut out (digitally zoomed in). Dynamic chemical information was extracted as described above in a moving average kind of manner over time using overlapping windows of two cumulatively averaged frames (frames $1 + 2$, $2 + 3$, etc.). The Fast Scan acquired on the same location as the Slow Scan was treated in three distinct ways. Again, the individual 200 frames were summed up and the resulting image background was subtracted and filtered. Similar to the Slow Scan, four raw frames were Median filtered and cumulatively averaged, the resulting image was then filtered and analyzed in terms of peak intensity ratio determination. To capture the dynamic peak intensity ratio evolution over time, two similar but distinct approaches were chosen. A moving average approach as used for the Slow Scan (frames 1 - 4, 2 - 5, etc.) was applied using overlapping windows of now four consecutive frames, in contrast to a coarser binning kind of averaging in the time domain using nonoverlapping windows of four consecutive frames (frames 1 - 4, 5 - 8, etc.). The latter approach was chosen to effectively imitate a Slow Scan series by reduction of 200 frames to 50 and increasing the effective acquisition time. A schematic representation of the procedures described above to analyze the Slow Scan Series and Fast Scan Series is provided in Figure 3.3.

EDS maps were acquired at selected locations to correlate nanofaceting with Ag solute excess concentration in zone axis orientation immediately after image acquisition to avoid tilting and thus loss of spatial correlation. A Super-X windowless EDS detector was used at an acceleration voltage of 300 kV.

3.3.5 STEM image simulations details

Part of this work is the determination of the atomic occupancy of a single atomic CSL column at a grain boundary by making use of the Z-contrast of HAADF STEM images (see Chapter 4.2). The peak intensity ratio of the intragranular mean Cu(Ag) background and Ag-containing columns is not yet a truly quantitative concentration, since that ratio also depends on sample thickness. Consequently, STEM image simulations were performed for various thicknesses and Ag occupancies of individual columns in an idealized symmetrical $\sum 5(210)$ grain boundary segment. The simulated STEM images of a relaxed $\sum 5(210)$ grain boundary in Cu with different Ag contents are obtained by an implementation of the multislice algorithm [152] in Matlab. The structural units of the pure Cu grain boundary close to the interface were taken from Frolov et al. [64]. Ag atoms were randomly distributed within experimentally found Ag sites of the symmetric kite structure, i.e., the coincidence lattice sites, replacing 25, 50, 75, and 100 % of the Cu atoms in the respective column. A semi-convergence angle of 23.8 mrad and a theoretical probe size of 0.02 nm were realized for all

simulations. The signal was integrated over a semi-collection angle range between 73 and 200 mrad. The parameterization of the two-dimensional projected atomic potentials was implemented following Kirkland [152]. More than 100 frozen phonon configurations are used to include thermal atomic vibration. The mean square atomic displacements of Cu and Ag were taken from Peng et al. [173].

Compared to the small size of the aforementioned multi-slice simulation used in Chapter 4.2, large, asymmetric grain boundary (defect) containing simulation cells were simulated in Chapter 4.1 to assess the Ag induced structural faceting transition of that boundary. The cells contained over 200 000 atoms, which would exceed reasonable computation times by far using just the multi-slice approach, especially considering the required STEM simulation of millions of probe positions. For such problems, a new simulation methodology referred to as PRISM was recently developed by Ophus et al. [153, 154]. Applied to the present work in Chapter 4.1, simulation cells containing the atomic positions of performed MCMD simulations (compare Chapters 2.3.6, 3.3.7 and 4.1) [94] were used directly as input for the PRISM simulations. For the image simulations, the corresponding MCMD simulation block was replicated twice parallel to the tilt axis in order to increase sample thickness to about 10 nm employing 8 frozen phonon configurations. Only few frozen phonons were used, as the simulations were performed at high temperature and already contained thermal noise.

3.3.6 Atom probe tomography operation

All investigated samples were prepared by FIB milling, following work by Thompson et al. [155] and Miller et al. [156]. Final cleaning of the tips was accomplished with an ion beam of 5 kV and 41 pA, ensuring a Ga content <0.1 at.% in the analyzed regions. The needles were then transferred to the APT, cooled down and evacuated under ultra high vacuum. For controlled field evaporation from the needle's tip, laser pulses were applied at a repetition rate of 250 kHz.

A LEAP 3000X HRTM by Cameca Instruments cooled to 60 K was used in Chapter 4.1 [94] with laser pulses of 0.6 nJ resulting in a detection rate of 0.005 atoms per pulse. In Chapter 4.3 a LEAP 5000XS by Cameca Instruments was used also in laser mode with an energy of 60 pJ, and a detection rate of 0.007 atoms per pulse.

3.3.7 Atomistic simulations

In the present work segregation induced structural changes were investigated (Chapter 4.1) [94], which is most efficiently done by combining the two aforementioned methods to a so-called hybrid MCMD simulation, which is implemented in LAMMPS (a molecular dynamics program) and benefits from the high structural accuracy in MD simulations and the faster redistribution of solute atoms within the MC simulation. The Cu-Ag material system was

modeled using an embedded atom method potential developed by Williams et al. [174]. Timofey Frolov (Lawrence Livermore National Laboratory) was kind enough to perform the following simulations in a collaboration. The orientation of the GB in our simulations was chosen to match the experimental structure, with the {310} and {650} planes of the two crystals parallel to the boundary plane. These simulations were performed in a canonical (NVT constant) ensemble and a Nosé-Hoover thermostat. Such a boundary is aperiodic along the x direction. However, we used periodic boundary conditions only along the common [001] tilt axis, which corresponded to the y direction of the simulation block. Along the x direction the GB was terminated by an open surface following the methodology demonstrated in a previous study [64]. The open surface acts as a source and a sink of atoms enabling the automatic equilibration of the number of atoms at the GB which may be necessary for possible transformations. The dimensions of the simulation block were $35.0 \times 4.5 \times 20$ nm^3. The simulation cell containing the pure Cu grain boundary is shown in Figure 3.4, with all atoms visible and the coordinate system being indicated. In addition, zoomed-in views of the edge, at the open surface of the pure Cu and Cu-Ag cell are provided. The bicrystal with the Cu boundary terminated at an open surface was first annealed at 900, 800, 700 and 600 K (623-323°C) and no Ag was introduced. We did not explore temperatures below 600 K because of slow diffusion at GBs and inefficient structure sampling on the MD timescale. To model equilibrium segregation of Ag, we performed MCMD simulations with the chemical potential difference set to 0.5, 0.53 and 0.6 eV. We did not investigate higher values of the $\Delta\mu$ to avoid disordering or premelting of the boundary. Similar to the case of pure Cu, the simulation block was annealed by cooling from 900 K to 600 K in 100 K intervals. At each temperature the boundary was annealed for several tens of nanoseconds to allow for possible structural changes and diffusion of atoms to the surface. At the lowest temperature of 600 K we collected 70 snapshots, which were 2 ns apart from each other, to statistically analyze size and dynamics of the facets in both pure Cu and Cu-Ag systems. To obtain GB structures as close to equilibrium as possible, the MCMD simulations were performed for several hundreds of nanoseconds. Monitoring the change in mean facet length yielded no substantial change after about half the simulation duration with individual facet lengths fluctuating around the mean, which made us believe to have reached at least a close to ground state configuration. For such a complex grain boundary structure, hundreds of nanoseconds might not be enough to reach the lowest energy state within the limitations of the MD method. Despite these constraints, the obtained simulation results show the same segregation induced faceting, stabilized at the nanoscale (no coarsening), which was also observed experimentally.
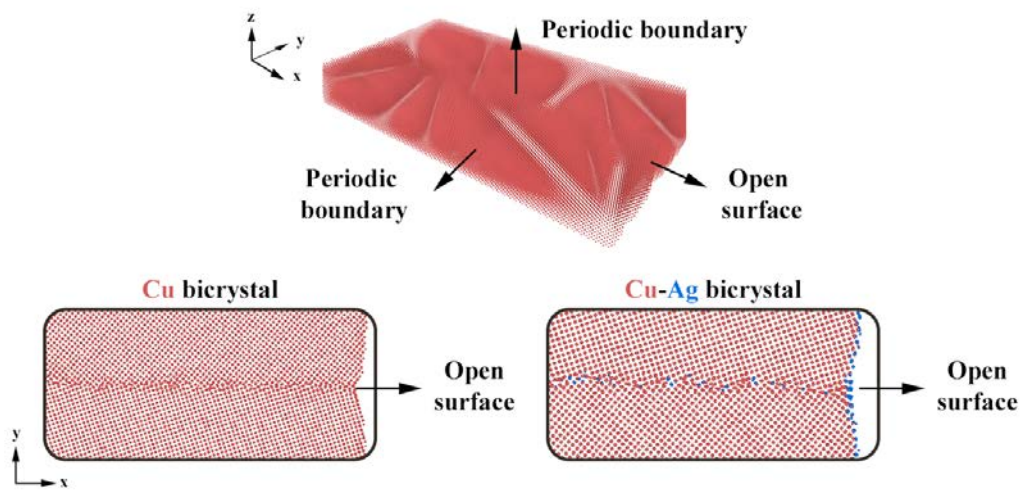
Figure 3.4: Snapshot of a simulation cell containing the asymmetric tilt grain boundary with the convention of the coordinate system and the boundary conditions for each axis being indicated [94]. The boundary plane lies in the x-y plane, while the x-direction terminates at an open surface important for self adjustment of the atomic density at the GB during structural transitions.

Chapter 4

Results and Discussion

4.1   Segregation induced nano-faceting transition at an asymmetric tilt grain boundary in copper

Nicolas J. Peter[1], Timofey Frolov[2], Maria J. Duarte[1], Raheleh Hadian[1], Colin Ophus[3], Christoph Kirchlechner[1], Christian H. Liebscher[1], Gerhard Dehm[1]

[1] Max-Planck Institut für Eisenforschung GmbH, 40237 Düsseldorf, Germany
[2] Lawrence Livermore National Laboratory, 94550-9234 Livermore, California, United States
[3] Lawrence Berkeley National Laboratory, 94720 Berkeley, California, United States

This chapter is based on:

Abstract

We show that chemistry can be used to trigger a nanofaceting transition. In particular, the segregation of Ag to an asymmetric tilt grain boundary in Cu is investigated. Aberration-corrected electron microscopy reveals that annealing the bicrystal results in the formation of nanometer-sized facets composed of preferentially Ag-segregated symmetric $\Sigma5\{210\}$ segments and Ag-depleted $\{230\}/\{100\}$ asymmetric segments. Our observations oppose an anticipated trend to form coarse facets. Atomistic simulations confirm the nanofacet formation observed in the experiment and demonstrate a concurrent grain boundary phase transition induced by the anisotropic segregation of Ag.

Main Text

Grain boundaries (GBs), as internal interfaces in polycrystals, strongly influence many properties of structural and functional materials [175]. Changes in grain boundary structure due to temperature, pressure, or chemistry can have a pronounced effect on GB energy, mobility, and cohesive strength ultimately influencing the macroscopic properties of these materials [80]. For example, Duscher et al. observed a monolayer of Bi atoms segregating to a $\Sigma 5$ GB in Cu, and it was proposed that bonding effects or the atomic size mismatch are causing embrittlement of otherwise ductile Cu [176,177]. Recent experimental studies suggested that abrupt changes in materials properties including diffusivity [22] and grain growth [15] can be explained by structural transitions at GBs [80]. While these studies linked the discontinuous changes in GB structure to important materials properties such as abnormal grain growth in ceramics [15], liquid metal embrittlement [76], and activated sintering [77], the atomic structure of these GB phases remains elusive. Theoretical investigation of transitions at interfaces dates back to some work of Gibbs, who considered the possibility of different interfacial states and derived the criteria for their equilibrium and stability [10]. Transitions at planar GBs were later discussed by Hart [11], who referred to them as "two-dimensional phase transformations." More recently, transitions at planar GBs were studied with phase field models [78], atomistic simulations [64], and lattice-gas models [79]. In addition to the conventional thermodynamic variables that could trigger changes in GB structure, Cahn introduced orientational degrees of freedom and categorized transitions at GBs into congruent and faceting types [12]. He suggested that faceting transitions should be much more common than the congruent transitions at planar boundaries. Temperature-induced GB faceting was reported in experimental studies [61,82,84] and facet formation mechanisms were explored by atomistic simulations in single component systems [55,65,85–87]. On the other hand, the effect of solute segregation on faceting is much less understood. The evolution of microscopically faceted boundaries was observed in Bi doped Cu bicrystals with increasing temperature and Bi concentration [9]. The direct observation of a reversible faceting transition in a well-defined boundary was demonstrated only in a single study by Ference and Balluffi for the Cu-Bi system [90]. However, both studies did not resolve the atomic structure of the segregated boundary and detected only relatively large facets with the size of several tens of nanometers and larger. More recently, Kundu et al. established a bilayer Bi segregation at about 100 nm long facets in a faceted Cu GB, but Bi decoration of the other facet type could not be determined [92]. On the other hand, stable nanofaceted GBs were observed using high resolution scanning transmission electron microscopy (STEM) in elemental systems and could potentially exist in doped systems [98,99]. Such small facets can be observed only with atomic scale resolution and could have been overlooked by previous studies. In this Letter
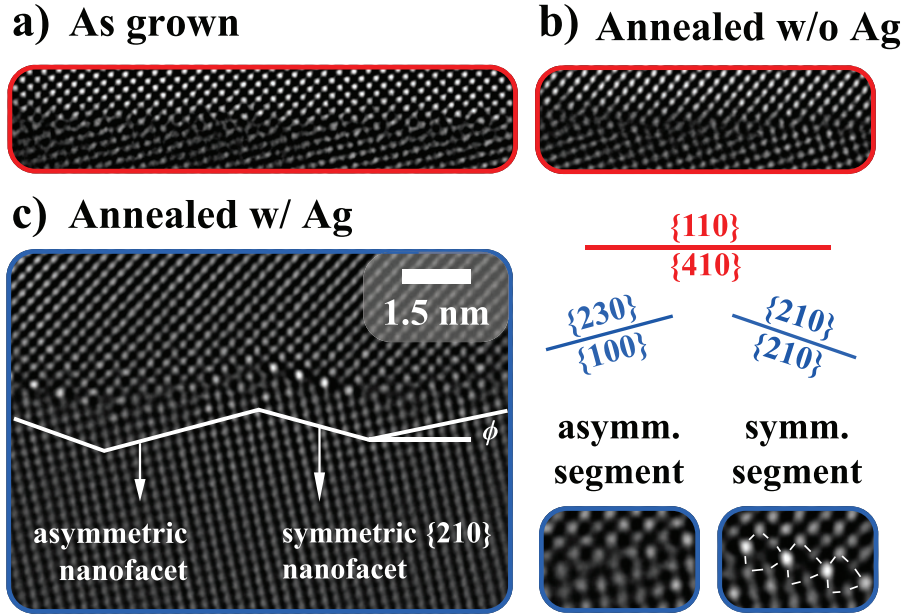
a) As grown

b) Annealed w/o Ag

c) Annealed w/ Ag

Figure 4.1: HAADF STEM micrographs in [001] zone axis orientation of (a) the relatively flat as-grown GB structure, (b) the relatively flat annealed GB structure, and (c) the Ag-segregated GB structure exhibiting distinct faceting with preferential segregation to the symmetric {210} segments. The scale is applicable to all three micrographs.

we use atomic resolution STEM, atom probe tomography (APT), and atomistic simulations to demonstrate a nanoscale faceting transition in an asymmetric Cu tilt grain boundary induced by segregation of Ag. The choice of the material system is motivated by recent measurements of Ag diffusion [22] in a symmetric $\Sigma 5$ Cu GB that reported a non-Arrhenius diffusion behavior and atomistic simulations that demonstrated a first-order transition in the same symmetric boundary [75]. A Cu bicrystal was grown by the Bridgman technique. The [001] axes of both seed crystals were parallel to the growth direction. The grains were misoriented by 54°, forming an asymmetric, noncoinciding lattice tilt boundary with a 31° inclination angle. To unambiguously prove a chemical trigger for a GB transition, ideally *in situ* segregation at atomic resolution would need to be performed at high temperatures. Since this is even now hard to realize *in situ*, the following approach was selected. The structure of the asymmetric GB was investigated following three different treatments with three different samples: (1) the pure as-grown state, (2) the pure Cu reference state annealed at 800°C (1073 K) for 120 h under high vacuum conditions, and (3) the Ag-segregated state after an annealing of sputter coated samples under the same conditions as in (2). All experimental details can be found in the Supplemental Material [178] and chapter 3. Representative high-angle annular dark-field (HAADF) STEM micrographs of each state of the GB are given in Figures 4.1a - 4.1c. The GB plane determined using the stereographic projection was close to the orientation {110}/{410}, where the indices correspond to the crystallographic planes of the

abutting grains parallel to the GB plane (Figure 4.1a). The overall Cu boundary appears to be macroscopically flat, with a certain roughness or short facets being visible at the atomic scale. The planar shape of the boundary suggests a weak inclination dependence of the GB energy (flat Wulff shape), which is consistent with published data obtained using atomistic calculations at 0 K [55]. After annealing, the pure Cu GB remained flat, and its inclination did not change significantly (Figure 4.1b). The new GB plane orientation was close to {110}/{310}, which is only a few degrees away from the as-grown state, confirming the inclinational isotropy of the GB energy in pure Cu. Very different behavior was observed in the sample doped with Ag. After annealing, the GB distinctly faceted at the atomic scale into an asymmetric segment close to {230}/{100}, and a symmetric $\Sigma5$ {210} segment (Figure 4.1c). Based on a section of the boundary with about 30 facets, segment lengths were measured to be 1.9 ± 0.9 nm and 1.8 ± 0.5 nm for the asymmetric and symmetric parts, respectively. The angle φ between the horizontal average boundary plane in the reference samples and the two facet segments is $\sim15°$, as indicated in Figure 4.1c. Bright atomic columns at the symmetric facet segments indicate Ag containing columns with a higher Z number than the surrounding grain interiors [142]. Consequently, preferential segregation to the symmetric segments was observed, while asymmetric segments contained little to no Ag atoms. In the symmetric facet segment Ag atoms occupy from 50 % to 100 % of the atomic columns located at the tips of the kite-shaped structural units, and we find evidence of beam-induced GB diffusion with the Ag atoms moving between different lattice sites [57]. The volume reconstruction of a boundary containing APT tip clearly identifies Ag solute excess along the GB plane with a peaking line profile of up to about 2 at. %, while the grain interior contains 0.16 at. % Ag - averaged from six different samples (Figure 4.2b). The APT measurements provide evidence that the GB is locally enriched in Ag, in agreement with the HAADF STEM results (Figure 4.1c). The 2D Ag density map reveals a nonhomogeneous decoration of the GB plane along the tilt axis (not accessible by STEM), in agreement with the observed preferential segregation and implying an in-depth reconstruction of the GB (Figure 4.2a). Such reconstructions were previously demonstrated by simulations and could be due to thermal fluctuations [179]. Another possibility is that the GB exhibits in-depth faceting-defaceting transitions induced by segregation [14]. The combination of STEM and APT establishes a correlation between Ag enriched areas and different structural motifs of the GB. The Ag content at the GB was quantified by calculating the atomic interfacial excess following [158, 159] (Figure 4.2c). A solute excess concentration of 2.76 at/nm^2 was determined as an average value for the whole boundary. To get further insights into the atomic details of the segregation induced faceting transition found in the experiment, we performed atomistic simulations. Here, we used the combined Monte Carlo and molecular dynamics (MCMD) approach implemented in LAMMPS [180]. The GB (image) simulation methodology is described in the Supplemental
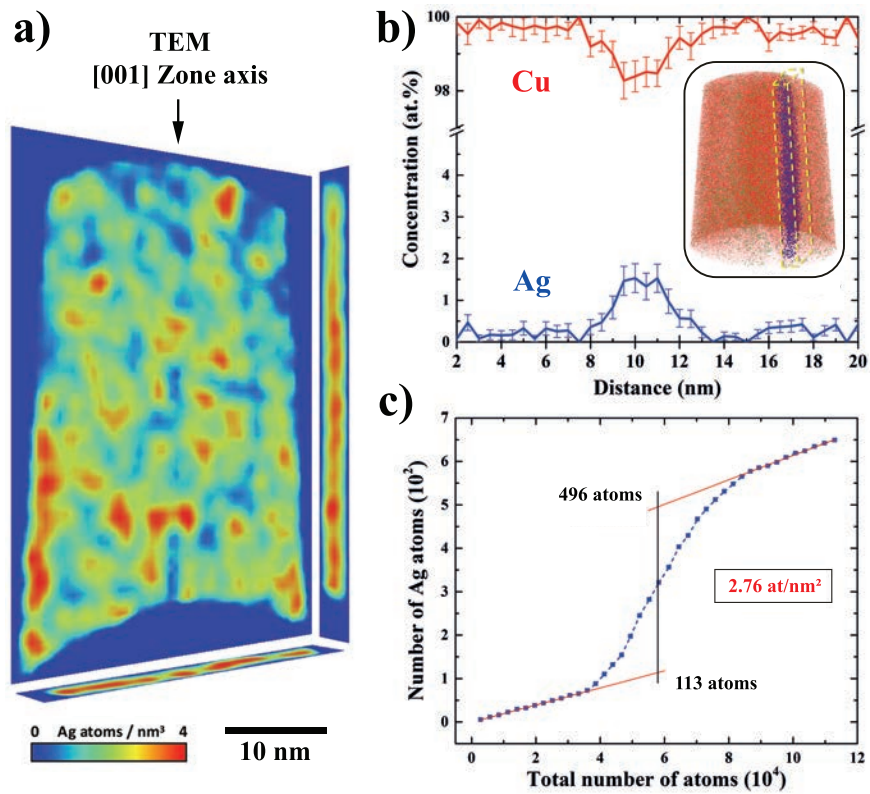
Figure 4.2: 3D APT reveals the inhomogeneous segregation of Ag to the asymmetric GB. (a) The projected Ag density plot of the GB. (b) 1D line profile across the boundary. (Inset) The APT reconstructed volume. (c) The Ag solute excess atom concentration determined across the GB.

Material [178], in previous work [64, 96, 168] and especially chapters 2 and 3. Two representative GB structures with Ag (blue boxes) and without Ag (red boxes) are shown in Figure 4.3. Using these structures, STEM images were simulated using PRISMATIC code [154]. The structure of the GB in pure Cu at 600 K is shown in Figure 4.3a to be relatively flat. Examination of different snapshots reveals small structural units of symmetric boundaries that appear as a result of thermal fluctuations. Specifically, the Cu embedded atom potential predicts three different GB phases for the $\Sigma 5$ $\{210\}$ symmetric boundary which were identified in Ref. [64] and called split kite (SK), filled kite (FK), and normal kite (NK). Small units of SK and FK can be identified in the image. In the Cu-Ag system the boundary structure is noticeably different. In agreement with our experimental findings, the GB faceted into symmetric $\{210\}$ and asymmetric $\{230\}/\{100\}$ segments, with large Ag atoms preferentially segregating to the $\{210\}$ segments. The asymmetric and symmetric facet lengths were found to be 1.4 ± 0.4 and 2.1 ± 0.7 nm, respectively, and the facet inclination angle φ was close to $15°$ on average, close to the experimental findings above. The preferential segregation of Ag atoms to symmetric segments is even more apparent in the simulated STEM images that show portions of the boundary with a higher intensity of Ag (compare to the enlarged area in Figure 4.3d). Moreover, in the faceted boundary we no longer observe the SK structural units found in pure Cu. This further confirms that a structural transformation took place and is consistent with a similar destabilization of the SK structure by Ag that has been previously demonstrated for a symmetric $\Sigma 5$ $\{210\}$ boundary [75, 96]. To quantify the structural transformation observed in the simulations, we analyzed the size of the fluctuating facets in both the Cu and the Cu-Ag system. At 600 K in pure Cu, the ratio of flat to faceted boundary parts reaches almost unity, while in the case of the Ag-segregated boundary, the nanofacet fraction increased up to 80 % on average. Thus, our experimental results and simulations are in qualitative agreement with each other in terms of the segregation-induced faceting, although the exact structures of the symmetric segments show some variation. It is important to note that the experimental structure was observed at room temperature, while simulations are performed at high temperature due to timescale limitations of the modeling. To make a better connection with room temperature structures found in the experiments, we performed GB segregation and free energy calculations for the $\{210\}$ symmetric GB at 300 K. Specifically, we investigate the possibility of a segregation-induced transition to the normal kite structure, which could take place at lower temperatures. Similar transitions have been demonstrated at high temperature in our previous studies [75, 96], but also recently with a symmetry breaking structural transition in the Ni-Mo system [181]. These calculations would also imply a possibility of a hierarchical phase transformation path, which could be difficult to observe experimentally. Using the MCMD approach with periodic boundary conditions, we modeled segregation to the three different GB phases of the symmetric $\Sigma 5$ $\{210\}$ $[001]$
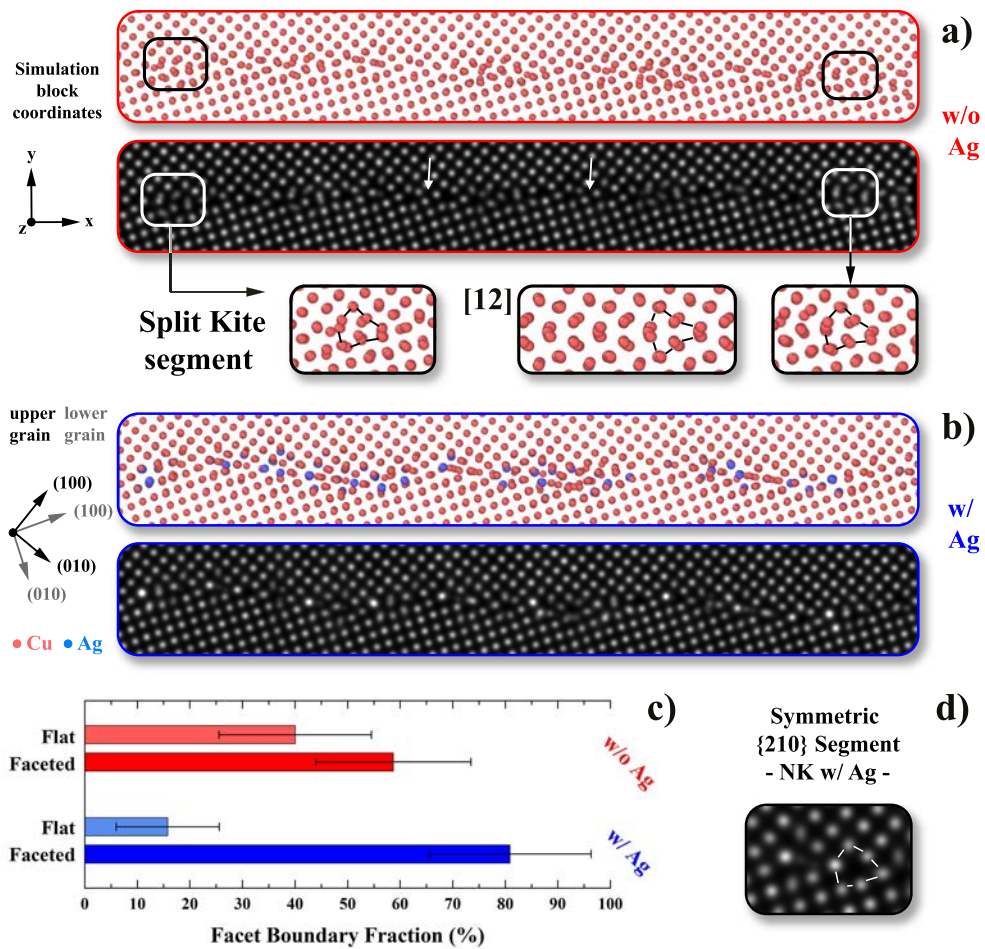
Figure 4.3: MCMD simulation results and the corresponding STEM image simulations for the annealed asymmetric Cu GB (a) without Ag. The highlighted areas are enlarged below the image simulation on the left and right sides to show the rare presence of split kite structures. As a split kite reference, the central structure is adopted with permission from Ref. [64]. Arrows indicate the location of GB disconnections. The MCMD simulation results with (b) the presence of Ag and (c) the respective statistical analysis results. An enlarged area of a symmetric {210} facet segment containing Ag is presented with the normal kite structure highlighted in (d).
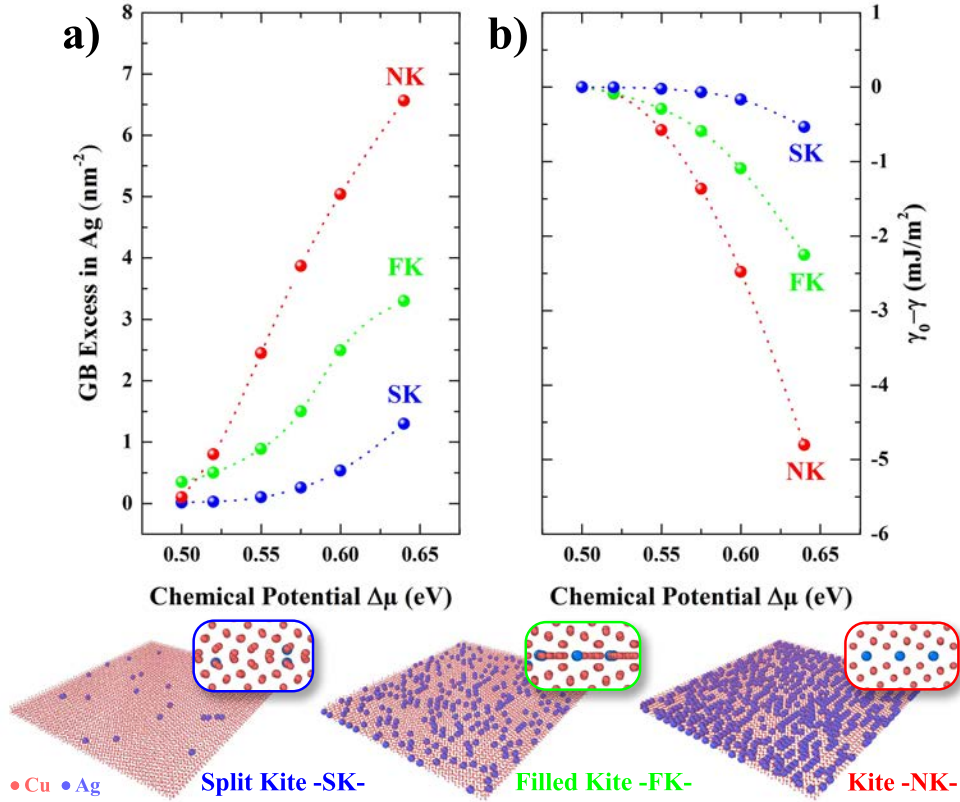
Figure 4.4: MCMD calculations of the equilibrium Ag segregation and GB free energy for the three possible kite structures of the symmetric tilt $\Sigma5\{210\}[001]$ boundary at 300 K. (a) The equilibrium segregation as a function of the chemical potential difference. Ag segregation for the NK can be almost an order of magnitude higher than for the SK structure. (b) The reduction in the GB free energy as a function of chemical potential difference indicates that Ag stabilizes the NK structure. (Bottom panels) GB planes of each structure with equilibrium segregation of Ag for the same value of the chemical potential difference $\Delta\mu = 0.55\,eV$ (same bulk composition). In the NK structure Ag atoms form almost a monolayer at the boundary, while the denser [64] SK structure has only a few Ag atoms.

GB at 300 K [75, 96]. The simulations were performed at six different values of the chemical potential difference $\Delta\mu = \mu_{Ag} - \mu_{Cu}$ to sample different concentrations of Ag. The snapshots of the boundary plane edge-on represent equilibrium segregation at a chemical potential of 0.55 eV, the same $\Delta\mu$ value used for faceting simulations. The snapshots reveal that while the SK phase contains only a few Ag atoms, the NK phase accommodates almost a monolayer of Ag for the same value of $\Delta\mu$ or concentration of Ag in the bulk. Figure 4.4a shows the $[N_{Ag}]_N$ plots as a function of $\Delta\mu$ which quantify this strong effect of GB structure on impurity segregation. We calculated the reduction in GB free energy of each of the three phases due to Ag by integrating the adsorption equation as $\gamma_0 - \gamma = -\int[N_{Ag}]_N d\Delta\mu$ [10](Figure 4.4b). The higher uptake of Ag by the NK structure effectively lowers the boundary free energy by a maximum value of 5 mJ/m^2, making it the most thermodynamically favorable configuration at higher Ag concentrations. The free energy analysis demonstrates that at

room temperature the symmetric segments of the faceted boundary should have NK structure, which was also observed in the experiment. Thus, our high temperature simulations and the free energy analysis combined are in agreement with the experimentally observed nanofaceted structure. The same simulations were performed for the asymmetric facet segment as well, supporting the above findings. These results can be found in the Supplemental Material (below the Main Text and in [178]). The experimental observations and atomistic simulations suggest the following mechanism for the Ag-triggered faceting transition. At first, annealing the Ag coated Cu bicrystal at 800 °C completely dissolves Ag in Cu [29]. This agrees well with APT measurements, that reveal a bulk Ag concentration of 0.16 at. %, allowing an estimation of the onset temperature of segregation to be $\sim$ 500 °C during slow cooling according to the equilibrium phase diagram [29]. The simulation results show a significant increase in facet fraction for the GB annealed in the presence of Ag at elevated temperatures and demonstrate that absorbed Ag atoms preferentially segregate to symmetric {210} segments. Our study shows that the segregation to GBs can be very anisotropic and can trigger nanofaceting transitions. The factors that control the faceted shape of a GB and the size of the facets include inclinational anisotropy of the GB free energy, elastic effects due to GB stress of different facets [86], and the elastic interaction between disconnections formed by GB facet junctions [99]. Our experiments and simulations demonstrate a faceted GB composed of Ag-rich and Ag denuded segments. According to the Gibbs adsorption equation and the free energy calculations performed in this work, the uneven segregation should promote stronger inclinational anisotropy. Segregation has a strong effect on GB stress, which is another factor controlling GB faceting. GB stress calculations for a $\Sigma 5$ symmetric tilt boundary in the same model system showed that initially tensile GB stress could be reduced to zero and could even become compressive as a result of segregation of large Ag atoms [97]. Since segregation depends on the inclination, this strong change in GB stress is expected to be different in different GB facets and to promote faceting. Finally, the interaction between the disconnections may be affected by segregation as it changes the excess volumes of the different GB facets. All of these energetic factors are strongly coupled to segregation. Therefore, it is difficult to distill what is the most important in our case. However, it is clear that impurity segregation promotes anisotropy and faceting. Our experiments confirm the weak inclinational anisotropy of the GB free energy in pure Cu [55]. However, the structures we observe in both the experiment and high-temperature simulations do not match previously published structures generated at 0 K composed of {310} and {210} kite motifs. From a kinetic perspective the Ag decorated symmetric {210} facets start forming at $\sim$500°C, assisted by thermally induced fluctuations in facet formation and dissolution. Consequently, intermediate asymmetric {230}/{100} segments form through step nucleation and migration to preserve the macroscopic GB plane orientation. According to Wu et al. [65], facet

coarsening requires the migration of the symmetric segment perpendicular to its plane along the asymmetric segment until it meets another symmetric facet. Since facet coarsening is related to the atomic mismatch on both sides of a grain boundary facet, the symmetric {210} segments are expected to exhibit a low energy barrier for coarsening, but strongly reduced coarsening is expected for the asymmetric segments. This is in good agreement with our experimental findings and implies that facet coarsening is kinetically limited, likely influencing microstructure evolution of such alloys. Two recent studies calculated the impact of solute segregation at symmetric $\Sigma 5$ GBs on macroscopic properties such as GB diffusion and sliding [23, 182]. In light of our findings, this emphasizes that the observed segregation-induced nanofaceting transition will have a strong influence on the interfacial properties since it goes even beyond the classical picture of Langmuir-McLean-type segregation. In conclusion, we present in this Letter the experimental observation of a chemically triggered structural transition of an asymmetric Cu GB induced by Ag segregation observed by STEM and APT. Stable nanofacets are formed consisting of nanoscale asymmetric Ag-depleted {230}/{100} and Ag-rich symmetric {210} segments. Combined MCMD simulations of a boundary with the same misorientation and asymmetric inclination reveal distinct faceting and facet stabilization by Ag segregation, supporting the experimental observations. Further simulations of different {210} GB phases establish that the {210} kite structure can accommodate the largest amount of Ag and should therefore be the most stable, as observed in the experiment. These types of segregation-induced faceting transitions with nanometer-sized facets can easily be overlooked, and only atomic resolution STEM is able to resolve them. The stabilization of nanometer-sized symmetric facets at an asymmetric GB indicates that these transitions can also occur for other GB inclinations whenever a solute has a low solubility in the bulk and symmetric GB structures with high solute adsorption exist.

Supplementary Material

To obtain GB structures as close to equilibrium as possible, the MDMC simulations were performed for several hundreds of nanoseconds. Monitoring the change in mean facet length yielded no substantial change after about half the simulation duration with individual facet lengths fluctuating around the mean, which made us believe to have reached at least a close to ground state configuration. For such a complex grain boundary structure, hundreds of nanoseconds might not be enough to reach the lowest energy state within the limitations of the MD method. Despite these constraints, the obtained simulation results show the same segregation induced faceting, stabilized at the nanoscale (no coarsening), which was also observed experimentally. Snapshots of the different symmetric {210} kite structures as provided in Figure 4.4 in the main manuscript are shown in different views here in Figure

4.5. To show that all atoms were included in these projected views, we provide snapshots of the entire simulation cells along all three cartesian coordinates in Figure 4.5. The snapshots show results obtained from simulations at a chemical potential difference of $\Delta\mu = 0.55\,eV$. In Figure 4.4 of the main manuscript, we show simulation results of the Ag uptake (a) and change in free energy (b) for the symmetric facet segment and for the different symmetric kite structures. The same segregation calculations were performed for the asymmetric facet segment. The Ag segregation and the corresponding change in grain boundary free energy are shown here in Figure 4.6. The asymmetric facet segment is composed of flat, Ag lean regions separated by disconnections that are decorated with Ag leading to a largely non-uniform segregation at the asymmetric facet. The presence of these disconnections also explains the observed large Ag segregation. However, in the experiment only the flat, Ag lean segment is observed, as illustrated in Figure 4.7a, emphasizing the excellent agreement between experiment and simulation. In Figure 4.7a the Ag lean segment of the asymmetric facet is superimposed on the experimental image of the nano-faceted boundary. This segment is highlighted in the entire simulation cell in Figure 4.7b to illustrate regions with high and low segregation. Structures obtained for a chemical potential difference of $\Delta\mu = 0.52\,eV$ are shown.
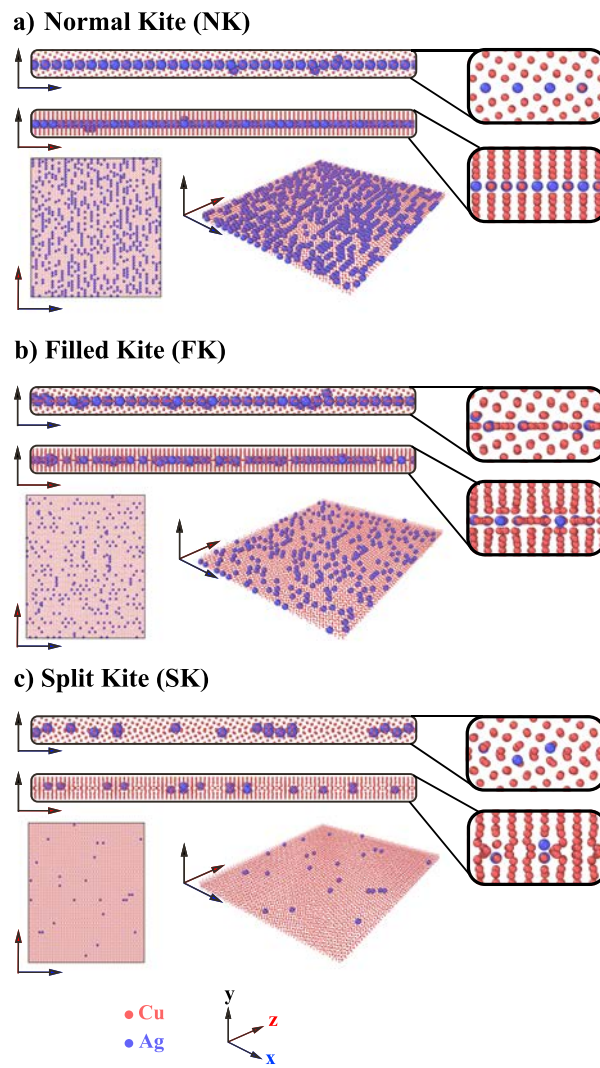
Figure 4.5: MCMD calculation snapshots of Ag segregation to the three different kite structures of the symmetric {210} boundary.

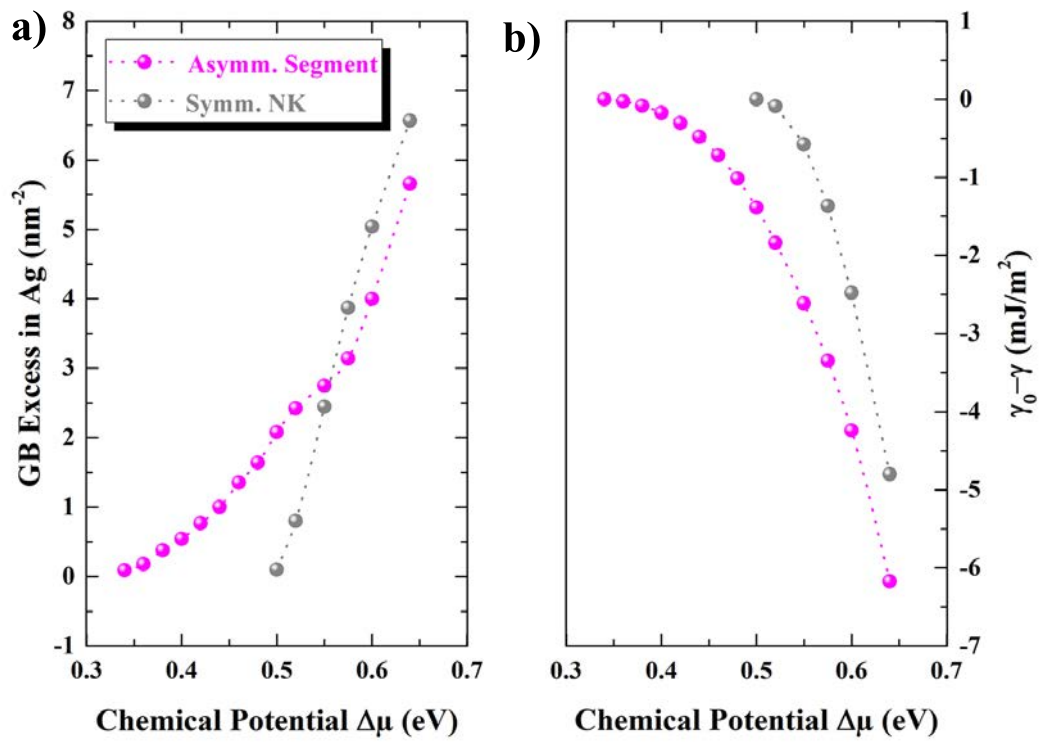Figure 4.6: Snapshots from MDMC simulations at T = 300K and $\Delta\mu = 0.55\,eV$ showing Ag segregation and GB free energy for the asymmetric facet segment. (a) Ag segregation as a function of chemical potential difference. (b) The relative grain boundary free energy reduction as a function of chemical potential difference in comparison to the Normal Kite structure.
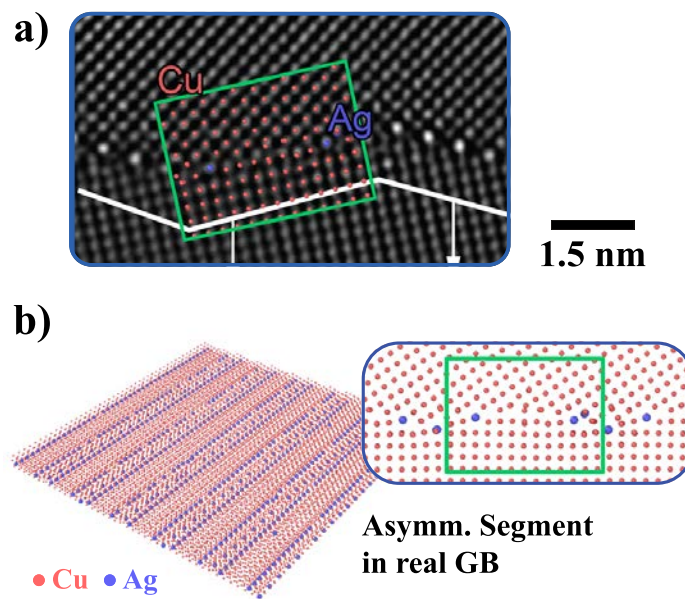
Figure 4.7: MCMD simulation results of the asymmetric facet segment structure. (a) Superposition of the simulated structure with the experimental STEM micrograph yields good agreement. (b) The entire simulation cell showing the non-uniform segregation pattern in perspective and edge-on, with the experimentally observed part being highlighted, i.e. the mostly Ag lean part. Structures obtained for a chemical potential difference of $\Delta\mu = 0.52\,eV$ are shown.

4.2 Beam-induced atomic migration at Ag-containing nanofacets at an asymmetric Cu grain boundary

Nicolas J. Peter, Christian H. Liebscher, Christoph Kirchlechner, Gerhard Dehm

Max-Planck Institut für Eisenforschung GmbH, 40237 Düsseldorf, Germany

Abstract

Besides the high spatial resolution achieved in aberration-corrected scanning transmission microscopy, beam-induced dynamic effects have to be considered for quantitative chemical characterization on the level of single atomic columns. The present study investigates the influence of imaging conditions in an aberration-corrected scanning transmission electron microscope on the beam-induced atomic migration at a complex Ag-segregated, nanofaceted Cu grain boundary. Three distinct imaging conditions including static single image and serial image acquisition have been utilized. Chemical information on the Ag column occupation of single atomic columns at the grain boundary was extracted by the evolution of peak intensity ratios and compared to idealized scanning transmission electron microscopy image simulations. The atomic column occupation is underestimated when using conventional single frame acquisition due to an averaging of Ag atomic migration events during acquisition. Possible migration paths for the beam-induced atomic motion at a complex Cu grain boundary are presented.

MOTIVATION

The addressed challenge to be solved in this section focuses on the determination of atomic migration events that happen during acquisition of an image or a spectrum at the atomic scale, especially at points of higher excess volume, higher vacancy concentration and less stable background conditions of low displacement threshold materials. To shed light on these events, the present study investigates a Ag containing asymmetric grain boundary in a Cu(Ag) alloy. From a methodical point of view, Cu(Ag) is a very suitable system for chemistry characterization by HAADF imaging, since the difference in atomic number is fairly large, i.e., $Z_{Cu} = 29$, $Z_{Ag} = 47$. Consequently, atomic columns containing Ag should be of higher peak intensity compared to pure Cu columns under HAADF conditions. Therefore, STEM image simulation in combination with STEM EELS thickness determination provides the required additional information needed to extract chemical information under HAADF imaging conditions, an approach that is also used for determining the number of atoms of individual atomic columns through peak integration [183]. The present study makes use of the high spatial resolution of an aberration-corrected STEM under HAADF imaging conditions to extract quantitative chemical information of Ag-containing grain boundary facets in Cu. It is the first approach to systematically study the influence of imaging conditions on the beam-induced atomic migration under standard, subdisplacement threshold energy conditions at a metallic grain boundary with nanoscale Ag-rich facets. The Cu(Ag) system was chosen as suitable model system exhibiting very stable, symmetric facets on an otherwise asymmetric grain boundary. Single frame acquisition is compared to serial image acquisition of different frame rates and peak intensity ratios of atomic columns of Cu and Ag were determined after digital post acquisition image processing. STEM image simulations of the symmetric Ag-containing boundary structure corresponding to the experimental observations was performed to verify the experimental assumptions and to obtain a trend on the influence of imaging conditions on the extracted Ag concentration in individual atomic columns at the boundary. Experimental procedures used are described in chapters 2 and 3. The TEM sample thickness was measured by EELS in a slightly thicker area of the sample adjacent to the area of interest. This provides an upper limit for the sample thickness, which amounted to 0.45 in units of the inelastic scattering mean free path corresponding to a sample thickness of less than 45 nm.

RESULTS

An asymmetric bicrystal was successfully grown according to the set-up misorientation of the seed crystals, i.e., a misorientation angle of 58° was found by electron backscatter diffraction

as well as high-resolution STEM. Figure 4.8a shows an as-captured HAADF-STEM micrograph of the Ag-segregated grain boundary acquired at a dwell time of 15 µs. Both grains were observed close to their crystallographic [001] tilt axis. The overall grain boundary orientation can be described as 58° [001], {110}/{610} with repeating symmetric 58° [001], {210} nanofacets that correspond to a symmetric $\sum$5 {210} grain boundary orientation within the Brandon criterion ($\pm$ 6.71° around 53.18°). These nanofacets contained three to four regularly spaced bright atomic columns compared to the intragranular atomic columns. Artifacts introduced by the scanning system like expanded, compressed, or bent lattice planes could be identified. Within the individual grains long range contrast changes were found most likely resulting from a bent sample and therefore differently fulfilled Bragg conditions. The same image after filtering (Gaussian and Butterworth) is presented in Figure 4.8b. The bright atomic columns remain clearly visible, while the long range contrast changes were replaced by more or less uniform background intensity. Artifacts (image distortions) from the scanning system are unaltered. Figures 4.8c and 4.8d represent the areas used to extract quantitative information in a static unfiltered and filtered state (Single Image), respectively. Peak intensity ratios of bright atomic columns were calculated to be 1.36 $\pm$ 0.11 (unfiltered) and 1.28 $\pm$ 0.09 (filtered), respectively, averaging over the eight most apparent columns (indicated by arrows in Figure 4.8c). All peak intensity ratios, also of the Slow Scan and the Fast Scan, are summarized and visualized in the Discussion section (Figure 4.13).

In case of the Slow Scan series that was obtained at a pixel dwell time of 5 µs, Figure 4.9a presents a representative raw frame of the series. Most obvious was the reduced intensity in the image compared to the Single Image; however, there was still sufficient intensity to identify the brighter Ag-containing atomic columns. Artifacts of the scanning system were less apparent but could still be identified, especially the Fast Scan noise. To capture more of the dynamics and to achieve a better peak intensity ratio determination, two of these raw frames were filtered and cumulatively averaged (Figure 4.9b). The bright Ag-containing atomic columns are still clearly visible. Scanning artifacts seem to be reduced compared to Figure 4.8b and even the structure of the symmetric facets can be identified in such an image. The right highlighted facet containing three bright columns was chosen for peak intensity ratio determination over time. The resulting ratio versus time profile is presented in the Supplementary Material (Figure 4.15). The ratio of column 1 (Figure 4.9b) over time was averaged to be 1.77 $\pm$ 0.16, while the ratio of column 2 was calculated to be 1.55 $\pm$ 0.20, and the ratio of column 3 to 2.05 $\pm$ 0.10. The cumulatively averaged and filtered Slow Scan summed up image using all 17 frames is presented in Figure 4.9c. A significantly increased signal-to-noise ratio was found and only reduced scanning artifacts remained including Fast Scan noise. The atomic structure of the symmetric facets is resolved and, in addition, the asymmetric parts of the grain boundary became more accessible in terms
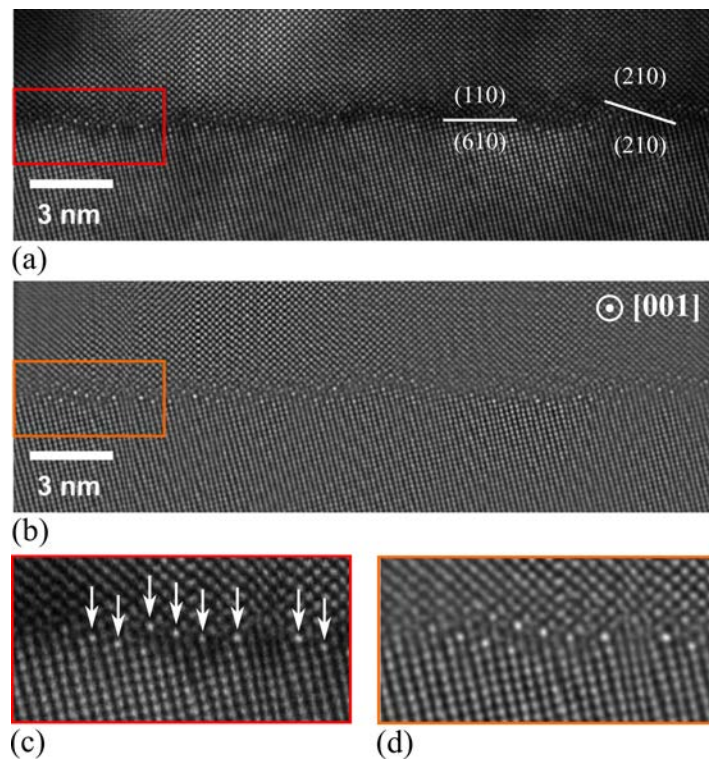
Figure 4.8: Single Image of the Ag-segregated asymmetric Cu grain boundary. The acquired raw image is presented along with the crystallography in (a). The filtered image used to study the influence of image processing on peak intensity ratio determination (b). Enlarged views of the respective areas used for extraction of chemical information for the unfiltered state (c) and the filtered state (d). Arrows indicate atomic columns that were analyzed.
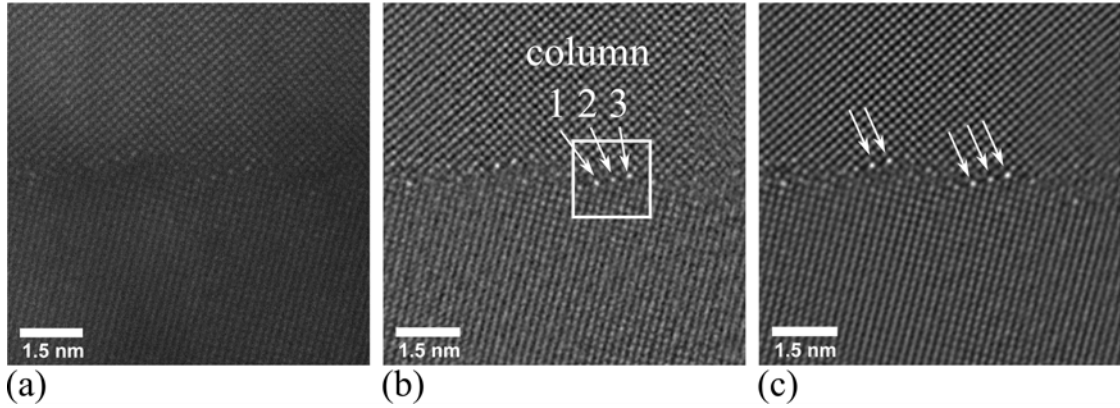
Figure 4.9: A representative raw frame of the Slow Scan series is shown in (a), while a cumulatively averaged and filtered image from two raw frames is presented in (b). The time evolution of peak intensity ratios was extracted from the three major peaks in the highlighted area. The cumulatively summed up image of all 17 frames of the series is provided in (c) with atomic columns taken for analysis indicated by arrows.

of structure compared to individual raw frames or in case of two summed frames. The five apparent bright columns (indicated by arrows) were chosen to determine an averaged mean peak intensity ratio of 2.01 ± 0.20 that can effectively be compared to the Single Image's ratio.

A representative raw frame of the Fast Scan series acquired at a pixel dwell time of 1 μs is provided in Figure 4.10a. The signal-to-noise ratio was just sufficient to trace atomic column positions in the upper grain, while only lattice planes are discernable in the lower grain. Positions of bright atomic columns at the grain boundary were hardly recognizable. The situation changed if four of these raw images were cumulatively averaged and filtered as shown in Figure 4.10b. Bright columns could clearly be identified and atomic positions became much more apparent. Atomic columns of the grain interior revealed random mosaic-like intensity increases, while the bright columns of the nanofacets remained the most intense ones. This averaged image was the basis to dynamically track the peak intensity ratio of the central three Ag columns within the highlighted frame. To effectively mimic a Slow Scan series with these averaged frames, a binning in the time domain was used to track the peak intensity ratio over time. The peak intensity ratios of the left (1.88 ± 0.13), middle (1.81 ± 0.15), and right (2.01 ± 0.13) atomic columns in the highlighted frame were tracked and the resulting profile is provided in the Supplementary Material (Figure 4.15). Similarly to the Slow Scan series before, peak intensity ratios were tracked over time in a moving average fashion for the left (2.47 ± 0.28), middle (2.05 ± 0.27), and right (2.90 ± 0.11) atomic column as well. A rigidly aligned, unfiltered sum image of the 200 individual frames is shown in Figure 4.10c, where the atomic structure of the grain boundary is well resolved, especially at the symmetric facets. However, the upper grain is closer to perfect zone axis orientation
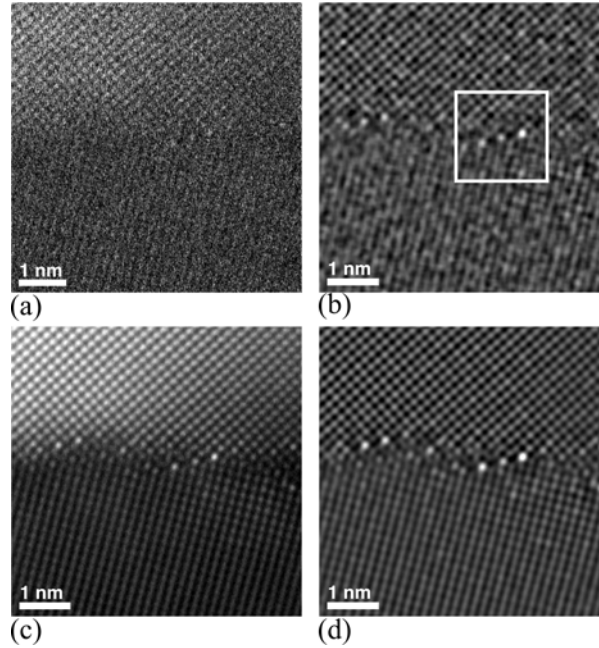
Figure 4.10: A representative raw frame of the Fast Scan series is shown in (a), while a cumulatively averaged and filtered image from four raw frames is presented in (b). The time evolution of peak intensity ratios was extracted from the three major peaks in the highlighted area. The unfiltered cumulatively summed up image of all 200 frames of the series is provided in (c), while the filtered image is given in (d).

and the atomic column intensity is therefore brighter compared to the lower grain. The bright Ag-containing columns were clearly distinguishable, even from the bright appearing upper grain. The mosaic-like increased intensity of random columns inside both grains was still captured, however, not as well as in the images that were only averaged over four raw frames. To effectively mimic a Single Image case, Figure 4.10c was filtered and background subtracted and the resulting image (Figure 4.10d) was used to determine an average peak intensity ratio for the exact same five atomic columns along the grain boundary as used for the Slow Scan series. A mean ratio of 2.14 ± 0.21 was extracted.

The dynamic evolution of the individual columns in the highlighted frame area of Figure 4.10b was studied by inspection of the respective images to observe atomic migration events and the columns' peak intensity ratio was tracked over time to quantify these events in terms of Ag column occupation (Figure 4.11). The three dynamically tracked Ag-containing atomic columns are encircled in different colors (Figures 4.11a - 4.11c) corresponding to the respective peak intensity ratio evolutions in the time profile below in Figure 4.11d. The time of their appearance is given in the images and highlighted on the time axis of the graph (it is referred to the online Supplementary Material of [57] for the compiled video of all frames). Proper inspection revealed in (a) that the central column had lowest intensity, while the right column had highest intensity and the left column's intensity is of rather intermediate

intensity. 3.4 seconds and 7 seconds later, the intensities reveal clear relative changes in intensity with the temporal variations plotted in Figure 4.11d. In addition, it can be seen in Figure 4.11c that a bright column appeared next to the right column within the symmetric kite structure (indicated by an arrow). In the open space of the kite structure between the left and the central column bright pixels were seen that imply atomic scattering through this position. In general, it has to be noted that according to the moving average peak intensity ratio evolution, the right column remained the brightest and almost exclusively constant with a peak intensity ratio of 2.94. If the ratio changed, it only decreased implying that 2.94 corresponds to the global maximum within the acquired timeframe. It is speculated that the right column is fully occupied by Ag atoms. Thus, the peak intensity ratio was linearly translated into an atomic column occupancy of 100 % Ag in Figure 4.11d (right axis). Both the central and left columns were highly dynamic and constantly increased and decreased in intensity, e.g., the central column exhibits a peak-to-valley time period of about 2.7 s on average. The average peak intensity ratio of all three columns is plotted over time (Figure 4.11e) revealing some modulations, which indicates that Ag exchange happens not only between the 3 columns but also with neighboring regions inside the grains.

STEM simulation results were used as comparison for experimentally obtained peak intensity ratios focusing especially on sample thickness and Ag content within an atomic column (Figure 4.12). The deduced ratios for the different parameters are summarized in Figure 4.12a. Four different peak intensity ratio evolutions are presented corresponding to different Ag occupancies within an individual atomic column of the symmetric {210} kite structure. The horizontal red line indicates the experimentally determined highest peak intensity ratio, which was assumed to be a pure Ag column. In general, it was seen that the profiles tend to follow a hyperbolic trend with a maximum being located between 20 and 30 nm TEM sample thickness. In addition, the experimentally found ratio agrees well with a simulated, fully occupied (100 % Ag) atomic column in a 10 nm or 30 nm thick sample. The experimental reference structure of the symmetric Ag-containing {210} facet is shown in Figure 4.12b. All three Ag columns were connected by the same motif, in literature described as a kite structure [64]. According to these experimental findings, STEM image simulations were set up. Image simulation results for a thickness of 30 nm are visualized in Figures 4.12c - 4.12f for varying Ag occupancies of 25 %, 50 %, 75 %, and 100 %, respectively. Extracted peak intensity ratios are stated as inset.

Discussion

Ag segregation toward the asymmetric grain boundary resulted in regularly spaced symmetric (210) nanofacets along the interface. These usually exclusively consist of 3 - 4 bright
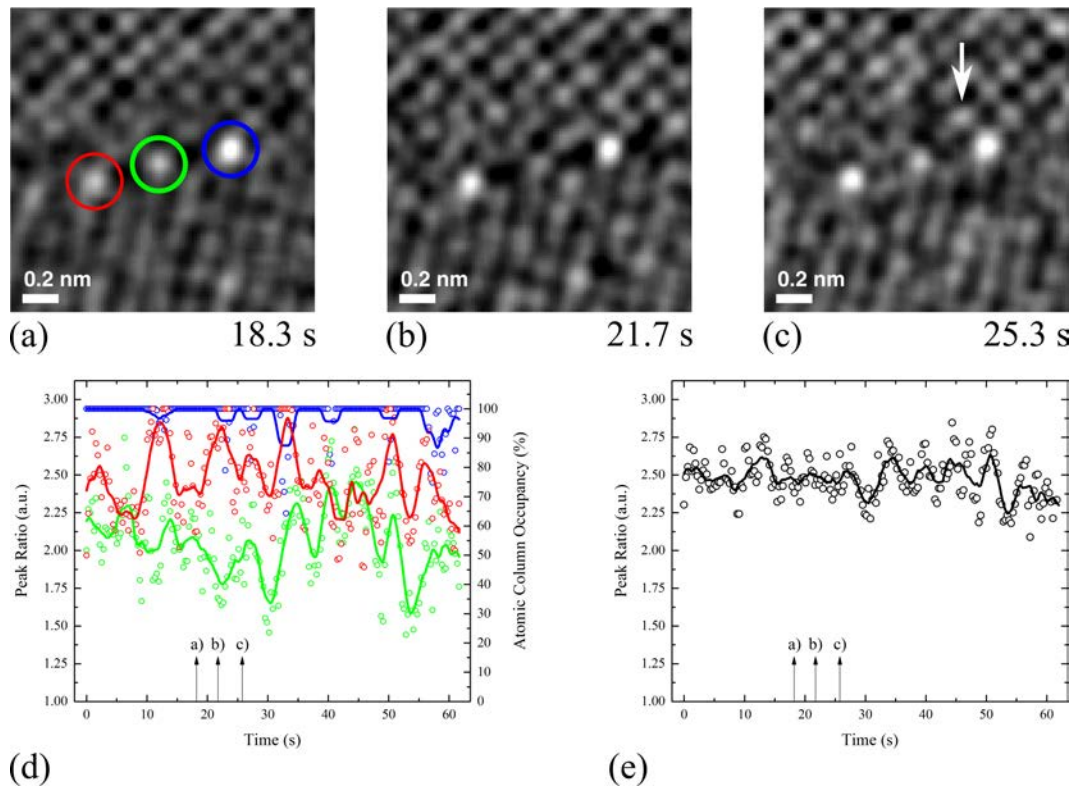
Figure 4.11: From the highlighted area in Figure 4.10, the peak intensity ratio over time was extracted. Three electron micrographs (a), (b), and (c) at different moments in time are illustrated with their respective time stamps highlighting three individual atomic columns corresponding to the quantitative graph in (d). Each colored curve of the graph represents the peak intensity ratio of the respective column with the average intensity taken from within the Cu grains. The avergaed intensity of all three columns over time is given in (e) highlighting the Ag inflow and outflow events to the nanofacet.
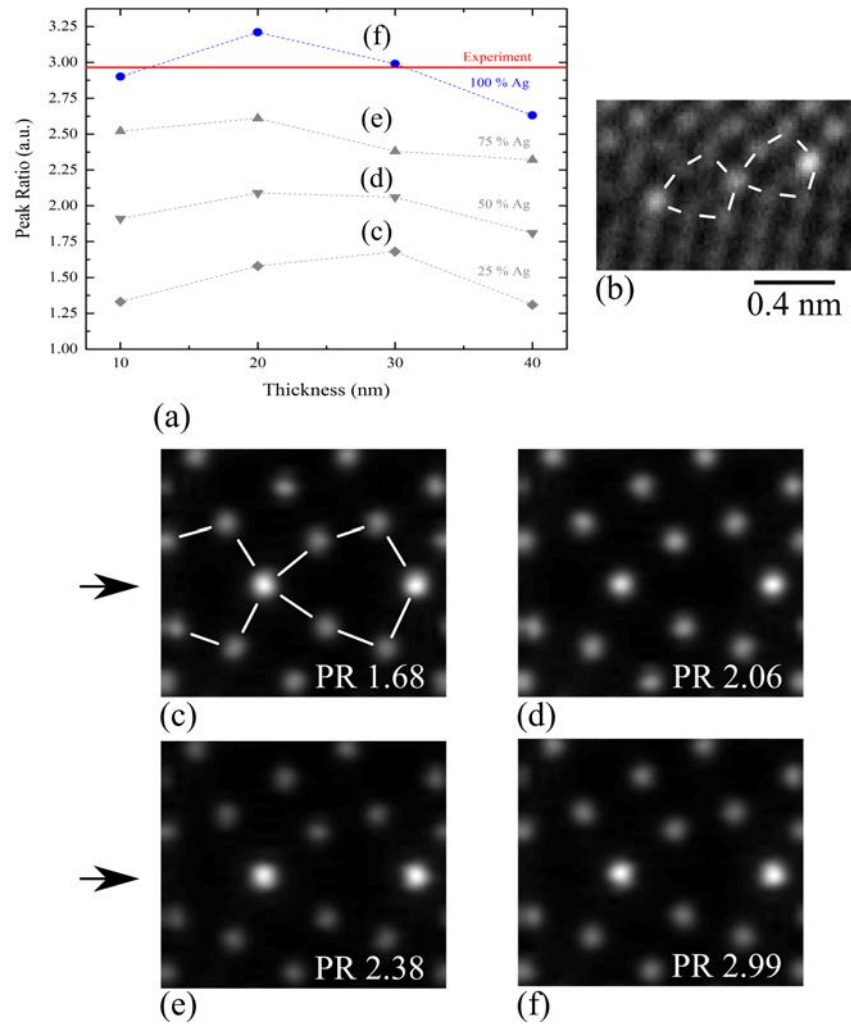
Figure 4.12: STEM image simulation results are presented. Graph (a) summarizes all simulated peak ratios for different thicknesses and Ag occupancies of individual atomic columns. The horizontal line indicates the experimentally found peak ratio for an almost fully occupied column. The experimental grain boundary structure of the symmetric $\Sigma5(210)$ facet is obtained from digitally zooming in to Figure 4.9c with structural guidelines being overlaid in (b). Simulated STEM images are presented for a constant thickness of 30 nm in (c)–(f) along with their extracted peak ratios (PR), respectively. Ag columns were introduced in the boundary plane by black arrows in front of (c) and (d) according to the experimental findings in (b).

atomic columns compared to the surrounding columns within the grains. Bright columns of higher intensity in HAADF conditions result from increased scattering of higher atomic number elements like Ag compared to Cu. EDS confirmed Ag enrichment at the grain boundary (see Supplementary Material Figure 4.16). Beam-induced migration events at the symmetric (210) kite structure are assumed to happen either between the Ag columns directly across the excess volume, which is considered very unlikely due to the large jump distance, or along other paths assuming a coupled collective migration between Ag columns within a single nanofacet, as observed experimentally. Regarding knock-on beam damage during image acquisition, the maximum energy transferred during a head-on elastic scattering event between a 300 kV incident electron and a Cu lattice atom was calculated to be about 12.5 eV [138]. The threshold energy to displace a Cu atom from its lattice site, however, is about 20 eV corresponding to an incident energy of 420 keV [138]. In case of Ag, a similar threshold energy of approximately 21 eV was found [184], however, only 7.4 eV are elastically transferred. The situation changes at interfaces with a certain excess volume like a grain boundary due to the lower coordination of atoms there. In Ag, the energy required to displace an atom from the surface, probably the lower bound energetic case, is reduced to 3 eV [184]. In the present study, it is expected that the transferred energy is just high enough to either strongly deflect atoms from their boundary site or even displace them into neighboring vacancies or less likely substitute lattice positions, with Cu being more affected due to the higher transferred energy. All experimentally determined peak intensity ratios are summarized for the individual imaging conditions and their respective global electron doses D_{glo} (per frame) for comparison (Figure 4.13). The ratios are set in relation to the atomic column occupancy that was linearly interpolated from 0 % for a peak intensity ratio of 1 (pure Cu) to 100 % for a ratio of 2.94, the maximum ratio found in our experiments. First, the results of the three distinct image acquisition schemes are discussed separately. Afterward the findings are correlated between these schemes to finally summarize the impact of imaging conditions, respectively, electron dose, on the qualitative and quantitative chemical information obtained from HAADF images at impurity decorated grain boundaries.

In case of Single Image acquisition, the influence of filtering was examined, which was applied to reduce effects from diffraction contrast, due to the disorientation of the sample, as much as possible. Background subtraction in the chosen system seems more complex compared to nanoparticle studies since the background information is still required in the chosen approach to determine peak intensity ratios but is also constantly changing due to beam-induced Ag migration at the boundary and inside the grains. No significant changes could be identified between the determined peak intensity ratios, with the filtered image's ratio being slightly above the unfiltered one but still well within its standard deviation. It is concluded that image filtering as applied in the present study is not the main influence
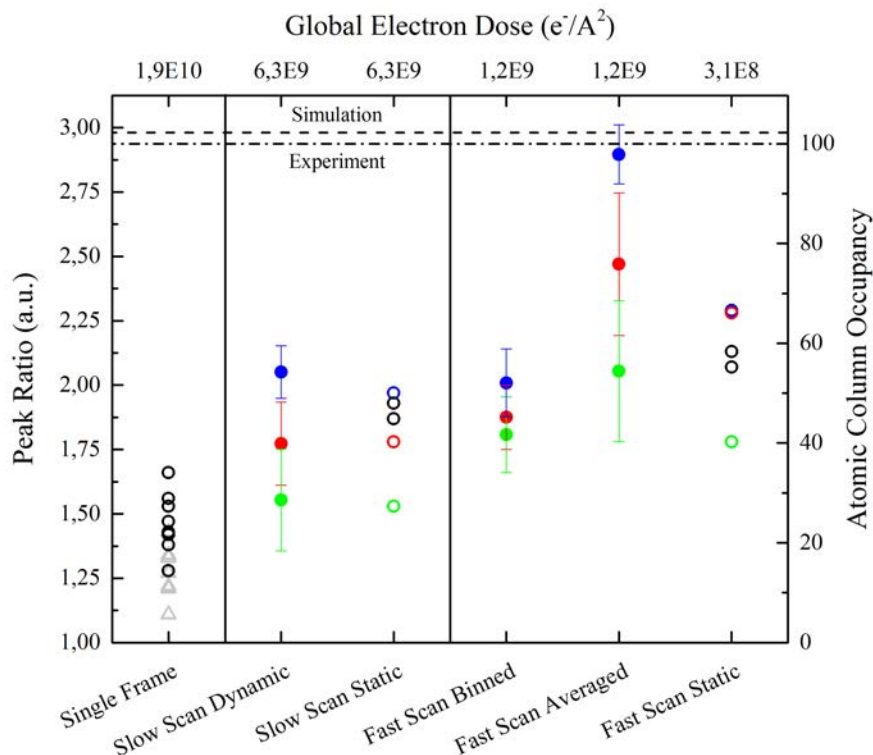
Figure 4.13: Master plot including all determined peak intensity ratios for the different acquisition procedures and their respective doses. Atomic column occupancy is normalized to the highest determined peak ratio of the Fast Scan Average series that is shown to be very likely a full atomic column by simulations. The Slow Scan captures similarly well the relative atomic column ratios but underestimates the exact occupancy of an individual column while static and Single Image acquisition is shown to always misinterpret the chemical information as well as lacking the dynamics of the observed system. Open symbols represent peak ratios of individual columns, colored points are used for the same atomic columns defined in Figures 4.9 and 4.10 and gray triangles refer to columns of the unfiltered static image.

on the quantitative information of HAADF images in the present set-up, but should always be considered. This agrees well with findings of Robb & Craven, who developed an image processing based technique on semiconductor superlattices extracting peak intensity ratio maps from HAADF images [185]. It was shown there that background subtraction affects the peak intensity ratio by less than 1.5 %. Considering the Slow Scan series, it is found that dynamic chemical information of individual atomic columns can be extracted using the applied moving average method in form of a progressive time evolution. The calculated mean ratios indicate that clear differences can be identified between different columns. Considering the static summed up image from 17 individual frames, the mean peak intensity ratio is overestimating the ratio of at least two atomic columns, i.e., the left red and central green column. In case of the Fast Scan series, the dynamic determination of individual and defined atomic column peak intensity ratios was achieved in a moving average manner. The highest peak intensity ratios of all imaging conditions were determined for these imaging conditions although being acquired on the exact same site as the Slow Scan and using the exact same analysis procedure. A clear difference in time is seen for individual columns (Figure 4.11) resulting in clearly separated mean ratios in Figure 4.13 (Fast Scan Averaged). The exact same series was used in a different manner, i.e., four individual frames were cumulatively summed up and the 200 acquired frames "binned" in the time domain using nonoverlapping windows of these four frames so that only 50 frames remained compared to the previous moving average fashion. The peak intensity ratio evolution of this binned dataset (Fast Scan Binned) surprisingly revealed strongly reduced ratios of up to about 50 % for the blue bright atomic column on the right side of the nanofacet. In addition, the intensity ratio between the two left columns could no longer be differentiated and even the clearly brighter right column is no longer significantly different falling within the standard deviation of almost both the other two columns. These differences between the averaged and binned datasets clearly visualize that dynamic peak intensity ratio evolutions can no longer be captured, due to the loss of available information. The binned dataset effectively mimics a four times increased pixel dwell time and frame acquisition time/electron dose. Increasing these times or doses actually means that peak intensities of individual columns change. This becomes very clear for the blue bright column on the right side of the nanofacet. While the moving average captures minor decreases in intensity clearly, the binning procedure rather averages these migration events and is thereby effectively lowered. On the other hand, increased times or electron doses for intragranular atomic columns increases the amount of statistical Ag migration being captured. This effectively increases the reference column intensity. Consequently, both effects sum up and lower the determined peak intensity ratio. Finally, the summed up static image of all 200 frames can be used to evaluate an average concentration of several atomic columns. Compared to the binned dataset the static image slightly overestimates the

mean ratio of atomic columns, while it clearly underestimates the ratio compared to the averaged dataset. It has to be noted that the unfiltered, cross-correlated image (Figure 4.10c), for which sample drift was refined to the peak location of the brightest Ag column in the nanofacet, clearly shows atomic resolution indicating that the cross-correlation worked properly. Sample drift as well as the scan distortions were not significant explaining also the close outcome of the nonrigid registration approach (Supplementary Material Figure 4.17). Comparison of the three different datasets reveals certain similarities and distinct differences that result in points to be aware of when attempting to extract quantitative chemical information from structurally and chemically complex interfaces by aberration-corrected HAADF images (Figure 4.13). It appears that Single Image acquisition does not capture accurate peak intensity ratios, neither in unfiltered nor in a filtered state. All extracted static mean ratios from the Slow and Fast Scan datasets were significantly higher, i.e., they are found to agree very well with each other around a ratio of 2.1, indicating the stability of the analysis procedure having in mind that both datasets were acquired at the same location and analyzed by the exact same procedure. No hydrocarbon formation was visible within the two minutes of total acquisition time for both series. In addition, beam-induced effects are shown in the present study to locally have strong effects on individual nanofacets over time but the remarkable stability of the entire nanofacet structure ensured comparable results of the two consecutive series, i.e., the flux of Ag atoms in and out the Ag-containing columns in the symmetric kites was shown to be fairly constant over time (Figure 4.11). For the case of static Single Image acquisition, the peak intensity ratio and hence information on the Ag column occupation are largely underestimated since atomic migration events are averaging out the HAADF signal during acquisition. In addition, the high electron dose leads to local displacements of atomic columns and hence the atomic column peak intensity is smeared out. Considering the high mobility of the Ag atoms, it is even possible that Ag-containing columns adopt the same intensity as the bulk Cu columns even preventing a qualitative interpretation of Ag segregation. A similar underestimation of Ag column occupation is observed for simple binning, due to a loss of information in the time domain that translates to a loss of Ag migration events and hence a lower average column peak intensity. Contrarily, the moving average method is suitable to extract at least relative chemical information of individual atomic columns in case of slower acquisition times. Comparing the dynamic Slow Scan data with the dynamic Fast Scan data (Averaged) a rough agreement of the relative peak intensity ratios is seen. Applying shortest pixel dwell times (local electron doses) to reduce beam-induced migration events and to capture the atomic motion - as seen from the Fast Scan series (Averaged) far less underestimates the Ag column occupancy. In addition, the lowered dwell time reduces 1) capturing statistical occurrence of Ag atoms in intragranular reference columns and 2) averaging of Ag segregate columns, thereby being more precise in terms of peak intensity ra-

tio determination compared to slower (lower) dwell times (local electron doses). For precise chemical characterization, the simple HAADF contrast relation of the intensity being equal to Z^α, with α being equal to 2, is rather an idealized assumption [186]. In reality, α is in fact a complex function of specimen-related and microscope-related factors, like specimen thickness, crystal structure, crystal orientation, and the annular detector geometry [187]. To find an accurate approximation of the exponent a for the chosen system and set-up, STEM image simulation was applied (Figure 4.12), especially focusing on the influence of Ag occupancy of individual atomic columns and sample thickness. Image simulations were often successfully applied before, to study the influence of parameters like thickness on the peak intensity ratio of gallium and arsenic under HAADF imaging conditions [188]. Duscher et al. for instance simulated the influence of bismuth segregated atoms at a grain boundary following the experimentally determined grain boundary structure and bismuth locations therein [177]. The obtained findings for bismuth were then briefly applied to Ag segregation assuming the same segregation site within the kite structure. However, the performed experiments of the present study indicate a different segregation site of Ag in the kite structure as predicted by Duscher et al., but agrees with molecular dynamics simulation results by Frolov et al. [75]. The experimentally determined structure found in the present study is provided along with the simulated structure. Simulations revealed a maximum peak intensity ratio for fully occupied atomic columns to be about 3.25 at a simulated sample thickness of 20 nm. Comparison with the experimental ratio of the Fast Scan series (2.94), agreement is found for simulated sample thicknesses of either 10 nm (2.9) or 30 nm (2.99). However, it should be mentioned that the experimentally determined column intensities can be tampered by a reconstruction of the grain boundary within the thin foil or by scan noise effects and the image simulations only consider a perfect symmetrical grain boundary segment without depth reconstruction. Thus, the given quantitative Ag occupation values, expressed by the extracted peak ratios, are estimates but clearly indicate that different columns in a nanofacet contain different amounts of Ag and that the determined relative Ag occupation is strongly influenced by the imaging conditions. Regarding the real sample thickness of less than 45 nm determined by EELS, a sample thickness of 30 – 40 nm seems most realistic. The experimentally found peak intensity ratios were previously just linearly translated into Ag atomic column occupancies under the assumption that the right column consists purely of Ag and therefore reveals the highest peak intensity ratio (Figures 4.11 and 4.13). This assumption could be validated by the image simulation results, thereby showing the linear translation to be a reasonable approximation for quantitatively extracting chemical information. Additionally, simulation results indicate an almost linear dependence of the peak intensity ratio of Ag/Cu with thickness and therefore the ratio is a suitable measure for Ag column occupation. The accuracy is certainly not on a single atom level but can still be used in the first approach for the present

complex boundary conditions to extract quantitative information over time. Especially the slight misorientation of the lower grain from perfect zone axis orientation introduces uncertainties when attempting to count the number of atoms in a column by reduced electron channeling. In addition, for sample thicknesses of > 10 nm cross-talk between neighboring columns has to be considered. More thorough studies of atom-counting techniques in such systems would be very beneficial not only to extract meaningful quantitative information, but ideally to also locate the Ag atoms within the column to get an indication of the three-dimensional decoration [145]. Rapidly acquired HAADF image series capture Ag migration events at nanofaceted grain boundary segments and hence the extracted peak intensity ratio evolution can be inspected that would be lost when taking single frame images (see Figure 4.8). Three distinct events are shown in the representative images and highlighted in the peak intensity ratio evolution as (a) - (c). Examination of the compiled video (see online Supplementary Material of [57]) in combination with the obtained quantitative chemistry evolution allows formulation of beam-induced migration mechanisms schematically shown in Fig. 8 and referred to as events 1 - 3. From Figure 4.11a to Figure 4.11b an opposing peak intensity ratio evolution is seen for the two left atomic columns in the observed nanofacet. The video indicates that this beam-induced event is likely associated to a favored migration path along the symmetric kite structure and is, to the best knowledge, the first direct dynamic visualization of such an event that occurs several times within the course of the experiment. Although there is only limited literature on atomistic diffusion mechanisms, the described findings agree well with the simulation by Ma et al [189]. They simulated diffusion of Au in Ag along a symmetrical (210) grain boundary and found an overall maintained grain boundary structure with an easy vacancy-based diffusion path [138]. According to Ma et al. several vacancies must move to facilitate the migration of the actual segregate atom. This is similar to the well-known 6 jump cycle in lattice diffusion [190]. However, in the experiments electron beam irradiation induced interstitial or substitutional migration events within the crystal lattice, requiring a certain amount of vacancies, cannot be excluded experimentally (event 2 in Figure 4.14). The last event observed in Figure 4.11c is referred to as 3 in Figure 4.14. In certain frames, the kite structure contains intensity at unexpected positions, namely the excess volume of the kite. Since the major migration path is expected to be along the structure rather than through this free volume, 3 is described as electron beam-induced displacement of either Ag atoms but more likely Cu atoms (more transferred energy per atom) within at least a single atomic column of the kite structure. It is speculated that in this case the transferred energy of an electron to that atom is not sufficient to displace it from its lattice site but still enough to partially displace it around its thermally vibrating equilibrium position. Using just slightly higher acquisition times or higher electron doses may average over too many of these events simultaneously, which might then be the reason for
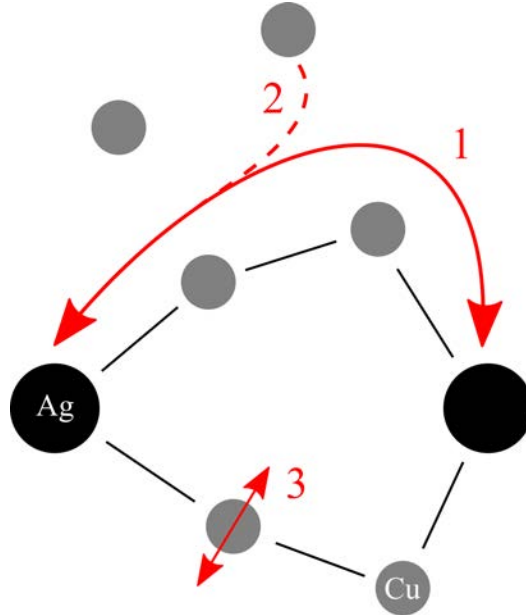
Figure 4.14: Schematic visualization of the identified beam-induced migration mechanisms captured by the proposed method. Favorable migration of Ag along the kite structure was identified in "1", while absorption from (and likely also release into) as well as strong displacements around the intracolumnar equilibrium lattice position are shown in "2" and "3", respectively.

less captured dynamic information for Slow Scan or Single Image conditions. Interestingly, only the two just discussed atomic columns' respective intensities are sig- nificantly changing, in contrast to the third column within the facet that remains almost constant in intensity. Since combined experimental observation and simulations are able to show that it is most likely a fully occupied Ag column, a state both the other two columns do not reach over the course of the experiment, it is proposed that fully occupied atomic columns must retain an energetically favorable and stable "binding-like" configuration, similar to a metastable state. Major disturbance of this arrange- ment seems to transition it into a rather labile configuration leaving room for dynamic events as described above. Both of the less occupied columns should try to reach this favorable state, however, might compete with the available Ag atoms under a constant in and out flux and therefore might not reach the metastable configuration.

Conclusions

The present chapter determines the influence of imaging conditions on the measured Ag column occupancy at nanofacets of an asymmetrical Cu grain boundary. In addition, insights in the atomic migration paths could be explored in the time domain using STEM. The study of atomic scale segregation phenomena at grain boundaries is of great interest to reveal the underlying segregation mechanisms. The combination of experimental STEM imaging

and STEM image simulations was successfully applied to capture the influence of beam-induced atomic migration on the determined Ag occupation under typical high-resolution STEM conditions. Three distinct and comparable acquisition procedures, considering single, serial, and fast image acquisition, resulted in significantly different Ag occupation values for the individual atomic columns in the nanofacets. These findings emphasize possible artifacts due to beam-induced atomic motion that tamper the extraction of qualitative and quantitative chemical information at complex interfaces. The implications for the analyzed imaging conditions are summarized as follows:

1. Single Image acquisition underestimates the determined peak intensity ratios and in the worst case can lead to chemical misinterpretation, since multiple Ag migration events are averaged during the image acquisition. In this case, the determined Ag column positions can even be misinterpreted because of the strong displacement of Ag atoms from their equilibrium positions by the electron beam.

2. Serial image acquisition is considered favorable at least to sample some migration events, but with increasing acquisition times (electron doses) the accuracy of the extracted Ag occupation decreases and smears out similar to the effects described in (1).

3. Shortest acquisition times just above a reasonable signal-to-noise ratio in combination with a cumulative averaging (moving average) give the highest Ag occupation values because migration of at least several atoms can be inspected and considered when extracting peak intensity ratios. However, even in this situation scan distortions and nonlinear imaging effects have to be taken into account when attempting to extract meaningful chemical information.

Supplementary Material

To view supplementary material for this article [57] and especially the movie file, it is referred to the article's webpage https://doi.org/10.1557/jmr.2016.398.
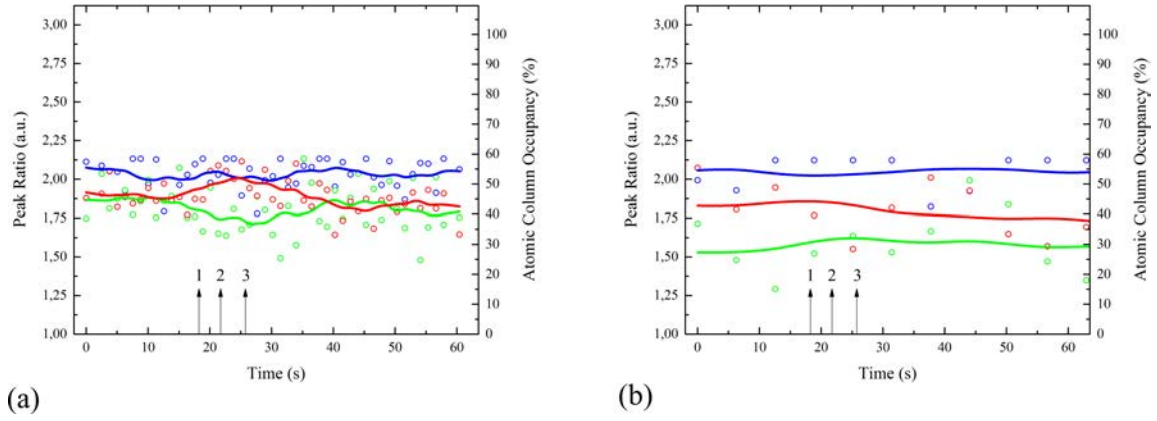
Figure 4.15: Peak intensity ratio profiles of (a) a Fast Scan series, which was binned in the time domain to effectively mimic a Slow Scan series and (b) the peak intensity ratio profile of an actual Slow Scan series.
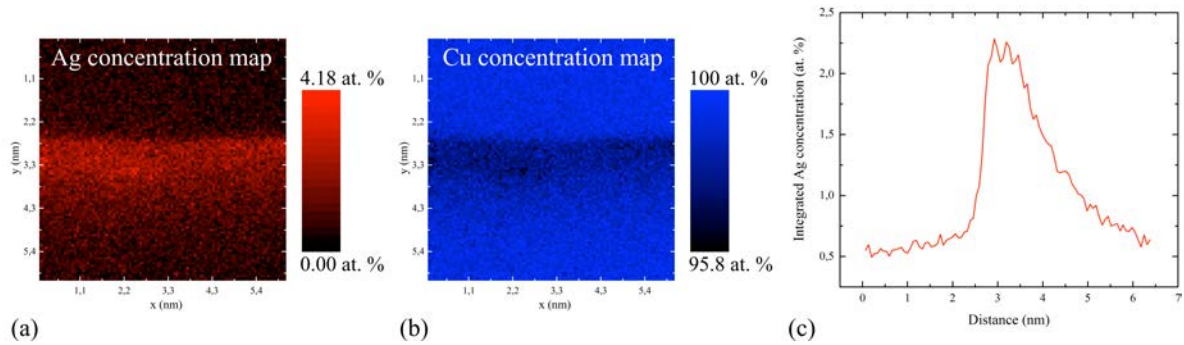

Figure 4.16: EDS confirmation of Ag enrichment at the grain boundary. A prinicipal component analysis yielded (a) the Ag concentration map, (b) the Cu concentration map and (c) an integrated line profile showing the Ag concentration across the grain boundary.
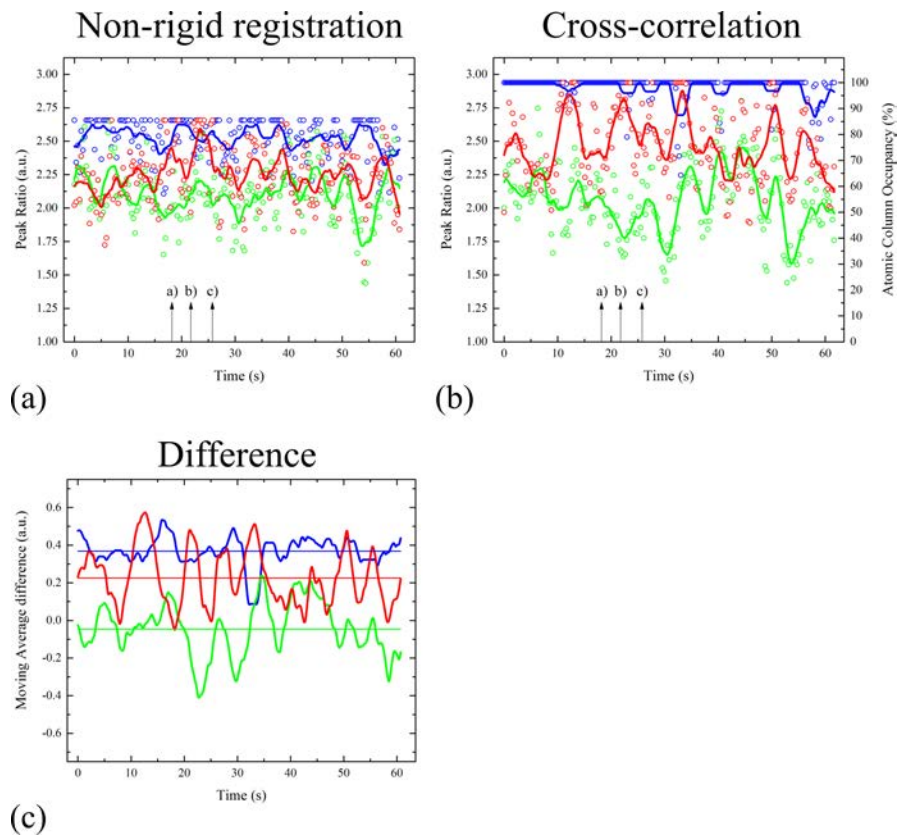
Figure 4.17: Comparison of a peak intensity ratio profiles obtained on the same data set, by (a) a non-rigid registration method and (b) the discussed cross-correlation method. To highlight the differences between both methods, the difference profile is plotted in (c).

4.3 Faceting diagram for Ag segregation induced nanofaceting at an asymmetric Cu tilt grain boundary

NICOLAS J. PETER, MARIA J. DUARTE, CHRISTOPH KIRCHLECHNER, CHRISTIAN H. LIEBSCHER, GERHARD DEHM

Max-Planck Institut für Eisenforschung GmbH, 40237 Düsseldorf, Germany

ABSTRACT

In this work, we experimentally establish the isothermal nanofacet evolution at an asymmetric $\Sigma 5$ tilt grain boundary in the Cu-Ag system using a diffusion couple approach. We investigate the nanofacet formation along the grain boundary in dependence of the Ag solute excess concentration. The initial grain boundary dissociates into asymmetric Ag-lean segments and Ag-rich symmetric (210) segments. Increasing Ag excess leads to an increase in Ag-rich facet segment length, while the length of the asymmetric facets remains constant. From this, we construct a grain boundary nanofaceting diagram deduced from our experiments relating local atomic structure, overall inclination and Ag solute excess.

MAIN TEXT

Grain boundaries (GBs) are interfaces separating adjoining crystals with different misorientation. They are amongst the most important material defects and their associated structure and properties determine their influence on the behavior of polycrystalline materials. An easy categorization is based on the coincide site lattice (CSL), which identifies special CSL boundaries e.g. for distinct tilt angles. One well-known and studied type of boundaries is the $\sum5$-type, which includes in particular the symmetric (310) and (210) boundaries with [001] tilt axis. These have been serving for various studies of grain boundaries. However, much less is known about the asymmetric inclinations between these two symmetric boundaries. Medlin et al., for instance, reported a decomposition of an asymmetric $\sum5$ grain boundary in iron to decompose into a faceted boundary composed of symmetric (310) and (210) facet segments [99]. In fact, Tschopp et al. simulated the grain boundary energies of several of these asymmetric inclinations in copper and aluminum and chose some specific inclinations to also investigate their structure [55]. Many other studies investigated the structure of $\sum5$-type GBs experimentally [99] and theoretically [64] in different materials and it is by now accepted that the two symmetric (310) and (210) variants are composed of a distinct, reoccuring arrangement of kite-shaped motifs. Going further Frolov et al. even investigated temperature induced structural changes of the symmetric variants upon segregation in the Cu-Ag system [75]. In early work, Gibbs established that interfacial transitions can be described by equilibrium thermodynamics [10] and Hart later proposed that transitions at GBs are possible and referred to them as "two-dimensional phase transitions" [11]. The thermodynamic description of these transitions was extended by Cahn and Rottman [12, 13] who categorized them into faceting and congruent (all 5 degrees of freedom remain constant) transitions. Both types, non-congruent (faceting) and congruent transitions are referred to as GB phase transformations [14] or synonymously GB complexion transitions [15, 191]. However, these transitions are typically studied in perfectly symmetric and planar GBs [177, 192, 193] and mostly derived from indirect experimental measurements [22, 194] or atomistic simulations [75]. Instances of how complex such GB transitions can be and how factors like temperature and chemistry can influence a GB's structure were recently demonstrated by scanning transmission electron microscopy (STEM). Hu et al. found a temperature dependent segregation behavior including a first order congruent transition at low temperatures in a planar Au-doped Si GB using atomistic calculations [195]. Very recently, a complex co-segregation pattern including segregation induced symmetry changes and order losses at a planar WC grain boundary was discovered [196]. A comprehensive review on evidence of grain boundary transitions can be found in a recent review article [197].

Already Cahn discussed that most GB transitions involve faceting [12] and such transitions

have been observed experimentally in many materials [81–83]. Faceting-roughening phenomena of GBs were recently summarized by Straumal et al. for a great amount of different grain boundary types and in different material systems [198]. The majority of experimental and simulation work established a clear dependence of faceting-defaceting transitions on temperature in pure metal GBs [61, 82, 84, 85]. Some work also focused on how structural defects of a grain boundary (GB dislocations) may influence faceting by pinning or dragging facets during defect motion [88]. Transitions influenced by chemical stimulus, for instance by segregation, are much less understood in the case of GB faceting as compared to the segregation behavior of planar boundaries. Changing the chemistry at GBs by adsorption of solute excess significantly changes the energy of such boundaries and consequently structural transitions are likely to occur. Early work showed structural transitions at a low angle grain boundary in the Fe-Au system [199]. Faceting transitions were frequently observed in the last decades in the Cu-Bi binary system since Bi promotes GB embrittlement [9]. Experimentally, only one carefully performed *in situ* experiment conducted by Ference and Baluffi unambiguously demonstrated that reversible faceting-defaceting can be induced by solute adsorption [90]. However, faceting occurred on a scale of several tens to hundreds of nanometers and the characterization of the atomic GB structure and chemistry was not possible at that time. Four decades ago Loier and Boos demonstrated already how small additions of Bi induce striations and faceting of Ni grain boundaries [91]. Yu et al. recently found distinct segregation patterns of Bi solutes at a microfaceted general GB in Ni [93] after having shown that such patterns may be the underlying reason for detrimental effects of Bi segregation on mechanical properties in Ni [76]. Our recent work combining atomic resolution imaging and atomistic modelling demonstrated that Ag segregation can act as chemical trigger promoting a nanofaceting transition of an asymmetric $\sum 5$ tilt grain boundary in Cu [94]. However, temperature [64], pressure [95] or solute excess concentration [90, 96] strongly influence GB transitions [97] and their concentration dependence is usually established by atomistic modeling.

Here, we report the experimental assessment of GB plane and faceting evolution in dependence on the Ag solute excess concentration at an initially asymmetric $\sum 5$ tilt grain boundary in Cu. The concentration dependence was observed using atomic resolution STEM in combination with energy dispersive X-ray spectroscopy (EDS) and atom probe tomography (APT) in close vicinity to the interface of a Cu-Ag diffusion couple. A Ag reservoir was sputter deposited on top of a bicrystal containing the GB to create the diffusion couple. For consistency, we refer to the surface of the bicrystal (the interface to the Ag reservoir) as surface.

A pure Cu reference boundary of the bicrystal's top surface before Ag deposition was observed at three distinct magnifications (Figure 4.18b). The boundary appears to be entirely
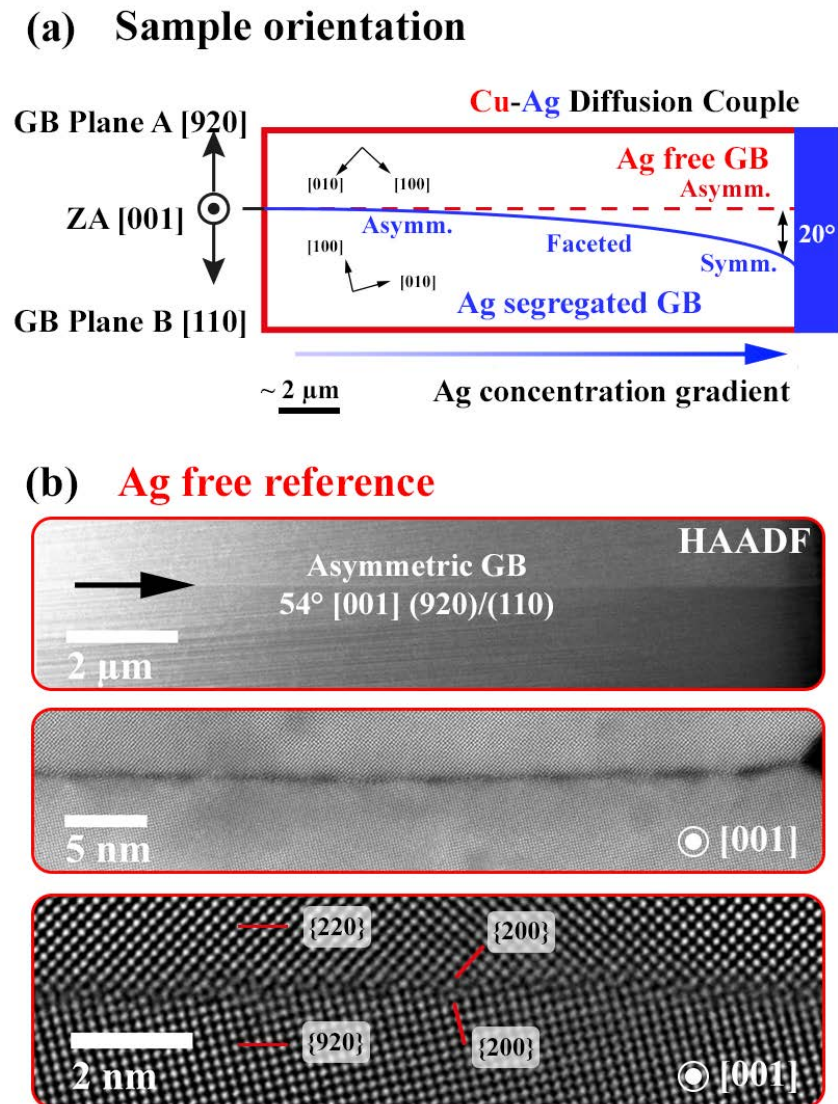
Figure 4.18: (a) Schematic representation of the diffusion couple's arrangement and the crystallography of the grown bicrystal containing the asymmetric tilt grain boundary and how the boundary behaves after segregation. (b) HAADF-STEM micrographs of the asymmetric, Ag-free, $\sum 5$ reference boundary at different magnifications. {200} planes and planes belonging to the grain boundary are indicated in the bottom micrograph. All micrographs are in [001] zone axis orientation.

flat for at least 13 µm from the top surface into the bulk as determined by STEM, even at higher magnification. Atomic resolution imaging reveals the local atomic arrangement and although some sub-nanometer roughness can be associated to the asymmetric GB; we refer to this boundary as flat reference boundary. The reference GB was determined to be close to an asymmetric $\sum$5 34°[001] (920)/(110) boundary, which is in close agreement to our previously investigated GB showing the Ag induced nanofaceting [94]. After Ag diffusion, the overall macroscopic grain boundary (observed at low magnification) is no longer straight and a seemingly continuous curvature from the bulk to the surface was induced. A schematic representation of the grain boundary after segregation is given in Figure 4.18a and an experimental HAADF STEM micrograph of a part of the grain boundary close to the surface at low magnification in Figure 4.19. Micrographs were then acquired at certain locations and at high magnifications along the segregated GB to study the overall plane evolution connected with the nanofacet formation and the associated Ag excess. Representative locations (see Figure 4.19 positions 4 to 1, from Cu(Ag) GB close to the surface) are marked in the overview image and are presented in more detail below. We observe a gradual transition from a flat segregated boundary (1 in Figure 4.19, compare STEM-EDS results), in close resemblance to the Ag-free reference, to a symmetric $\sum$5 (210) GB (4 in Figure 4.19) as further indicated by the adoption of the kite motif [75, 94] in the enlarged area next to the micrograph of position 4. The intermediate GB adopts a nanofaceted state containing Ag-rich, symmetric $\sum$5 (210) segments and newly formed, asymmetric and Ag-lean $\sum$5 segments with a GB plane close to (320)/(100). Almost all kite tip positions are occupied by Ag (bright columns in HAADF STEM). In addition, we occasionally observe image contrast indicating Ag occupation of non-kite tip positions at the GB, as well. Therefore, it is reasonable to believe that the symmetric GB close to the surface is covered close to a monolayer of Ag. The symmetric $\sum$5 (210) GB plane was measured to be $\sim 20°$ inclined with respect to the non-faceted, asymmetric $\sum$5 (920)/(110) reference boundary plane. It has to be noted, that an overall increase in Ag concentration resulting from the Ag concentration gradient refers to the overall concentration at the grain boundary (and the bulk). Locally, the Ag-rich and Ag-lean facet segments exhibit relatively constant coverage, i.e. close to monolayer or close to no coverage, respectively.

The precise solute excess concentration and localized elemental distribution were determined along the boundary by APT and STEM-EDS, respectively. An APT specimen extracted close to the sample surface (Tip 1, position 4 in Figure 4.19) was found to have a peak concentration of $\sim$3.6 at. % Ag (black line) as determined from the integrated line profiles across the GB (Figure 4.20a, upper graph). A specimen extracted from below the sample surface (Tip 2, at position 2-3 in Figure 4.19) only contained a peak solute excess of $\sim$2.4 at. % Ag (Figure 4.20a, lower graph). A depletion zone is visible for the Ag concentration next
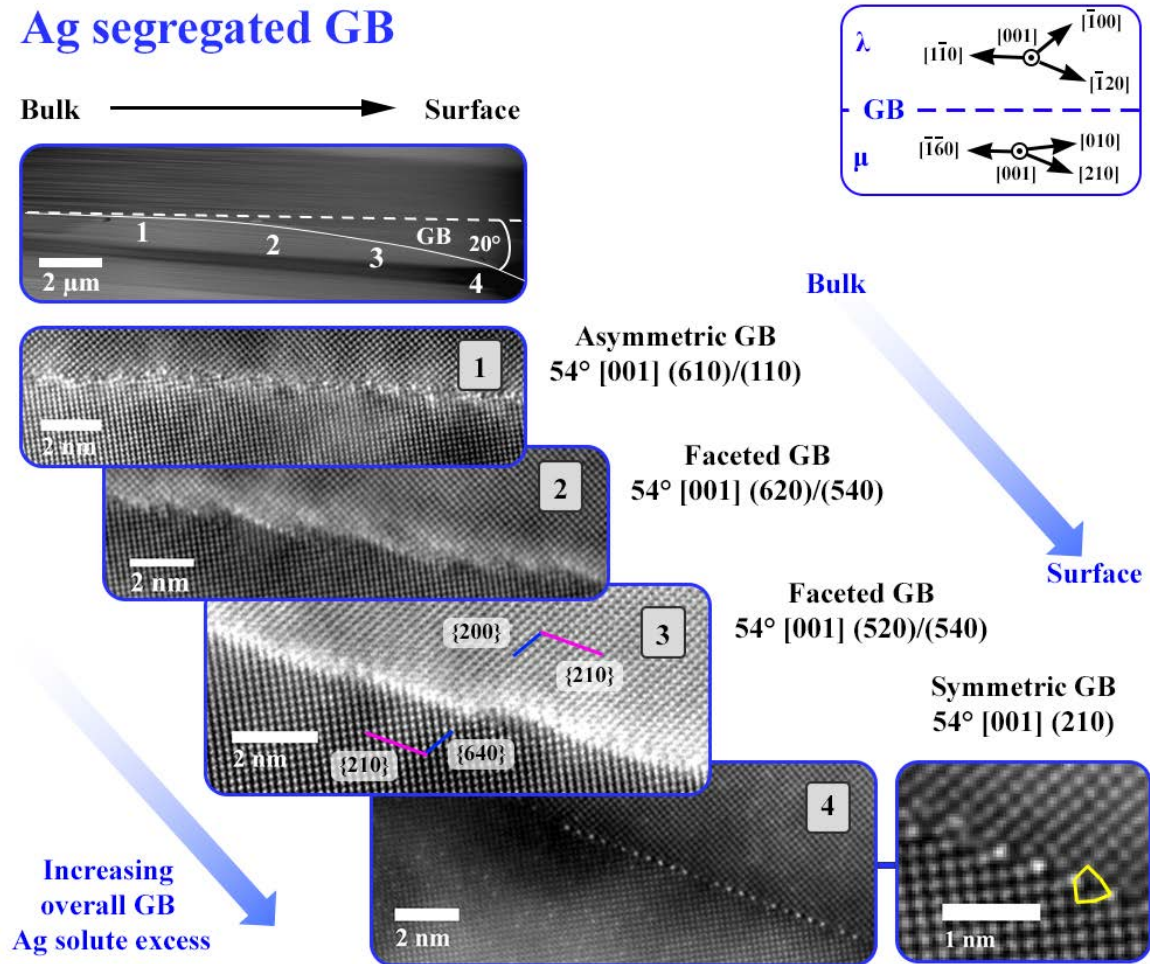
Figure 4.19: The curved Ag segregated GB as an overview image at lower magnification along with micrographs along a boundary over a distance of about 15 µm indicating the changes from an asymmetric GB (bulk) over the nanofaceted state with increasing symmetric facet segments to a solely symmetric GB (surface) and an atomic resolution micrograph to capture the symmetric $\sum 5$ (210) GB's kite structure. All HAADF-STEM micrographs were acquired in [001] zone axis orientation. Planes belonging to the asymmetric (320)/(100) and symmetric (210) facet segments are indicated with blue bars in panel 3 and for all grain boundary types in the upper right corner of this figure (λ and μ referring to the upper and lower grain, respectively). The increasing overall GB Ag solute excess towards the surface is to be seen as an average solute excess over multiple symmetric and asymmetric facets. The solute excess at individual facet segments remains approximately the same, i.e. almost a monolayer for the symmetric facet segment and almost no solute excess at the asymmetric facet segment.

to the enriched GB in both specimen. In the case of the less segregated GB (Tip 2), the Ag concentration recovers towards the outer APT needle's surface and reaches saturation at a level of about 1.3 at. % at about 25 nm from the GB. For Tip 1, the depletion extends much further and saturation is not reached inside the specimen volume. From the course of the concentration profile we expect a saturation level of around 1.7 at. % at about 45 nm from the GB deduced from a second order polynomial fitting. To determine the respective bulk Ag concentration more reliable, we created cylinders of the same dimensions (25 nm x 10 nm x 40 nm) inside the two volumes and placed them parallel to the GB at a fixed distance of 20 nm (in saturation level of Tip 2). Bulk concentrations of 1.43 ± 0.015 at. % and 1.23 ± 0.011 at. % were extracted for Tip 1 and Tip 2, respectively. The precise location of the extracted tips within a few µm is hardly possible to be determined after FIB milling preparation. The bulk Ag concentrations appear reasonable considering the low Ag solubility according to the equilibrium phase diagram [29]. In addition, Ag density maps of thin slices (1 nm thickness) through the reconstructed volumes of these two APT tips - one from a surface-near region (Tip 1) and one extracted from an approximate location 3 in Figure 4.19 (Tip 2) - revealed a non-faceted, Ag-rich boundary close to the surface and further towards the bulk a faceted, Ag-rich boundary. This transition agrees well with our experimental STEM micrographs. Across these two boundaries we calculated the solute excess concentration following our previously applied approach [94, 158] and revealed for Tip 1 a Ag excess concentration of 4.96 at/nm^2, while the faceted GB (Tip 2) showed an average excess concentration of 3.39 at/nm^2. Based on the latter, we chose a maximum value for the color bar to qualitatively best show the faceted GB state. These results appear reasonable, as STEM results revealed preferential segregation to symmetric $\sum$5 (210) GB portions, which dominate at the surface, but contribute less for deeper measurement locations into the bulk due to the increasing incorporation of asymmetric Ag-lean segments. In addition, the diffusion gradient from the surface into the bulk reduces the Ag excess concentration at the GB, which therefore appears to be coupled with the facet lengths. The excess of the non-faceted, symmetric $\sum$5 (210) boundary close to the surface is just slightly below the monolayer solute excess of roughly 6 at/nm^2, which is calculated by the number of atoms on a (210) plane unit area. However, STEM micrographs at the very surface revealed some areas in which two bright atomic columns appear next to each other, which is why we assume to have at least monolayer coverage at the very surface of the diffusion couple, i.e. close to the Ag reservoir. The drawback of such compositionally sensitive APT measurements is the lack of atomically resolved structural features in the analyzed volume. Consequently, STEM-EDS was used in order to correlate the occurrence of the three structural states observed with their solute excess at different locations along the segregated boundary. Integrated intensity line profiles for the Ag-L$_\alpha$ peak were extracted from EDS maps at the investigated locations and three

representative profiles (close to positions 1, 2 and 4) for the three observed GB states are plotted after applying of a moving average algorithm for visibility in Figure 4.20b normalized to the background intensity. The inset shows EDS spectra integrated in a region of about 10 x 15 nm^2 of the expected Ag-L$_\alpha$ peak for a GB containing area and an area inside one grain for comparison. We would like to point out that EDS maps were acquired in zone axis orientation immediately after image acquisition to avoid tilting and loss of spatial correlation. In this case, quantification of the EDS data is no longer applicable through the Cliff-Lorimer method and intensive simulation work would have to be performed to account for effects like beam spreading and electron channelling [137]. Therefore, we do not give absolute concentration values from EDS but normalize our results to the concentration expected for monolayer coverage by integrating the peak intensity and collapsing it to a GB width of 0.12 nm, as this width provides a Ag reference concentration of 100 % for the data set closest to the surface. This assumption is based on our experimental HAADF STEM results. STEM-EDS analyses show a clear increase of Ag from the bulk towards the surface.

The combination of structural and compositional characterization of the observed faceting evolution enables a comprehensive view on the evolution of individual facet segments. In fact, we composed a segregation-induced GB faceting diagram for the investigated GB under the chosen diffusion conditions (Figure 4.21). Plotting the facet segment length against the relative Ag monolayer coverage (Figure 4.21a) as determined by EDS along the GB (Figure 4.21b) reveals a concentration window for faceting to occur. While the asymmetric facet segment length was found to be independent of the Ag excess and remained at a length l of about 1 nm, the symmetric facet segments almost linearly grew with increasing excess concentration starting from 1 nm (R-square of 0.96). Therefore, the reason for an increasing global GB inclination lies in growing symmetric facet segments. Thus there are three clearly distinguishable GB states as a function of overall Ag excess solute: (i) non-faceted, asymmetric and Ag-lean (Figure 4.19-1), (ii) preferentially Ag segregated and nanofaceted (Figures 4.19-2 and 4.19-3) as well as (iii) non-faceted, symmetric and Ag-rich (Figure 4.19-4).

The present results confirm our previous findings [94] that after Ag segregation induced facet formation there is preferential segregation occurring to only the symmetric facet segments, while the asymmetric segments remain Ag-lean. To make a better connection between facet segment length, Ag segregation and especially overall GB inclination, we plotted the relative Ag excess concentration as obtained by EDS under the assumption of full monolayer coverage for the symmetric $\sum 5$ (210) GB close to the surface (Fig. 21b). At this point, the boundary was about 20° inclined from the asymmetric reference GB. To describe the relation between Ag concentration and facet length, we normalize the ratio of the asymmetric segment length (ASL) and the symmetric facet segment length (SSL) using the "facet segment ratio" parameter FSR . FSR is calculated as $FSR = SSL/(ASL + SSL)$. Consequently, the Ag-rich,
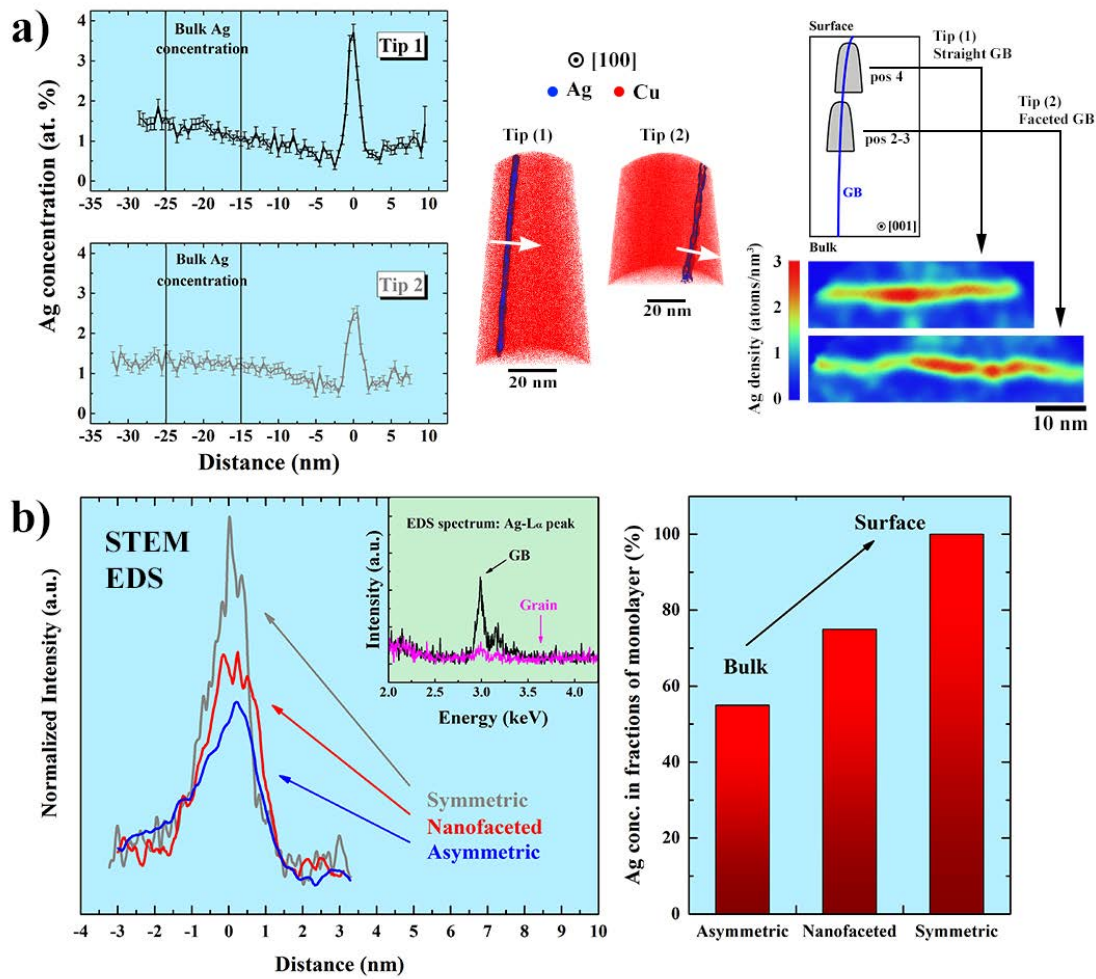
Figure 4.20: (a) APT results of the Ag segregated GB. The extracted concentration profile across the boundary is given, while Ag density maps are shown representative for two different samples - one at the surface (corresponding to position 4 in Fig. 2), one deeper into the bulk (corresponding to position 2-3 in Fig. 2) - highlighting the different GB states. (b) STEM-EDS results across the GB at three representative locations. In the nanofaceted case, EDS information is collected across the GB containing multiple facets. EDS data was collected in zone axis orientation at the exact location where micrographs were recorded.

symmetric $\sum 5$ (210) GB close to the surface does not show any faceting and FSR = 1 (ASL = 0). The purely asymmetric reference GB at inclination 0° has consequently no symmetric segments and thus FSR = 0. The ASL was determined above to be approximately constant with a length of ∼1 nm for the faceted GB. Under the assumption of full monolayer coverage for FSR = 1 supported by STEM observations, we drew a dashed line (red) to indicate an anticipated linear decrease of Ag excess with a linearly decreasing amount of the symmetric segment fraction. Our experimental results are given as individual data points and are linearly fitted (white) with a R-square value of 0.93. Indeed, our results follow the anticipated, ideal line in reasonable agreement (compare red and white lines), which leads us to the conclusion that for the nanofaceted boundary portion symmetric facet segments always are at least close to monolayer coverage, while it indicates that asymmetric segments of the nanofaceted grain boundary section are close to being Ag-free. This extends our previous findings deduced from a GB faceted at a single Ag concentration to the entire faceting range. No faceting was observed below FSR = 0.5, which means below these equisized nanofacets, faceting disappears and a purely asymmetric GB takes up the Ag excess. However, the excess uptake does not exceed about 30 % of the symmetric $\sum 5$ (210) GB's excess. This does not necessarily imply a generally fixed saturation level, as it depends on the local chemical potential, which is influenced also by the annealing temperature and subsequent cooling/quenching conditions. In light of an extrapolation of the facet data to FSR = 0 in Figure 4b (white dashed line), the asymmetric GB should have a Ag concentration of around 16 % of a $\sum 5$ (210) boundary. As this is less than the actually observed 30 %, the asymmetric GB seems much more favorable to be preserved compared to inducing a GB dissociation. This agrees well with our previous MD simulation results, which indicate Ag solute excess being absorbed at the asymmetric boundary already starting at a chemical potential around $\mu = 0.35\,eV$, while the symmetric $\sum 5$ (210) boundary starts taking up Ag only above chemical potentials of $\mu = 0.5\,eV$ [94]. Thus, Ag uptake of the asymmetric boundary before the threshold concentration seems to be a prerequisite to induce the nanofaceting. Finally, the jump from about 30 % relative Ag monolayer coverage (FSR = 0) to about 50 % when nanofaceting is induced, strongly indicates a first order GB transition occurring.

Similar GB phase diagrams have been established for different transitions like GB premelting, intergranular film formation or for multilayer segregation patterns as a function of concentration [197]. However, only few such GB phase diagrams could be established, yet. We present here the first experimental GB nanofaceting diagram as a function of solute excess concentration, similar to GB segregation diagrams as proposed by Lejček and Hofman for iron GBs [200] or Watanabe et al.'s hardening/segregation GB diagrams in iron alloys [201], but focusing on the atomic grain boundary structure evolution. Establishing such diagrams, analogous to bulk phase diagrams, may offer new possibilities for microstructure engineer-
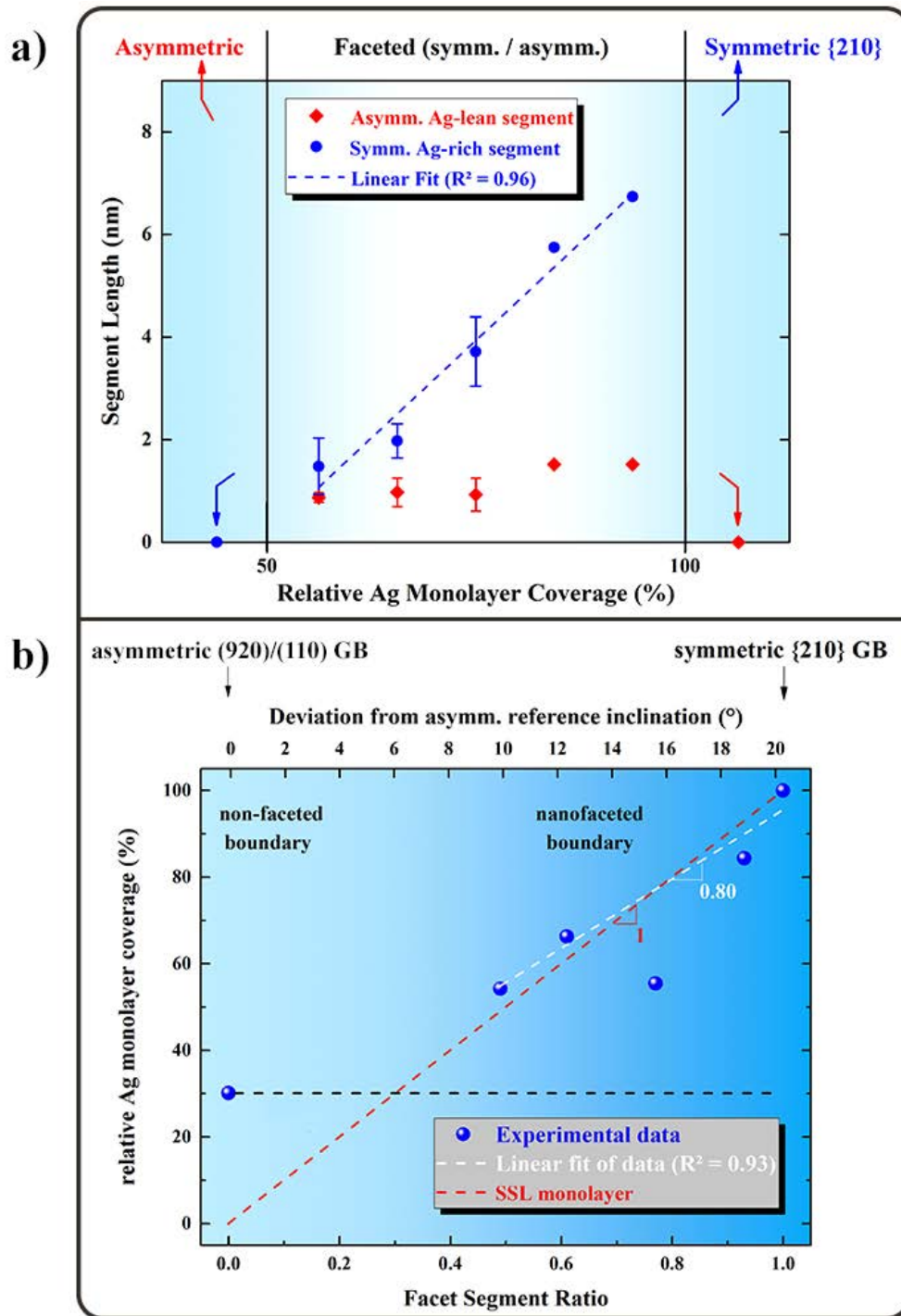
Figure 4.21: (a) GB faceting diagram presenting the facet segment length evolution along the boundary as a function of Ag solute excess concentration. Three distinct GB states appear: (i) asymmetric and not faceted for low Ag excess, (ii) nanofaceted, preferentially segregated boundary within a solute excess window and (iii) symmetric and not faceted boundary for high Ag excess. (b) Correlation between faceting, inclination and overall inclination of the GB including a linear fit through recorded data points (white line), a straight line to highlight an expected linear dependence of Ag content in facets (red) and the boundary specific Ag excess at the asymmetric GB.

ing in order to tune macroscopic materials properties. Although the preferential segregation might appear as an exception from the Langmuir McLean adsorption behavior in terms of homogeneous GB decoration, the individual segments still follow Langmuir McLean. Regarding the asymmetric segregated and the symmetric $\sum 5$ (210) GB, we were able to use the Langmuir McLean relation to deduce the ratio of their respective segregation energies and found that the Gibbs segregation energy of the symmetric boundary is approximately 1.08 times the energy of the asymmetric GB. Nevertheless, adjusted segregation models accounting for such faceting transitions are becoming necessary for these cases.

Our experimental findings enable us to propose a mechanistic picture of the observed faceting phenomenon. We showed previously experimentally and by simulations that heat treatment at 800°C (1073 K) does not induce nanofaceting at the asymmetric $\sum 5$ GB studied here, while Ag segregation does. Consequently, heating the boundary to 800°C leaves the boundary intact, possibly with increased disorder. Mishin and co-workers showed in a series of studies on Cu-Ag GBs that increasing temperature, but also increasing Ag solute excess can significantly influence how ordered a GB is referred to the perfect bulk lattice [202–205]. At such high temperatures, Ag atoms are going almost completely in solid solution and diffuse from the surface through the bulk and along the boundary creating a Ag concentration gradient. The solidus line was likely not crossed, as no homogeneous nucleation of Ag precipitates was observed inside the grains. Upon cooling, the disordered grain boundary restores its low temperature structure, while still remaining in the solid solubility region according to the equilibrium phase diagram [29]. Judging from the determined bulk Ag concentration of about 1.5 at. %, the solidus line is crossed at around 550°C (823 K). At this point, Ag starts to segregate towards the GB upon further cooling to minimize the energy of the system. The amount of Ag segregating to the boundary is depth dependent due to the created concentration gradient. Eventually, a critical threshold concentration is reached to initiate nucleation of the symmetric $\sum 5$ (210) facets, since the observed normal kite structure (Figure 4.19, 2-4) can absorb the highest amount of Ag excess and leads to the largest reduction in energy compared to segregation to the initial asymmetric GB [94]. The nucleation of symmetric Ag-rich facets is the initial step dissociating the asymmetric GB into a nanofaceted boundary. The local amount of Ag solute excess at the boundary, which is dictated by the concentration gradient in the bulk, determines the density of nucleation sites and provides the driving force for facet growth. This chemical stimulus in addition to the grain boundary energy anisotropy provides a sufficiently large driving force for the GB to migrate towards the symmetric $\sum 5$ (210) inclination although this increases its total length. Following the trend of having more Ag towards the surface, symmetric facets grow longer towards the surface until a continuous $\sum 5$ (210) GB is formed close to the surface. Below an estimated critical Ag threshold concentration of around 0.6 at.% for the bulk Ag content faceting will not occur considering a

constant segregation factor ($\beta = \frac{GB_{concentration}}{Bulk_{concentration}}$). However, as the bulk diffusion gradient cannot be quantified here accurately, the threshold concentration cannot be determined precisely neither. The nucleation of the Ag-rich $\sum 5$ (210) facet segments at the initially asymmetric GB is accompanied by the nucleation of the asymmetric facet segment and the associated GB disconnections or facet junctions, which are also necessary to migrate the boundary to compensate for the overall change in inclination towards the surface. The defects are likely involved in the migration of the GB to compensate for the inclination change induced by nucleation the symmetric facet segments. For instance, the migration of a flat, symmetric GB was shown theoretically for an Al $\sum 7$ GB to function via a nucleation process of islands on the grain boundary plane [179] (also regarded as disconnection nucleation for $\sum 13$ and $\sum 17$ Cu boundaries [206, 207]) and to be highly temperature dependent between 500 K to 700 K [179], which is close or even in the temperature range we expect our facet nucleation to occur. Please note that we cannot rule out the presence of secondary GB dislocations and their role during GB migration in this study, which would require further investigation. The question remains, why a nanofaceted GB portion is found instead of coarse facets or even just a curved GB. In general, the energy of faceted GB following Hamilton et al. is composed of two parts: (i) the contribution of the GB energies of the two facet segments $\gamma_{1,2}$ along with the contribution of facet junctions γ_j as well as (ii) the interaction between facet junctions γ_{j-j}. The overall GB energy γ_{GB} can thus be described as $\gamma_{GB} = \gamma_1 + \gamma_2 + \frac{2\gamma_j}{\Lambda} + \frac{\gamma_{j-j}}{\Lambda}$, with Λ being the facet period (length). For our purposes we neglect the interaction of the junction term here leading to $\gamma_{GB} = \gamma_1 + \gamma_2 + \frac{2\gamma_j}{\Lambda}$. Hamilton et al. demonstrated by simulation work that finite facet lengths of $\sum 3$ GBs in Al are not a thermodynamic equilibrium state of these boundaries, due to the interfacial line tension not being sufficient to stabilize finite facet lengths [86]. Thus, these GBs inherently want to create coarse facets to increase the spacing of the GB facet junctions and thus decrease γ_{GB}. This theory was confirmed experimentally by Medlin et al. for an asymmetric $\sum 5$ GB in Fe [99] and atomistic simulations by Wu et al. for different asymmetric and symmetric GBs in Al [65]. In the former study by Medlin et al. it was shown that secondary grain boundary dislocations can stabilize a finite facet length if they are pinned to the facet junctions. In contrast, Wu et al. found that migration kinetics during facet coarsening can promote the formation of finite sized facets. Instead of a continuous decrease in energy for increasing facet periods, migration of facet segments can impose a multitude of energy barriers depending on the structure of the facet segment resulting in the inhibition of further migration and therefore stabilization of finite length facets. Both [99] and [65] do not consider segregation effects. In the present study, the energy change due to segregation can be expressed generally through $\Delta\gamma_{GB} = \Delta\gamma_{ASL} + \Delta\gamma_{SSL} + \frac{2\Delta\gamma_j}{\Lambda}$. However, considering the preferential segregation to the symmetric portion and no noticeable segregation to facet junctions, the energy reduction is mainly attributed to the reduction in energy

due to the formation of symmetric $\sum 5$ (210) segments, thus following $\Delta\gamma_{GB} \approx \Delta\gamma_{SSL}$. Please note that Medlin et al. describe how secondary GB dislocations can impose a finite length to the faceted boundary [99], which could not be studied here, but would be interesting to investigate in the future. Nevertheless, it would be interesting to study effects of segregation to junctions and how they influence the energetics of the systems including the interaction between junctions, which was neglected here. Segregation to facet junctions was for example recently observed at faceted Si [208] and Cu GBs [7].

In conclusion, we present the first GB faceting diagram by studying the influence of Ag solute excess concentration on facet formation in an asymmetric $\sum 5$ tilt grain boundary via aberration corrected STEM, STEM-EDS and APT. After having established a Ag concentration gradient by a diffusion couple approach, we were able to distinguish different structural arrangements (faceting states) along the boundary as a function of Ag solute excess concentration. The total length of the GB in the $\sum 5$ misorientation system (54°) increases by more than 15 % compared to its initial (Ag-free) position, revealing a lower energy state after Ag segregation. In the bulk at low Ag solute excess relative to the surface, the initially asymmetric $\sum 5$ GB remains structurally unaffected but takes up Ag. Exceeding a threshold amount of solute excess, the boundary undergoes a first order transition and becomes nanofaceted. One facet segment changes its grain boundary plane, but remains asymmetric, Ag-lean and constant in length, while the other segment was determined to be a symmetric $\sum 5$ (210) type, with increasing length towards the surface and being enriched in Ag. At the surface, highest amounts of available Ag allow for a planar $\sum 5$ (210) GB containing close to a monolayer of Ag. The experimental results and established faceting diagram are discussed in light of previous segregation diagrams and the Langmuir McLean relation and, additionally, reasons for a finite facet length at the nanoscale are presented, which are focused on the points that the symmetric facet segment reduces the overall GB energy most upon segregation and that the asymmetric segment acts as a kinetic barrier for facet growth. It has to be noted that a continuously curved grain boundary, in contrast to a faceted boundary may be connected differently to physical properties such as mobility or plastic deformation. In fact, continuous curvatures at lower magnifications might be related to nanofaceting transitions as observed in the present study more often for doped material systems. Still, such phenomena would only be resolved with adequate characterization techniques of highest resolution.

4.4 Influence of Ag segregation induced grain boundary nanofaceting on plastic deformation mechanisms in Cu

Nicolas J. Peter[1], Tobias Brink[1], Subin Lee[1], Blazej Grabowski[2], Christian H. Liebscher[1], Christoph Kirchlechner[1], Gerhard Dehm[1]

[1]Max-Planck Institut für Eisenforschung GmbH, 40237 Düsseldorf, Germany
[2]University of Stuttgart, 70569 Stuttgart, Germany

This chapter is based on ongoing work.

Abstract

The investigated Ag segregation induced grain boundary nanofaceting transition at an asymmetric tilt grain boundary in Cu was examined in this chapter in terms of how it influences mechanical performance and especially the plastic deformation mechanisms. Therefore, a pure Cu reference GB was characterized to match the boundary studied in previous chapters by atomically resolved STEM. In situ TEM compression and straining experiments on the pure Cu and the preferentially segregated, nanofaceted Cu(Ag) grain boundary were carried out. To confirm and complement the experimental findings, atomistic simulations were performed in collaboration with Tobias Brink. The obtained results confirmed that a GB phase transition can influence the plastic deformation behavior as the segregation induced nanofaceting transition had structural and chemical implications. Changes in GB structure and introduction of facet junctions prevented deformation twin growth in Cu(Ag), which prevails in pure Cu, and results in frequent nucleation of extended stacking faults along the boundary. Ag absorption at the symmetric $\sum 5$ (210) boundary portions inverted the sign of the resolved shear stress, which consequently opposed dislocation emission from the boundary. Thus, the grain boundary transition could be linked to change in plasticity behavior and, thus, was shown to be potentially very significant to tailor a material's properties for

load bearing applications.

Motivation

Grain boundaries in metals separate crystalline regions with different crystallographic orientations and therefore pose an obstacle to dislocation motion from one grain to its neighbor. As a consequence, polycrystals containing many grain boundaries are typically stronger than their single crystalline equivalents due to their intrinsic geometric constraints. Generally, grain boundaries are considered obstacles for dislocation motion due to two main factors and are thus increasing a material's strength compared to the single crystalline reference. On the one hand, dislocations gliding towards a grain boundary will have to work against a strain field resulting from the distorted atomic arrangement in the grain boundary core. On the other hand, as the crystallographic orientation of two neighboring grains usually differs, an incoming dislocation will have to change direction, i.e. its slip system, to be transferred from one grain to the next. However, the precise mechanisms of how dislocations and grain boundaries interact have not been clarified in detail, except for the distinct case of the Hall-Petch relation [2,3], in which dislocation pile ups are considered as one possible mechanism. Depending on a material's grain size, its grain boundary fraction varies and thus its strength should intuitively be adjusted by this parameter. Besides the impact on mechanical properties, the higher excess volume of most grain boundaries allows for faster diffusion as compared to both adjacent grains and the relatively easier accommodation of impurity atoms in comparison to inside the respective grains [43]. In summary, grain boundaries are well known to have strong influence on several different material properties at the micrometer scale, but also for bulk materials. In fact, a whole research field emerged dealing with how to modify grain boundaries inside a material to influence the material's behavior, which is referred to as grain boundary engineering [209].

In order to link structural grain boundary transitions to mechanical properties, such as plastic deformation behavior, the nucleation and emission of dislocations at and from the grain boundary has to be studied, as well as the interaction of dislocations with the interface. Mainly TEM studies revealed a wealth of mechanisms involving the interaction between dislocations and grain boundaries. Besides acting as sources [210–213] and sinks [210,213,214] for dislocations, grain boundaries were also found to transmit and even reflect dislocations [17,215–217]. Regarding dislocation transmission, Lee et al. proposed an empiric set of three conditions that could explain most experimentally observed transmission events based on geometric and shear component considerations [17,218,219]:

1. The direction of the line of intersection of the slip plane with the grain boundary of the incoming I_i and outgoing I_o dislocation - $I_i \cdot I_o$ - should be a maximum. Alternatively, the angle between both lines of intersection θ made by the slip planes and the grain boundary can be analyzed, which should be a minimum to allow for slip transmission,
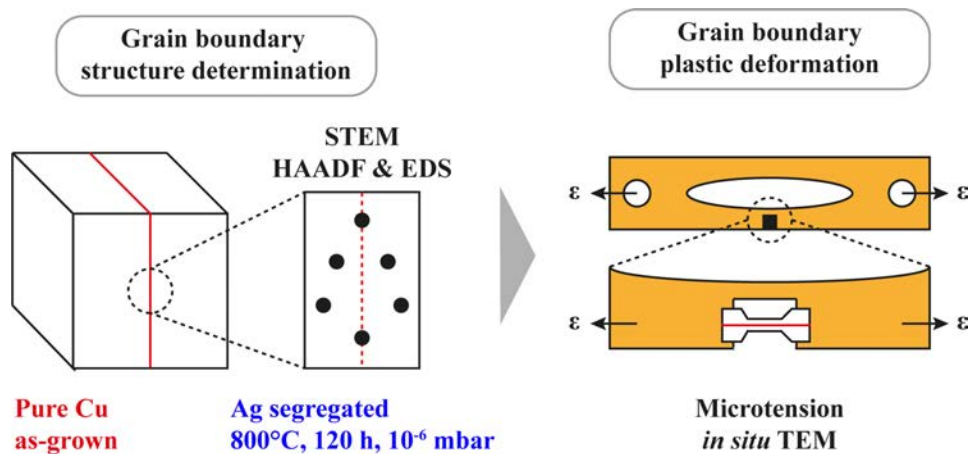
Figure 4.22: Experimental sequence to link the grain boundary structure to changes in mechanical response or plastic deformation behavior. After careful grain boundary structure characterization of the different boundary states (compare chapters 4.1 - 4.3), microcompression and microtension experiments are performed *in situ* inside the SEM and TEM.

as diffusion based climb would be necessary to overcome this barrier.

2. The relative resolved shear stress acting on the incoming and outgoing slip systems should be large.

3. The magnitude of the Burgers vector of the residual grain boundary dislocation created in the boundary as a result of the transmission process should be minimal.

In contrast, the nucleation process of dislocations from a grain boundary is a complex phenomenon. Models proposed from observations based on electron microscopy studies could explain many observations but could never unravel the underlying atomistic mechanisms. Even simulation studies could only shine limited light on the nucleation mechanisms of dislocations from a grain boundary. Therefore Kacher et al. were recently still claiming: "What constitutes a grain boundary dislocation source remains an interesting and important question" [210].

As discussed in depth in chapters 2.2.2 and 4.1 – 4.3, grain boundaries are capable of undergoing transitions changing their structural arrangement. The occurance of grain boundary transitions implies that such an interfacial transition should also have an influence on length scales above the atomic scale, possibly even affecting a material's bulk properties. Up to date, however, research efforts focused mainly on the characterization of the different grain boundary states and transitions, especially at the atomic scale [197]. Additionally, focus was put on establishing so-called grain boundary phase diagrams, to predict the existence and the type of grain boundary states depending on the thermodynamic boundary conditions [220]. Absent from literature remains the direct correlation between a grain boundary transitioning into a different (complexion) state and the influence of the transition on properties, such as

diffusion, migration or mechanical properties, although there are some indications that such transitions are responsible for abnormal grain growths and thus influence a grain boundary's ability to migrate [221]. Nevertheless, so far, the (local) atomic structure of a grain boundary and its impact on the interaction between dislocations and grain boundaries has not been correlated directly, but might lead to a better understanding of the mechanisms, how they work and how they can be used to influence a material's overall performance.

In the present study, we build on our knowledge from previous work, that identified a chemically (Ag) induced faceting transition at an asymmetric tilt grain boundary in Cu (chapters 4.1 - 4.3), by investigating the plastic deformation behavior of the same bicrystals (grain boundaries). The experimental procedure to achieve the correlation between grain boundary structure and plastic deformability is schematically shown in Figure 4.22. HAADF STEM and EDS have been used to determine grain boundary structure and chemical composition, which has been main topic of chapters 4.1, 4.2 and 4.3. In the present chapter the mechanical studies build on these results. Plastic deformation is observed using *in situ* TEM tensile testing. Our results indicate that the asymmetric Cu reference boundary deforms plastically mainly by partial dislocation emission and creation of few extended stacking faults followed by twin growth along the grain boundary. In addition, we see in Cu(Ag) bicrystals that the grain boundary faceting transition does alter the plastic deformation behavior and we were able to link it to different structural states of the boundary. The Ag-segregated, nanofaceted Cu(Ag) grain boundary part deformed via partial dislocation emission from the facet junctions, while no twin growth was observed. In contrast, the Ag-segregated symmetric $\Sigma 5$ (210) part of the grain boundary (highest Ag concentration) did not show any deformation features.

Sample Preparation

Two grain boundaries were investigated in this study. First, the asymmetric, pure Cu grain boundary served as reference grain boundary. The bicrystal grown according to chapter 3.1 was used to create a well oriented concentration profile along the grain boundary as in chapter 4.3 (compare Figure 3.1c for geometry). Characterization of the pure Cu reference boundary was achieved by preparing a TEM lamella using the FIB, as described in detail in chapter 3.3.3. The location was chosen within few tens of micrometers away of the location where mechanical testing samples were extracted, in order to determine the grain boundary as close as possible. In addition, the Ag segregation induced faceting transition was achieved with the same heat treatment as described in chapter 3.2.2 (Figure 3.2) with influences on the Cu(Ag) boundary as discussed in chapter 4.3 (Ag concentration dependent grain boundary states).
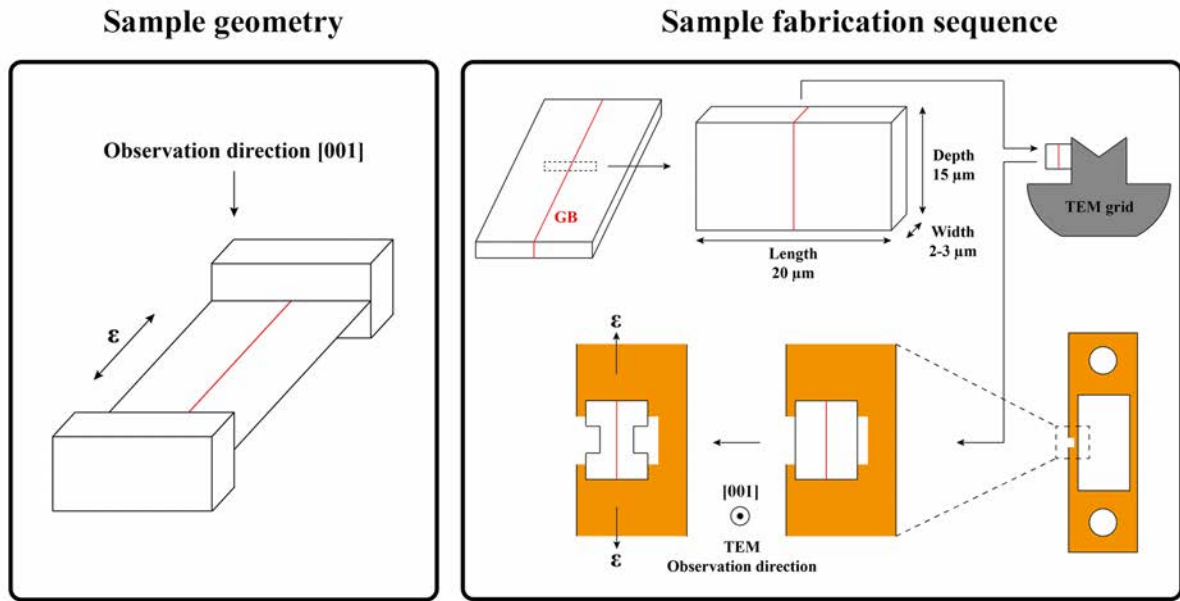
Figure 4.23: Sample geometry and FIB-based fabrication sequence of tensile testing samples. Thin film tensile test samples containing the grain boundary were fabricated for straining on a Cu-support chip in a TEM straining holder. The exact fabrication sequence is described in the text.

From the two bicrystals, i.e. the pure Cu and Cu(Ag) bicrystals, miniaturized tensile specimen were prepared. The geometry for tensile testing samples is schematically presented in Figure 4.23 along with their fabrication sequence. Note that also SEM and TEM pillar compression was performed, which are presented and discussed in the Appendix, as their results were not conclusive. For all experiments, the observation direction ([001] zone axis) was kept the same during sample preparation, as used in previous chapters, in order to be able to compare results and to ensure appropriate imaging conditions, especially important for *in situ* TEM experiments. Specimens were eroded from the grown bicrystal in the same way as for the diffusion couple approach in chapter 4.3 (see chapter 3.2.2, especially Figure 3.1c), however, actual testing samples required additional fabrication steps inside the FIB to result in tension samples (Figure 4.23).

In situ TEM tensile testing of thin, grain boundary containing foils (Figure 4.23) was performed and provided evidence, in combination with atomistic simulations, for a changing plastic deformation behavior following the chemically triggered GB phase transition described in the previous chapters. Thin films facilitate slip analysis and the tensile geometry is less prone to experimental errors like misalignment or taper, as compared to compression samples. Tensile samples were FIB prepared in a FEI Helios 600(i) FIB machine and mounted to a special support chip for the TEM Gatan straining holder. The Cu support chip had to be prepared for the experiment before usage by FIB milling a deep trench into the side of it as

electron microscopy window. The experimental fabrication procedure is schematically shown in Figure 4.23. Again, first a cross-section was prepared from the bulk bicrystal. Dimensions of the lamella were about 20 µm length, 2-3 µm width and about 15 µm depth. The lamella was transferred to a TEM grid and fixed to the side of one of the fingers. Subsequently, the TEM grid's orientation was changed from standing vertically to lying horizontally and from there the lamella detached again for transferal to the previously prepared straining holder support chip. The lamella was laid on the electron microscopy window with the grain boundary ideally aligned parallel to the long axis of the support chip, i.e. the straining direction. At this point, the lamella was thinned to a thickness of about 100 nm from the side, i.e. perpendicular to the grain boundary. To ensure plastic deformation occurring in the central portion of the lamella, the gauge section diameter was reduced to increase stresses in this area. Finally, the lamella was ion showered at 5 kV and carefully annealed at 500°C for 45 minutes to reduce FIB damage. The support chip was fixed to the straining holder by screws and pulled in a direction parallel to the grain boundary. However, it is likely that slight torque might act on the lamella. Nevertheless, the influence should be minimal resulting in an almost perfect uniaxial stress state inside the strained lamella.

Atomistic simulations

In order to confirm the experimental results and to learn more about different grain boundary properties and how the bicrystals containing the different grain boundaries deform plastically, atomistic simulations were performed in close collaboration by Tobias Brink (Max-Planck Institut für Eisenforschung GmbH). In particular, molecular dynamics (MD) simulations were used with the embedded atom method [222] and the Cu(Ag) potential developed by Williams et al. [174]. Two crystals were oriented following the previous STEM characterization to form the different grain boundaries of interest. For example, the pure Cu reference grain boundary was formed in a way that the crystals' {410} and {110} planes face each other, respectively, and were then brought into contact. Equilibration was performed at 300 K for times ranging from 100 ps to 1 ns, depending on the grain boundary plane. Simulation cell dimensions were generally 35 x 20 x 10 nm^3 containing 400.000 to 500.000 atoms (see e.g. Figure 4.26), except for special cases that will be mentioned explicitly. The nanofaceted Cu(Ag) boundary was constructed as described above, however, knowing from experiment that the different facet segments are preferentially segregated, all Cu atoms at the CSL positions in the symmetric Σ5 (210) GB's kite structure were substituted for Ag atoms. The facet junctions were constructed without Burgers vector containing defects, but by aligning CSL lattice sites properly with the facet junctions. Different boundary conditions were used for the different simulation types. The shear stress state of the boundary at 0 K and the twin growths

simulations were performed using periodic boundary conditions in pulling direction. To pull on the simulation cell, the cell was scaled in pulling direction. The Poisson ratios of the two crystals were adjusted to avoid necking during deformation, which has shown to introduce artifacts. All simulated tensile deformations used a constant engineering strain rate of 10^7 s^{-1}. For the resolved shear stress component maps, the simulation cell was considerably larger than described above to avoid influences from strain fields interacting with the simulation cell boundaries, i.e. 160 x 90 x 4 nm^3, and the cells were strained in tensile direction by about 1 % within the elastic regime. For the twin growth simulations, the cells were notched in the central part of the open surface of the stiffer grain µ, to emit partial dislocations towards and across the grain boundary (around 2 % tensile strain). After transmission of one or two partial dislocations, the notch was closed artificially by unloading the cell, introduction of few "filling atoms" and relaxation, before the cell was strained back to the stress state reached before. Finally, further tensile straining (to about 6 %) lead to distinct partial dislocation behaviors for the different grain boundaries, i.e. twin growth or dense stacking fault creation. To study dislocation emission from the grain boundary, large simulation cells, as used for the stress maps, were used to avoid nucleation events from the surfaces or the surface-grain boundary areas. The crystal structures as well as defects were identified using common neighbor analysis with an adaptive cutoff [223, 224], while dislocations were identified using the dislocation extraction algorithm (DXA), both as implemented in Ovito [225].

Results

1. Grain boundary characterization

The pure Cu reference grain boundary was characterized via STEM, only being separated by few tens of micrometers from the location for mechanical testing. The prepared sample was investigated at different magnifications and does reveal a straight grain boundary down to the near atomic level (Figure 4.24a - 4.24c). To distinguish the two constituent grains of the bicrystal, the left grain in Figure 4.24a is referred to as grain µ, while the right grain is referred to as grain λ, as highlighted in the HAADF STEM micrograph in Figure 4.24a. Grains with these crystallographic orientations are consistently referred to following this definition in the following experimental and simulation results. Highlighting the {200} planes in the atomically resolved micrograph (Figure 4.24c) visualizes the asymmetric nature of the grain boundary. The boundary plane and approximate compression/tensile directions (indicated by arrows in Figure 4.24c) of the respective grains were determined using the Fast Fourier transform (Figure 4.24d) of the atomically resolved micrograph in Figure 4.24c. The grain boundary (white dashed line describes the grain boundary normal) was determined

Table 4.1: Deformation-related GB parameters derived experimentally describing the elastic and plastic response of the bicrystal's constituent grains μ and λ.

	Young's modulus (GPa)	Schmid factor (full dislocations)	Schmid factor (partial dislocations)	
			leading	trailing
Grain λ	81	0.485	0.47	0.38
Grain μ	122.5	0.45	0.47	0.31

to be close (± 4°) to a 54°[001](110)/(920) boundary with an asymmetric inclination of 31° away from the symmetric Σ5[001](210) boundary, as determined in the previous chapters as well. The tension directions were found to be close to <430> (yellow, Grain μ) and <310> (green, Grain λ). Both orientations were plotted on an inverse pole figure with the Young's modulus E ranging from 66.7 GPa for [001] to 191.1 GPa for [111] in steps of 10 GPa and the Schmid factor m of the primary slip system (full dislocations, $\vec{b} = \frac{1}{2}\langle 110 \rangle$) ranging from 0.27 at the outer [111] pole to 0.5 at the central [123] orientation in steps of 0.02 overlayed as grey scale and blue contour lines, respectively, to capture the anisotropy of Cu in terms of mechanical properties (Figure 4.24e) and how it relates to the present orientations. The inverse pole figure reveals that the two tensile orientations introduce a relatively strong anisotropy in terms of elasticity to the bicrystalline system ($\Delta E \simeq 40$ GPa) and just a minor plastic incompatibility ($\Delta m \simeq 0.02$). In contrast to the minor difference in Schmid factor for full dislocations, there is a considerable difference between the maximum Schmid factors for leading and trailing partial dislocations of type $\vec{b} = \frac{1}{6}\langle 112 \rangle$ ($\Delta m \simeq 0.13$), while the Schmid factor of the leading partial is close to the Schmid factor of full dislocations. Exact values are given in Table 4.1 for the two grains, respectively.

To study the influence of Ag on the grain boundary to relate it to plastic deformation mechanisms, the boundary had to be decorated with Ag through a segregation heat treatment. This Ag segregated boundary was analyzed and discussed in detail in the previous chapters 4.1 to 4.3 and [57,94]. To give a brief summary here (Figure 4.25), the grain boundary on a macroscopic scale curved away from the straight reference orientation towards a symmetric Σ5 (210) grain boundary in direction of increasing Ag excess (and bulk) concentration (chapter 4.3). Grains μ and λ are highlighted in Figure 4.25a, respectively. The curvature is caused by a segregation induced nanofaceting transition of the asymmetric reference boundary, in which the original grain boundary plane is abandoned and preferentially segregated facets formed with Ag-rich symmetric Σ5 (210) segments and newly formed, Ag-lean, asymmetric {230}/{100} segments (chapter 4.1 and [94]). While the length of the symmetric segment was dependent on Ag concentration, the asymmetric segment remained constant in length acting as kinetic barrier and resulting in the overall grain boundary curvature (chapter 4.3). As a consequence, the boundary is found to adopt three states along the Ag concentration
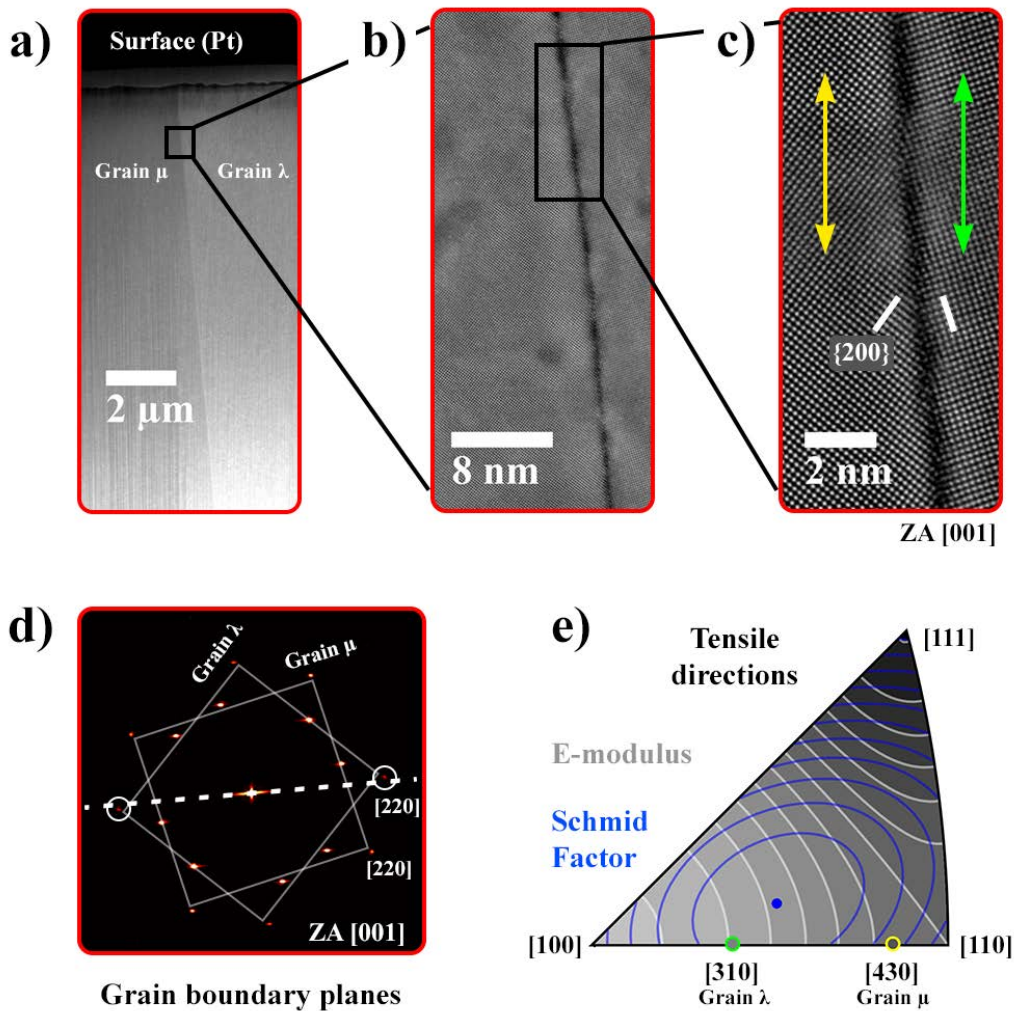
Figure 4.24: Reference boundary characterization for mechanical testing regarding grain boundary structure. The bicrystal showed a straight grain boundary from the surface into the bulk at increasing magnification (a) - (c). The highest magnification at atomic resolution (c) contains arrows indicating the compression and tension directions for mechanical testing and white lines indicating {200} planes of the respective grains to highlight the asymmetry. The Fast Fourier transform of (c) is presented in (d), where reflections from both grains were outlined. The straining directions plotted on an inverse pole figure are shown in (e), along with contour lines of the Young's modulus (grey) and the Schmid factor of the primary slip system (blue) being overlayed. The former ranges from 66.7 GPa for [001] to 191.1 GPa for [111] in steps of 10 GPa, while the latter ranges from 0.27 at the outer [111] pole to 0.5 at the central [123] orientation in steps of 0.02.

gradient from bulk (low Ag content) towards the surface (high Ag content): (i) the segregated asymmetric (reference) grain boundary (Figure 4.25b) that undergoes a first order transition into (ii) the preferentially segregated nanofaceted state (Figure 4.25c) of which the Ag-rich segment grows into (iii) a continuous symmetric $\Sigma 5$ (210) grain boundary (Figure 4.25d).

Grain boundary parameters such as the GB stress are much harder to access experimentally as compared to the grain boundary structure, however, atomistic simulations provide a suitable tool to obtain such information. Two basic simulation cells were used in the present study (Figure 4.26), one containing the pure and straight Cu reference {710}/{110} boundary (Figure 4.26a), the other containing the preferentially segregated, nanofaceted Cu(Ag) boundary (Figure 4.26b). The asymmetric segment has a boundary plane close to {210}/{510}, while the Ag containing segment is a symmetric $\Sigma 5$ (210) boundary. Grains μ and λ are highlighted, respectively. The structure of the pure Cu reference boundary and the grain boundary plane orientations match the experimentally obtained ones well. The inset of Figure 4.26a shows a zoomed-in view of the structure containing a recurring motif resembling a triangle or an inclined single kite motif (highlighted in a black circle). Comparison e.g. with Figure 2.4c confirms a good agreement of the grain boundary structure between simulation and experiment. In case of the nanofaceted grain boundary, facet segment lengths of around 2 nm were constructed in good agreement with experiment. While the symmetric $\Sigma 5$ (210) boundary shows the well-known and accepted kite structure, as also seen in STEM micrographs (chapter 4.1, 4.2 and 4.3, as well as Figure 4.25d), the asymmetric segment deviates slightly from the experimental boundary to keep the overall GB horizontal in the simulation cell. In fact, the asymmetric segment is inclined about 2° more towards Grain μ, however, it still remains asymmetric and the slight deviation is expected to have a minor influence on the outcome of further simulations.

From the MD simulations, the Young's modulus and the Schmid factors for the different dislocation types can be obtained for the two constituent grains. The actual values are presented in Table 4.2. All of the Schmid factors match within about 0.5 to 3 % the experimentally determined values, while the Young's modulus matches within 4 to 8 % of the experimental values (compare with Table 4.1). Nevertheless, the elastic and plastic deformation anisotropy (regarding full and leading partial dislocations) - the main features - are captured well. The elastic anisotropy between both grains is large (ΔE 40-50 GPa), while the plastic deformation anisotropy is small regarding Schmid factor differences between full and leading partial dislocations ($\Delta < 0.02$), but also between the respective grains for these dislocation structures (Δfull < 0.05, Δleading < 0.005). However, the plastic deformation anisotropy regarding the differences between leading and trailing partial dislocations (Δ $0.09 - 0.17$) as well as for the trailing partial dislocations in the two neighboring grains (Δ 0.08) remains considerably high.
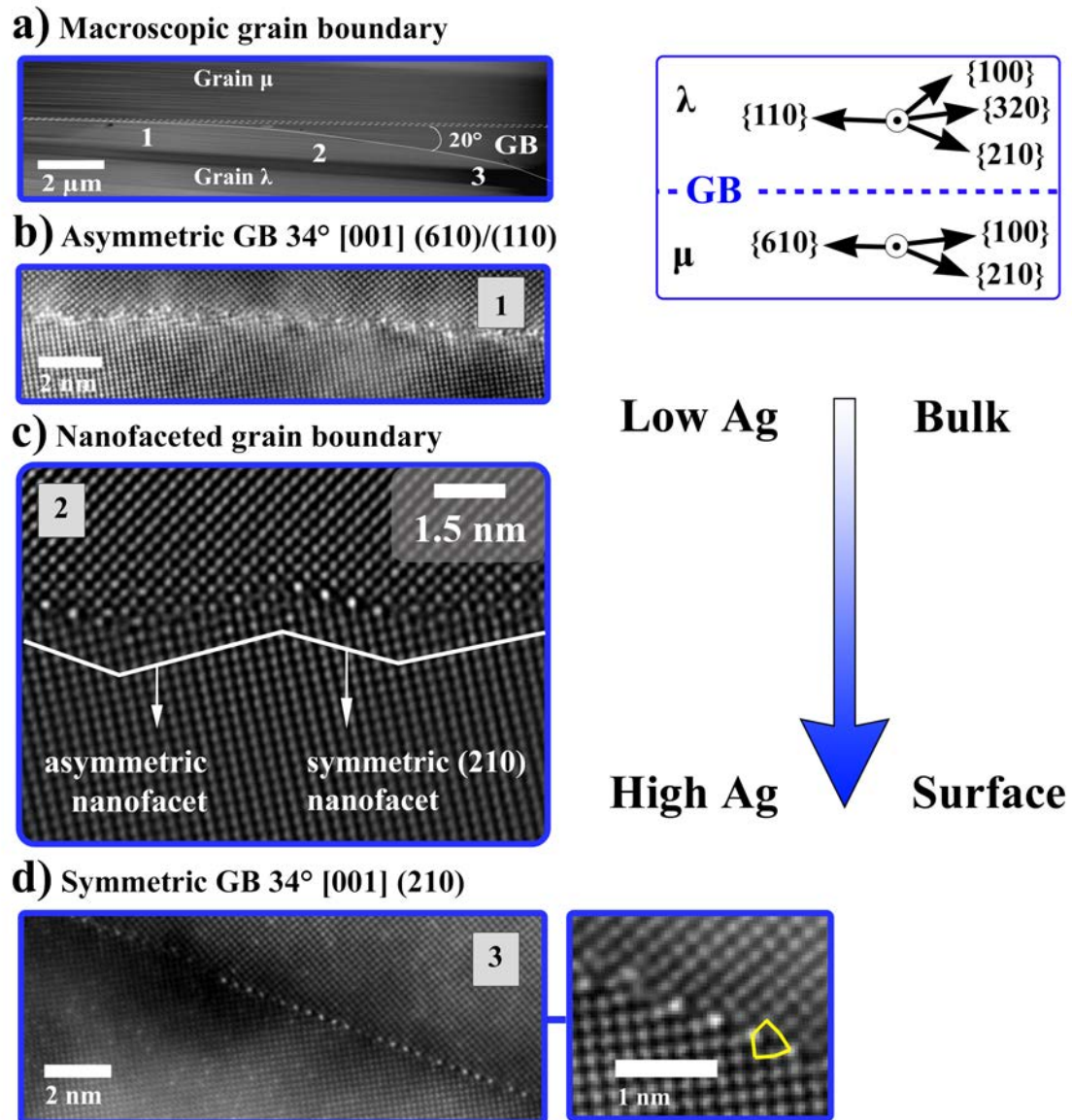
127

Figure 4.25: Characterization of the Cu(Ag) segregated grain boundary at different depth by HAADF STEM. The overall grain boundary curved away from its straight reference state upon segregation (a). Inside the bulk, at low Ag contents, the boundary structure and plane were close to the reference boundary (b), while it transitioned into a preferentially segregated nanofaceted state (c) and finally evolved into a completely segregated, perfectly symmetric $\Sigma5$ (210) boundary (d). All high-resolution micrographs were captured in [001] zone axis orientation. (a), (b) and (d) were adopted from chapter 4.3, while (c) was adopted from chapter 4.1 [94].
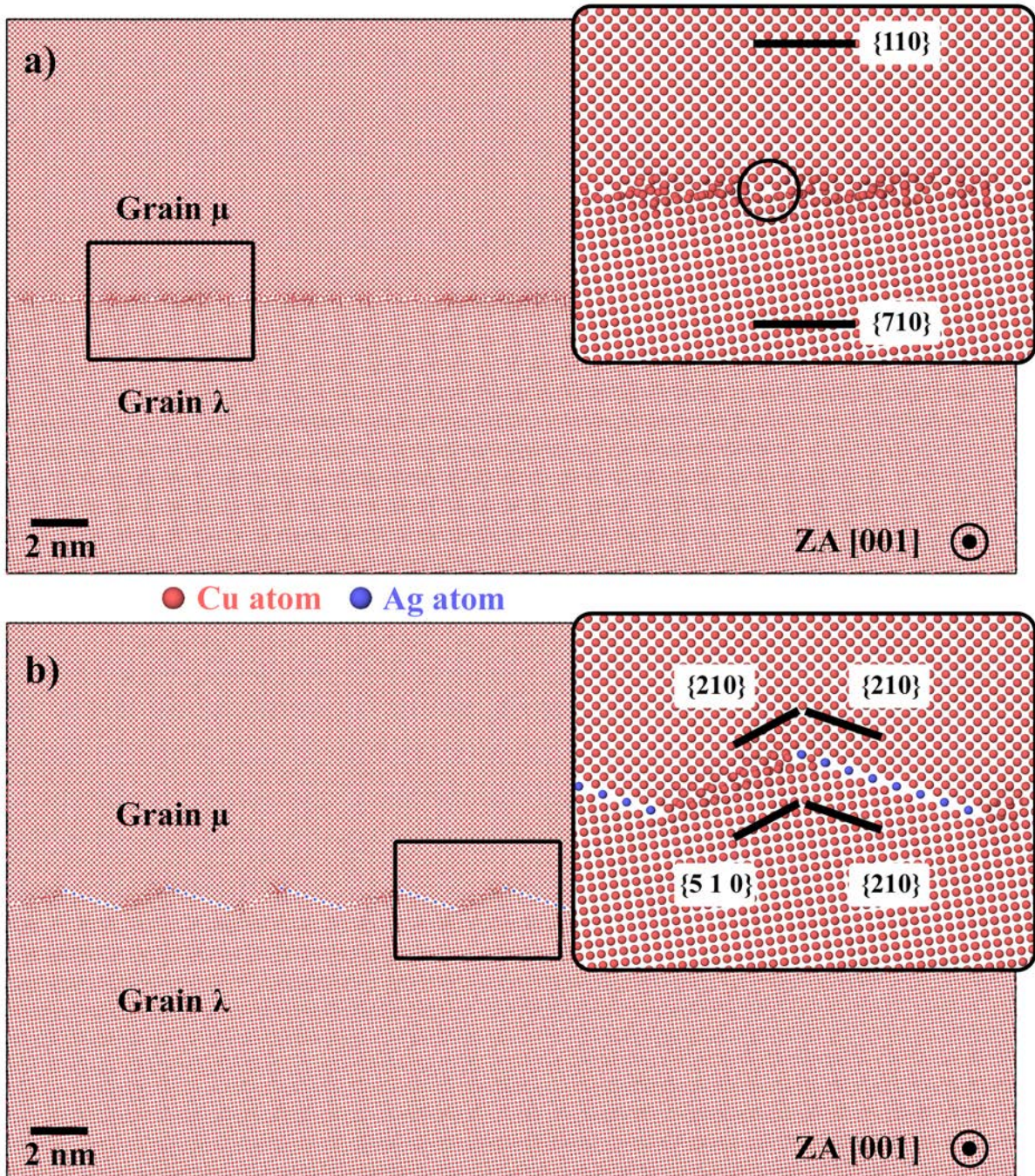
Figure 4.26: General MD simulation cells for calculation of thermodynamic grain boundary excess parameters in Table 4.3. All simulation cells contained different grain boundaries, as close as possible to the experimentally determined boundaries characterized in chapters 4.1 - 4.3 and in Figures 4.24 and 4.25. The pure Cu, asymmetric grain boundary {710}/{110} is presented in (a), while the preferentially segregated, nanofaceted Cu(Ag) boundary is shown in (b). The asymmetric segment has a boundary plane close to {510}/{210}, while the Ag containing segment is a symmetric Σ5 (210). Cu atoms in red color, Ag atoms in blue color. Note that removal of Ag from the faceted boundary in (b) results in defaceting.

Table 4.2: Deformation-related GB parameters derived from MD simulations describing the elastic and plastic response of the bicrystal's constituent grains μ and λ.

	Young's modulus (GPa)	Schmid factor (full dislocations)	Schmid factor (partial dislocations)	
			leading	trailing
Grain λ	74	0.490	0.471	0.378
Grain μ	128	0.443	0.467	0.299

In addition to the parameters relevant for deformation, the atomistic simulations allow for calculation of even more (thermodynamic) parameters, such as the grain boundary potential energy γ_{GB}, the excess grain boundary volume ΔV and the grain boundary stress tensor components τ_{ii} (as described by T. Frolov and Y. Mishin in [97, 226]). In the present study, τ_{11} and τ_{22} are referring to the in-plane stress components parallel and perpendicular to the tilt axis, respectively. The calculations of these parameters are performed for the different relevant grain boundary types studied here individually, and in addition for the pure Cu, symmetric $\Sigma 5$ (210) grain boundary (symmetric facet segment with Ag atoms removed), as reference to validate our methodological approach. Note that Ag induces the nanofaceting transition of the reference GB and consequently removal of these Ag atoms to create a pure faceted GB results in defaceting, what we also observe in our simulations. The exact, calculated values are given in Table 4.3. Note that all presented values are calculated at 0 K without externally applied tensile stress (undeformed). In fact, the calculated reference GB parameters are reproducing Frolov and Mishin's values identically [64]. The introduction of Ag into that symmetric $\Sigma 5$ (210) grain boundary causes some significant changes to the thermodynamic parameters, i.e. the excess volume is doubled, while τ_{22} almost vanishes, leaving the boundary under tensile stress in only one direction τ_{11}. This τ_{11} component is just slightly affected by the incorporation of Ag. Regarding the asymmetric (pure Cu) grain boundary and asymmetric (pure Cu) facet segment, calculation of the stress tensor components is not straight forward due to their complex structure and no clearly repeatable unit cell for periodic boundary conditions. Therefore, periodic boundary conditions with asymmetric grain boundary inclinations in the $\Sigma 5$ misorientation system were chosen as close as possible to the experimentally determined boundary for the GB stress calculations (Figure 4.26) based on [55]. Instead of the as-grown {410}/{110} straight Cu reference grain boundary before the nanofaceting transition, the closest boundary used for calculating the grain boundary stresses was the {710}/{110} grain boundary. Regarding the Ag-free, asymmetric {510}/{210} facet segment of the nanofaceted boundary, the {430}/{100} grain boundary was used, which is actually a little closer to the experimentally determined {230}/{100} (all thermodynamic GB parameters calculated with these boundaries are marked with [*] and [$] in Table 4.3, respectively). In comparison to the GB stresses of the symmetric boundaries,

Table 4.3: Thermodynamic excess parameters for different GBs required in this chapter. The parameters involved the GB potential energy γ_{GB}, the excess GB volume ΔV, the GB stress components parallel and perpendicular to the tilt axis τ_{ii} and the resolved shear stresses acting on the slip planes of the primary slip systems of the two constituent grains τ_{RSS-i} after rotating the GB stress tensor accordingly.

Properties	Type	symm. (210) pure Cu	symm. (210) Cu(Ag)	asymm. GB {410}/{110}	asymm. facet {210}/{510}
$\gamma_{GB} (J/m^2)$		0.95	1.55	0.98	0.97
ΔV (Å)		0.32	0.66	0.33	0.33
$\tau_{11}(J/m^2)$		1.17	0.97	0.48[*]	0.74[$]
$\tau_{22}(J/m^2)$		1.49	0.09	0.46[*]	0.77[$]
$\tau_{RSS-\mu}(J/m^2)$		0.08	-0.42	-0.01[*]	-0.01[$]
$\tau_{RSS-\lambda}(J/m^2)$		0.36	-0.19	0.11[*]	0.15[$]

[*]calculated for the closest asymmetric GB with a periodic unit cell: {710}/{110} GB plane (Figure 4.26)

[$]calculated for the closest asymmetric GB with a periodic unit cell: {430}/{100} GB plane

the asymmetric boundaries reveal rather isotropic GB stresses ($\tau_{11} \simeq \tau_{22}$) than anisotropic ones. Nevertheless, the GB core of all these boundaries appears to be under tension (τ_{11} & $\tau_{22} > 0$) [97]. As a planar grain boundary only has two components τ_{11} and τ_{22}, these describe the complete stress tensor of the boundary. Rotation of the stress tensor to match the orientation of the constituent grains' orientation yields the resolved shear stress acting on the respective slip planes of the primary slip systems τ_{RSS-i}. There are three cases for this resolved shear stress (RSS), namely being negative (acting against dislocation motion), being zero (no influence on dislocations) and positive (supporting dislocation motion). In the particular case of the investigated boundaries and tension directions here (Table 4.3), the resolved shear stresses τ_{RSS-i} are all reduced compared to the respective intrinsic GB stresses τ_{ii} to just slightly above zero. Exceptional is the case for the symmetric $\Sigma 5$ (210) grain boundary. The resolved shear stresses for that boundary drop below zero for both grains upon Ag addition, thereby acting against dislocation motion in both grains for the given tensile orientations. This demonstrates the significant chemical influence of Ag segregation on the acting resolved shear stress changing from supporting dislocation motion to counteracting dislocation activity.

To visualize the stress state evolution of the different GB's during deformation (stresses in Table 4.3 are calculated without deformation), large simulation cells were elastically strained to 1 % and the shear stress component acting on the slip plane of Grain μ is plotted as two dimensional maps for the different boundaries (Figure 4.27), i.e. the asymmetric, initial Cu grain boundary before the faceting transition occurred (Figure 4.27a), the nanofaceted GB with Ag-free asymmetric segments and Ag-rich symmetric $\Sigma 5$ (210) segments (Figure 4.27b), as well as the nanofaceted GB with the same structural arrangement but without containing Ag (Figure 4.27c) acting as reference boundary to study the effect of Ag on the

symmetric segment. All asymmetric segments, no matter whether the straight Cu reference or the inclined Ag-free facet segments, behave similarly by locally adopting areas of different shear stress components acting along with the external stress field (positive shear stress) or against it (negative shear stress). This matches the average value close to zero (-0.01) provided in Table 4.3. Contrary to the asymmetric boundaries, the symmetric facet segment behaves in distinct ways depending on its composition. For the pure Cu case (Figure 4.27c), a white line appears at the GB core along the facet segment, indicating that the shear stress component continuously vanishes at this point, which is reflected by an average RSS close to zero (0.08) provided in Table 4.3. Note that this boundary is not stable without Ag, which induces the faceting. This effect is even magnified when Ag is introduced, as the resolved shear stress turns negative (blue) in this case (average RSS of -0.42 in Table 4.3). In addition to the stress states of the facet segments, the junctions were found to cause a stress field as well, extending into the neighboring grains as e.g. highlighted in Figure 4.27b (black circle).

2. Deformation results from experiment and simulations

In situ TEM tensile tests of bicrystals containing the pure Cu tilt grain boundary were used to obtain information of their plastic deformation behavior. Close to dogbone shaped samples were fabricated to electron transparency containing the grain boundary aligned almost parallel to the tensile direction as shown schematically in Figure 4.28a along with the real sample in Figure 4.28b. Deformation of the bicrystalline sample revealed several features. A few plastic deformation bands formed during straining at a density of 0.76 μm^{-1}, initially about 141 ± 24 nm wide in projection (compare top band in Figure 4.28c). Correcting for the projection, the actual length of the inclined deformation bands slightly increases to about 174 nm on average. However, quickly one band became the major carrier of plastic deformation growing in width to about 700 - 800 nm (compare lower band in Figure 4.28c). Inspection of the transition from plastically unaffected areas to within the large deformation feature not only revealed the change in grain boundary direction, but also a width reduction of the grain boundary (Figure 4.28d), which is either a sign of thickness reduction of the sample or an inclination change of the boundary. In contrast, inspection of the small deformation band, which typically exhibits sharp boundaries in the grains and no directional change of the contained grain boundary segment, reveals that the deformation band is a feature running on an inclined plane, almost perfectly matching at the grain boundary (Figure 4.28e). Overlaying the directions of these defined bands on an atomically resolved HAADF STEM micrograph of the grain boundary, reveals a perfect match with the <110> directions of the two grains (Figure 4.28f). Finally, the *in situ* video footage showed that such features appear to be emitted from the grain boundary into the grains exhibiting stacking fault contrast (Figure
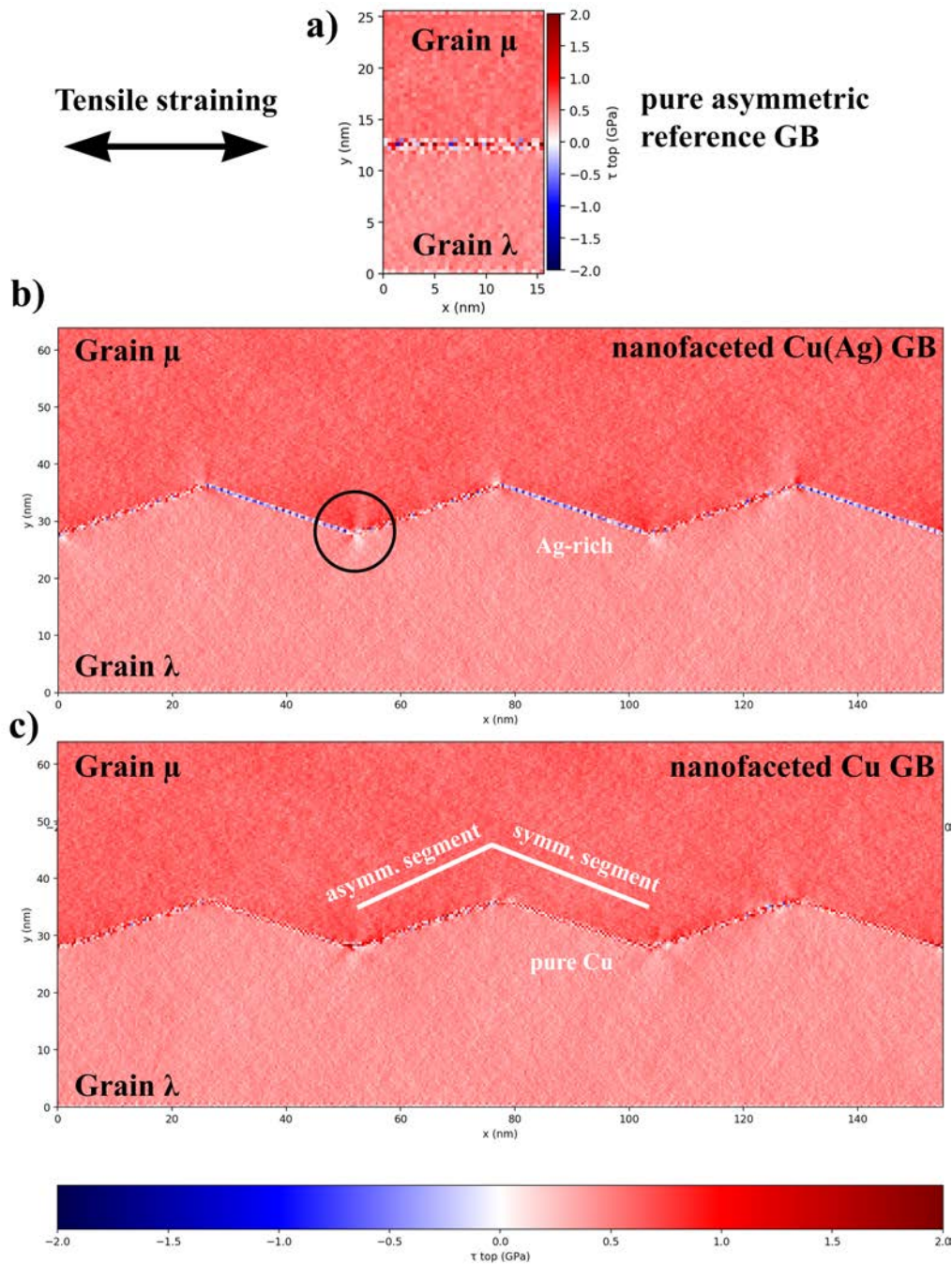
Figure 4.27: Visualization of the resolved shear stress acting on slip plane of grain μ for an elastic tensile deformation of 1%. Analyzed were the pure Cu reference GB before the nanofaceting transition (a), the nanofaceted Cu(Ag) (b) and, in order to study the influence of Ag, the nanofaceted GB with all Ag atoms being substituted with Cu atoms, although this configuration is not stable (c).
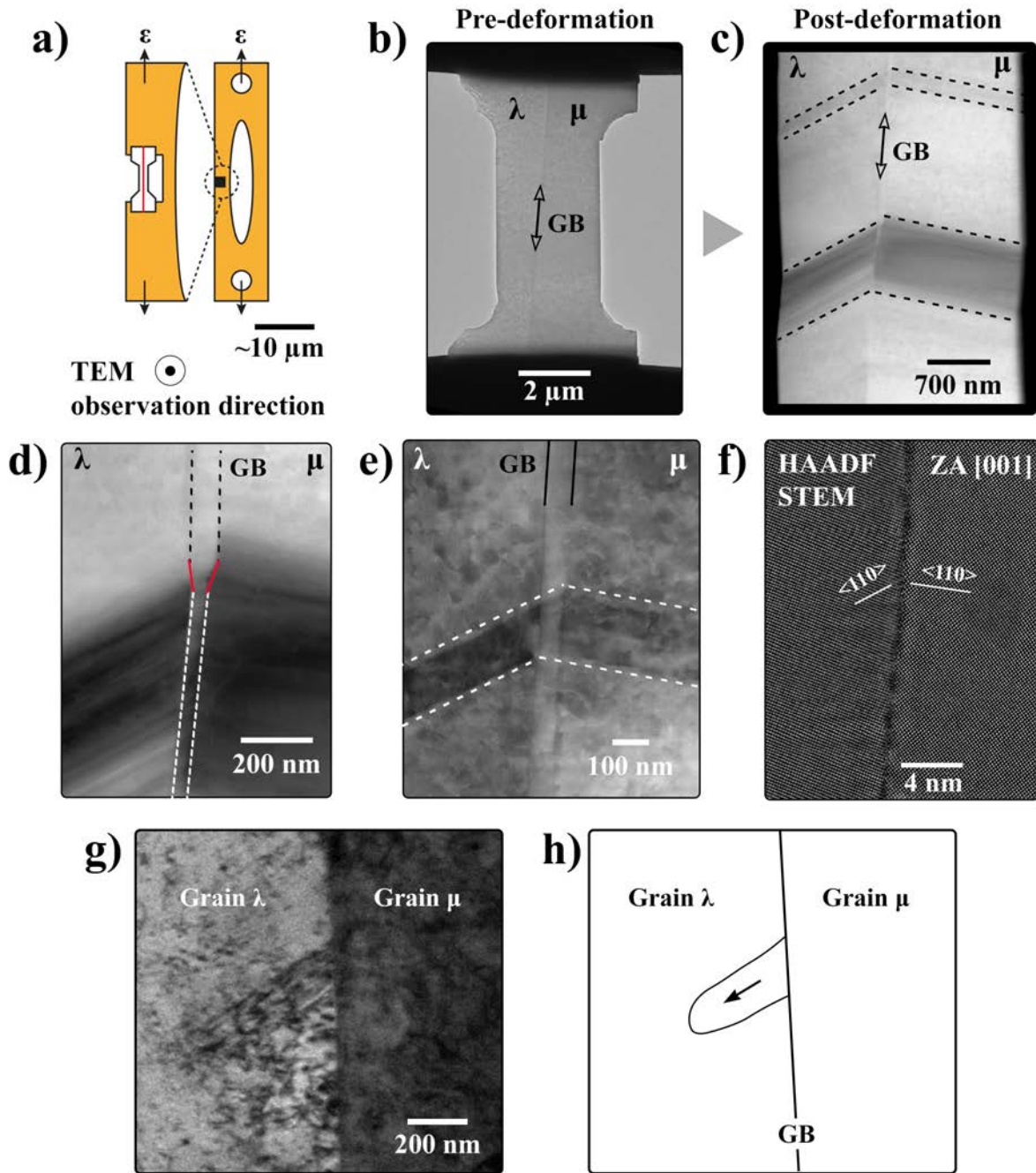
Figure 4.28: *In situ* TEM tensile test results of the pure Cu grain boundary. The overall schematic sample arrangement (a) is shown along with a bright field TEM image of an actual tensile sample containing the grain boundary (b). Upon deformation, bands of varying width formed along the sample imaged here using HAADF STEM (c). Closer inspection by HAADF STEM revealed a reduced grain boundary width inside these deformation bands (d) and that these bands run on inclined and defined crystallographic planes through the sample (e). The formation of these bands is following the <110> type direction as can be seen in the atomically resolved HAADF STEM image of the boundary (f). From the video footage of the *in situ* TEM (bright field) experiment (g), the direction of the emission can be determined, which is schematically provided in (h). Grains λ and μ are highlighted. Emission occurs into grain λ, which is the less stiff grain.

4.28g), which is schematically visualized in Figure 4.28h. However, it remains unclear if this event is a true emission event or if it is caused by dislocation activity in the neighboring grain, and thus would be described rather as a transmission phenomenon.

It remains to be clarified, what exactly the plastic deformation feature is that forms during straining in Figure 4.28. Therefore, we performed selected area electron diffraction outside and inside of such a band (Figure 4.29a). Outside the deformation zone it was possible to tilt into a [114] zone axis (ZA) orientation (Figure 4.29b), while these tilting conditions ensured a [011] ZA orientation inside the deformation feature (Figure 4.29c). Overlaying these two diffraction patterns reveals a perfect alignment of the [114] ZA reflections with the {113} and {200} reflections of the [011] ZA. Thanks to Michael Herbig (Max-Planck-Institut für Eisenforschung GmbH) using the TOCA software [227, 228], we were able to plot the {111} poles of both these ZA orientations into a stereographic projection (Figure 4.29e), revealing one shared set of planes. Plotting the grain boundary plane (orange) and grain boundary normal (green) into the stereographic projection, oriented as in the dark field TEM image (Figure 4.29a), identifies the shared {111} planes to be the boundary planes. It also clarifies that the boundary plane is 54° inclined with respect to the viewing direction. Rotation of the {111} poles accordingly visualizes nicely the mirror symmetry at the boundary plane and thus, we were able to identify the boundaries of the deformation bands to be symmetric (coherent) $\Sigma 3$ 60° (111) twin boundaries, thereby creating an inclined stacking fault in between these boundaries, which is responsible for the different contrast in HAADF STEM micrographs (compare Figure 4.30).

The Cu(Ag) bicrystal was plastically deformed *in situ* inside the TEM in the same fashion as the pure Cu bicrystal (described above) to have a consistent comparison, in order to link differences in plastic deformation behavior to the chemically induced nanofaceting transition. Grains λ and μ are highlighted for reference. A comparison of both outcomes is presented for the pure Cu bicrystal (Figure 4.30a), as already discussed above, and for the Ag segregated Cu(Ag) bicrystal in Figure 4.30b, both being HAADF STEM micrographs. For the Cu(Ag) case, two distinct regions were observed along the grain boundary (Figure 4.30b). Region 1 was free of plastic deformation events and close to the sample surface with highest Ag concentration, while in region 2 the same plastic deformation structures were observed as for the pure Cu reference, however, the density was much higher (2.27 μm^{-1}) and no major growing band structure could be observed. The width of these features in the Cu(Ag) case was measured to be 135 ± 13 nm (about 167 nm on average after projection correction), very close to the measured width of the small structures of the pure Cu sample. Luckily, few of these stacking faults were emitted from the grain boundary, terminated inside a grain and could therefore be examined in more detail, for example the highlighted feature in Figure 4.30b. This exact same feature is observed under different tilting conditions (Figure 4.30c
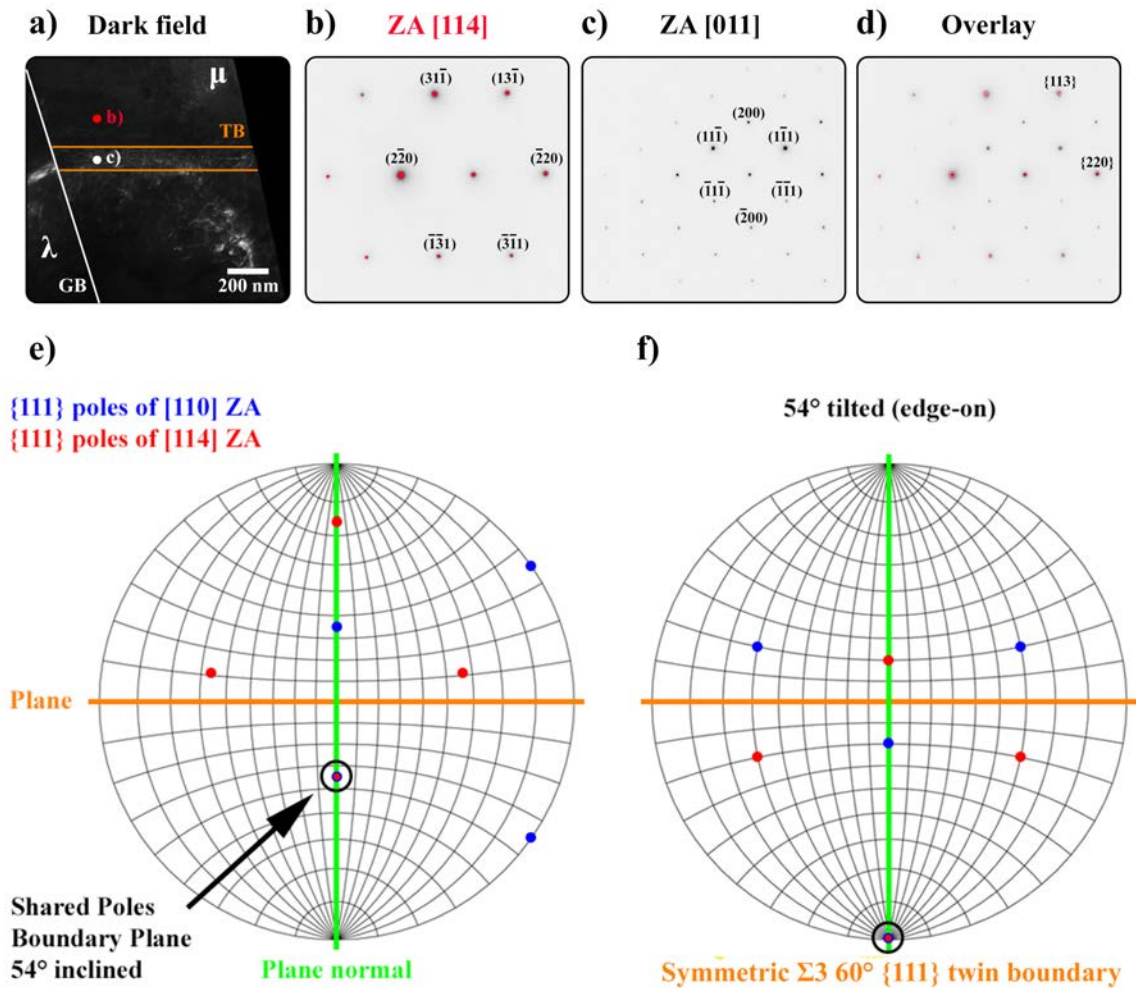
Figure 4.29: Identification of plastic deformation band as symmetric Σ3 twin. Dark field TEM images were obtained to identify the deformation band (a) and perform selected area electron diffraction at distinct locations inside and outside of the deformation structure. Grains λ and μ are highlighted in (a). While outside the band it could be tilted into a [114] ZA orientation (b), inside the band, a [011] zone axis emerged for these tilting conditions (c). An overlay of both diffraction patterns revealed full coherence of the {113} and {200} planes (d) and plotting the {111} poles of the respective orientations into the stereographic projection showed that the boundary plane shares a common {111} pole (e). Finally, it was discovered that the feature is inclined by 54°. Rotation of the poles revealed the mirror symmetry across the grain boundary plane and as conclusion the deformation bands could be identified as stacking fault areas, which are terminated by symmetric (coherent) Σ3 {111} twin boundaries.
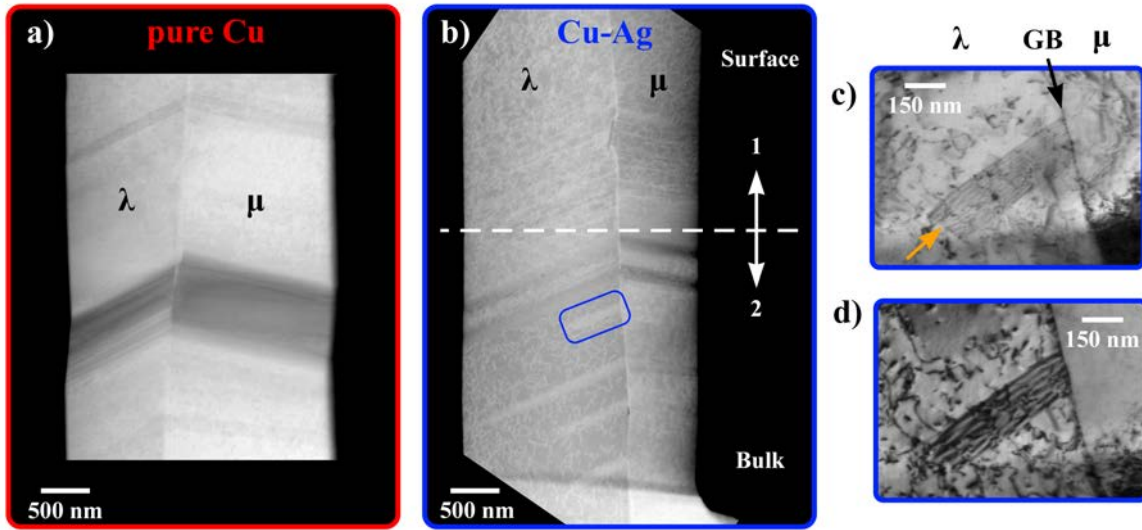
Figure 4.30: Comparison of plastic deformation behavior between the pure and Ag segregated grain boundary. The plastic deformation outcome of the pure Cu grain boundary, as in Figure 4.28, is shown for reference (a). The segregated Cu(Ag) grain boundary post tension revealed two distinct regions 1 (close to the surface) and 2 (towards the bulk), with no and frequent plastic deformation events occurring, respectively (b). One deformation feature that did not extend completely through the bicrystal has been observed in two different tilting conditions to reveal information about dislocation contents in both grains (c) and (d). While these two micrographs are bright field TEM images, (a) and (b) are HAADF STEM images. Grains λ and μ are highlighted.

and 4.30d). The feature always exhibits a typical stacking fault contrast (stripes) and is terminated by a leading partial dislocation line inside the grain (arrow in Figure 4.30c). In addition, the different tilting conditions lead to improved visibility of the dislocation arrangement in the neighboring grain and support that these stacking faults are emitted from the boundary itself without being the result of a pile up in the neighboring grain. Yet dislocation transmission across the boundary cannot be excluded generally.

Different deformation patterns were observed for the straight Cu reference grain boundary and the preferentially segregated, nanofaceted Cu(Ag) grain boundary (Figure 4.30). To comprehend more the deformation behavior of the two boundaries, tensile deformation was performed on large simulation cells containing previously introduced stacking faults (Figure 4.31). The asymmetric, pure Cu grain boundary as well as the nanofaceted, preferentially segregated grain boundary deformed in excellent agreement with the experiments described above. De facto, the pure Cu grain boundary (Figure 4.31a) emitted only few partial dislocations (density of 0.06 nm^{-1}) creating only few stacking faults (red). However, further deformation was accomplished by formation of a wide twin (green) along the grain boundary (grey) and extending across the boundary. Opposed to this deformation behavior, the nanofaceted Cu(Ag) grain boundary (Figure 4.31b) does emit a multitude of stacking faults (density of 0.22 nm^{-1}), which are hardly growing in size (forming wide twins). Summarized,
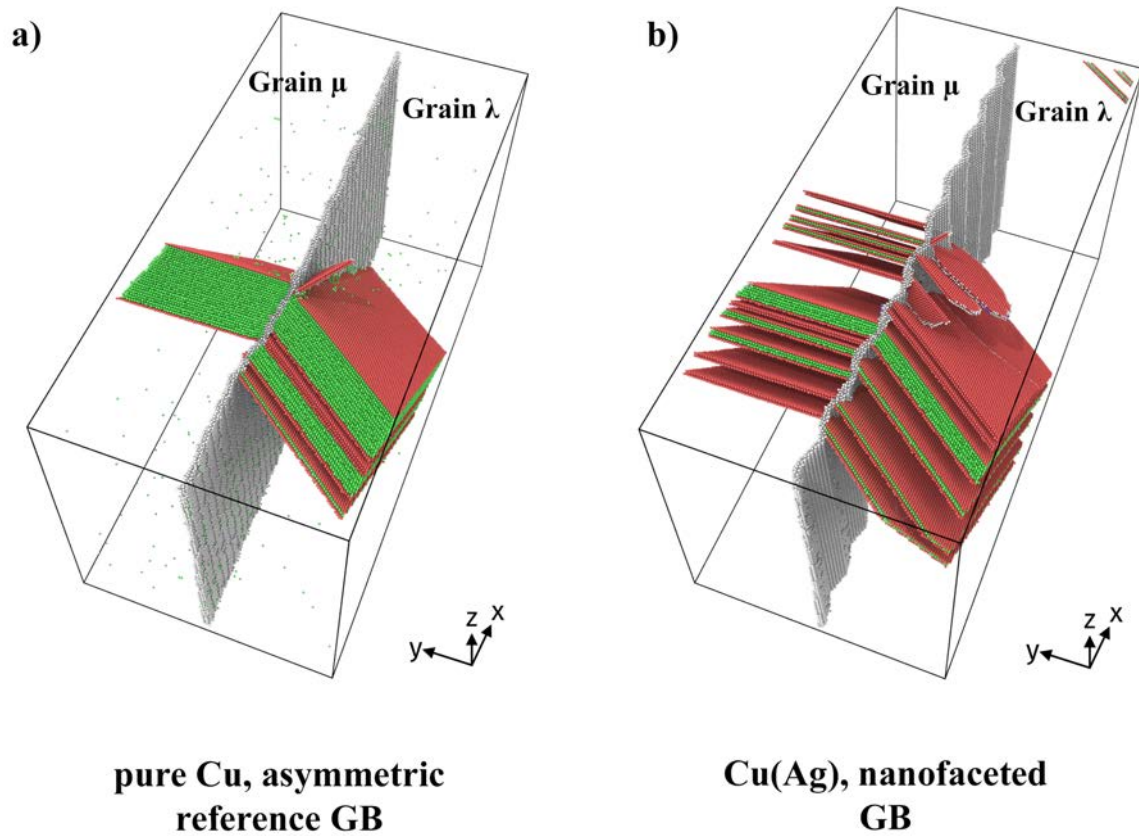
Figure 4.31: Deformation differences obtained by MD simulations for the asymmetric, pure Cu reference GB (a) and the preferentially segregated, nanofaceted Cu(Ag) grain boundary (b) at about 6 % total tensile strain in x-direction. While for the asymmetric, pure Cu boundary few stacking faults are emitted before twin growth, the nanofaceted Cu(Ag) boundary reveals a high density of stacking faults being emitted without pronounced twin growth. Stacking faults are shown in red, fcc crystal structure misoriented by 60° inside the twin in green, and the initial grain boundary in grey.
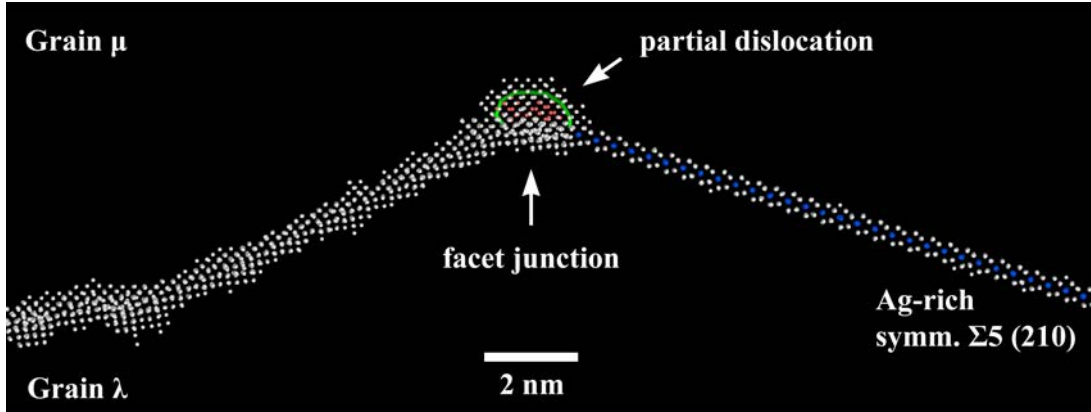
Figure 4.32: Simulated partial dislocation emission event occuring in the nanofaceted Cu(Ag) grain boundary at the facet junction into grain µ as initial plastic deformation event in the whole simulation cell. Here only a magnified view of the junction is shown for clarity.

this means that the pure Cu boundary before the nanofaceting transition does create stacking faults at low density, with one or just few major twins forming, while after the Ag-induced nanofaceting transition, the boundary creates stacking faults at much higher density, which in turn hardly turn into major deformation twins.

In order to explain the discrepancy between the deformation mechanisms of the pure Cu grain boundary and the nanofaceted Cu(Ag) boundary, MD simulations of the nanofaceted boundary were performed to resolve the nucleation event and especially the location of that event. The first nucleation event of a partial dislocation into grain µ creating a stacking fault is shown as zoomed-in view of the whole simulation cell in Figure 4.32. Obviously, the partial dislocation (green line) emission occurs from a facet junction.

Discussion

1. Grain boundary characterization

In light of the obtained results, several points about the dislocation - grain boundary interactions in the studied bicrystals are discussed in the following, with particular emphasize on how Ag coverage and Ag induced structural changes affect these interactions. It could be shown that the initial boundary studied in this chapter (Figure 4.24), is very close to the grain boundaries studied in the previous chapters (chapters 4.1 - 4.3). Building on that knowledge, Ag segregation achieved by the same treatment as before results in a concentration dependent nanofaceting transition. In addition, the Cu reference and Cu(Ag) faceted boundary were investigated by MD simulations and were constructed to match the experimentally de-

termined boundaries as close as possible. For this purpose, mainly the asymmetric Ag-lean (Ag-free in the simulation cell) segment had a slightly different inclination as compared to the experiment, which should not change the outcome significantly, especially as e.g. the stress maps of the different asymmetric boundaries (Figures 4.27a and 4.27b) do not exhibit obvious differences. To assess the plastic deformation response in more detail, the tension axis of both grains was determined and different deformation parameters extracted, which match well between simulation and experiment. Per definition, the stiffer grain is referred to as grain μ, while the other grain is referred to as grain λ. Regarding plastic and elastic compatibility of the two grains, it appeared that the two grains' Schmid factors for full dislocations are comparable, while their difference in elastic modulus in testing direction is significant, i.e. ca. 40 GPa. Consequently, one grain might already be loaded enough to deform plastically (grain μ), while the other one is still being elastically deformed (grain λ). This may e.g. influence dislocation transmission, as the stiffer grain would initially not allow for dislocation transmission until the yield stress is reached there, but also dislocation nucleation from the boundary with even higher energy barriers [229]. Interestingly, the Schmid factors of both grains are almost the same for full and leading partial dislocation emission, but significantly higher than trailing partial dislocation's Schmid factors. This means that besides full dislocations being the expected plastic deformation carrier in Cu, deformation twinning could be a competing plastic deformation mechanism for the investigated system and its deformation directions [230]. More interesting is the influence of the chemically induced GB transition on thermodynamic parameters of the grain boundary and the resulting consequences (Table 4.3). In this regard, the most influential property for the present study appears to be the grain boundary stress and its resolved shear stress components acting on the {111} slip planes of the abutting grains for the given deformation axis. In fact, the asymmetric, initial grain boundary and the asymmetric facet segment behave very similar, with RSS spots acting on the slip plane (promoting dislocation activity) followed by spots where RSS is acting against the dislocation activity (Figure 4.27). In contrast, dislocation interaction of the symmetric Σ5 (210) grain boundary (and facet segment) is effectively decommissioned, as the RSS component strongly acts against dislocation motion. This relates to both transmission and nucleation as the RSS would effectively block incoming dislocations and prevent emission, respectively. A third feature involved in faceted grain boundaries are the facet junctions. Sometimes these junctions contain Burgers vector components [99], however, they do not have to contain these. In fact, in the present study, the facets were constructed in a way that the facet junctions do not contain such a component. Nevertheless, the junctions typically possess a strain field (and strain energy), which might be different for the two possible junctions of a faceted boundary [208]. As a result of these grain boundary components, the chemically induced nanofaceting transition creates a grain boundary structure that seems

to be aligned only for plastic deformation mechanisms that allow for interaction with the asymmetric facet segment or the facet junctions for the applied straining direction. From the structure and the associated parameters for deformation under the present loading conditions, certain predictions for the deformation behavior could be obtained. In the following, the actual deformation results are discussed.

2. Deformation behavior

Initially, the main carrier of plastic deformation during *in situ* TEM tension testing of the pure Cu bicrystal (Figure 4.28) could be identified to be the nucleation and emission of partial dislocations from the grain boundary leaving behind a stacking fault (Figures 4.28g, 4.29, 4.30c and 4.30d). It has been reported earlier that from *in situ* TEM studies it appears that dislocation nucleation from grain boundaries is the dominant mechanism in the initial stage of deformation of polycrystals [231]. To achieve dislocation nucleation from a grain boundary, a dislocation source that lies within the boundary has to be activated. Neither experiments nor atomistic simulations have been able to resolve the nucleation process conclusively, leading to a recent claim by Kacher et al. that "what constitutes a grain boundary dislocation source remains an interesting and important question" [210]. However, atomistic simulations were able to provide some insights into the mechanisms of dislocation emission. For example, van Swygenhoven et al. found that atomic shuffling and stress-assisted free volume migration are responsible for partial dislocation nucleation from a GB [232]. This can be described in a way that many atomic displacements within the boundary occur to eventually form the Burgers vector required for emission of the dislocation. It was argued by the authors that an atomic rearrangement along the interface then lowered the grain boundary energy sufficiently to render trailing partial emission unnecessary. In a follow up study by van Swygenhoven et al., the reason for leading partial emission and stacking fault creation in comparison to full dislocation emission was justified with the ratio between intrinsic and unstable stacking fault energy [233]. Contributions that were not taken into consideration in these studies were pointed out by Tschopp et al. to be the effect of loading mode (tension vs. compression) or the resolved stress acting on the emission of the trailing partial dislocation [234]. As a matter of fact, their study found that for many grain boundaries there exists an asymmetry between tension and compression. In the former case, typically partial dislocations are emitted from the boundary, while in the latter case full dislocations nucleate. In the present study both tension and compression experiments were performed. While our tensile tests on thin foils were found to cause partial dislocation emission resulting in intrinsic stacking faults, our compression experiments (Appendix) revealed not only full dislocation activity but also partial dislocation emission supporting that the partial dislocation is not just a loading axis

141

phenomenon. In addition, it might seem surprising that the main carrier of plastic deformation in the present Cu bicrystals has been determined to be partial dislocations, as Cu is known to deform by full dislocations. However, for fcc metals, such as Au, it was shown that the deformation mechanism changes from full dislocation motion to partial dislocation motion if the sample dimension is reduced below a critical thickness [235]. However, this critical thickness was found in Au and Al to be in the tens of nanometers [235, 236], while the investigated samples in the present study remain at thicknesses above 100 nm and, therefore, deformation through partial dislocations appears to be related to the grain boundary. Finally, the Schmid factors for full, leading partial and trailing partial dislocations were obtained from the determined loading directions of the bicrystal's constituent grains (Tables 4.1 and 4.2). While they don't provide a clear indication for full or partial dislocation activity, it is clear that in case of partial dislocation activity, there is a good chance for the trailing partial dislocation to remain pinned in the grain boundary, as the Schmid factor for this dislocation is significantly lower than for the leading partial or full dislocations.

Following the argument of Tschopp et al. that loading mode or resolved stresses acting on the emission of the trailing partial dislocation may have to be taken into consideration to understand the emission process, the former one has been answered, however, the latter is hard to achieve. In fact, determination of grain boundary stresses from thermodynamic considerations was only established after Tschopp's suggestion by Frolov and Mishin [97]. Calculation of these GB stresses provides the full stress tensor that has been rotated in the present study to the respective primary slip planes in the bicrystal's constituent grains λ and μ to obtain the resolved shear stress components acting on the primary slip systems for the determined loading directions (Table 4.3). For the pure, asymmetric Cu reference grain boundary (and the asymmetric facet segment), the RSS component was found to be on average close to zero, indicating that overall there is no clear support for dislocation nucleation from the boundary. However, locally there are hot spots of high shear stress components that would promote nucleation events and underline the importance of the local atomic arrangement of such complex, asymmetric boundaries. Therefore, few of these events occur along that boundary until another mechanism is activated, namely the growth of one stacking fault into a widening deformation twin to become the major deformation carrier, which should be energetically more beneficial (Figure 4.28c).

In summary, Schmid factor analysis left open whether full or partial dislocations would be involved in plastic deformation, however, the performed experiment and atomistic simulations showed that partial dislocation emission prevails. Although the overall resolved shear stress component would not support dislocation activity strongly, the local atomic arrangement of the grain boundary becomes the important factor. As the atomic structure of the asymmetric, pure Cu reference GB is complex (Figures 4.24c and 4.28f), as also shown in chapters 4.1 to

4.3, some arrangements allow the boundary to adopt a beneficial RSS component supporting dislocation nucleation. The energy barrier to overcome for this emission event $E_{Cu}^{Emission}$ should be proportional to the unstable stacking fault energy γ_{USFE} and the stacking fault's associated strain energy E_{Strain} leading to $E_{Cu}^{Emission} \sim \gamma_{USFE} + E_{Strain}$.

After emission of a leading partial dislocation from a grain boundary, three processes can follow resulting in different deformation features. These can be explained by exploration of the generalized planar fault energy (GPFE) curve of a material, as nicely described in [237]. First, trailing partial dislocation emission can follow the already emitted leading partial resulting in the creation of a full dislocation and in the material to deform via full slip processes. Besides this mechanism, a second leading partial dislocation can be emitted. The difference of the second and third possible processes being the location of this emission. If the second partial is emitted on a plane directly next to the plane of the first leading partial, a micro-twin is formed. Repeating this mechanism leads to deformation via deformation twin growth. In contrast, the second leading partial dislocation can be emitted on a parallel plane but not directly adjacent to the first leading partial. This mode leads to accumulation of extended stacking faults as deformation carrier. A material's behavior after emission of the first leading partial, according to these three cases, depends on the different energy barriers and their relative magnitude to each other. For example, Rice found a criterion that allows to predict if a material deforms via mechanism one (trailing partial emission) or by emission of a second leading partial (mechanisms two and three) depending on γ_{USFE} and the material's intrinsic stacking fault energy γ_{ISFE} [238]. If the ratio $\frac{\gamma_{ISFE}}{\gamma_{USFE}}$ is close to unity, a trailing partial is likely to be emitted to form a dissociated full dislocation, while a second leading partial is emitted for a ratio different from unity. In case of copper, this ratio has been determined to be between 0.15 and 0.3 [237], explaining the tendency of Cu to deform via stacking fault related processes after a first leading partial has been emitted e.g. from a grain boundary. In addition, Tadmor and Hai proposed a criterion for the onset of deformation twinning [239] based on the ratio between the unstable twinning fault energy γ_{UTFE} (to create a micro-twin) and γ_{USFE}. The lower $\frac{\gamma_{UTFE}}{\gamma_{USFE}}$ (the lower bound typically being unity), the more likely it is to emit a second leading partial for twin formation. For Cu, this ratio was found to be 1.05 - 1.1, in agreement with the criterion by Rice. There are other criteria, such as the twinnability parameter [240, 241] or the intrinsic slip barrier [242], which mostly depend on the aforementioned parameters as well, and consequently discriminate between the same deformation modes. In summary, the deformation mode, after the first partial dislocation has been emitted, depends strongly on the GPFE curve of the material. Especially the unstable stacking fault energy and the unstable twinning fault energy determine the shape of the GPFE curve. If all these energy barriers are close (a rather symmetric GPFE curve), deformation twinning is energetically not much more costly compared to full dislocation activity after

a first leading partial has been emitted, as is the case for Cu. However, the local atomic structure also plays a significant role in determining the location of highest resolved shear stress acting on the slip plane, which might dictate the deformation mode. Different shapes of the GPFE curve (more asymmetry) can result in different deformation modes for different materials. For reference, Jo et al. investigated the differences in this curve leading to different deformation behaviors for many fcc materials in detail [242].

Quickly after few stacking faults were created at the local stress hot spots by leading partial emission, one stacking fault became the major carrier of further plastic deformation by growing in width along the grain boundary (Figure 4.28c) forming a growing deformation twin. For this process to happen, first a second intrinsic stacking fault has to be created right next to an already existing one, thereby creating a micro-twin (equivalent to an extrinsic stacking fault), which is bordered by two symmetric $\Sigma 3$ (111) twin boundaries. In Cu, this second stacking fault requires less energy for being created through partial dislocation nucleation and emission according to its GPFE curve as compared to the first one, i.e. the γ_{UTFE} contributes in contrast to the γ_{USFE}. Thus, this process can be regarded as a separate event, which happens to be located on the {111} plane next to the already existing one, possibly supported by atomic rearrangements inside the boundary during deformation. This is in agreement with previous experimental work. Wang et al. [243] has reported an *in situ* TEM study of twinned Cu, which clearly identified partial dislocation emission from the grain boundary on a glide plane next to the twin boundary in agreement with the results of the present thesis work. This behavior was reasoned in the experiment with a high density of twin boundary - grain boundary intersections, which act as stress concentration points and thus promote partial dislocation emission. This same twin growth mechanism has also been observed experimentally e.g. for TiAl [244]. The energy for the observed twin growth ($E_{Cu}^{Twingrowth}$) in the present study should be following $E_{Cu}^{Twingrowth} \sim 2 \cdot \gamma_{TFE} \cdot \Delta x + E_{Strain}$, with $2 \cdot \gamma_{TFE}$ being the twin fault energy that is just slightly above the γ_{ITFE} in the case of Cu, and a small increment related to the width increase of the fault Δx along the grain boundary.

Comparing the obtained *in situ* TEM tension results from pure Cu and Cu(Ag) bicrystals (Figure 4.30) reveals some interesting changes, which are even confirmed from the performed atomistic simulations (Figure 4.31). In the Ag segregated sample, two distinct regions were identified. In a region 1 close to the initial bicrystals' surface (high Ag content, compare chapter 4.3), no signs of plastic deformation were found, while a second region 2 further away from the boundary (low Ag content, compare chapter 4.3) contained multiple stacking faults, i.e. a three times higher density than the pure Cu reference, and no stacking fault was found to become a major deformation twin. In chapter 4.3, we thoroughly investigated the concentration dependence of the Ag induced grain boundary transition and are confident to
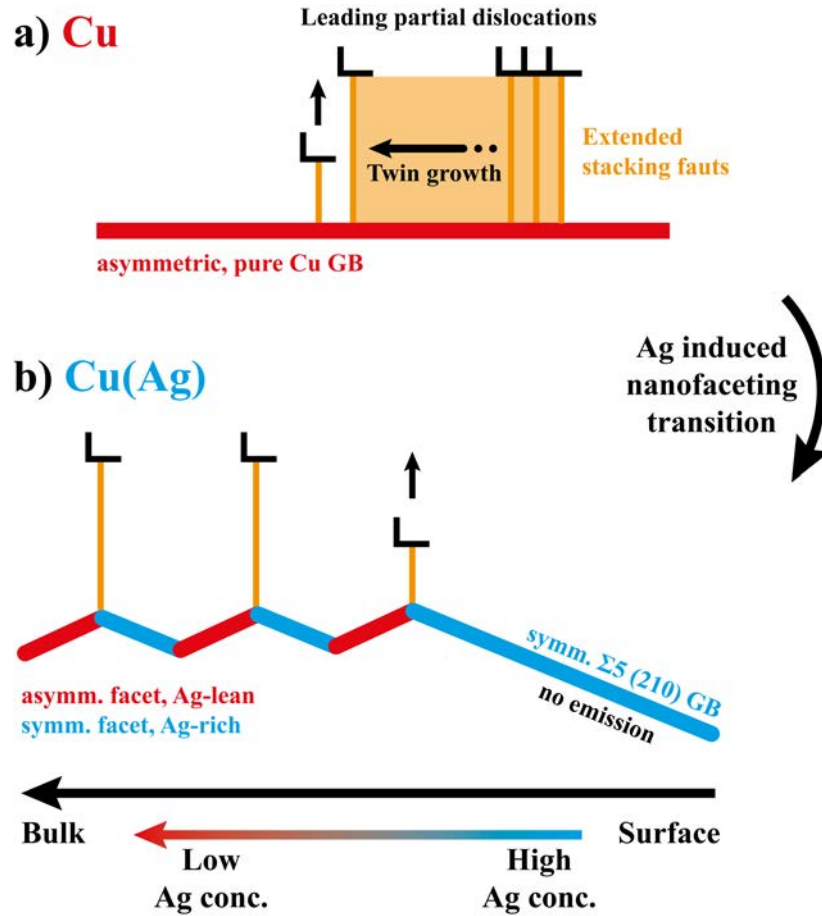
Figure 4.33: Schematic summary of how the Ag induced nanofaceting grain boundary transition influences the plastic deformation behavior in two ways. On the one hand, a structural transition from an asymmetric to a nanofaceted state changes the deformation behavior from deformation twin growth along the boundary to frequent stacking fault emission from grain boundary facet junctions. On the other hand, Ag decoration of the symmetric Σ5 (210) boundary changes the resolved shear stress component of the GB stress tensor to act against dislocation nucleation.

relate region 1 of the tested bicrystal to contain mainly the Ag-decorated (about monolayer coverage), symmetric $\sum 5$ (210) grain boundary. In contrast, region 2 is likely containing the preferentially segregated, nanofaceted grain boundary.

In region 1 containing the Ag-rich, symmetric Σ5 (210) grain boundary, no stacking faults were created. Considering the negative resolved shear stress component acting on the slip plane (Table 4.3) counteracting the nucleation of partial dislocations, overcoming a considerable energy barrier would be required for this, which is obviously much lower in region 2, as all deformation occurs in this latter region. The same argument holds true for the Ag-rich symmetric facet segment in region 2. It is effectively not regarded as contributor to the plastic deformation. On the contrary, this means that the asymmetric facet segment and the facet junction between the asymmetric and symmetric segment are responsible for plastic

deformation to occur in the bicrystals in the observed fashion. This agrees with findings of an atomistic simulation study, which investigated the energy barriers for dislocation nucleation from different grain boundaries in Ni [229]. It was reported there that energy barriers for nucleation from grain boundaries with rather complex structures ($\Sigma5$, $\Sigma9$ and $\Sigma19$) are significantly lower than for grain boundaries containing simple motifs ($\Sigma3$, $\Sigma11$). In light of the boundaries of the present study, the complex structure of the asymmetric segment should be much more active in terms of dislocation nucleation. Nonetheless, if only the asymmetric facet segment would be responsible for plastic deformation, a pattern similar to the pure Cu reference boundary should evolve for increasing strain. Therefore, the facet junction should have an important impact, which is confirmed by the performed atomistic simulations (Figure 4.32) showing that partial dislocations are emitted initially from the grain boundary's facet junctions. This happens as a result of the junction's associated strain field, which lowers the energy barrier for nucleation to below any other nucleation barrier of the different grain boundaries. In fact, different junctions can have different strain fields depending on the underlying atomic structure at the junction, even along the same faceted grain boundary as recently reported by Liebscher et al. for a Si grain boundary [208]. The fact that strain fields (stress-strain concentrations) from additional defects lower the energy barrier or increase the chances for nucleation has been reported in different studies for fcc metals [229,243]. In effect that means that the energy required for partial dislocation emission from the facet junction $E_{Cu(Ag)}^{Junction}$ should follow a similar relation as $E_{Cu}^{Emission}$, however with an energy contribution from its associated strain field $E_{Strain}^{Junction}$ lowering the overall energy. The emission cost hierarchy would then follow $E_{Cu(Ag)}^{Junction} \sim \gamma_{USFE} + E_{Strain} - E_{Strain}^{Junction} < E_{Cu}^{Twingrowth} < E_{Cu}^{Emission}$.

Considering the discussed plastic deformation behaviors for the asymmetric Cu reference GB and the nanofaceted Cu(Ag) grain boundary, it is clear that the GB nanofaceting transition does have an influence on plastic deformation. A schematic overview of the influence and the changing deformation behavior is provided in Figure 4.33. While the asymmetric, pure Cu reference boundary deforms mainly by deformation twin growth, nanofaceting manifests its influence via a combination of structural and chemistry related effects; GB structural changes in terms of the introduction of facet junctions and symmetric $\Sigma5$ (210) segments, chemistry related changes in terms of the introduction of Ag into the symmetric $\Sigma5$ (210) segment effectively changing the boundary's stress state to prohibit dislocation activity for the present loading conditions. The introduction of nanofacets mainly results in the prevention of twin growth by providing sufficient partial nucleation sites manifested as facet junctions. Consequently, the three determined states of the Cu(Ag) grain boundary resulting from the segregation treatment for increasing Ag excess concentration (chapter 4.3), namely (i) the asymmetric, straight grain boundary, (ii) the nanofaceted boundary and (iii) the continuous symmetric $\Sigma5$ (210) boundary, are deforming in different modes, namely (i) deformation

twin growth, (ii) extended stacking fault creation and (iii) supression of partial dislocation emission, respectively.

Changes in plastic deformation behavior are expected to also affect the mechanical response of a material. The investigated bicrystals (grain boundaries) of the present study, and in particular the GB nanofaceting transition, lead to GB structure and GB composition related changes. For now, dislocation free bicrystals are assumed. Although chemistry was found to be the reason for the GB transition, its influence on mechanical performance was mainly related to pronounced changes in the GB stresses τ_{ii} and especially the corresponding shear stress components acting on the primary slip planes of the respective grains τ_{RSS-i} (compare with the symmetric $\Sigma 5$ (210) grain boundaries with and without Ag in Table 4.3). Therefore, the influence of chemistry is expected to affect the yield strength and flow stress of the bicrystals depending on the sign and magnitude of τ_{RSS-i}, which is likely controlled by the Ag concentration and strongly dependent on the deformation direction. In addition, the state of the grain boundary is important. For a continuous, Ag-rich and symmetric $\Sigma 5$ (210) grain boundary the chemical influence governs the mechanical response. Under the present conditions, this would result in an increase of the yield strength compared to the pure Cu reference boundary, as the τ_{RSS-i} are negative in that case and thus act against dislocation emission from the boundary. However, if the tested bicrystal contains parts of the nanofaceted grain boundary, the structural influence becomes the dominant influence, as the facet junctions have to overcome the lowest energy barrier for partial dislocation nucleation compared to the symmetric $\Sigma 5$ (210) grain boundary containing Ag, but also regarding the Ag-lean asymmetric facet segment and the pure Cu (Ag-free) asymmetric facet segment. Consequently, if the bicrystal contains either both the continuous, Ag-rich $\Sigma 5$ (210) grain boundary and the preferentially segregated, nanofaceted grain boundary or only the nanofaceted boundary, a decrease of the yield strength is expected as compared to the pure Cu reference. If we now also consider full dislocation activity to occur during plastic deformation in the bicrystals, twinning has often been found to cause increases in hardening of a material. In fact, the contribution of twins on the flow stress can be calculated according to

$$\Delta\sigma_t = M \cdot \beta \cdot G \cdot \vec{b} \cdot \left(\frac{1}{D} + \frac{1}{d_t} \right) \qquad (4.1)$$

with M being the Taylor factor (3.06), β being 0.24, G being the shear modulus (44.7 GPa for Cu), $\vec{b}$ being the Burgers vector (0.256 nm for Cu), D being the materials grain size and d_t being the twin spacing [245]. Considering the grain size to be infinite ($\frac{1}{D} \rightarrow 0$), the contributions at already fairly high strains can be calculated using the determined twin densities to about 6.5 MPa for the asymmetric, pure Cu bicrystal and about 19 MPa in case of the nanofaceted Cu(Ag) bicrystal. However, the former bicrystal would rather deform via

deformation twin growth. Consequently, the influence on hardening is expected to be rather moderate.

Conclusions

The grain boundary phase transformation, studied in this thesis work, was examined in terms of mechanical properties and especially with respect to plasticity mechanisms. Therefore, the pure Cu asymmetric reference boundary was characterized and tested first. The structure was found to match the boundary in the previous chapters and therefore it was possible to build on the knowledge regarding the GB nanofaceting transition. From the performed *in situ* TEM tensile experiments, the asymmetric Cu reference GB was found to mainly deform by deformation twin growth after some extended stacking faults were emitted from the boundary. In contrast, the preferentially segregated, nanofaceted Cu(Ag) grain boundary and continuous, Ag-rich symmetric $\Sigma 5$ (210) boundary were found to deform through high density stacking fault emission or not at all, respectively. The difference in behavior is explained by help of the generalized planar fault energy curve and by the introduction of facet junctions (structural GB change) upon the nanofaceting transition and a resolved shear stress component counteracting dislocation nucleation caused by Ag adsorption (chemistry related change). Consequently, it could experimentally be shown for the first time that a nanofaceting transition can impact the plastic deformation behavior of bicrystals for the applied loading conditions, which was even confirmed and supported by atomistic simulations replicating the experimental results and providing deeper insights in the role of the facet junctions and the thermodynamic GB properties. The findings indicate that the chemically induced GB nanofaceting transition can alter the deformability of a material by reducing the activation energy for partial dislocation nucleation and changing the GB stress, thus bearing the potential to be an important factor to tailor a material's properties e.g. for load bearing applications e.g. in nanocrystalline materials. The figure of merit for such optimization procedures would be the grain boundary stress. Proper combination of deformation axis and segregant adjusts this parameter and the resulting shear stress components of the stress tensor, in order to support or oppose dislocation activity. In addition, targeted introduction of stress-strain concentration sites along the boundary, such as facet junctions, would allow for changes in the mechanical response.

Chapter 5

Conclusion

The perfectness of a metal's crystal lattice typically defines it's macroscopic properties, such as diffusion or mechanical properties. Increasing amounts of defects, e.g. dislocations, grain boundaries and solute atoms, may have significant influence on a variety of these properties. Consequently, the behavior of these defect structures and the interaction with each other is of great importance to understand, in order to improve the ability of tailoring material properties to specific application requirements.

In the present thesis work, mainly aberration-corrected and *in situ* S/TEM were used along with APT and atomistic simulations to comprehensively investigate a chemically induced nanofaceting grain boundary phase transition in the Cu-Ag system and to link this transition to changes in plasticity mechanisms. A pure Cu bicrystal grown by the Bridgman method and containing an atomically rather flat, asymmetric, close to 54° [001] (110)/(920) tilt grain boundary, was used as reference grain boundary. Thermal annealing did not have a significant influence on the grain boundary structure. However, the same thermal treatment in presence of Ag revealed a chemically induced transition from the flat reference boundary, to a nanofaceted grain boundary. The flat reference decomposed into a new asymmetric segment with a close to (110)/(230) boundary plane and a symmetric $\sum5$ (210) facet segment. Chemical inspection complements the findings that these facet segments are preferentially segregated in a way that the asymmetric segment is Ag-lean, while the symmetric segment is Ag-rich.

After the structural aspects of the transition were unraveled, more quantitative chemical information was gathered by optimizing STEM imaging and image processing techniques. Comparing different acquisition methods, namely single image acquisition vs. serial image acquisition, the Ag occupancy of individual atomic columns inside the symmetric, Ag-rich $\sum5$ (210) facet segments could be determined to be at least 50 %, but rather approaching 100 % by studying extracted STEM peak intensity ratios. The sequential imaging capabilities of the STEM then allowed for a time-resolved quantification, which revealed that the Ag containing segments remain stable over time even under constant high energy electron bombardment, with Ag atoms mostly fluctuating inside the Ag-rich segments, but not significantly into the Ag-lean segment of the abutting grains.

Investigation of the concentration dependence of the nanofaceting transition was accomplished by characterization of the grain boundary along a concentration gradient, which was created by a Cu-Ag diffusion couple approach. It was found with this approach, that the pure Cu reference boundary can take up Ag solute until a critical threshold concentration induces the nanofaceting transition into equisized facet segments as characterized before. However, while the asymmetric, Ag-lean segments remain constant in size, the symmetric, Ag-rich segments increased in lengths with increasing Ag concnetration. Eventually, these symmetric segments grow in length until a Ag decorated, continuous, symmetric $\Sigma5$ (210)

boundary remains. From these results, it was possible to establish a nanofaceting diagram for the studied grain boundary in the Cu(Ag) system. Our simulation results indicate a thermodynamic driving force to form symmetric $\sum 5$ (210) facet segments to reduce the grain boundary energy, however, the asymmetric facet segment, formed to accomodate the inclination change, acts as kinetic barrier for facet growth resulting in the continuous inclination change at the macroscopic scale and continuous symmetric segment length increase at the atomic scale. As the atomic scale has not been accessable easily before the introduction of commercial aberration-correctors for STEM, these mechanisms might be occuring more often in other material and grain boundary systems, which underlines the importance of this research.

The grain boundary phase transformation, studied in this thesis work, was examined in terms of mechanical properties and especially with respect to plasticity mechanisms. Therefore, the pure Cu asymmetric reference boundary was characterized and tested first. The structure was found to match the boundary in the prvious chapters and therefore it was possible to build on the knowledge regarding the GB nanofaceting transition. From the performed *in situ* TEM tensile experiments, the asymmetric Cu reference GB was found to mainly deform by deformation twin growth after some extended stacking faults were emitted from the boundary. In contrast, the preferentially segregated, nanofaceted Cu(Ag) grain boundary and continuous, Ag-rich symmetric $\Sigma 5$ (210) boundary were found to deform through high density stacking fault emission or not at all, respectively. The difference in behavior is explained by help of the generalized planar fault energy curve, by the introduction of facet junctions (structural GB change) upon the nanofaceting transition and a resolved shear stress component counteracting dislocation nucleation caused by Ag adsorption (chemistry related change). Consequently, it could experimentally be shown for the first time that a nanofaceting transition can impact the plastic deformation behavior of bicrystals for the applied laoding conditions, which was even confirmed and supported by atomistic simulations replicating the experimental results and providing deeper insights in the role of the facet junctions. The findings indicate that the chemically induced GB nanofaceting transition can significantly alter the deformability of a material by reducing the activation barrier for partial dislocation nucleation and changing the GB stress, thus bearing the potential to be an important factor to tailor a material's properties e.g. for load bearing applications e.g. in nanocrystalline materials.

Chapter 6

Appendix

SAMPLE PREPARATION

For investigations of the mechanical size-effect of the asymmetric tilt grain boundary, annular compression samples (pillars) were fabricated at different diameters by FIB machining. The size range can be divided into two regimes. On the one hand, micron-sized compression pillars were prepared for *in situ* SEM testing to indirectly study the collective dislocation behavior within the tested samples and to obtain mechanical properties like yield- and flow stresses. Micropillars with outer diameters of 10 µm, 5 µm and 2.5 µm were fabricated by FIB machining in a Zeiss Auriga dual-beam machine and tested using an ASMEC UNAT 2 indenter inside a Zeiss Gemini SEM. For the 10 µm diameter samples, rough cuts were performed in a Xe-plasma operated FEI Helios plasma FIB to benefit from an approximated 20 fold increase in milling rate according to the vendor, due to the bigger ion mass of Xe relative to Ga. On the other hand, nanometer-sized compression pillars for *in situ* TEM testing were prepared with diameters decreasing from 600 nm down to 200 nm in 100 nm increments to directly visualize and track individual dislocations and their interactions with the grain boundary. Electron transparency for TEM experiments was reached at pillar diameters of around 300-400 nm at the used TEM acceleration voltage of 200-300 kV. Bigger diameters up to 600 nm were used to bridge the gap to *in situ* SEM experiments. Plastic deformation features on bicrystalline micropillars were investigated by STEM of post mortem pillars with a diameter of 10 µm. Pillars of that size were perfectly suited for a conventional lift-out procedure, followed by thinning to electron transparency inside a FIB machine.

Perfect annular compression samples provide a beneficial uniaxial strain field throughout the sample and therefore facilitate the analysis compared to, for example, complex, strain gradient involving (nano)indentation experiments. In addition, the ease of sample preparation and site specific fabrication provide a tool for defined testing of microstructural features con-
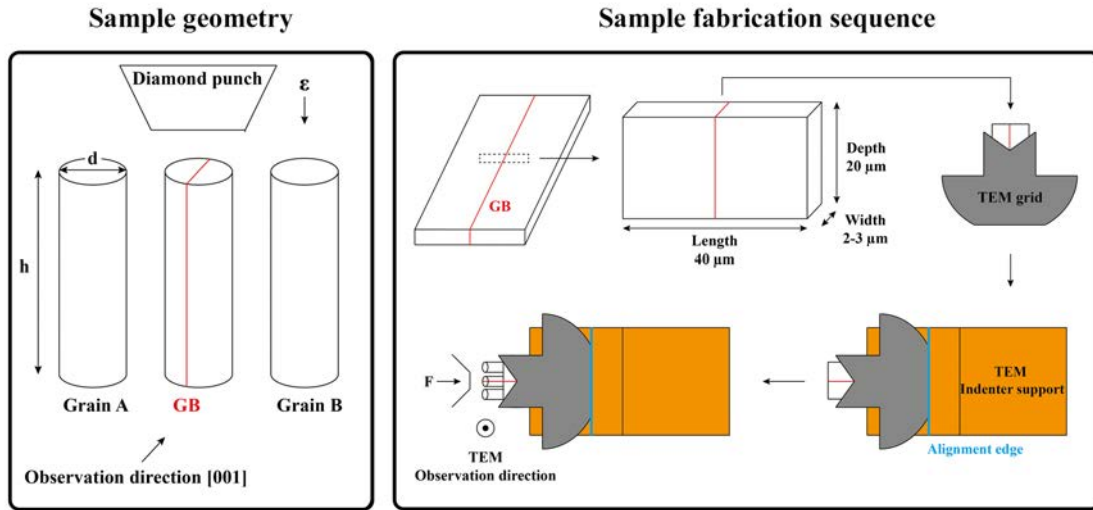
Figure 6.1: Sample geometry and FIB-based fabrication sequence of *in situ* TEM compression testing samples. Free-standing, annular compression samples have been fabricated in each of the two grains (single crystalline) and containing the grain boundary (bicrystalline). The exact fabrication sequence is described in the text.

tained in the samples volume, i.e. a grain boundary in the present work. It was shown before that a pillar aspect ratio of about 3:1 (height:diameter) is most suitable for ideal *in situ* miniaturized compression tests along with other recommendations [246]. This aspect ratio has been used in numerous other studies and is also aimed for in the present thesis work. Grain boundary containing pillars were prepared with the grain boundary running through the entire pillar parallel to the loading direction and single crystalline pillars of each of the abutting grains were tested for reference. Imrich et al. previously investigated the influence of the boundary plane orientation with respect to the loading axis [247]. It was found that for the performed tests (similar geometry to the present ones), the described grain boundary plane inclination yields best chances for observing dislocations interacting with the grain boundary and reduces the shear stress acting on the boundary close to zero for a perfect vertical alignment.

While micropillars for *in situ* SEM testing could be milled in a bulk sample, the preparation of nanopillars for *in situ* TEM compression experiments required some additional steps as illustrated in Figure 6.1. First, a large cross-section was prepared from the bulk bicrystal by FIB machining using the plasma FIB. The dimensions of the lift-out lamella were approximately 40 µm length, 2-3 µm width and about 20 µm depth. This lamella was transferred with a micromanipulator and attached via Pt-deposition to a TEM grid. Omniprobe Mo grids were used with M-shaped posts and a central finger. The finger was not used for fixation following Imrich et al. who showed that for such a one-sided fixation and loading condition bending moments were induced. These negatively influence the mechanical response of such

samples [248]. In contrast, locating the lamella to the central portion of the M-shaped post allowed fixation along the entire lamella's length and same loading conditions for all nanopillars. The grid was placed on a Cu support, which was obtained commercially along with the used indentation system, a Hysitron PI-95 Picoindenter. The support contains an alignment edge perpendicular to the indenter axis, which allows for precise alignment of the TEM grid with the indenter. Unfortunately, during the lift-out procedure, the lamella surface cannot be aligned properly, due to the unprecise FIB stage movements. These few degrees of deviation are corrected after the previous alignment by FIB cutting the lamella's top surface parallel to the alignment edge. Finally, nanopillars are annularly milled from the top of the lamella as described above in a Zeiss Auriga FIB machine. This procedure secures adequately aligned compression experiments inside the TEM with the TEM observation direction allowing for observation close to a known zone axis orientation.

To understand the difference between the microcompression data of the samples smaller and bigger than 300 - 400 nm, we prepared TEM compression samples ranging from 600 nm down to 200 nm, covering both size regimes and observed their condition before testing (Figure 6.2). It was found by EBSD that the compression direction of TEM samples after lift out matched the compression direction determined by STEM within few degrees (compare Figure 6.2a to Figure 4.24). In addition, most pillars below the critical size were predominantly dislocation free after annealing, containing, if at all, only one visible dislocation in their volume. In contrast, above the critical size, pillars contained few to several dislocations in their volume, although dislocation densities were determined to be similar in all sizes, i.e. around 3 x 10^{13} m^{-2} (Figure 6.2b). The dislocation density was determined using the established line intercept method [249].

Results

Post mortem inspection of annular, microcompression samples revealed for larger pillars (above 300 - 400 nm) a primary main slip system, which is rotated by about 35° from one grain to the other in accordance with the misorientation angle (compare with black arrows in Figure 6.3a). At the grain boundary, where the two slip systems meet, they do not fully coincide, but are rather slightly misaligned. For smaller samples (Figure 6.2b), the same holds true, however, in the two grains secondary slip systems got activated relatively more often (e.g. in Figure 6.3b at the top of grain 1) and the compression samples deformed mostly on few distinct slip systems compared to the bigger pillars, especially for samples containing the grain boundary.

In terms of mechanical performance, stress vs. strain curves were recorded during compression testing of the increasingly smaller, annular pillars (Figure 6.4a). Two main observations
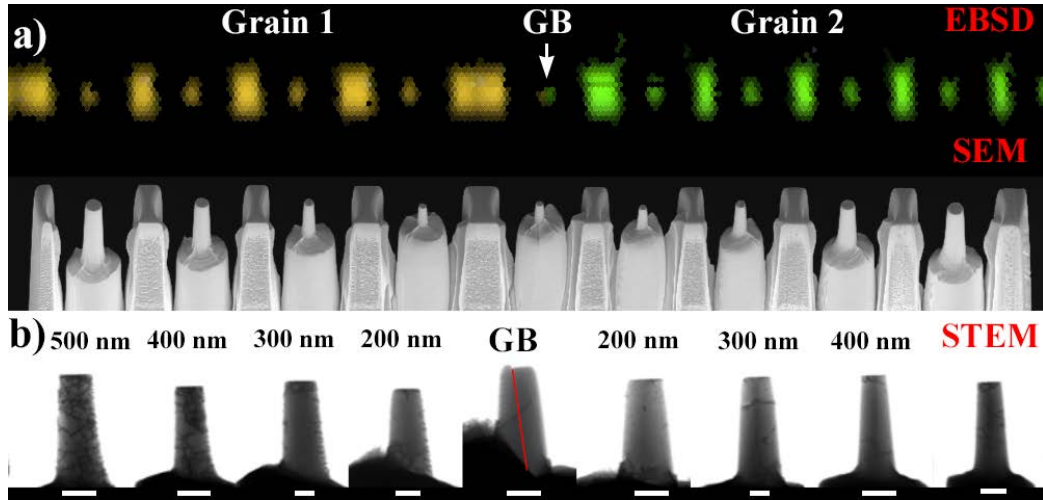
Figure 6.2: Microstructure characterization of TEM micropillars in the pre-deformed state. EBSD and SEM were used to confirm compression direction and morphology (a), while STEM bright field micrographs were recorded to investigate the microstructure and especially defect (dislocation) content of the microcompresssion specimens (b).

were found, namely an increase in yield strength and at the same time a reduced number, but significantly stronger, strain bursts for decreasing pillar dimensions. This includes the single crystalline reference samples, but also the grain boundary containing ones. It has to be stressed that the pillars tested in the SEM were strained in true displacement-control mode, while the indenter used for pillar compression inside the TEM was operated with a displacement-controlled feedback loop, of the inherently force-controlled TEM nanoindentation device. The only noticable difference between single crystals and bicrystal is, that for larger strains, the grain boundary leads to a mild apparent hardening. Extraction of the yield strengths (first deviation of elastic slope) of all curves and plotting them in a log-log diagram against sample size (top diameter) or grain size (half of top diameter) reveals the well known, "smaller is stronger" size effect for fcc metals. However, it appears that for pillars below 300 - 400 nm the yield strength increases faster (steeper slope) than for pillars with bigger diameters. Fitting power law functions according to $y = ax^m$ results in linear fit lines in the graphs (dashed lines in Figures 6.4b and 6.4c) with slopes of -0.56 and -0.54 for the two single crystals, respectively, and -0.55 for the bicrystal (300 nm - 10 µm). In contrast, slopes for smaller diameters were much steeper with slopes of -0.98 and -1.03 for the two single crystals, respectively, and -1.75 for the bicrystal. a and m are fitting parameters; the latter being the slope of the straight line (size scaling exponent). Distinguishing between grain size (Figure 6.4b) and sample size (Figure 6.4c) only shifts the grain boundary line to smaller diameters keeping the slope constant. It appears, that the data of the grain boundary fits very well to the single crystalline reference data in the sample size plot, while deviding it in half to obtain the grain size plot has the bicrystal data being weaker than the single crystals.

a) SEM post-microcompression

Grain 1 GB Grain 2

2.5 µm

600 nm
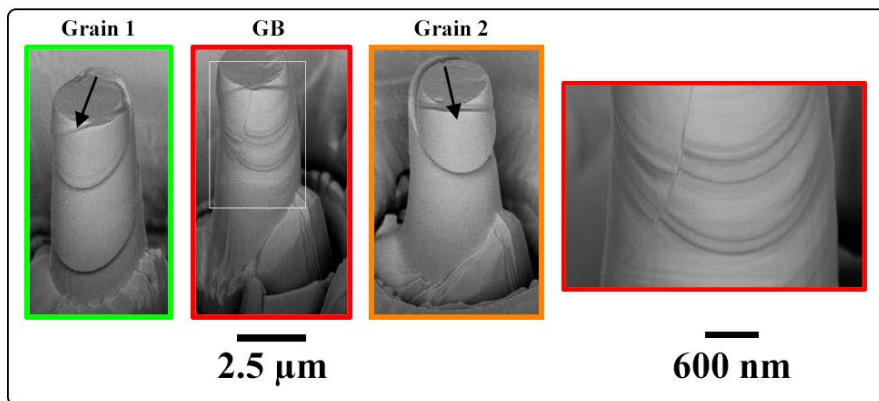
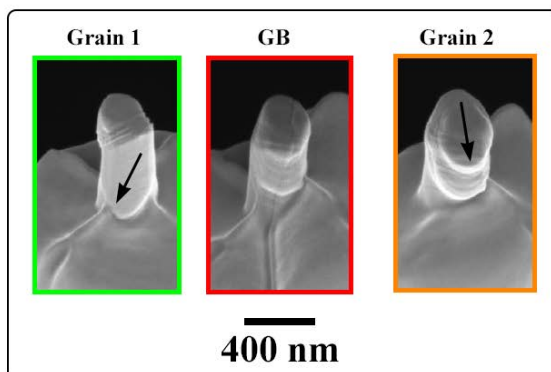**b) TEM post-microcompression**

Grain 1 GB Grain 2

400 nm

Figure 6.3: Post mortem SEM micrographs of microcompression samples. Representative, singlecrystalline pillars (green and orange) as well as a bicrystal (red) are shown including a higher magnification image of the grain boundary, in this case with a top diameter of 2.5 µm tested in the SEM (a). In the contrary, post mortem SEM images of small TEM tested pillars are presented with top diameters of roughly 300 nm (b). Black arrows are overlayed to highlight the primary slip systems in both grains that are rotated by about 35° to each other.
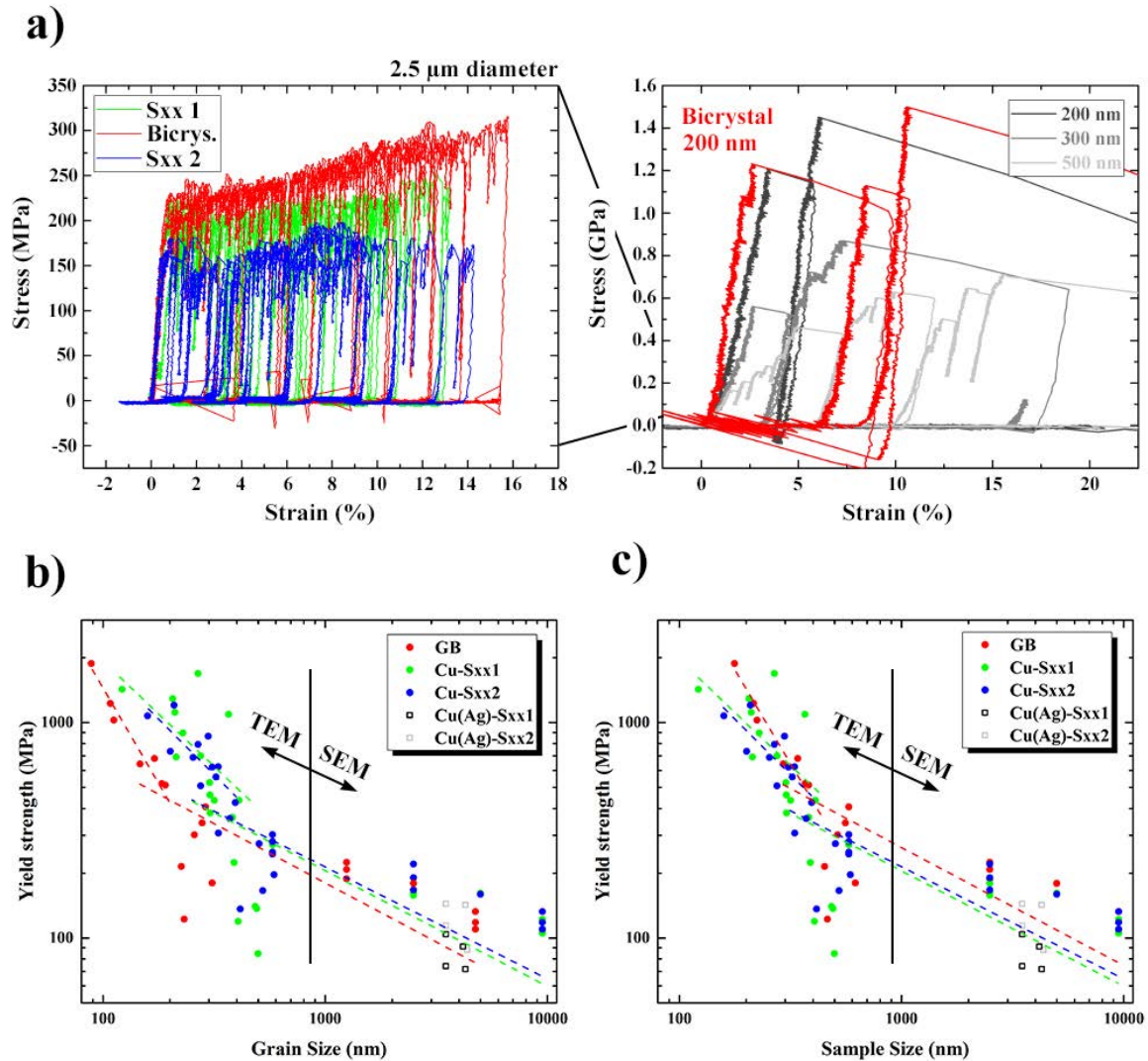
Figure 6.4: Quantitative mechanical testing results of micropillar compression in the SEM and TEM. Representative stress vs. strain curves for pillars of different top diameters, ranging from 200 nm up to 2.5 µm, are presented in (a). The curves for 2.5 µm pillars are shown independently on the left for clarity, as their flow stresses were too low in comparison to the submicrometer sized pillars. Stress vs. strain curves of bicrystals are plotted in red. The yield strength plotted against the grain size (b) or against the sample size (c) reveal the size-scaling effect and have a power law function fitted for interpretation (dashed lines).

In order to study the prevailing plasticity mechanisms at the grain boundary we lifted out a compressed bicrystalline pillar for observation in STEM (Figure 6.5a). The atomic structure and plane of the grain boundary post compression was characterized and compared to the initial reference grain boundary. It appeared that no obvious changes occurred close to the pillar's surface and although significant strain was applied to the pillar, the boundary remained unaffected (Figure 6.5b). At deeper locations (Figure 6.5c), we observed dislocation networks, indicated by dashed black lines, which form a type of band that changes its direction at the grain boundary. Within this band we found two major features. On the one hand, the grain boundary was curved in S-type fashion to offset the straight grain boundary coming from the surface, from the exiting boundary below the band (Figure 6.5c). The offset distance was measured to be around 168 nm. On the other hand, we were no longer able to observe the atomic structure of the grain boundary, as a twist component of 3.08° was introduced upon compression, which did not allow observation of both grains in zone axis at the same time anymore. The twist angle was determined by inspection of the CBED pattern and measuring the separation of the pole centers (Figure 6.5d). The micrograph was callibrated as the bright CBED disc diameter is set through the convergence angle of the STEM to 23.8 mrad.

In summary, the pure Cu grain boundary was thoroughly studied in terms of mechanical performance and plastic deformation behavior. It was found that the grain boundary is the same as studied in the previous chapters 4.1 to 4.3 and that in terms of mechanical properties, the boundary does not appear to provide a significant stimulus to manifest itself in increased yield strengths of the bicrystals compared to the single crystals. In terms of plastic deformation, inclined deformation bands formed, which are either narrow but with sharp boundaries, or wide with more diffuse boundaries accompanied by a bending of the grain boundary in distinct areas between the boundaries. Both types of of these deformation bands line up at the grain boundary almost perfectly.

From the performed compression experiments, few pillar sizes ensured electron transparency inside the TEM, which enabled the observation of plasticity mechanisms in these samples to support the results obtained for thin foil tensile testing. Figure 6.6 shows an in situ TEM (bright field) compressed, bicrystalline pillar (grains λ and μ are highlighted in Figure 6.6a) revealing different deformation mechanisms. Initially, dislocations were nucleated at the top surface due to stress concentrations during contact formation (Figure 6.6a). Further loading of the pillar showed how such dislocations were pinned at the grain boundary and moved discontinuously along the boundary (Figure 6.6b). Partial dislocation emission from the boundary resulted in the formation of a stacking fault (Figure 6.6c) and emission of the trailing partial dislocation after 0.54 seconds (further loading) lead to the annihilation of the stacking fault. The same process occured a second time at a later point during compression of
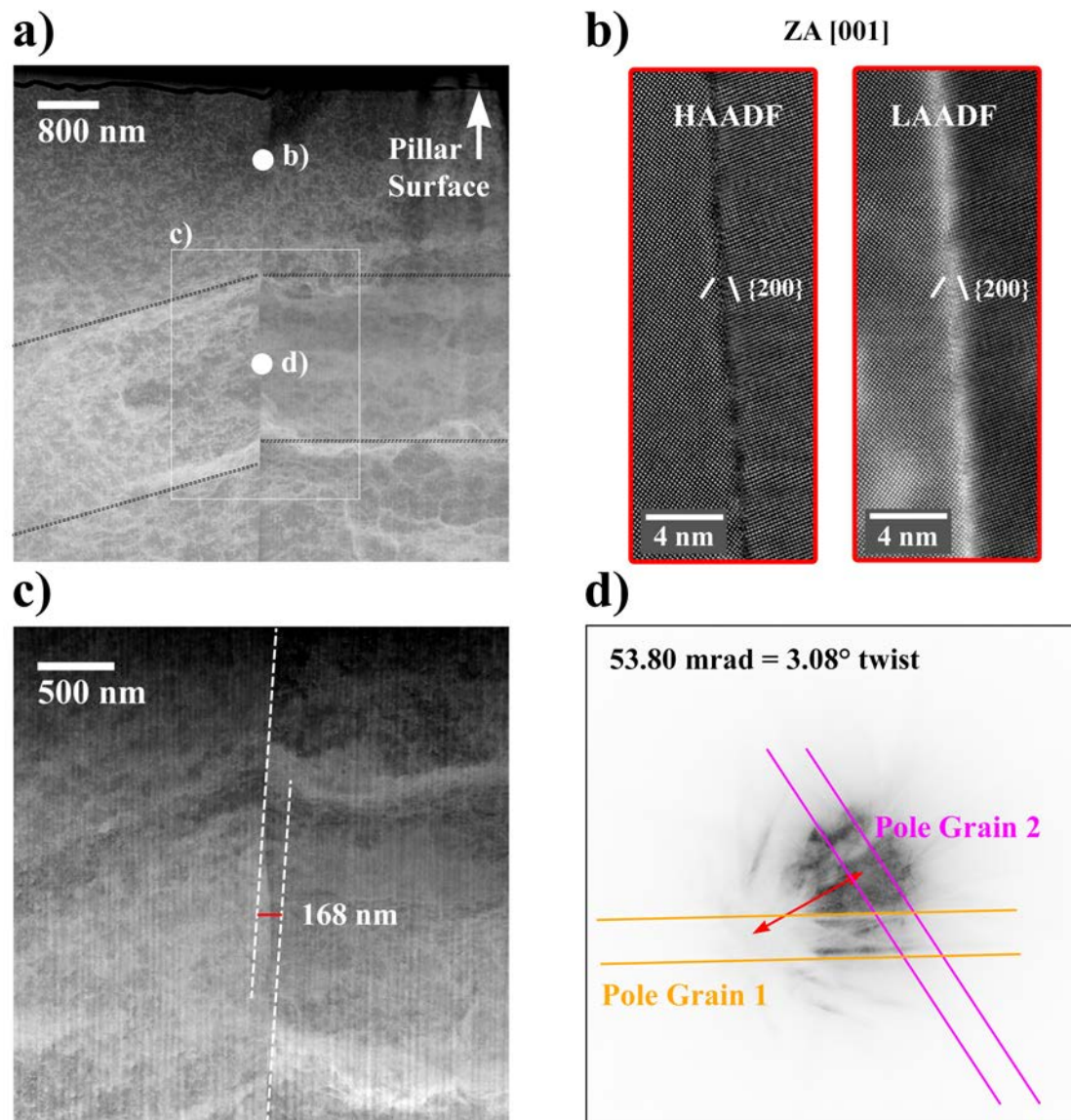
Figure 6.5: Post mortem microstructure characterization of a tested micropillar. Cross-sectional STEM micrograph of the top region of a tested micropillar with a field of view of about 6.4 μm into the sample (a) with different locations highlighted that were used for further analysis. In the top region, the boundary remained unaffected from straining down to the atomic scale as shown by LAADF (strain contrast) and HAADF (Z-number contrast) micrographs (b). {200} planes are marked by white lines. Further into the pillar, dislocation networks formed in distinct orientations to one another, highlighted by black lines in (a), in between which the grain boundary bowed in S-shape fashion to offset the straight unaffected boundary by about 168 nm (c). The atomic structure of the grain boundary could no longer be identified as in (b), as additionally to the bowing of the boundary, a twist component of 3.08° was introduced as determined from the recorded CBED pattern (d).

Table 6.1: Stresses acting on dislocation loop bowing out from grain boundary into grain λ related to the micrographs in Figure 6.6.

Dislocation loop appearance based on Figure 6.6	Stress experienced by dislocation loop
(e)	99 MPa
(f)	108 MPa
(g)	127 MPa

the same pillar lasting 1.64 seconds. Finally, full dislocation loops were observed to bow out from the grain boundary (Figure 6.6d). Although the dislocation structure and processes were observed relatively clearly in the right grain of Figure 6.6, generally it was hardly possible to clearly identify the dislocation reactions caused by, or causing the dislocation reactions in the left grain. Nevertheless, the observed mechanisms clearly hint towards an emission process from the grain boundary, potentially a nucleation mechanism or the emission resulting from a dislocation transmission process across the boundary. The bowing out of a dislocation does allow to calculate local internal stresses acting on this dislocations. The evolution of a dislocation loop bowing out from the grain boundary is visualized by a series of micrographs from an *in situ* TEM compression experiment in Figures 6.6e - 6.6h. The appearance of the individual dislocation loop states is sequentially extracted and shown in Figure 6.6i. The dislocation bows out increasingly into the right grain λ, until in the last micrograph it interacted with another dislocation (marked by a second arrow) resulting in its retraction. The stress τ acting on the dislocation to bow out was calculated for each micrograph according to $\tau = \frac{G\vec{b}}{2R}$, with R representing the radius of curvature of the dislocation line. The radius was corrected for the projection, as the angle between the {111} glide plain is inclined by 54° with regard to the {100} plane (also compare Figure 4.29). Therefore, the larger real radius was obtained by dividing the observed (projected) radius by $\sin(36°) \simeq 0.59$. The calculated stress levels for Figures 6.6e - 6.6g are given in Table 6.1. Increasing stress levels ranging from 99 to 127 MPa were found before dislocation interaction caused retraction of the loop.

DISCUSSION

The pure Cu grain boundary's mechanical response was studied by *in situ* SEM/TEM microcompression experiments, which determined stress levels at given strains. Close observation of the recorded stress vs. strain diagrams (Figure 6.3) showed the common observation for fcc metals that for smaller samples the yield stress increases. Plotting the yield strength against the pillar diameter reveals the well known "smaller is stronger" size scaling behavior (Figure 6.3c), in which the yield strength increases with decreasing sample size [250–256] due to the reduced volume and thus reduced number of available dislocation sources. A striking
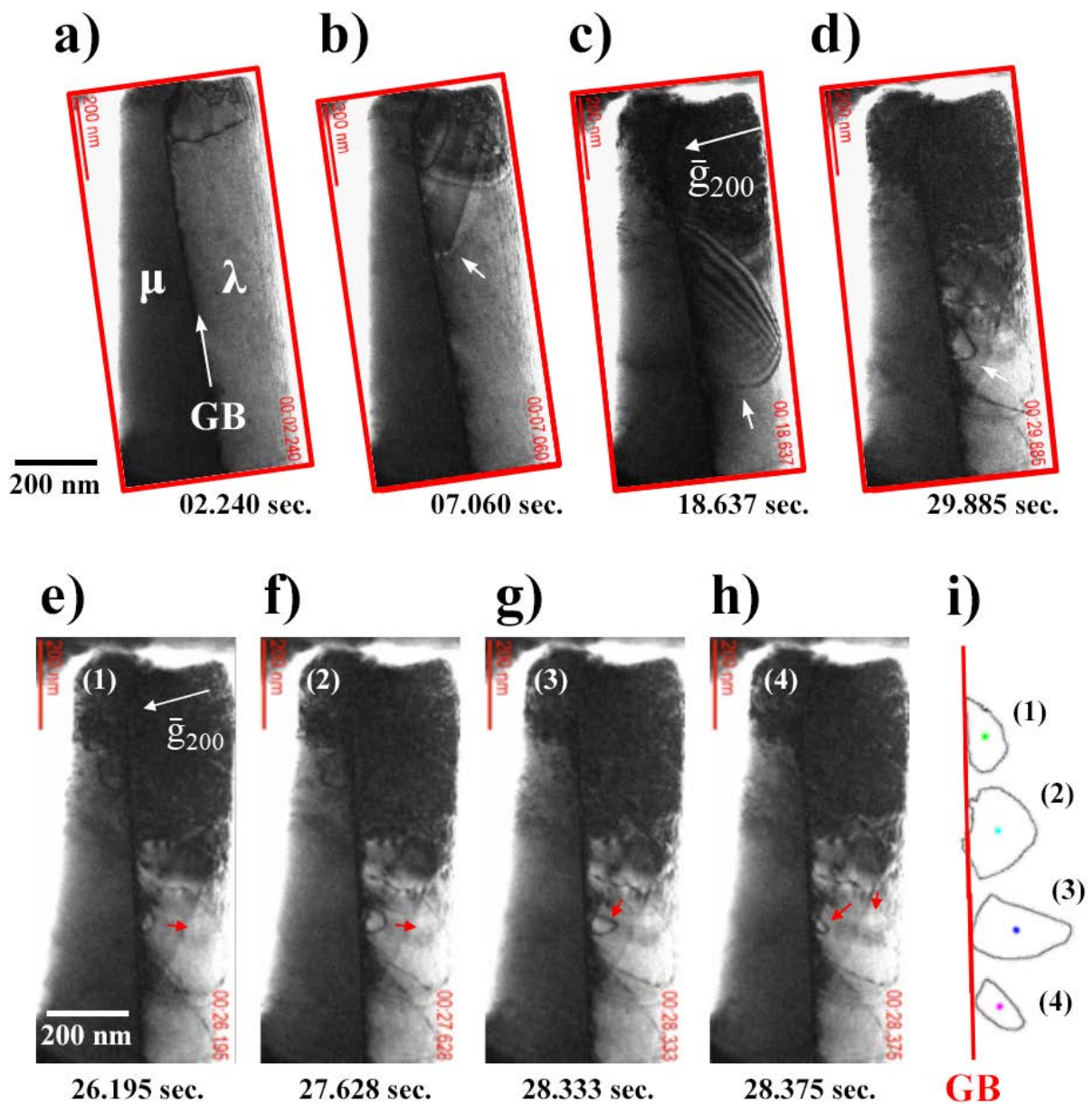
Figure 6.6: Summary of dislocation interaction types with the asymmetric tilt grain boundary. Grains λ and μ are highlighted in (a). Observed were, dislocation emission from the top of the dislocation free pillar upon contact formation (a), dislocation attachment to the grain boundary and discontinuous (pinned) motion of the dislocation line along the boundary (b), leading partial dislocation emission from the boundary into grain λ creating a stacking fault (c), as well as trailing partial emission going in hand with the annihilation of the stacking fault. Finally dislocations bowing out from the grain boundary were observed (d) and analyzed in a time sequence in more detail (e) - (h). The shapes of the individual dislocation line shapes at the different time steps were extracted and plotted underneath each other for better visibility in (i).

observation is the change in slope for pillar diameters below 300 - 400 nm. These samples reveal a much faster increase of the yield strength as compared to bigger samples. Although, different indentation devices were used for SEM ($>$ 1µm sample diameter) and TEM ($<$ 1 µm sample diameter) testing, it is unlikely that the device has a significant influence on the yield strength of the structures, as pillars tested in TEM, with diameters 400 - 600 nm, are still relatively well aligned with the SEM tested samples. Post mortem morphology did not reveal any major differences either (Figure 6.2). Investigation of the TEM pillars in terms of microstructure, and in particular in terms of dislocation content (Figure 6.1), revealed a constant, relatively low dislocation density for all different pillar sizes at around 3 x 10^{13} m^{-2}. However, constant dislocation density relates to drastic differences in actual dislocation content for different sample sizes. In fact, below 300 - 400 nm hardly any dislocation lines were found, while increasing amounts of dislocations remained in the bigger structures. Keeping in mind that the TEM pillars were annealed after fabrication and before testing, and SEM pillars not, SEM pillars are likely to have even more defects inside. As a consequence, smallest diameters tested more or less defect free structures, while bigger sizes tested defective structures, which is crucial in these size ranges as shown by Bei and George et al. for samples with FIB induced damage or pre-strained samples (increasing dislocation content starting at zero) [257, 258]. A final comparison can be made by plotting the size scaling behavior as function of grain size (Figure 4.26b) or sample size (Figure 4.26c), as recently proposed by Malyar et al. [25]. In their experimental study, the power law fit of the bicrystal was shifted to higher stresses when sample size was considered, but aligned almost perfectly with the single crystalline references when grain size was considered. This suggested that bicrystals possessing grain boundaries with easy slip transfer and without a back-stress caused by a dislocation pile-up show the same size scaling as the corresponding single crystals due to the same dislocation source statistics. This suggested that the grain size needs to be considered as the characteristic length scale instead of the pillar diameter. In addition, *in situ* µLaue diffraction experiments were performed by this group on the same boundary revealing an increase in grain boundary misorientation angle being indicative for dislocation absorption at the grain boundary. Regarding the present thesis work, the categorization to have grain or sample size as characteristic length scale seems difficult, as the slope does remain approximately the same for single crystals and bicrystals here, however, the shift seems not to be definite for the data obtained, which is partially also related to the change in slope for smaller structures. More experiments to increase statistics could help to get a clearer picture. Nevertheless, the boundary does reflect similar behavior as described in [25] for a penetrable grain boundary. Post mortem analysis of micrometer sized compression samples in the present study were analysed in STEM (Figure 6.4). Deflection of the grain boundary was only occuring in distinct regions along the boundary. Two striking observations were made, first, a

boundary deflection of about 170 nm and, second, the introduction of a twist component of about 3°. Both observation can be seen as strong indication for dislocation absorption at the grain boundary, as found by Malyar et al during µLaue experiments. Considering a Burgers vector length of 0.256 nm for Cu, the measured boundary deflection equals the amount of 656 full dislocations being absorbed into the boundary and a 3° twist component does agree well with about 2.5° change in grain boundary angle reported by Malyar et al. [25]. However, it could be argued that this occurs as a result of the elastic anisotropy. Mechanisms that could theoretically occur due to this anisotropy are elasto-plastic buckling or shear coupled GB motion. The former being unlikely as a rough estimate would lead to a critical load for buckling to occur on the order of 1 Newton, which exceeds experimental loads significantly. Finally, it has to be mentioned that from the obtained results, conclusive statements could not be drawn in regard of the influence of a nanofaceting of the grain boundary on mechanical properties. Especially the dislocation content appears to complicate the experiment, as small pillars for in situ TEM compression received an additional thermal treatment resulting in almost dislocation free pillars. Cu(Ag) pillars also experienced an additional heat treatment, i.e. the segregation treatment, which resulted also in a different defect content and lowered the yield strength of the single crystals already by up to 30 MPa (Figure 6.3b and 6.3c). To separate these effects a lot more samples would be required to capture the underlying statistics well enough. For comparison, Malyar et al. demonstrated for example experimentally that the barrier strength for slip transfer across a coherent $\sum 3$ {111} twin boundary is on the order of just 17 MPa [259]. However, Sangid et al. found that the energy barrier for dislocation nucleation and transmission is higher for $\Sigma 3$ grain boundaries than for $\Sigma 5$ boundaries [229], which effectively means, that influences of the Ag-induced GB transition on plastic deformation behavior should dissappear in the dislocation density difference of the samples. Nevertheless, bicrystalline compression samples with diameters allowing electron transparancy revealed deformation mechanisms that can be compared to the in situ TEM tensile tests on bicrystalline thin foils (Figure 4.29). In fact, the compression results comprehend and partly confirm the tensile testing results and will be discussed in the following at the adequate position in chapter 4.4.

List of Figures

List of Tables

Bibliography

[1] Brand, A., Allen, L., Altman, M., Hlava, M. & Scott, J. Beyond authorship: attribution, contribution, collaboration, and credit. *Learned Publishing* **28**, 151–155 (2015).

[2] Petch, N. The cleavage strengh of polycrystals. *Journal of the Iron and Steel Institute* **174**, 25–28 (1953).

[3] Hall, E. The deformation and ageing of mild steel: III discussion of results. *Proceedings of the Physical Society. Section B* **64**, 747 (1951).

[4] Ames, M. *et al.* Unraveling the nature of room temperature grain growth in nanocrystalline materials. *Acta Materialia* **56**, 4255–4266 (2008).

[5] Tschopp, M., Murdoch, H., Kecskes, L. & Darling, K. "Bulk" nanocrystalline metals: review of the current state of the art and future opportunities for copper and copper alloys. *JOM* **66**, 1000–1019 (2014).

[6] Wang, N., Ji, Y., Wang, Y., Wen, Y. & Chen, L.-Q. Two modes of grain boundary pinning by coherent precipitates. *Acta Materialia* **135**, 226–232 (2017).

[7] Meiners, T., Duarte, J., Richter, G., Dehm, G. & Liebscher, C. Tantalum and zirconium induced structural transitions at complex [111] tilt grain boundaries in copper. *Acta Materialia* **190**, 93–104 (2020).

[8] Chookajorn, T., Murdoch, H. A. & Schuh, C. A. Design of stable nanocrystalline alloys. *Science* **337**, 951–954 (2012).

[9] Sigle, W., Ciiang, L.-S. & Gust, W. On the correlation between grain-boundary segregation, faceting and embrittlement in Bi-doped Cu. *Philosophical Magazine A* **82**, 1595–1608 (2002).

[10] Gibbs, J. W. *The Collected Works of J. Willard Gibbs-Volume 1: Thermodynamics* (Yale University Press, 1945).

[11] Hart, E. W. Two-dimensional phase transformation in grain boundaries. *Scripta Metallurgica* **2**, 179–182 (1968).

[12] Cahn, J. Transitions and phase equilibria among grain boundary structures. *Le Journal de Physique Colloques* **43**, C6–199 (1982).

[13] Rottman, C. Theory of phase transitions at internal interfaces. *Le Journal de Physique Colloques* **49**, C5–313 (1988).

[14] O'Brien, C., Barr, C., Price, P., Hattar, K. & Foiles, S. Grain boundary phase transformations in PtAu and relevance to thermal stabilization of bulk nanocrystalline metals. *Journal of Materials Science* **53**, 2911–2927 (2018).

[15] Dillon, S. J., Tang, M., Carter, W. C. & Harmer, M. P. Complexion: A new concept for kinetic engineering in materials science. *Acta Materialia* **55**, 6208–6218 (2007).

[16] Mompiou, F. *et al.* Inter- and intragranular plasticity mechanisms in ultrafine-grained Al thin films: An in situ tem study. *Acta Materialia* **61**, 205–216 (2013).

[17] Lee, T., Robertson, I. & Birnbaum, H. TEM in situ deformation study of the interaction of lattice dislocations with grain boundaries in metals. *Philosophical Magazine A* **62**, 131–153 (1990).

[18] International Copper Association. Global-2019-semis-end-use-data. URL `https://copperalliance.org/wp-content/uploads/2017/03/Global-2018-Semis-End-Use-Data-Set.xlsx`.

[19] Navigant Research. Study: Is there a threat to copper in renewables? URL `https://copperalliance.org/wp-content/uploads/2019/04/navigant-is-there-a-threat-to-copper-in-renewables.pdf`.

[20] International Copper Association. Renewables to significantly increase copper demand by 2027. URL `https://copperalliance.org/wp-content/uploads/2019/04/fact-sheet-renewables-to-significantly-increase-copper-demand-by-2027.pdf`.

[21] Divinski, S., Lohmann, M. & Herzig, C. Ag grain boundary diffusion and segregation in Cu: Measurements in the types B and C diffusion regimes. *Acta Materialia* **49**, 249–261 (2001).

[22] Divinski, S. V., Edelhoff, H. & Prokofjev, S. Diffusion and segregation of silver in copper $\Sigma 5$ (310) grain boundary. *Physical Review B* **85**, 144104 (2012).

[23] Razumovskiy, V., Divinski, S. & Romaner, L. Solute segregation in Cu: DFT vs. Experiment. *Acta Materialia* **147**, 122–132 (2018).

[24] Imrich, P. J., Kirchlechner, C., Motz, C. & Dehm, G. Differences in deformation behavior of bicrystalline Cu micropillars containing a twin boundary or a large-angle grain boundary. *Acta Materialia* **73**, 240–250 (2014).

[25] Malyar, N., Micha, J.-S., Dehm, G. & Kirchlechner, C. Size effect in bi-crystalline micropillars with a penetrable high angle grain boundary. *Acta Materialia* **129**, 312–320 (2017).

[26] Kirchlechner, C. *et al.* Investigation of reversible plasticity in a micron-sized, single crystalline copper bending beam by X-ray μ Laue diffraction. *Philosophical Magazine* **92**, 3231–3242 (2012).

[27] Heckman, N. M., Berwind, M. F., Eberl, C. & Hodge, A. M. Microstructural deformation in fatigued nanotwinned copper alloys. *Acta Materialia* **144**, 138–144 (2018).

[28] Li, Y., Tao, N. & Lu, K. Microstructural evolution and nanostructure formation in copper during dynamic plastic deformation at cryogenic temperatures. *Acta Materialia* **56**, 230–241 (2008).

[29] Subramanian, P. & Perepezko, J. The Ag-Cu (silver-copper) system. *Journal of Phase Equilibria* **14**, 62–75 (1993).

[30] Li, W. *et al.* Printable and flexible copper–silver alloy electrodes with high conductivity and ultrahigh oxidation resistance. *ACS Applied Materials & Interfaces* **9**, 24711–24721 (2017).

[31] Leoni AG. Cables with innovative conductor materials - cuag. URL `https://d1619fmrcx9c43.cloudfront.net/fileadmin/automotive_cables/publications/data_sheet/copper_silver.pdf?1475650294`.

[32] Li, J. *et al.* Ultrahigh oxidation resistance and high electrical conductivity in copper-silver powder. *Scientific Reports* **6**, 1–10 (2016).

[33] Sakai, Y. & Schneider-Muntau, H.-J. Ultra-high strength, high conductivity Cu-Ag alloy wires. *Acta Materialia* **45**, 1017 – 1023 (1997).

[34] Seah, M. Adsorption-induced interface decohesion. *Acta Metallurgica* **28**, 955–962 (1980).

[35] Lozovoi, A. & Paxton, A. Boron in copper: A perfect misfit in the bulk and cohesion enhancer at a grain boundary. *Physical Review B* **77**, 165413 (2008).

[36] Nieh, T. & Nix, W. Embrittlement of copper due to segregation of oxygen to grain boundaries. *Metallurgical Transactions A* **12**, 893–901 (1981).

[37] Lozovoi, A., Paxton, A. & Finnis, M. Structural and chemical embrittlement of grain boundaries by impurities: a general theory and first-principles calculations for copper. *Physical Review B* **74**, 155416 (2006).

[38] Meiners, T., Peng, Z., Gault, B., Liebscher, C. H. & Dehm, G. Sulfur – induced embrittlement in high-purity, polycrystalline copper. *Acta Materialia* **156**, 64 – 75 (2018).

[39] Korzhavyi, P., Abrikosov, I. & Johansson, B. Theoretical investigation of sulfur solubility in pure copper and dilute copper-based alloys. *Acta Materialia* **47**, 1417 – 1424 (1999).

[40] Gottstein, G. *Physikalische Grundlagen der Materialkunde* (Springer-Verlag, 2007).

[41] Peierls, R. The size of a dislocation. *Proceedings of the Physical Society* **52**, 34 (1940).

[42] Nabarro, F. Dislocations in a simple cubic lattice. *Proceedings of the Physical Society* **59**, 256 (1947).

[43] Lejcek, P. *Grain boundary segregation in metals*, vol. 136 (Springer Science & Business Media, 2010).

[44] Gleiter, H. The structure and properties of high-angle grain boundaries in metals. *Physica Status Solidi (b)* **45**, 9–38 (1971).

[45] Priester, L. *Grain boundaries: from theory to engineering*, vol. 172 (Springer Science & Business Media, 2012).

[46] Brillouin, M. Théorie des déformations permanentes des métaux industriels. *Annales de chimie et de physique* **13**, 377–404 (1898).

[47] Rosenhain, W. & Ewen, D. The intercrystalline cohesion of metals (second paper). *Journal of the Institute of Metals* **10**, 119 (1913).

[48] Shewmon, P. *Transformations in metals*. McGraw-Hill series in materials science and engineering (McGraw-Hill, 1969).

[49] Ashby, M. Boundary defects, and atomistic aspects of boundary sliding and diffusional creep. *Surface Science* **31**, 498 – 542 (1972).

[50] Zhang, H., Srolovitz, D. J., Douglas, J. F. & Warren, J. A. Grain boundaries exhibit the dynamics of glass-forming liquids. *Proceedings of the National Academy of Sciences* **106**, 7735–7740 (2009).

[51] Read, W. T. & Shockley, W. Dislocation models of crystal grain boundaries. *Physical Review* **78**, 275–289 (1950).

[52] Brandon, D. The structure of high-angle grain boundaries. *Acta Metallurgica* **14**, 1479–1484 (1966).

[53] Winning, M., Gottstein, G. & Shvindlerman, L. On the mechanisms of grain boundary migration. *Acta Materialia* **50**, 353–363 (2002).

[54] Glicksman, M. & Vold, C. Heterophase dislocations—an approach towards interpreting high temperature grain boundary behavior. *Surface Science* **31**, 50–67 (1972).

[55] Tschopp, M. & McDowell, D. Asymmetric tilt grain boundary structure and energy in copper and aluminium. *Philosophical Magazine* **87**, 3871–3892 (2007).

[56] Kronberg, M. & Wilson, u. F. Secondary recrystallization in copper. *JOM* **1**, 501–514 (1949).

[57] Peter, N. J., Liebscher, C. H., Kirchlechner, C. & Dehm, G. Beam-induced atomic migration at Ag-containing nanofacets at an asymmetric Cu grain boundary. *Journal of Materials Research* **32**, 968–982 (2017).

[58] Ranganathan, S. On the geometry of coincidence-site lattices. *Acta Crystallographica* **21**, 197–199 (1966).

[59] Frolov, T. *et al.* Grain boundary phases in bcc metals. *Nanoscale* **10**, 8253–8268 (2018).

[60] Luzzi, D. E., Yan, M., Šob, M. & Vitek, V. Atomic structure of a grain boundary in a metallic alloy: Combined electron microscope and theoretical study. *Physical Review Letters* **67**, 1894 (1991).

[61] Bowers, M., Ophus, C., Gautam, A., Lancon, F. & Dahmen, U. Step coalescence by collective motion at an incommensurate grain boundary. *Physical Review Letters* **116**, 106102 (2016).

[62] Zhang, W., Sachenko, P. & Gladwell, I. Thermal grain boundary grooving with anisotropic surface free energies. *Acta Materialia* **52**, 107–116 (2004).

[63] Jones, D. The measurement of solid-liquid interfacial energies from the shapes of grain-boundary grooves. *Philosophical Magazine* **27**, 569–584 (1973).

[64] Frolov, T., Olmsted, D. L., Asta, M. & Mishin, Y. Structural phase transformations in metallic grain boundaries. *Nature Communications* **4**, 1899 (2013).

[65] Wu, Z., Zhang, Y. & Srolovitz, D. Grain boundary finite length faceting. *Acta Materialia* **57**, 4278–4287 (2009).

[66] Hristova, E., Janisch, R., Drautz, R. & Hartmaier, A. Solubility of carbon in α-iron under volumetric strain and close to the Sigma (3 1 0)[0 0 1] grain boundary: comparison of DFT and empirical potential methods. *Computational Materials Science* **50**, 1088–1096 (2011).

[67] Scheiber, D., Pippan, R., Puschnig, P. & Romaner, L. Ab initio calculations of grain boundaries in bcc metals. *Modelling and Simulation in Materials Science and Engineering* **24**, 035013 (2016).

[68] Han, J., Thomas, S. L. & Srolovitz, D. J. Grain-boundary kinetics: A unified approach. *Progress in Materials Science* **98**, 386–476 (2018).

[69] Bollmann, W. *Crystal defects and crystalline interfaces* (Springer Science & Business Media, 2012).

[70] Pond, R. & Bollmann, W. The symmetry and interfacial structure of bicrystals. *Philosophical Transactions of the Royal Society of London. Series A, Mathematical and Physical Sciences* **292**, 449–472 (1979).

[71] Sutton, A. P., Balluffi, R. W. & Sutton, A. Interfaces in crystalline materials (1995).

[72] Cahn, J. Adapting thermodynamics for materials science problems. *Journal of Phase Equilibria* **15**, 373–379 (1994).

[73] Gibbs, J. W. The collected works of J. Willard Gibbs. Tech. Rep., Yale Univ. Press, (1948).

[74] Hart, E. W. *Grain Boundary Phase Transformations*, 155–170 (Springer US, New York, NY, 1972).

[75] Frolov, T., Divinski, S. V., Asta, M. & Mishin, Y. Effect of interface phase transformations on diffusion and segregation in high-angle grain boundaries. *Physical Review Letters* **110**, 255502 (2013).

[76] Luo, J., Cheng, H., Asl, K. M., Kiely, C. J. & Harmer, M. P. The role of a bilayer interfacial phase on liquid metal embrittlement. *Science* **333**, 1730–1733 (2011).

[77] Luo, J., Wang, H. & Chiang, Y.-M. Origin of solid-state activated sintering in Bi_2O_3-doped ZnO. *Journal of the American Ceramic Society* **82**, 916–920 (1999).

[78] Tang, M., Carter, W. C. & Cannon, R. M. Diffuse interface model for structural transitions of grain boundaries. *Physical Review B* **73**, 024102 (2006).

[79] Rickman, J. & Luo, J. Layering transitions at grain boundaries. *Current Opinion in Solid State and Materials Science* **20**, 225–230 (2016).

[80] Cantwell, P. R. *et al.* Grain boundary complexions. *Acta Materialia* **62**, 1–48 (2014).

[81] Donald, A. & Brown, L. Grain boundary faceting in Cu-Bi alloys. *Acta Metallurgica* **27**, 59–66 (1979).

[82] Choi, J. S. & Yoon, D. Y. The temperature dependence of abnormal grain growth and grain boundary faceting in 316L stainless steel. *ISIJ International* **41**, 478–483 (2001).

[83] Koo, J. B. & Yoon, D. Y. The dependence of normal and abnormal grain growth in silver on annealing temperature and atmosphere. *Metallurgical and Materials Transactions A* **32**, 469–475 (2001).

[84] Barg, A., Rabkin, E. & Gust, W. Faceting transformation and energy of a Σ3 grain boundary in silver. *Acta Metallurgica et Materialia* **43**, 4067–4074 (1995).

[85] Brown, J. A. & Mishin, Y. Dissociation and faceting of asymmetrical tilt grain boundaries: Molecular dynamics simulations of copper. *Physical Review B* **76**, 134118 (2007).

[86] Hamilton, J. C., Siegel, D. J., Daruka, I. & Léonard, F. Why do grain boundaries exhibit finite facet lengths? *Physical Review Letters* **90**, 246102 (2003).

[87] Hadian, R., Grabowski, B., Finnis, M. W. & Neugebauer, J. Migration mechanisms of a faceted grain boundary. *Physical Review Materials* **2**, 043601 (2018).

[88] Shibata, N., Oba, F., Yamamoto, T., Sakuma, T. & Ikuhara, Y. Grain-boundary faceting at a Σ3 [110]/{112} grain boundary in a cubic zirconia bicrystal. *Philosophical Magazine* **83**, 2221–2246 (2003).

[89] Medlin, D., Cohen, D. & Pond, R. Accommodation of coherency strain by interfacial disconnections at a $90\,^\circ< 110>$ grain boundary in gold. *Philosophical Magazine Letters* **83**, 223–232 (2003).

[90] Ference, T. & Balluffi, R. Observation of a reversible grain boundary faceting transition induced by changes of composition. *Scripta Metallurgica* **22**, 1929–1934 (1988).

[91] Loier, C. & Boos, J. Striation and faceting of grain boundaries in nickel due to sulfur and other elements. *Metallurgical Transactions A* **12**, 129–135 (1981).

[92] Kundu, A., Asl, K. M., Luo, J. & Harmer, M. P. Identification of a bilayer grain boundary complexion in Bi-doped Cu. *Scripta Materialia* **68**, 146–149 (2013).

[93] Yu, Z. *et al.* Segregation-induced ordered superstructures at general grain boundaries in a nickel-bismuth alloy. *Science* **358**, 97–101 (2017).

[94] Peter, N. J. *et al.* Segregation-induced nanofaceting transition at an asymmetric tilt grain boundary in copper. *Physical Review Letters* **121**, 255502 (2018).

[95] Harris, D. J., Watson, G. W. & Parker, S. C. Computer simulation of pressure-induced structural transitions in MgO [001] tilt grain boundaries. *American Mineralogist* **84**, 138–143 (1999).

[96] Frolov, T., Asta, M. & Mishin, Y. Segregation-induced phase transformations in grain boundaries. *Physical Review B* **92**, 020103 (2015).

[97] Frolov, T. & Mishin, Y. Thermodynamics of coherent interfaces under mechanical stresses. II. application to atomistic simulation of grain boundaries. *Physical Review B* **85**, 224107 (2012).

[98] Stoffers, A. *et al.* Complex nanotwin substructure of an asymmetric Σ9 tilt grain boundary in a silicon polycrystal. *Physical Review Letters* **115**, 235502 (2015).

[99] Medlin, D., Hattar, K., Zimmerman, J., Abdeljawad, F. & Foiles, S. Defect character at grain boundary facet junctions: Analysis of an asymmetric $\Sigma = 5$ grain boundary in Fe. *Acta Materialia* **124**, 383–396 (2017).

[100] Hondros, E., Seah, M., Hofmann, S. & Lejcek, P. Physical metallurgy. *Elsevier Sci Pub BV, Netherlands* **856** (1983).

[101] Feng, B. *et al.* Atomically ordered solute segregation behaviour in an oxide grain boundary. *Nature Communications* **7**, 11079 (2016).

[102] Kondo, S., Ishihara, A., Tochigi, E., Shibata, N. & Ikuhara, Y. Direct observation of atomic-scale fracture path within ceramic grain boundary core. *Nature Communications* **10**, 2112 (2019).

[103] Faulkner, R. Segregation to boundaries and interfaces in solids. *International Materials Reviews* **41**, 198–208 (1996).

[104] Hume-Rothery, W. & Raynor, G. The structure of metals and alloys, Institute of metals (1969).

[105] Hondros, E. & Seah, M. Grain boundary activity measurements by auger electron spectroscopy. *Scripta Metallurgica* **6**, 1007–1012 (1972).

[106] Hondros, E. & Seah, M. Segregation to interfaces. *International Metals Reviews* **22**, 262–301 (1977).

[107] MacLean, D. Grain boundaries in metals (1957).

[108] Raabe, D. *et al.* Grain boundary segregation engineering in metallic alloys: A pathway to the design of interfaces. *Current Opinion in Solid State and Materials Science* **18**, 253–261 (2014).

[109] Petzow, G. Metallographisches, keramographisches und plastographisches Ätzen (2006).

[110] Castellano, G., Osan, J. & Trincavelli, J. Analytical model for the Bremsstrahlung spectrum in the 0.25–20 keV photon energy range. *Spectrochimica Acta Part B: Atomic Spectroscopy* **59**, 313–319 (2004).

[111] Reimer, L. Scanning electron microscopy: physics of image formation and microanalysis (2000).

[112] Giannuzzi, L. A. *et al.* *Introduction to focused ion beams: instrumentation, theory, techniques and practice* (Springer Science & Business Media, 2004).

[113] Orloff, J., Swanson, L. & Utlaut, M. *High resolution focused ion beams: FIB and its applications: Fib and its applications: the physics of liquid metal ion sources and ion optics and their application to focused ion beam technology* (Springer Science & Business Media, 2003).

[114] Williams, D. B. & Carter, C. B. *Transmission electron microscopy: a textbook for materials science* (Springer, New York, 2008), 2nd ed edn.

[115] Fultz, B. & Howe, J. M. *Transmission electron microscopy and diffractometry of materials* (Springer Science & Business Media, 2012).

[116] Egerton, R. F. *et al.* *Physical principles of electron microscopy*, vol. 56 (Springer, 2005).

[117] Pennycook, S. J. & Nellist, P. D. *Scanning transmission electron microscopy: imaging and analysis* (Springer Science & Business Media, 2011).

[118] Pennycook, S. J. Scanning transmission electron microscopy: Z-contrast imaging. *Characterization of Materials* 1–29 (2002).

[119] Pennycook, S. *et al.* Scanning transmission electron microscopy for nanostructure characterization. In *Scanning microscopy for nanotechnology*, 152–191 (Springer, 2006).

[120] Morishita, S. *et al.* Attainment of 40.5 pm spatial resolution using 300 kV scanning transmission electron microscope equipped with fifth-order aberration corrector. *Microscopy* **67**, 46–50 (2018).

[121] Nellist, P. D. *Scanning Transmission Electron Microscopy*, 2–2 (Springer International Publishing, Cham, 2019).

[122] Weyland, M. & Muller, D. A. Tuning the convergence angle for optimum STEM performance. *arXiv preprint arXiv:2008.12870* (2020).

[123] Zamani, R. R., Hage, F. S., Lehmann, S., Ramasse, Q. M. & Dick, K. A. Atomic-resolution spectrum imaging of semiconductor nanowires. *Nano Letters* **18**, 1557–1563 (2017).

[124] Longo, P., Thomas, P., Aitouchen, A., Schaffer, B. & Twesten, R. D. Simultaneous EELS/EDS composition mapping at atomic resolution using fast STEM spectrum-imaging. *Microscopy Today* **21**, 36–40 (2013).

[125] Wenner, S., Jones, L., Marioara, C. D. & Holmestad, R. Atomic-resolution chemical mapping of ordered precipitates in al alloys using energy-dispersive x-ray spectroscopy. *Micron* **96**, 103–111 (2017).

[126] Pennycook, S. & Jesson, D. Atomic resolution Z-contrast imaging of interfaces. *Acta Metallurgica et Materialia* **40**, S149–S159 (1992).

[127] Hartel, P., Rose, H. & Dinges, C. Conditions and reasons for incoherent imaging in STEM. *Ultramicroscopy* **63**, 93–114 (1996).

[128] URL https://www.globalsino.com/EM/page2754.html.

[129] Borisevich, A. Y., Lupini, A. R. & Pennycook, S. J. Depth sectioning with the aberration-corrected scanning transmission electron microscope. *Proceedings of the National Academy of Sciences* **103**, 3044–3048 (2006).

[130] van Benthem, K. & Pennycook, S. 4.09 - Atomic resolution characterization of semiconductor materials by aberration-corrected transmission electron microscopy. In Bhattacharya, P., Fornari, R. & Kamimura, H. (eds.) *Comprehensive Semiconductor Science and Technology*, 287 – 307 (Elsevier, Amsterdam, 2011).

[131] Pennycook, S., Jesson, D., Chisholm, M., Ferridge, A. & Seddon, M. Sub-angstrom microscopy through incoherent imaging and image reconstruction. Tech. Rep., Oak Ridge National Lab. (1992).

[132] Watanabe, M. *et al.* Improvements in the X-ray analytical capabilities of a scanning transmission electron microscope by spherical-aberration correction. *Microscopy and Microanalysis* **12**, 515–526 (2006).

[133] http://photos.labwrench.com/equipmentManuals/11006 4390.pdf. Chemistem technology - a revolution in EDX analytics.

[134] Meiners, T. Grain boundary structure, phase transitions and segregation phenomena in copper alloys (2020).

[135] Castaing, R. Application of electron probes to local chemical and crystallographic analysis. *Ph. D. Thesis (University of Paris)* (1951).

[136] Cliff, G. & Lorimer, G. The quantitative analysis of thin specimens. *Journal of Microscopy* **103**, 203–207 (1975).

[137] Kothleitner, G. *et al.* Quantitative elemental mapping at atomic resolution using X-ray spectroscopy. *Physical Review Letters* **112**, 085501 (2014).

[138] Egerton, R., Li, P. & Malac, M. Radiation damage in the TEM and SEM. *Micron* **35**, 399–409 (2004).

[139] Kisielowski, C. *et al.* Detection of single atoms and buried defects in three dimensions by aberration-corrected electron microscope with 0.5-Å information limit. *Microscopy and Microanalysis* **14**, 469–477 (2008).

[140] Wang, Y. *et al.* Atomic-scale quantitative analysis of lattice distortions at interfaces of two-dimensionally Sr-doped La_2CuO_4 superlattices. *ACS Applied Materials & Interfaces* **8**, 6763–6769 (2016).

[141] Krivanek, O. L. *et al.* Gentle STEM: ADF imaging and EELS at low primary energies. *Ultramicroscopy* **110**, 935–945 (2010).

[142] McBride, J. R., Kippeny, T. C., Pennycook, S. J. & Rosenthal, S. J. Aberration-corrected Z-contrast scanning transmission electron microscopy of CdSe nanocrystals. *Nano Letters* **4**, 1279–1283 (2004).

[143] Van Aert, S. *et al.* Procedure to count atoms with trustworthy single-atom sensitivity. *Physical Review B* **87**, 064107 (2013).

[144] De Backer, A. *et al.* Dose limited reliability of quantitative annular dark field scanning transmission electron microscopy for nano-particle atom-counting. *Ultramicroscopy* **151**, 56–61 (2015).

[145] Van den Bos, K. H. *et al.* Unscrambling mixed elements using high angle annular dark field scanning transmission electron microscopy. *Physical Review Letters* **116**, 246101 (2016).

[146] MacArthur, K. *et al.* Probe integrated scattering cross sections in the analysis of atomic resolution HAADF stem images. *Ultramicroscopy* **133**, 109–119 (2013).

[147] Ishikawa, R. *et al.* Direct observation of dopant atom diffusion in a bulk semiconductor crystal enhanced by a large size mismatch. *Physical Review Letters* **113**, 155501 (2014).

[148] Han, C. W. *et al.* Migration of single iridium atoms and tri-iridium clusters on MgO surfaces: Aberration-corrected STEM imaging and ab initio calculations. *The Journal of Physical Chemistry Letters* **6**, 4675–4679 (2015).

[149] Yankovich, A. B. *et al.* Picometre-precision analysis of scanning transmission electron microscopy images of platinum nanocatalysts. *Nature Communications* **5**, 1–7 (2014).

[150] Jones, L. Quantitative ADF STEM: acquisition, analysis and interpretation. In *IOP Conference Series: Materials Science and Engineering*, vol. 109, 012008 (IOP Publishing, 2016).

[151] Findlay, S. D. *et al.* Annular bright-field scanning transmission electron microscopy: Direct and robust atomic-resolution imaging of light elements in crystalline materials. *Microscopy Today* **25**, 36–41 (2017).

[152] Kirkland, E. J. *Advanced computing in electron microscopy* (Springer, New York, 2010), second edition edn.

[153] Ophus, C. A fast image simulation algorithm for scanning transmission electron microscopy. *Advanced Structural and Chemical Imaging* **3**, 13 (2017).

[154] Pryor, A., Ophus, C. & Miao, J. A streaming multi-GPU implementation of image simulation algorithms for scanning transmission electron microscopy. *Advanced Structural and Chemical Imaging* **3**, 15 (2017).

[155] Thompson, K. *et al.* In situ site-specific specimen preparation for atom probe tomography. *Ultramicroscopy* **107**, 131–139 (2007).

[156] Miller, M., Russell, K. & Thompson, G. Strategies for fabricating atom probe specimens with a dual beam FIB. *Ultramicroscopy* **102**, 287–298 (2005).

[157] Schwarz, T. *et al.* Atom probe study of $Cu_2ZnSnSe_4$ thin-films prepared by co-evaporation and post-deposition annealing. *Applied Physics Letters* **102**, 042101 (2013).

[158] Felfer, P. J. *et al.* A quantitative atom probe study of the Nb excess at prior austenite grain boundaries in a nb microalloyed strip-cast steel. *Acta Materialia* **60**, 5049–5055 (2012).

[159] Krakauer, B. W. & Seidman, D. N. Absolute atomic-scale measurements of the Gibbsian interfacial excess of solute at internal interfaces. *Physical Review B* **48**, 6724 (1993).

[160] Gault, B., Moody, M. P., Cairney, J. M. & Ringer, S. P. *Atom probe microscopy*, vol. 160 (Springer Science & Business Media, 2012).

[161] Allen, M. P. *et al.* Introduction to molecular dynamics simulation. *Computational Soft Matter: from synthetic polymers to proteins* **23**, 1–28 (2004).

[162] Brink, T. *Heterogeneities in Metallic Glasses: Atomistic Computer Simulations on the Structure and Mechanical Properties of Copper-Zirconium Alloys and Composites*. Ph.D. thesis, Technische Universität Darmstadt, Darmstadt (2017).

[163] Lennard-Jones, J. E. Cohesion. *Proceedings of the Physical Society* **43**, 461 (1931).

[164] Stott, M. & Zaremba, E. Quasiatoms: An approach to atoms in nonuniform electronic systems. *Physical Review B* **22**, 1564 (1980).

[165] Daw, M. S. & Baskes, M. I. Embedded-atom method: Derivation and application to impurities, surfaces, and other defects in metals. *Physical Review B* **29**, 6443 (1984).

[166] Nosé, S. A unified formulation of the constant temperature molecular dynamics methods. *The Journal of Chemical Physics* **81**, 511–519 (1984).

[167] Hoover, W. G. Canonical dynamics: Equilibrium phase-space distributions. *Physical Review A* **31**, 1695 (1985).

[168] Sadigh, B. *et al.* Scalable parallel Monte Carlo algorithm for atomistic simulations of precipitation in alloys. *Physical Review B* **85**, 184203 (2012).

[169] Hastings, W. K. Monte Carlo sampling methods using Markov chains and their applications (1970).

[170] van de Walle, A. v. & Asta, M. Self-driven lattice-model monte carlo simulations of alloy thermodynamic properties and phase diagrams. *Modelling and Simulation in Materials Science and Engineering* **10**, 521 (2002).

[171] Jones, L. *et al.* Smart align–a new tool for robust non-rigid registration of scanning microscope data. *Advanced Structural and Chemical Imaging* **1**, 1–16 (2015).

[172] Hsieh, W.-K., Chen, F.-R., Kai, J.-J. & Kirkland, A. Resolution extension and exit wave reconstruction in complex HREM. *Ultramicroscopy* **98**, 99–114 (2004).

[173] Peng, L.-M., Ren, G., Dudarev, S. & Whelan, M. Debye–waller factors and absorptive scattering factors of elemental crystals. *Acta Crystallographica Section A: Foundations of Crystallography* **52**, 456–470 (1996).

[174] Williams, P., Mishin, Y. & Hamilton, J. An embedded-atom potential for the Cu–Ag system. *Modelling and Simulation in Materials Science and Engineering* **14**, 817 (2006).

[175] Sutton, A. & Balluffi, R. *Interfaces in Crystalline Materials*. Oxford Classic Texts in the Physical Sciences (OUP Oxford, 2006).

[176] Schweinfest, R., Paxton, A. T. & Finnis, M. W. Bismuth embrittlement of copper is an atomic size effect. *Nature* **432**, 1008 (2004).

[177] Duscher, G., Chisholm, M. F., Alber, U. & Rühle, M. Bismuth-induced embrittlement of copper grain boundaries. *Nature Materials* **3**, 621–626 (2004).

[178] *See Supplemental Material at http://link.aps.org/ supplemental/10.1103/PhysRevLett.121.255502 for all the experimental and simulation details* .

[179] Hadian, R., Grabowski, B., Race, C. P. & Neugebauer, J. Atomistic migration mechanisms of atomically flat, stepped, and kinked grain boundaries. *Physical Review B* **94**, 165413 (2016).

[180] Plimpton, S. Fast parallel algorithms for short-range molecular dynamics. *Journal of Computational Physics* **117**, 1–19 (1995).

[181] Yang, S., Zhou, N., Zheng, H., Ong, S. P. & Luo, J. First-order interfacial transformations with a critical point: Breaking the symmetry at a symmetric tilt grain boundary. *Physical Review Letters* **120**, 085702 (2018).

[182] Schusteritsch, G., Kühne, T. D., Guo, Z. X. & Kaxiras, E. The effect of Ag, Pb and Bi impurities on grain boundary sliding and intergranular decohesion in copper. *Philosophical Magazine* **96**, 2868–2886 (2016).

[183] LeBeau, J. M., Findlay, S. D., Allen, L. J. & Stemmer, S. Standardless atom counting in scanning transmission electron microscopy. *Nano Letters* **10**, 4405–4408 (2010).

[184] Grønlund, F. & Moore, W. J. Sputtering of silver by light ions with energies from 2 to 12 keV. *The Journal of Chemical Physics* **32**, 1540–1545 (1960).

[185] Robb, P. D. & Craven, A. J. Column ratio mapping: A processing technique for atomic resolution high-angle annular dark-field (HAADF) images. *Ultramicroscopy* **109**, 61–69 (2008).

[186] Pennycook, S. Z-contrast transmission electron microscopy: direct atomic imaging of materials. *Annual Review of Materials Science* **22**, 171–195 (1992).

[187] Wang, Z. *et al.* Quantitative Z-contrast imaging in the scanning transmission electron microscope with size-selected clusters. *Physical Review B* **84**, 073408 (2011).

[188] Ishizuka, K. A practical approach for STEM image simulation based on the FFT multislice method. *Ultramicroscopy* **90**, 71–83 (2002).

[189] Ma, Q., Liu, C., Adams, J. & Balluffi, R. Diffusion along [001] tilt boundaries in the Au/Ag system–II. atomistic modeling and interpretation. *Acta Metallurgica et Materialia* **41**, 143–151 (1993).

[190] Mishin, Y., Herzig, C., Bernardini, J. & Gust, W. Grain boundary diffusion: fundamentals to recent developments. *International Materials Reviews* **42**, 155–178 (1997).

[191] Kaplan, W. D., Chatain, D., Wynblatt, P. & Carter, W. C. A review of wetting versus adsorption, complexions, and related phenomena: the rosetta stone of wetting. *Journal of Materials Science* **48**, 5681–5717 (2013).

[192] Meiners, T., Frolov, T., Rudd, R. E., Dehm, G. & Liebscher, C. H. Observations of grain-boundary phase transformations in an elemental metal. *Nature* **579**, 375–378 (2020).

[193] Parajuli, P. *et al.* Misorientation dependence grain boundary complexions in $< 111>$ symmetric tilt Al grain boundaries. *Acta Materialia* **181**, 216–227 (2019).

[194] Prokoshkina, D., Esin, V. A. & Divinski, S. V. Experimental evidence for anomalous grain boundary diffusion of Fe in Cu and Cu-Fe alloys. *Acta Materialia* **133**, 240–246 (2017).

[195] Hu, C. & Luo, J. First-order grain boundary transformations in Au-doped Si: Hybrid Monte Carlo and molecular dynamics simulations verified by first-principles calculations. *Scripta Materialia* **158**, 11–15 (2019).

[196] Luo, Z. *et al.* A highly asymmetric interfacial superstructure in WC: Expanding the classic grain boundary segregation and new complexion theories. *Materials Horizons* **7**, 173–180 (2020).

[197] Cantwell, P. R. *et al.* Grain boundary complexion transitions. *Annual Review of Materials Research* **50**, 465–492 (2020).

[198] Straumal, B., Kogtenkova, O., Gornakova, A., Sursaeva, V. & Baretzky, B. Grain boundary faceting–roughening phenomena. *Journal of Materials Science* **51**, 382–404 (2016).

[199] Sickafus, K. E. & Sass, S. Grain boundary structural transformations induced by solute segregation. *Acta Metallurgica* **35**, 69–79 (1987).

[200] Lejček, P. & Hofmann, S. Grain boundary segregation diagrams of α-iron. *Interface Science* **1**, 163–174 (1993).

[201] Watanabe, T., Kitamura, S. & Karashima, S. Grain boundary hardening and segregation in alpha iron-tin alloy. *Acta Metallurgica* **28**, 455–463 (1980).

[202] Williams, P. & Mishin, Y. Thermodynamics of grain boundary premelting in alloys. II. atomistic simulation. *Acta Materialia* **57**, 3786–3794 (2009).

[203] Suzuki, A. & Mishin, Y. Atomic mechanisms of grain boundary diffusion: Low versus high temperatures. *Journal of Materials Science* **40**, 3155–3161 (2005).

[204] Koju, R. & Mishin, Y. Relationship between grain boundary segregation and grain boundary diffusion in Cu-Ag alloys. *arXiv preprint arXiv:2006.06591* (2020).

[205] Hickman, J. & Mishin, Y. Disjoining potential and grain boundary premelting in binary alloys. *Physical Review B* **93**, 224108 (2016).

[206] Combe, N., Mompiou, F. & Legros, M. Disconnections kinks and competing modes in shear-coupled grain boundary migration. *Physical Review B* **93**, 024109 (2016).

[207] Rajabzadeh, A., Mompiou, F., Legros, M. & Combe, N. Elementary mechanisms of shear-coupled grain boundary migration. *Physical Review Letters* **110**, 265507 (2013).

[208] Liebscher, C. H. *et al.* Strain-induced asymmetric line segregation at faceted Si grain boundaries. *Physical Review Letters* **121**, 015702 (2018).

[209] Randle, V. Grain boundary engineering: an overview after 25 years. *Materials science and technology* **26**, 253–261 (2010).

[210] Kacher, J., Eftink, B., Cui, B. & Robertson, I. Dislocation interactions with grain boundaries. *Current Opinion in Solid State and Materials Science* **18**, 227–243 (2014).

[211] Bäro, G., Gleiter, H. & Hornbogen, E. Korngrenzen als Versetzungsquellen. *Materials Science and Engineering* **3**, 92–104 (1968).

[212] Bond, G., Robertson, I. & Birnbaum, H. Effect of boron on the mechanism of strain transfer across grain boundaries in Ni$_3$Al. *Journal of Materials Research* **2**, 436–440 (1987).

[213] Berghezan, A. & Fourdeux, A. Transmission electron microscopy studies of the mechanism of plastic deformation. *Journal of Applied Physics* **30**, 1913–1922 (1959).

[214] Dingley, D. & Pond, R. On the interaction of crystal dislocations with grain boundaries. *Acta Metallurgica* **27**, 667–682 (1979).

[215] Shen, Z., Wagoner, R. & Clark, W. Dislocation and grain boundary interactions in metals. *Acta Metallurgica* **36**, 3231–3242 (1988).

[216] Robertson, I. M., Cui, B. & He, M.-R. Dislocation grain boundary interactions in irradiated metals. In *EPJ Web of Conferences*, vol. 115, 04001 (EDP Sciences, 2016).

[217] Lee, T., Robertson, I. & Birnbaum, H. An in situ transmission electron microscope deformation study of the slip transfer mechanisms in metals. *Metallurgical Transactions A* **21**, 2437–2447 (1990).

[218] Lee, T., Robertson, I. & Birnbaum, H. Anomalous slip in an fcc system. *Ultramicroscopy* **29**, 212–216 (1989).

[219] Lee, T., Robertson, I. & Birnbaum, H. Prediction of slip transfer mechanisms across grain boundaries. *Scripta Metallurgica* **23**, 799–803 (1989).

[220] Zhou, N., Yu, Z., Zhang, Y., Harmer, M. P. & Luo, J. Calculation and validation of a grain boundary complexion diagram for Bi-doped Ni. *Scripta Materialia* **130**, 165–169 (2017).

[221] Dillon, S. J. & Harmer, M. P. Relating grain-boundary complexion to grain-boundary kinetics I: Calcia-doped alumina. *Journal of the American Ceramic Society* **91**, 2304–2313 (2008).

[222] Daw, M. S. & Baskes, M. I. Semiempirical, quantum mechanical calculation of hydrogen embrittlement in metals. *Physical Review Letters* **50**, 1285 (1983).

[223] Honeycutt, J. D. & Andersen, H. C. Molecular dynamics study of melting and freezing of small Lennard-Jones clusters. *Journal of Physical Chemistry* **91**, 4950–4963 (1987).

[224] Stukowski, A. Structure identification methods for atomistic simulations of crystalline materials. *Modelling and Simulation in Materials Science and Engineering* **20**, 045021 (2012).

[225] Stukowski, A. Visualization and analysis of atomistic simulation data with OVITO–the Open Visualization Tool. *Modelling and Simulation in Materials Science and Engineering* **18**, 015012 (2009).

[226] Frolov, T. & Mishin, Y. Thermodynamics of coherent interfaces under mechanical stresses. I. Theory. *Physical Review B* **85**, 224106 (2012).

[227] Zaefferer, S. New developments of computer-aided crystallographic analysis in transmission electron microscopy. *Journal of Applied Crystallography* **33**, 10–25 (2000).

[228] Zaefferer, S. Computer-aided crystallographic analysis in the tem. *Advances in imaging and electron physics* **125**, 356–415 (2002).

[229] Sangid, M. D., Ezaz, T., Sehitoglu, H. & Robertson, I. M. Energy of slip transmission and nucleation at grain boundaries. *Acta Materialia* **59**, 283–296 (2011).

[230] Jung, I.-C., Cho, L. & De Cooman, B. C. In situ observation of the influence of Al on deformation-induced twinning in TWIP steel. *ISIJ International* **55**, 870–876 (2015).

[231] Valiev, R., Gertsman, V. Y. & Kaibyshev, O. Grain boundary structure and properties under external influences. *Physica Status Solidi A* **97**, 11–56 (1986).

[232] Van Swygenhoven, H., Derlet, P. & Hasnaoui, A. Atomic mechanism for dislocation emission from nanosized grain boundaries. *Physical Review B* **66**, 024101 (2002).

[233] Van Swygenhoven, H., Derlet, P. M. & Frøseth, A. Stacking fault energies and slip in nanocrystalline metals. *Nature Materials* **3**, 399–403 (2004).

[234] Tschopp, M. A., Spearot, D. E., McDowell, D. L. & Hirth, J. Influence of grain boundary structure on dislocation nucleation in fcc metals. *Dislocations in solids* **14**, 43–139 (2008).

[235] Oh, S. H., Legros, M., Kiener, D., Gruber, P. & Dehm, G. In situ TEM straining of single crystal Au films on polyimide: Change of deformation mechanisms at the nanoscale. *Acta Materialia* **55**, 5558–5571 (2007).

[236] Chen, M. *et al.* Deformation twinning in nanocrystalline aluminum. *Science* **300**, 1275–1277 (2003).

[237] Zhao, D., Løvvik, O. M., Marthinsen, K. & Li, Y. Impurity effect of Mg on the generalized planar fault energy of Al. *Journal of Materials Science* **51**, 6552–6568 (2016).

[238] Rice, J. R. Dislocation nucleation from a crack tip: An analysis based on the Peierls concept. *Journal of the Mechanics and Physics of Solids* **40**, 239–271 (1992).

[239] Tadmor, E. & Hai, S. A Peierls criterion for the onset of deformation twinning at a crack tip. *Journal of the Mechanics and Physics of Solids* **51**, 765–793 (2003).

[240] Tadmor, E. & Bernstein, N. A first-principles measure for the twinnability of fcc metals. *Journal of the Mechanics and Physics of Solids* **52**, 2507–2519 (2004).

[241] Bernstein, N. & Tadmor, E. Tight-binding calculations of stacking energies and twinnability in fcc metals. *Physical Review B* **69**, 094116 (2004).

[242] Jo, M. *et al.* Theory for plasticity of face-centered cubic metals. *Proceedings of the National Academy of Sciences* **111**, 6560–6565 (2014).

[243] Wang, Y., Sui, M. & Ma, E. In situ observation of twin boundary migration in copper with nanoscale twins during tensile deformation. *Philosophical Magazine Letters* **87**, 935–942 (2007).

[244] Hsiung, L., Schwartz, A. & Nieh, T. In situ TEM observations of interface sliding and migration in a refined lamellar TiAl alloy. *Intermetallics* **12**, 727–732 (2004).

[245] Shen, Y.-F. *et al.* Deformation mechanisms of a 20Mn TWIP steel investigated by in situ neutron diffraction and TEM. *Acta Materialia* **61**, 6093–6106 (2013).

[246] Zhang, H., Schuster, B. E., Wei, Q. & Ramesh, K. T. The design of accurate micro-compression experiments. *Scripta Materialia* **54**, 181–186 (2006).

[247] Imrich, P. J., Kirchlechner, C. & Dehm, G. Influence of inclined twin boundaries on the deformation behavior of Cu micropillars. *Materials Science and Engineering: A* **642**, 65–70 (2015).

[248] Imrich, P. J., Kirchlechner, C., Kiener, D. & Dehm, G. In situ TEM microcompression of single and bicrystalline samples: insights and limitations. *JOM* **67**, 1704–1712 (2015).

[249] Norfleet, D., Dimiduk, D., Polasik, S., Uchic, M. & Mills, M. Dislocation structures and their relationship to strength in deformed nickel microcrystals. *Acta Materialia* **56**, 2988–3001 (2008).

[250] Greer, J. R. & De Hosson, J. T. M. Plasticity in small-sized metallic systems: Intrinsic versus extrinsic size effect. *Progress in Materials Science* **56**, 654–724 (2011).

[251] Frick, C., Clark, B., Orso, S., Schneider, A. & Arzt, E. Size effect on strength and strain hardening of small-scale [1 1 1] nickel compression pillars. *Materials Science and Engineering: A* **489**, 319–329 (2008).

[252] Dimiduk, D., Uchic, M. & Parthasarathy, T. Size-affected single-slip behavior of pure nickel microcrystals. *Acta Materialia* **53**, 4065–4077 (2005).

[253] Greer, J. R., Oliver, W. C. & Nix, W. D. Size dependence of mechanical properties of gold at the micron scale in the absence of strain gradients. *Acta Materialia* **53**, 1821–1830 (2005).

[254] Greer, J. R. & Nix, W. D. Nanoscale gold pillars strengthened through dislocation starvation. *Physical Review B* **73**, 245410 (2006).

[255] Kiener, D., Motz, C. & Dehm, G. Micro-compression testing: A critical discussion of experimental constraints. *Materials Science and Engineering: A* **505**, 79–87 (2009).

[256] Ng, K. & Ngan, A. Stochastic nature of plasticity of aluminum micro-pillars. *Acta Materialia* **56**, 1712–1720 (2008).

[257] Bei, H., Shim, S., Miller, M., Pharr, G. & George, E. Effects of focused ion beam milling on the nanomechanical behavior of a molybdenum-alloy single crystal. *Applied Physics Letters* **91**, 111915 (2007).

[258] Bei, H., Shim, S., Pharr, G. M. & George, E. P. Effects of pre-strain on the compressive stress–strain response of Mo-alloy single-crystal micropillars. *Acta Materialia* **56**, 4762–4770 (2008).

[259] Malyar, N., Micha, J.-S., Dehm, G. & Kirchlechner, C. Dislocation-twin boundary interaction in small scale Cu Bi-crystals loaded in different crystallographic directions. *Acta Materialia* **129**, 91–97 (2017).

Scientific Curriculum Vitae

Personal Information

Name	Nicolas J. PETER
Date of Birth	April 30$^{\text{th}}$, 1988
Place of Birth	Cologne, Germany
Nationality	German

Education

2015 - present	**Dissertation**
	"Structure, chemistry and nanomechanics of grain boundaries in Cu"
	Ruhr Universität Bochum (Germany) / Fakultät für Maschinenbau
	Advisor: Prof. Dr. Gerhard Dehm
2013 - 2014	**Master thesis**
	"Helium irradiation-induced effects on tensile properties of interface-containing bi-material nanostructures"
	California Institute of Technology (USA)
	Advisor: Prof. Dr. Julia R. Greer / Co-advisor: Prof. Dr. Eduard Arzt
	Grade: 1.0
2012 - 2015	**Master studies**
	"Microtechnology & Nanostructures"
	Saarland University (Germany) / Naturwissenschaftlich Tech. Fakultät II
	Degree "Master of Science" (M.Sc.) - Grade: 1.6

2011	**Bachelor thesis**
	"Superhydrophilic to superhydrophobic wetting properties of poly(dimethylsiloxane) by different plasma combinations"
	Peking University (China)
	Advisor: Prof. Dr. Haixia Zhang / Co-advisor: Prof. Dr. Helmut Seidel
	Grade: 1.3
2008 - 2012	**Bachelor studies**
	"Microtechnology & Nanostructures"
	Saarland University (Germany) / Naturwissenschaftlich Tech. Fakultät II
	Degree "Bachelor of Science" (B.Sc.) - Grade: 2.3
2007	**Abitur**
	("University entrance qualification")
	Albert-Einstein-Gymnasium Völklingen (Germany)

Research Activity

2017	**Visiting Researcher**
	"In-situ TEM nanomechanics at high frame rates"
	Lawrence Berkeley National Laboratory / National Center for Electron Microscopy
	Advisor: Prof. Dr. Andrew Minor / Co-advisor: Dr. Vasfi B. Özdöl
2010 - 2015	**Student assistant**
	"Structure-property relationships in biological materials and metals"
	Leibniz Institute for New Materials / JRG Metallic Microstructures
	Advisor: Prof. Dr. Eduard Arzt / Co-acdvisor: Dr. Andreas S. Schneider

2010	**Practical Training**
	"Piezoresistive pressure sensor fabrication"
	Saarland University / Hochschule Kaiserslautern-Zweibrücken
	Prof. Dr. Helmut Seidel

2009 - 2010	**Student assistant**
	"Assembly of a versatile control and data acquisition system (VenDASys)"
	Saarland University / Lab for Measurement Technologies
	Advisor: Prof. Dr. Andreas Schütze / Co-advisor: Dr. René Sallier

Publications

During doctorate

2021	**N.J. Peter**, T. Brink, S. Lee, C.H. Liebscher, C. Kirchlechner and G. Dehm, "Influence of Ag segregation induced grain boundary faceting on plastic deformation mechanisms in Cu" in preparation
2021	**N.J. Peter**, E. Gärtner, H.Y. Jung, V. Uhlenwinkel, E. Jägle and G. Dehm, "Separating the influence of dislocation density and Al2O3 nanoparticles in an additively manufactured CoCrFeNi alloy" in preparation
2021	**N.J. Peter**, Erika Griesshaber, Christian Reisecker, Sabine Hild, Mariana V.G. Oliveira, Andreas Ziegler, Wolfgang W. Schmahl, Eduard Arzt, and Andreas S. Schneider, "Microstructure, texture and material property relationships in bivalve and gastropod shells" to be submitted
2021	**N.J. Peter**, M.J. Duarte, C. Kirchlechner, C.H. Liebscher and G. Dehm, "Faceting diagram for Ag segregation induced nanofaceting at an asymmetric Cu tilt grain boundary", *Acta Materialia,* vol. 214, pp. 116960, 2021

2021   E. Gärtner, H.Y. Jung, N.J. Peter, G. Dehm, E.A. Jägle, V. Uhlenwinkel, and L. Mädler, "Cohesion reduction of metal powders for additive manufacturingby nanoparticle dry-coating", *Powder Technology,* vol. 379, pp. 585-595, 2021

2020   C.M. Laursen, **N.J. Peter**, G. Gerstein, H.J. Maier, G. Dehm and C.P. Frick, "Influence of Ti_3Ni_4 Precipitates on the Indentation Induced Two-Way Shape-Memory Effect in Nickel-Titanium", *Materials Sciences and Engineering A,* vol. 792, pp. 139373, 2020

2020   H.Y. Jung, **N.J. Peter**, E. Gärtner, V. Uhlenwinkel, G. Dehm, D. Raabe and E.A. Jägle, "Bulk nanostructured AlCoCrFeMnNi chemically complex alloy synthesized by laser-powder bed fusion", *Additive Manufacturing,* vol. 35, pp. 101337, 2020

2020   M. Haines, **N.J. Peter**, E. Jägle, D. Raabe, and S.S. Babu, "In-situ synthesis of oxides by reactive process atmospheres during L-PBF of stainless steel", *Additive manufacturing,* vol. 33, pp. 101178, 2020

2020   H. Zhao, L. Huber, W. Lu, **N.J. Peter**, D. An, F. De Geuser, D. Ponge, J. Neugebauer, B. Gault and D. Raabe, "Interplay of Chemistry and Faceting at Grain Boundaries in a model Al-alloy" *Physical Review Letters*, vol. 124, pp. 106102, 2020

2020   **N.J. Peter**, M.J. Duarte, C.H. Liebscher, V. Uhlenwinkel, E.A. Jägle, and G. Dehm, "Early stage phase seperation of $AlCoCr_{0.75}Cu_{0.5}FeNi$ high-entropy powder at the nanoscale", *Journal of Alloys and Compounds,* vol. 820, pp. 153149, 2020

2019   S.-P. Tsai, P. Konijnenberg, S. Zaefferer, **N. Peter**, B. Gault, K. Kawano-Miyata, D. An, and T.A. Griffiths, "Correlative Microscopy Observation (3D EBSD + APT + TEM) on Intergranular Corrosion Behaviors in 316L Stainless Steel", *Microscopy and Microanalysis,* vol. 25, no. S2, pp. 748-749, 2019

2019   C. Gerlitzky, T.H. Tran, S. Zhang, **N.J. Peter**, C. Kuhn, C. Scheu, M. Rohwerder, and P. Groche, "3D cold pressure welded components - From the bonding mechanisms to the production of high strength joints", *Materials Science and Engineering Technology,* vol. 50, pp. 1-11, 2019

2019   P. Kürnsteiner, A. Hariharan, H.Y. Jung, **N. Peter**, M.B. Wilms, A. Weisheit, P. Barriobero-Vila, B. Gault, D. Raabe, E.A. Jägle, "Application of Atom Probe Tomography to Complex Microstructures of Laser Additively Manufactured Samples", *Microscopy and Microanalysis,* vol. 25, no. S2, pp. 2514-2515, 2019

2019   **N.J. Peter**, C. Gerlitzky, A. Altin, S. Wohletz, W. Krieger, T.H. Tran, C.H. Liebscher, G. Dehm, P. Groche and A. Erbe, "Atomic level bonding mechanism in steel/aluminium joints produced by cold pressure welding", *Materialia,* vol. 7, pp. 100396, 2019

2018   **N.J. Peter**, T. Frolov, J. Duarte, R. Hadian, C. Ophus, C.H. Liebscher, C. Kirchlechner, and G. Dehm, "Segregation induced nano-faceting of an asymmetric tilt grain boundary in copper", *Physical Review Letters,* vol. 121, pp. 255502, 2018

2018   S. Gleich, B. Breitbach, **N.J. Peter**, R. Soler, H. Bolvardi, J.M. Schneider, G. Dehm, and C. Scheu, "Thermal stability of nanocomposite Mo_2BC hard coatings deposited by magnetron sputtering", *Surface and Coatings Technology*, vol. 349, pp. 378-383, 2018

2017   **N.J. Peter**, C.H. Liebscher, C. Kirchlechner, and G. Dehm, "Beam-induced atomic migration at Ag-containing nanofacets at an asymmetric Cu grain boundary", *Journal of Materials Research*, vol. 32, no. 5, pp. 968-982, 2017

2017   S. Fleischmann, A. Tolosa, M. Zeiger, B. Krüner, **N.J. Peter**, I. Grobelseck, A. Quade, A. Kruth, and V. Presser, "Vanadia-titania multilayer nanodecoration of carbon onions via atomic layer deposition for high performance electrochemical energy storage", *Journal of Materials Chemistry A*, vol. 101, no. 22, pp. 2792-2801, 2017

2016   J. Busom, A. Schreiber, A. Tolosa, N. Jäckel, I. Grobelseck, **N.J. Peter**, and V. Presser, "Sputtering of sub-micrometer aluminium layers as compact, high-performance, light-weight current collector for supercapacitors", *Journal of Power Sources*, vol. 329, pp. 432-440, 2016

2016   M. Zeiger, T. Ariyanto, B. Krüner, **N.J. Peter**, S. Fleischmann, B.J.M. Etzold, and V. Presser, "Vanadium pentoxide/carbide-derived carbon core-shell hybrid particles for high performance electrochemical energy storage", *Journal of Materials Chemistry A*, vol. 4, no. 48, pp. 18899-18909, 2016

Before doctorate

2014   F. Wählisch, **N.J. Peter**, O.T. Abad, M.V.G. Oliveira, A.S. Schneider, W. Schmahl, E. Griesshaber, and R. Bennewitz, "Surviving the surf: The tribomechanical properties of the periostracum of Mytilus sp." *Acta biomaterialia*, vol. 10, no. 9, pp. 3978-3985, 2014

2014   E. Qin, **N.J. Peter**, M. Frensemeier, C.P. Frick, E. Arzt, and A.S. Schneider, "Vickers Indentation Induced One-Way and Two-Way Shape Memory Effect in Austenitic NiTi", *Advanced Engineering Materials*, vol. 16, no. 1, pp. 72-79, 2014

2013   Z. Chen, S. Diebels, **N.J. Peter**, and A.S. Schneider, "Identification of finite viscoelasticity and adhesion effects in nanoindentation of a soft polymer by inverse method", *Computational Materials Science*, vol. 72, pp. 127-139, 2013

2013   **N.J. Peter**, M. Frensemeier, E. Qin, C.P. Frick, E. Arzt, and A.S. Schneider, "Indentation-induced two-way shape-memory effect in NiTi", *Nano/Micro Engineered and Molecular Systems (NEMS), 2013 8th IEEE International Conference on*, IEEE, 2013

2013   X. Zhang, S. Chu, **N. Peter**, and H. Zhang, "Fabrication of tunable wetting PDMS membrane by nanostructuring and plasma treatment", *Nano/Micro Engineered and Molecular Systems (NEMS), 2013 8th IEEE International Conference on*, IEEE, 2013

2013   X. Zhang, B. Jin, S. Chu, **N. Peter**, F. Zhu, and H. Zhang, "Single-step fabrication of superhydrophobic micro/nano dual-scale PDMS film replicated from ultralow-surface-energy mold", *Micro Electro Mechanical Systems (MEMS), 2013 IEEE 26th International Conference on*, IEEE, 2013

2012   **N.J. Peter**, X. Zhang, S. Chu, F. Zhu, H. Seidel, and H. Zhang, "Tunable wetting behavior of nanostructured poly(dimethylsiloxane) by plasma combination treatments", *Applied Physics Letters*, vol. 101, no. 22, pp. 221601, 2012

2012   A.S. Schneider, B. Heiland, **N.J. Peter**, C. Guth, E. Arzt, and I.M. Weiss, "Hierarchical super-structure identified by polarized light microscopy, electron microscopy and nanoindentation: Implications for the limits of biological control over the growth mode of abalone sea shells", *BMC biophysics*, vol. 5, no. 1, pp. 19, 2012

Patents:

2015	Patent CN102583233 B (Registration number CN201210066386.7):
	Translated title: "A method to create poly(dimethylsiloxane) surfaces with different wetting behaviors based on nanostructured substrates"
	Submitted: March 14th 2012
	Published: January 14th 2015
	Applicant: Peking University
	Inventors: Zhang H., Zhang X., Peter N., Zhu F., Chu S.

Proposals:

2020	"Mechanical properties and hydrogen tolerance of particle-reinforced CCA produced by additive manufacturing (MarioCCArt)"
	submitted to the German Research Foundation's (DFG) priority programme: "Compositionally Complex Alloys - High Entropy Alloys" (CCA-HEA, SPP 2006)
	Authors: Eric A. Jägle, Gerhard Dehm, Volker Uhlenwinkel, Eric Gärtner, Nicolas J. Peter
	GRANTED

Achievements

2016	Research visit scholar ship from the GERMAN ACADEMIC EXCHANGE SERVICE (DAAD) granted
2016	Research visit proposal at NATIONAL CENTER FOR ELECTRON MICROSCOPY (Berkeley, USA) accepted after internal review process
2015	Best talk award - 3rd prize at INASCON 2015 conference
2012	SCIENCE EXCELLENCE scholarship awarded by MLP SE

Düsseldorf, June 18th 2021